Title
The Variability of Atmospheric Rivers on Different Time Scales and Their Representation in Reanalyses and Observations

Author
Ma, Weiming

Publication Date
2022

Peer reviewed|Thesis/dissertation

UNIVERSITY OF CALIFORNIA

Los Angeles

The Variability of Atmospheric Rivers on Different Time Scales and Their Representation in Reanalyses and Observations

A dissertation submitted in partial satisfaction
of the requirements for the degree
Doctor of Philosophy in Atmospheric and Oceanic Sciences

by

Weiming Ma

2022

Abstract of the Dissertation

The Variability of Atmospheric Rivers on Different Time Scales and Their Representation in Reanalyses and Observations

by

Weiming Ma
Doctor of Philosophy in Atmospheric and Oceanic Sciences
University of California, Los Angeles, 2022
Professor Gang Chen, Chair

Atmospheric rivers (ARs) are filaments of enhanced water vapor transport in the atmosphere. Globally, ARs play a key role in the meridional moisture transport. Regionally, ARs can either serve as freshwater suppliers or culprits behind many of the weather hazards. ARs and their impacts have been studied extensively. However, what controls the variability of ARs on different time scales remains largely unknown. In particular, further studies are especially needed to better understand the relative role of circulation (dynamic) variability versus moisture (thermodynamic) variability, internal variability versus sea surface temperature (SST)/ sea ice variability and anthropogenic forcing versus internal variability originated from SST/sea ice variability in controlling the variability of ARs and their associated precipitation on different time scales. In addition, reanalyses have long been used as proxies of observations in AR studies. Yet, the representation of ARs and their associated precipitation in reanalyses remain unknown. Although satellite observations have also been used to study ARs, previous satellite-based AR studies used only the moisture component (integrated water vapor or IWV) to detect ARs. While ARs have been defined as filaments of enhanced moisture transport in the atmosphere, detecting ARs with only the moisture field would inevitably run the risk of detecting those filamentary features with high moisture content, but relatively weak transport component.

In this dissertation, we will address the research gaps above from five different angles. First, we investigate the relative role of SST/sea ice versus internal variability in driving the interannual variability of winter AR activities over the North Hemisphere. We show that, while both SST/sea ice and internal variability play roles in driving the interannual AR variability, their roles differ across ocean basins. Over the North Pacific, SST/sea ice variability exerts substantially stronger control on the AR variability compared to interval variability. However, both SST/sea ice and internal variability play comparable roles in modulating the AR variability over the North Atlantic. Second, on longer time scale, we discover that ARs over the Southern Hemisphere have been shifting poleward in the past four decades. Using a simple scaling method, we find that this poleward shift in the ARs is mostly driven by the poleward shift of the westerly jet (dynamic) while the contribution from the changes in the moisture field is relatively minor. Using two ensembles from the Community Earth System Model (CESM), one with fully coupled oceans and another one driven by observed SST/sea ice, we show that anthropogenic forcing is mainly responsible for the observed poleward shift. However, the negative phase of Interdecadal Pacific Oscillation (IPO) in recent decades also further drives the poleward shift in ARs. Third, ARs are expected to change under a warmer climate. However, the AR response to warming is determined by numerous factors. Two of the most prominent factors are the warming of the tropical upper troposphere, which can drive the poleward shift of the westerly jet, and the amplified warming of the polar regions, which can drive the equatorward shift of the westerly jet. Using nine models participated in the Polar Amplification Model Intercomparison Project (PAMIP), we investigate how Arctic Amplification and its associated sea ice loss would affect the boreal winter AR activities over the Northern Hemisphere. We find that, in response to Arctic sea ice loss, ARs extend northeastward over North Pacific and shift equatorward over North Atlantic. We further demonstrate that these response patterns are mostly determined by the responses in the circulation. Fourth, using a moisture budget approach, the relative contribution of dynamic change versus thermodynamic change to the intensification of extreme precipitation along

the North American West Coast (predominantly driven by ARs) is also quantified. We show the intensification of the extreme precipitation along the North American West Coast is mostly driven by the increase in moisture while the contribution from the dynamic change is minor. Lastly, we develop a novel method to detect ARs in satellite observations using both IWV and wind information based on the geostrophic winds. Using this method, we create satellite-based AR statistics and use these statistics to evaluate the performance of seven commonly used reanalyses in representing ARs and their associated precipitation. We show that both satellite observation and reanalyses show high agreement with each other in representing the AR frequency distribution. In terms of AR precipitation, ARs in reanalyses tend to precipitate too lightly and too often.

Our studies shed light on the mechanisms driving the variability of ARs across different time scales. These findings have important implications. First, given the more important role SST/sea ice variability in controlling the AR interannual variability, ARs in the North Pacific are likely more predictable than those over the North Atlantic. Better SST forecast can thus likely lead to better AR forecast along the North American West Coast. Second, on the interdecadal time scale, internal variability related to ocean processes still plays an important role in modulating AR variability. Internal variability should thus be taken into consideration when studying future AR response under warming. Third, our results indicate that the thermodynamic aspect of the AR and AR precipitation response is quite robust. We thus need to constrain the response in circulation to reduce the AR response uncertainty. Lastly, the finding that ARs in reanalyses tend to precipitate too often and too lightly directly questions the use of reanalysis-based precipitation in AR studies.

The dissertation of Weiming Ma is approved.

Karen McKinnon

Fred Martin Ralph

Alexander D. Hall

J. David Neelin

Gang Chen, Committee Chair

University of California, Los Angeles

2022

Table of Contents

List of Figures

List of Tables

Acknowledgments

My great-grandfather was in the U.S. West Coast more than one hundred years ago. He eventually returned to his hometown – a small farming village in Southern China. More than one hundred years later, most of his story has been lost in time. All I know is that, after returning to China, he used the money he made in the U.S. to purchase lands and properties and build a family. He never went back to the U.S. and spent the rest of his life in that small village. I had attempted to put all the pieces together and hoped to recover his story. Then I realized that this task is no longer possible. From time to time, I can't help but wonder: How did he make a living in the U.S.? Could he speak English? What did his life look like back then in the U.S.? Why did he decide to return to China eventually? I have no answer. I can only fill these voids with imaginations. In my imaginations, my great-grandfather sometimes worked at a laundry in Chinatown and spoke absolutely no English. Occasionally, I decide that I am going to let my great-grandfather be a chef in a Chinese restaurant. He made the best Chop Suey in town. However, out of all the versions, here is my favorite: my great-grandfather, who was a bounty hunter, could draw his Colt.45 faster than Billy the Kid.

Just like I would image what kinds of story my great-grandfather had lived, I suspect that he also imaged what kinds of life his offspring would live. No matter what he had ever imaged, I bet he could never image that his son, who happens to be my grandfather, would lose all the lands and properties through gambling one day. So here I am. After more than one hundred years, his great-grandson immigrated again to the U.S. for more or less the same reason - to make a living.

Life was hard when I first arrived in the U.S. Although I didn't work at a laundry in Chinatown, I spoke absolutely no English. I could not image how I could get through that period of time without the help from many of the great teachers and mentors I had met. I would like to thank all of them here: my high school math teacher Mrs. Li at Franklin High

School who always reached out to help me and encouraged me to realize my full potential; my Asian American History professor Tracy Lai at Seattle Central College who encouraged me to keep trying and keep writing (I confess. I drop writing during my PhD.); Professor Qiang Fu at UW who offered to write me a recommendation letter when he learned about my plan for graduate school; Professor Daehyun Kim at UW who gave me much guidance during my time at UW as well as during my graduate school application. I also want to thank Drs. Balwinder Singh, Phil Rasch, Hailong Wang and Hui Wan at PNNL for their great mentorship and tolerance on my stupidity during my time there in 2017. I have such a great experience (if the quality of the Asian food there is not considered) working at PNNL. I decide to go back for a postdoc.

I am deeply indebted to Professor Cecilia Bitz at UW. CC changed my life. Without her help, I would not be where I am today. I first knew CC in her climate dynamic class. I was quiet in her class. One day, she approached me and asked if I was interested in doing a research project with her. I was insecure and thought I was not good enough for any projects. So I said no. It wasn't until after I graduated, I realized that I probably should give research a try. I summoned up enough courage to send CC an email and didn't expect any replies. CC replied me and told me that she would be happy to work with me. That email was the start of everything happened afterward. I will be forever grateful to CC's help and encouragements. Her enthusiasm, her curiosity, her kindness and willingness to extend a helping hand will always be a source of inspiration to me. I will strive to become a scientist and a person like her.

I am also extremely fortunate to have Professor Gang Chen as my PhD advisor. When I first started my PhD, I knew very little about how to do research. Given my progress in the first two years of PhD, I thought I would give up before Gang giving up on me. However, Gang reassured me that he would help me and make sure that I would be able to graduate. Gang shows great patience to me. He is always willing to give me time to grow. He is also very good at seizing every opportunity to teach me how to do research. Without

him, I would not grow into who I am today. Growing up in an environment where asking for help was not encouraged and too often was associated with causing troubles, I have the inclination to deal with problems on my own. I suspect that Gang sees this inclination in me. He makes efforts to encourage me to ask for help if needed. I am deeply grateful for Gang's encouragements and his immense help during my PhD journey. I confess. I did occasionally make some complaints about Gang when I felt a little bit stressed out (Gang wouldn't see this sentence!). To be honest, I could not image that I can find another advisor who fits me better than Gang. If I were fortunate enough to become a faculty member one day, I will strive to become an advisor like Gang. Of course, I will also not get mad if my students complain about me when they feel a little bit stressed out (My potential future students will not see this sentence!).

Although she is no longer with me, I want to express my great gratitude to my grandma Xinqu Huang for her unconditional love. My grandma never received any formal education. She would always be proud of me no matter what I can achieve. I can already image what her reaction will be if I tell her that I just got my PhD. "Hi, grandma. I just received my PhD!" My grandma will be ecstatic. Then she will ask me: "What is PhD? By the way, have you eaten already?" "Nah, not important, just something trivial. Grandma, what have you cooked for dinner tonight?" Grandma, I miss you.

My immense gratitude also goes to my doctoral committee members, Professors David Neelin, Alex Hall, Marty Ralph and Karen McKinnon, for their willingness to serve in my committee and all the constructive feedback on my research. Thanks should also go to all my collaborators: Bin Guan, Jesse Norris, Yannick Peings, Pengfei Zhang, Hui Su and Christine Shields. Their constructive and insightful feedback have helped improved my research greatly. I have also learned a lot from them.

I cannot image what my graduate school experiences would look like without the support from all my lovely friends. I find myself very lucky. Somehow, all of the friends I made during graduate school have perfect temper. While I always seize every opportunity to "make fun

of' them, they never get mad at me (If they do, they never show it.). Through this, I was able to maintain a relatively balanced mental state at the expense of theirs. Many thanks and apologies go to: Yue Huang (Occasionally, she seems to care about me.), Donglai Ma (He is from the Ma Clan.), Jiaqi Shen (She just told me that I need to acknowledge her.), Danny Leung, Kenyon Chow, Yidongfang Si (At least, she seemed genuine when she told me that she thought I was born in 1995.), Bowen Ge (We are in the same group.), Xiuyuan Ding (We are in the same group. He shows me more respect than Bowen does.), Gavin Madakumbura (His diligence makes me feel guilty.), Todd Emmenegger (I made fun of him in front of the entire department, but he seemed to enjoy it.), Ning Kang, Sunny Yeh, Yi-Hung Kuo, Wu Sun, Alex Arnold, Daniel Clements, Daniel McCoy, Illian DeCorte and Calvin Howes. My dear friends, if you can go back in time, when I approached you for the first time, would you still stand there or simply walk away?

I also cannot thank my girlfriend Jiatong Chen enough. She is always there with me through all the ups and downs during my PhD journey. I lose count of how many times I made her listen to my complaints and negativities. (Of course, I had some good news to share occasionally.) She is a patient and excellent listener and always has her own ways of cheering me up (although she disagrees with me sometimes). Her presence provides a source of motivation to me and, surely, makes my PhD journey a lot more enjoyable. I will be forever grateful for her company, her understanding and, most importantly, her love.

Lastly, I want to thank myself for not giving up.

Time flies, it has been more than one hundred years since my great-grandfather first set foot in the U.S. Nothing has changed. Everything has changed. At the end, I didn't work at a laundry in Chinatown, nor do I become a chef in a Chinese restaurant. And bounty hunter has long disappeared as a profession. Just like I would image what kinds of story my great-grandfather had lived, I suspect that he also imaged what kinds of life his offspring would live. Would he ever image that his great-grandson, who happens to be me, will graduate with a PhD from one of the top universities in the U.S. one day?

Funding support for my graduate education was provided by the UCLA Atmospheric and Oceanic Sciences Departmental Fellowship and the UCLA Dissertation Year Fellowship. Research costs were supported by the NSF AGS-1832842 (Chapters 2 and 4), NASA 80NSS-C21K1522 (Chapter 2, 4, and 6), NSF AGS-1742178 (Chapters 3 and 5) and 1608775 (Chapter 3), and the DOE DE-SC0016117 (Chapter 5).

Vita

2020–2022	Ph.D. Candidate in Atmospheric Sciences, University of California Los Angeles, USA
2017–2020	M.S. in Atmospheric Sciences, University of California Los Angeles, USA
2014–2016	B.S. in Atmospheric Sciences, University of Washington, USA
2011–2014	A.S., Seattle Central College, USA

Publications

1. **Ma, W.**, Norris, J., Chen, G. (2020). Projected Changes to Extreme Precipitation Along North American West Coast From the CESM Large Ensemble. *Geophysical Research Letters*, 47(1), 1-10. https://doi.org/10.1029/2019GL086038

2. **Ma, W.**, Chen, G., Guan, B. (2020). Poleward Shift of Atmospheric Rivers in the Southern Hemisphere in Recent Decades. *Geophysical Research Letters*, 47(21), 1-11. https://doi.org/10.1029/2020GL089934

3. Zhang, P., Chen, G., **Ma, W.**, Ming, Y., Wu, Z. (2021). Robust atmospheric river response to global warming in idealized and comprehensive climate models. *Journal of Climate*, 34(18), 7717-7734. https://doi.org/10.1175/JCLI-D-20-1005.1

4. **Ma, W.**, Chen, G., Peings, Y., Alviz, N. (2021). Atmospheric River Response to

Arctic Sea Ice Loss in the Polar Amplification Model Intercomparison Project. *Geophysical Research Letters*, 1-12. https://doi.org/10.1029/2021gl094883

5. **Ma, W.**, Chen, G. (2022). What Controls the Interannual Variability of the Boreal Winter Atmospheric River Activities over the Northern Hemisphere? *Journal of Climate*, 1–39. https://doi.org/10.1175/jcli-d-22-0089.1

CHAPTER 1

Overview

Atmospheric rivers (ARs) are long and narrow bands of intense water vapor transport in the atmosphere. Despite occupying only small portion of the atmosphere at any given time, these filamentary features play a key role in the meridional moisture transport as well as exert profound impacts on regional hydrological climate. An earlier study reveals that at least 90% of the poleward atmospheric moisture transport is delivered by ARs (*Zhu and Newell*, 1998). On regional scale, depending on their strength and duration, ARs can be either beneficial or detrimental (*Ralph et al.*, 2019). On one hand, ARs contribute significantly to the annual total precipitation for many regions around the world (*Dettinger*, 2011; *Rutz and Steenburgh*, 2012; *Viale et al.*, 2018). ARs are also identified as an effective mechanism for terminating persistent droughts and have been termed "drought busters" (*Dettinger*, 2013). On the other hand, extreme AR events have been found behind many of the weather hazards, such as extreme precipitation (*Chen et al.*, 2018; *Lavers and Villarini*, 2013; *Ma et al.*, 2020a), floods (*Dettinger*, 2011; *Henn et al.*, 2020; *Paltan et al.*, 2017) and wind extremes (*Waliser and Guan*, 2017). In recent years, it is increasingly recognized that ARs can have strong influence on the polar climate, such as inducing sea ice loss (*Hegyi and Taylor*, 2018; *Wang et al.*, 2020; *Woods and Caballero*, 2016) and affecting ice shelf stability (*Djoumna and Holland*, 2021; *Mattingly et al.*, 2018; *Wille et al.*, 2022).

Given such important roles ARs play in our climate system, a better understanding on the factors controlling AR variability on different time scales would be especially beneficial in improving the AR predictability. On the interannual time scale, El Nino Southern Oscillation (ENSO) has been shown to exert strong control on the AR variability along the North

American West Coast, with its influence dependent on the ENSO flavors (*Kim et al.*, 2019). On the longer time scale, the variability of ARs depends strongly on the anthropogenic forcing but is also confounded by the decadal internal variability (*Dong et al.*, 2021; *Ma et al.*, 2020b). Regardless of the time scale considered, AR variability arises from two different sources, namely, the variability in circulation and the variability in the moisture. For example, it has been shown that ARs' response to anthropogenic warming is predominantly controlled by the moisture change (*Zhang et al.*, 2021).

Despite efforts have been made in studying the role of SST, such as that associated with ENSO, in modulating interannual AR variability, how internal variability can confound the effects of SST remains unexplored. On the longer time scale, attempts have been made to look at the relative roles of dynamic factor versus thermodynamic factor in determining the future AR response (*Gao et al.*, 2015; *Payne et al.*, 2020; *Zhang et al.*, 2021). However, besides decomposing the total AR response uncertainty into the dynamic versus thermodynamic components, AR response can be influenced by the responses in different parts of the climate system. Notably, two anthropogenically driven processes play key roles in causing the AR response uncertainty: namely, the warming of the tropical upper troposphere, which drives the poleward shift of the westerly jet, and the amplified warming of the polar regions, which drives the equatorward shift of the westerly jet. How each of these individual process influences AR response remains unknown. Besides AR uncertainty, the mechanisms concerning the AR-induced precipitation receive less attention. Further studies are thus needed to better understand how AR precipitation, especially AR extreme precipitation, is going to respond to warming. In addition, investigating the mechanisms driving AR variability relies heavily on reanalyses which have long been served as proxies of observations. Yet, how well these reanalyses in representing ARs and AR precipitation are unknown. The reason for that is because global AR statistics derived directly from observations are not available. In this dissertation, I will address the research gaps listed above in the following chapters.

In Chapter 2, we first identify and characterize the leading modes of winter AR frequency

variability over the North Pacific and North Atlantic in reanalysis. We then demonstrate that the atmospheric global climate models from the Coupled Model Intercomparison Project phase 6 (CMIP6) can simulate these leading modes with high skill. Using a combined singular value decomposition (SVD) method, we systematically quantify the relative roles of SST/sea ice and internal variability in driving the interannual variability of the identified leading modes. We find that SST/sea ice forcing can explain about half and a quarter of the observed variance for the leading modes over the North Pacific and North Atlantic, respectively. These results highlight the more predictable nature of the AR variability over the North Pacific and improve our understanding on the AR variability and the associated mechanisms over the Northern Hemisphere.

In Chapter 3, we investigate the trend of ARs in the Southern Hemisphere. We find that ARs have been shifting poleward in the Southern Hemisphere over the past four decades. We then develop a simple scaling method which allows us to decompose the total trend into a dynamic and a thermodynamic component. We show that the observed trend is mostly driven by the poleward shift of the westerly jet while the trend in the moisture field plays relatively minor role. Using two large ensembles based on the Community Earth System Model (CESM) (*Kay et al.*, 2015), one fully coupled and another one with prescribed SST/sea ice, we demonstrate the combined roles of anthropogenic forcing and interdecadal internal variability in driving the observed AR trend. The findings of this study have important implications and suggest that internal variability on the interdecadal time scale must be taken into account when studying AR response to future warming.

In Chapter 4, we focus on the impacts of Arctic Amplification and its associated sea ice loss on the variability of ARs over the Northern Hemisphere. Using nine models participated in the Polar Amplification Model Intercomparison Project (PAMIP) (*Smith et al.*, 2019), we find that, in response to Arctic sea ice loss, ARs extend northeastward over the North Pacific and shift equatorward over the North Atlantic. We also investigate the relative roles of dynamic versus thermodynamic components, as well as those of the internal variability versus

model difference in driving the AR response uncertainty. Potential emergent constraints are also explored which may help to reduce the AR response uncertainty. In this study, we investigate an important source of certainty in AR response to anthropogenic warming. These findings provide us a more complete understanding on AR response to warming.

In Chapter 5, instead of the AR characteristics, we shift our focus to the AR-induced extreme precipitation with recurrence interval ranging from 0.1 year to 50 years along the North American West Coast. We find that, under a warming climate, AR extreme precipitation intensifies nearly everywhere. Using a moisture budget approach, we show that the intensification of extreme precipitation over the midlatitudes is predominantly driven by the increases in atmospheric moisture, namely the thermodynamic component. Over the subtropics, while the thermodynamic component still contributes positively to AR extreme precipitation, the dynamical changes suppress the light to moderate precipitation while enhancing the most extreme precipitation substantially. This work elucidates the mechanisms driving the intensification of AR-induced extreme precipitation along the North American West Coast and has important implications for water resource management and infrastructure planning for the regions.

In Chapter 6, we develop a novel method to detect ARs in satellite observation using both the integrated water vapor (IWV) and geostrophic winds derived from geopotential height. Using data from the Atmospheric Infrared Sounder (AIRS) and the Advanced Microwave Sounding Unit (AMSU) (AIRS/AMSU), we generate a set of satellite-based global AR statistics. These satellite-based AR statistics are then used to evaluate the representation of ARs and AR precipitation in seven commonly used reanalyses. We find that reanalyses are consistent with satellite observations in the AR frequency distribution. However, ARs in reanalyses tend to precipitate too often and too lightly. In this study, for the first time, we detect ARs in satellite observations using not only the IWV, but also the wind information. These results can also provide us more guidance on the uses of reanalyses in future AR studies.

CHAPTER 2

What Controls the Interannual Variability of the Boreal Winter Atmospheric River Activities over the Northern Hemisphere?

[**Ma, W.**, Chen, G. (2022). What Controls the Interannual Variability of the Boreal Winter Atmospheric River Activities over the Northern Hemisphere? *Journal of Climate*, 1–39. https://doi.org/10.1175/jcli-d-22-0089.1]

Abstract

Interannual variability of the winter AR activities over the Northern hemisphere is investigated. The leading modes of AR variability over the North Pacific and North Atlantic are first identified and characterized. Over the Pacific, the first mode is characterized by a dipole structure with enhanced AR frequency along the AR peak region at about 30°N and reduced AR frequency further north. The second mode exhibits a tri-pole structure with a narrow band of positive AR anomalies at about 30°N and sandwiched by negative anomalies.Over the Atlantic, the first mode exhibits an equatorward shift of the ARs with positive anomalies and negative anomalies located on the equatorward and poleward side of the AR peak region at about 40°N respectively. The second mode is associated with the strengthening and east-

ward extension of the AR peak region which is sandwiched by negative anomalies. A large ensemble of atmospheric global climate models from the Coupled Model Intercomparison Project phase 6 (CMIP6), which shows high skills in simulating these modes, is then used to quantify the roles of sea surface temperature (SST) forcing versus internal atmospheric variability in driving the formation of these modes. Results show that SST forcing explains about half of the variance for the Pacific leading modes, while that number drops to about a quarter for the Atlantic leading modes, suggesting higher predictability for the Pacific AR variability. Additional ensemble driven only by observed tropical SST is further utilized to demonstrate the more important role that tropical SST plays in controlling the Pacific AR variability while both tropical and extratropical SST exert comparable influences on the Atlantic AR variability.

2.1 Introduction

Atmospheric rivers (ARs), defined as filaments of intense moisture transport in the atmosphere, exert profound impacts on the global hydrological cycle and regional weather extremes. Despite covering only about 10% of the latitude circumference in the midlatitudes at any given time, it is estimated that they are responsible for more than 90% of the poleward moisture transport (*Zhu and Newell*, 1998). ARs are important water suppliers for many regions around the world. On the one hand, they contribute significantly to the annual total precipitation to regions, such as the North American west coast, western Europe and Southern South America (*Dettinger*, 2011; *Rutz and Steenburgh*, 2012; *Lavers and Villarini*, 2015; *Viale et al.*, 2018). For example, it is estimated that California receives up to 50% of its annual total precipitation from ARs (*Dettinger*, 2011). On the other hand, they are also responsible for many weather extremes, such as extreme precipitation (*Lavers and Villarini*, 2013; *Leung and Qian*, 2009; *Lamjiri et al.*, 2017; *Ma et al.*, 2020a), extreme wind events (*Waliser and Guan*, 2017) and rain-on-snow events (*Guan et al.*, 2016; *Bozkurt et al.*, 2021; *McGowan et al.*, 2021). Recently, their presences in the tropics and the polar regions are

also starting to get recognized (*Woods and Caballero*, 2016; *Mattingly et al.*, 2018; *Nash et al.*, 2018; *Thapa et al.*, 2018; *Francis et al.*, 2020). ARs play complex roles in influencing the polar climate. Studies show that ARs can induce sea ice losses and ice sheet melting (*Mattingly et al.*, 2018; *Woods and Caballero*, 2016), but they can also cause anomalous snow accumulation (*Gorodetskaya et al.*, 2014). With ARs shifting poleward in both the present and future climate (*Zhang et al.*, 2021; *Gao et al.*, 2016; *Ma et al.*, 2020b), it's likely that ARs will exert stronger influences on the polar climate.

Considering the important roles that ARs play in the climate system, it is critical for both disaster preparation and water resource management to understand what controls their variability for timescales ranging from subseasonal-to-seasonal (S2S) to interannual. At the S2S timescale, Madden-Julian Oscillation (MJO) provides the dominant source of predictability for AR activities over the North Pacific (*Guan et al.*, 2012; *Zhou et al.*, 2021a), but its role is also modulated by the Quasi-biennial Oscillation (QBO) (*Mundhenk et al.*, 2018; *Baggett et al.*, 2017). By analyzing six decades of observed data, *Guirguis et al.* (2019) find that Arctic Oscillation, Eastern Pacific Oscillation and Western Pacific Oscillation strongly modulate subseasonal AR activities over Northern California, for which Northern California tends to receive more precipitation during boreal winter when these modes are in their negative phase. At the interannual timescale, *Gershunov et al.* (2017) find that landfalling ARs over the western North America during boreal winter are modulated by the Pacific Decadal Oscillation and the "blob" of warm SST off the Pacific Northwest (*Bond et al.*, 2015). ENSO, as the dominant mode of SST variability at the interannual timescale, has also been shown to exert strong influences on the AR landfalls along the North American west coast, with such influences being dependent on the ENSO flavors (*Kim et al.*, 2019; *Xiong and Ren*, 2021).

While ENSO can provide predictability for AR activities at the interannual timescale, internal atmospheric variability, which is intrinsic to the atmosphere, can also strongly modulate AR variability (*Teng and Branstator*, 2017; *Zhang et al.*, 2018; *Dong et al.*, 2018;

Kumar and Chen, 2017; *Chen et al.*, 2018; *Deser et al.*, 2018; *Cash and Burls*, 2019). One of such examples is the well-known failed 2016 winter rains in Southern California. The winter of 2015/16 was associated with a major El Nino event with magnitude comparable to the 1997/98 event. Historically, strong El Nino events tend to cause wet rainy seasons over California. This led to heightened expectations that the multi-year drought that California was experiencing at that time would finally be alleviated in 2016. However, the anticipated high rainfall in Southern California did not materialize that winter, leaving the drought continuing into 2017. A later modelling study suggests that this failed rainfall is not a response to the boundary forcing and attributes the cause to internal atmospheric variability (*Zhang et al.*, 2018). Indeed, using a large ensemble of models from the Atmospheric Model Intercomparison Project (AMIP) participated in CMIP5 (*Taylor et al.*, 2012), *Dong et al.* (2018) shows that about 80% of the interannual variability of winter precipitation in California is controlled by internal atmospheric variability. However, this view has been challenged recently. Using the newly defined ENSO Longitude Index, *Patricola et al.* (2020) argues that the failed 2016 winter rains in Southern California can be explained by the spatial pattern of the El Nino, rather than internal atmospheric variability. Given such complex interplay between the SST forcing and internal atmospheric variability in modulating AR and precipitation variability, a natural question to ask is what relative roles SST forcing versus internal atmospheric variability play in driving the interannual AR variability.

In this study, we will address the question posed above for the winter AR variability over the Northern hemisphere. To the best of our knowledge, only few studies have focused on the leading modes of winter AR variability over the North hemisphere so far, but the AR response to climate forcing is often dominated by the leading modes of low frequency variability. For example, by applying empirical orthogonal function (EOF) analysis to the integrated water vapor transport (IVT) field induced by ARs, *Dong et al.* (2018) identifies the two leading modes of winter AR variability over the North Pacific. They show that the first mode correlates strongly with the interannual variability of extreme precipitation

along the U.S. west coast. Over the North Atlantic, *Li et al.* (2022) identifies the first three modes of SST-forced winter AR variability using a 30-member ensemble of AMIP-style simulations. They also identify the large-scale climate modes behind these leading modes. In the first part of this study, we will first systematically identify and characterize the leading modes of interannual AR variability in the North Pacific and North Atlantic during winter in observation. A large ensemble of AMIP-type models from CMIP6 is then evaluated on their performance in simulating these modes (*Eyring et al.*, 2016). After showing that these models are capable of producing AR climatology and variability with high fidelity, we systematically quantify the roles of SST forcing versus internal atmospheric variability in driving the interannual variability of these modes. For the forced component of AR variability, the relative roles of tropical SST versus extratropical SST are also explored.

This paper is structured as follows. In section 2.2, we will first describe the observed datasets and the model datasets. We will then describe the AR detection algorithm and the EOF method used to extract the leading modes of AR frequency anomalies in observation. The singular value decomposition (SVD) method used to derive the leading modes of AR anomalies for the covariance between observation and models is also described in this section. Major findings will be presented in sections 2.3 and 2.4. A brief conclusion will be provided in section 2.5.

2.2 Data and Method

2.2.1 Observations and model datasets

This study focuses on the Northern Hemisphere winter season (December, January and February (DJF)) from 1979 to 2014, which covers the longest overlapping period between the observations and model datasets. The observed AR statistics are based on the daily mean of the 6-hourly horizontal winds and specific humidity at 1000, 850, 700 and 500 mb levels from the ECMWF Interim reanalysis (ERA-Interim) (*Dee et al.*, 2011) with spatial

resolution of 1.5°×1.5°. The detrended winter AR frequency anomalies are used to define the leading modes of AR variability on the interannual timescale, to be described in section 2c. Monthly sea level pressure from ERA-Interim is used to characterize the large-scale circulation associated with the leading modes of AR variability. Daily precipitation covering the period from 1996 to 2014 from Global Precipitation Climatology Project (GPCP) (*Huffman et al.*, 2001) is used to examine the winter mean and extreme precipitation anomalies associated with the leading modes of AR variability. In this study, the winter mean precipitation is defined as the total precipitation summed over all the daily precipitation during winter. Extreme precipitation is defined as the total precipitation summed over all the winter days with daily precipitation exceeding the 95th percentile of the winter daily precipitation. To test the robustness of the results, we also examine the daily precipitation calculated from the 12-hour accumulated precipitation from ERA-Interim, which covers the entire study period. The observed SST is from the Hadley Centre Sea Ice and Sea Surface temperature dataset (HadISST) (*Rayner et al.*, 2003).

AMIP models driven by observed changes in SST and sea ice are useful tools to study how boundary forcing drives the observed interannual variability of the atmosphere. To quantify the contributions of the SST/sea ice forcing versus the internal atmospheric variability in driving the interannual variability in ARs, a large ensemble of AMIP-type models participated in CMIP6 (i.e., 30 AMIP6 models) are used in this study. Some of the models contain more than one ensemble member, but only the first member with the tag "r1i1p1f1" is used. Details on the models' name, institution, horizontal resolution and the number of ensemble members used for each model are described in Table S1. Similar to ERA-Interim, daily horizontal winds and specific humidity at 1000, 850, 700 and 500 mb in the AMIP datasets are used to calculate the AR statistics.

In addition, we examine another model ensemble by including nine additional members for four of the models in the AMIP ensemble (i.e., ACCESS-ESM, CESM2, IPSL and MIROC6), making the ensemble size of each of these four models to be ten. We repeat the analysis with

this 40-member ensemble. The results based on this 40-member ensemble (not shown) are very similar to those based on the 30-member ensemble described in the previous paragraph. Therefore, only the results based on the 30-member ensemble are presented here except for Figures. 2.6 and 2.7.

Two additional ensembles from the CESM1 are also employed to investigate the roles of tropical SST versus extratropical SST in driving the AR variability. Similar to the AMIP models described above, one ensemble, which consists of 10 members, is driven by the observed global SST and sea ice and is termed "Global Ocean Global Atmosphere" (GOGA). Another ensemble, which also consists of 10 members, is driven by the observed SST only in the tropical ocean from $28°S$ to $28°N$ and climatological SST poleward of 35°. A linear interpolation zone is set between 28° and 35°. This ensemble is termed "Tropical Ocean Global Atmosphere" (TOGA). Daily horizontal winds and specific humidity at the lowest model level, 850, 500 and 200 mb are used to calculate AR statistics for these two ensembles.

2.2.2 AR detection algorithm

We employ the IVT-based AR detection algorithm developed by *Guan and Waliser* (2015). This algorithm detects ARs globally and is shown to compare favorably with other AR detection algorithms (*Guan and Waliser*, 2015). Many criteria, which are commonly used in other AR detection algorithms, are also employed in this algorithm, but the global algorithm used here helps identify large-scale AR activity patterns rather than local features. We will outline the major steps taken by this algorithm to detect ARs here. Readers are referred to *Guan and Waliser* (2015) for a more detailed description of the algorithm. Our analysis focuses on the winter mean AR frequency, which is defined as the fraction of time a grid point experiences AR condition in a given winter.

This algorithm first identifies contiguous regions of elevated IVT ("objects") based on the seasonally and regionally dependent 85^{th} percentile of IVT magnitude or100 $kgm^{-1}s^{-1}$, whichever is larger. To ensure coherence of the detected object, at least half of the grids

of the object should have the IVT direction within 45° of the object mean IVT direction. Since ARs are important for poleward moisture transport, the detected object is required to exhibit a mean poleward IVT of at least 50 $kgm^{-1}s^{1}$. A detected AR should also be longer than 2000 km and with a length-to-width ratio greater than 2. IVT is calculated by vertically integrating the moisture flux from the lowest vertical level to the highest vertical level using the 4 levels available for each dataset. The IVT threshold is calculated by using the entire study period of each individual dataset. Since this algorithm detects ARs based on a percentile threshold, the results in this study are not sensitive to the different vertical levels used among datasets (not shown).

2.2.3 Analysis Methods

EOF analysis is used to identify the leading modes of winter AR frequency anomalies over the North Pacific and North Atlantic, with the frequency weighted by the square root of the cosine of latitude. Following *Barnes and Polvani* (2013) and *Ma et al.* (2021), North Pacific and North Atlantic are defined as the regions from 0 to $90°N$ and $135°E$ to $125°W$ from 0 to $90°N$ and $60°W$ to 0°, respectively. Shifting the boundaries of these defined regions in either direction for a few degrees would not affect the results shown in this study. To evaluate the performance of AMIP models on simulating the leading modes in winter AR variability, centered pattern correlation is used to measure the spatial pattern similarity between the modes identified in observation and those derived from AMIP models. As we will show later, AMIP models generally show high skills in reproducing these leading modes, but biases still exist.

To quantify the contributions of SST/sea ice forcing versus internal atmospheric variability in the interannual variability of the observed leading modes, a combined SVD analysis (*Wallace et al.*, 1992; *Bretherton et al.*, 1992) between observation and AMIP ensemble is used in this study. Following *Mori et al.* (2019), SVD analysis of the covariance matrix of winter AR frequency anomalies between observation and simulations is used to derive the

leading modes of interannual AR variability. The spatial patterns derived from this covariance method are quantitively similar to those from the EOF analysis that is based on the variance of observations or individual simulations. But the leading modes obtained from this covariance method would explain the maximum squared temporal covariances between the observation and simulations over the analysis domains.

To carry out the SVD analysis, we first regrid all detrended winter AR frequency anomalies relative to their own climatology to a common spatial resolution of $1.5° \times 1.5°$. This can ensure that both observation and simulations have the same spatial dimension. A covariance matrix is then constructed between the observed AR anomalies and the simulated AR anomalies. More specifically, 30 members, one from each of the 30 AMIP models, are concatenated in the time dimension to form a matrix with time dimension size of 1050 (35 winters x 30 members, the row dimension).

$$M = \begin{pmatrix} model_1 & \cdots & model_{30} \\ \vdots & \ddots & \vdots \\ \vdots & \cdots & \vdots \end{pmatrix}$$

To match the time dimension size of 1050 in the simulations, we duplicate the observed time series 30 times to form a matrix for the observed anomalies.

$$O = \begin{pmatrix} observation & \cdots & observation \\ \vdots & \ddots & \vdots \\ \vdots & \cdots & \vdots \end{pmatrix}$$

The product of the two matrices along the time dimension forms a covariance matrix on which we carry out the SVD analysis (Eq. 2.1).

$$Cov[observation, models] = \frac{1}{1050 - 1}(OM^T) \tag{2.1}$$

The left and right singular vectors derived from this covariance matrix with largest singular values depict the spatial patterns of the leading modes of interannual winter AR variability in observation and simulations, respectively. The associated expansion coefficients (ECs) are obtained by projecting the detrended winter AR frequency anomalies onto the singular vectors, giving the time series for the 35-winter period in observation (also duplicates 30 times) and simulations in each ensemble member.

As will be shown in Figure 2.5, we evaluate models' skill in simulating AR variability which is defined as the standard deviation of winter AR frequency.

$$std(f)$$

where f is the time series of winter AR frequency for a mode with dimension of 35 (i.e. 35 winters). We further decompose the AR variability in models into a forced component driven by boundary forcing:

$$forced\ variability = std(\bar{f})$$

where $\bar{f}$ is the ensemble mean time series of winter AR frequency, and an internal variability component:

$$internal\ variability = \frac{1}{35}(\sum_{y=1}^{n} std(f_{all}^{y} - \bar{f}^{y}))$$

where y denotes the winter of the y^{th} year and *all* represents all models. For example, f_{all}^{1} represents the AR frequency of the 1^{st} winter (i.e. 1980) of all models (i.e. 30).

2.3 Observed EOF modes and model evaluations

2.3.1 The observed leading modes of winter AR variability based on EOF analysis

Figure 2.1 shows the observed leading EOF modes of winter AR anomalies over the North Pacific and the associated anomalies of sea level pressure, IVT, 850 mb zonal wind and integrated water vapor (IWV). The positive phase of the EOF mode is defined such that the anomalous AR frequency is enhanced over the U.S. west coast. The first mode is characterized by enhanced AR frequency over the AR maximum region and reduced AR activities further north (Fig. 2.1a). The spatial pattern of this mode is very similar to the first mode of the North Pacific winter AR variability based on AR IVT identified in *Dong et al.* (2018) (see their Fig 3c). The band of enhanced AR frequency extends northeastward and depicts higher than normal AR frequency along the North American west coast, especially along the U.S west coast. The associated sea level pressure anomaly pattern shows a low anomaly over the northeast Pacific, indicating southeastward shift of the Aleutian low (Fig. 2.1c). This low anomaly induces a cyclonic pattern in the IVT anomalies and enhances onshore IVT toward the west coast of North America. In agreement with the presence of a low anomaly over the northeast Pacific, the 850 mb zonal wind strengthens and extends eastward on the equatorward side of the climatological jet and weakens on the poleward side (Fig. 2.1e). This associated wind anomaly pattern also bears strong resemblance to the first EOF mode of 850 mb zonal wind anomalies over the Pacific (Fig. 2.A.1). Indeed, the principal component (PC) associated with AR variability correlates significantly with the PC of the 850mb zonal wind anomalies with correlation coefficient of 0.78. This implies that the interannual variability in ARs is mostly controlled by the variability in circulation. Moreover, the associated IWV shows positive anomalies over the eastern Pacific near/along the North American west coast (Fig. 2.1g). Both the positive anomalies in wind and IWV contribute to enhanced AR frequency along the North American west coast. Further away from the eastern Pacific,

negative IWV anomalies are seen nearly everywhere, even over regions with enhanced AR frequency. This again suggests a stronger role wind variability plays in regulating the AR variability.

The second mode depicts a narrow band of slightly enhanced AR frequency poleward of the AR maximum region, accompanied by negative AR anomalies on both sides of this positive AR anomaly (Fig. 2.1b). This mode also shows strong similarity to the second mode of the North Pacific winter AR variability in *Dong et al.* (2018) (see their Fig. 3f). The associated sea level pressure anomaly pattern shows a high anomaly over the central subtropical Pacific and a low anomaly over the northeast Pacific (Fig. 2.1d). This dipole pattern in sea level pressure resembles the North Pacific Oscillation (*Rogers*, 1981). Compared to the 1^{st} mode, the low anomaly is shifted northward and weaker in intensity (Fig. 2.1d and 2.1c), resulting in weaker IVT anomalies directed toward the northwestern U.S. and British Columbia. Consistent with the sea level pressure anomalies, the associated wind anomalies show strengthening and eastward extension of the jet (Fig. 2.1f). Since there is no significant IWV anomaly over the region off the west coast (Fig. 2.1h), the enhanced AR frequency there is mostly due to the strengthening of the winds.

Since ARs contribute significantly to both the mean and extreme precipitation for many regions around the world, Figure 2.2 displays the mean and extreme precipitation patterns associated with these leading AR modes. Consistent with the AR anomaly pattern (Fig. 2.1a), the first mode is associated with both enhanced mean and extreme precipitation over the eastern Pacific and along the U.S west coast (Fig. 2.2a and 2.2c). Reduced mean and extreme precipitation are found over the central north Pacific from about $30°N$ to $50°N$. Significant anomalies are also found in the tropics south of $20°N$, where no significant AR anomaly is found. Since most of the tropical precipitation is controlled by convective activities rather than ARs that are typically associated with cold fronts, significant precipitation anomalies over these latitudes likely result from the anomalies of these non-AR weather systems which covary with the AR mode. As shown in Figure 2.2b, the mean precipitation

anomalies associated with the second mode show a band of enhanced precipitation over regions at around $40°N$ stretching across the Pacific from about 180° to the coast of northwest U.S. Significant negative precipitation anomalies are also found over the coastal regions of northwest Pacific and central Pacific equatorward of the positive precipitation band. The negative anomalies over these regions are also significant for the extreme precipitation (Fig. 2.2d). Note that the GPCP covers a relatively short period. To test the robustness of the results, precipitation from ERA-Interim, which covers the whole period, is used to reproduce the above results. The anomaly patterns based on ERA-Interim are very similar to those based on GPCP, further corroborating the robustness of the results (Fig. 2.A.2).

We next switch to the leading EOF modes of ARs over the Atlantic, with the positive phase indicating enhanced AR frequency over the western Europe. The first mode shows substantial increases in AR frequency around $30°N$ stretching from the southeast of the U.S. to the Iberian Peninsula and northwest Africa (Fig. 2.3a). Reduced AR activities occur over higher latitudes stretching from northeast of the U.S. to the northwest of Europe. Consistent with the first mode of the North Atlantic winter AR variability in *Li et al.* (2022) (see their Fig. 2a), this pattern indicates the equatorward shift of ARs. Slightly higher than normal AR condition is also found over the Labrador Sea. Moreover, the first AR mode is closely related to the North Atlantic Oscillation (NAO) (*Hurrell et al.*, 2003) or a meridional shift of the Atlantic jet. The associated sea level pressure anomaly pattern shows a negative NAO-like pattern, with a positive anomaly poleward of about $70°N$ and a low anomaly over the north Atlantic from $30°N$ to $50°N$. This low anomaly induces a cyclonic anomaly in the IVT field, causing strong onshore IVT anomalies over the Iberian Peninsula and northwest Africa (Fig. 2.3c). Consistent with the equatorward shift of ARs, the associated zonal wind anomaly pattern also shows an equatorward shift of the jet with weakening of the winds on the poleward side and strengthening of the winds on the equatorward side of the jet (Fig. 2.3e). The associated IWV anomalies tend to have the same signs with the AR anomalies: regions with positive (negative) AR anomalies are also regions with positive (negative) IWV

anomalies (Fig. 2.3g).

As shown in Figure 2.3b, the second mode over the Atlantic shows enhanced AR frequency over the AR maximum region and reduced AR frequency on both sides, indicating the narrowing of the AR peak region rather than the shift by the first mode (Fig. 2.3a). This mode is also identified as the second mode of SST-forced North Atlantic winter AR variability in *Li et al.* (2022) (see their Fig. 4a). Compared to the spatial pattern in *Li et al.* (2022), the anomalies of this mode identified here extend more northeastward. This mode results in heightened AR activities over most of the coastal regions along the western Europe. The associated sea level pressure anomaly pattern shows a dipole structure with a low anomaly located at north Atlantic from $40°N$ to $70°N$ and a high anomaly from $20°N$ to $40°N$. This dipole structure enhances onshore IVT along the Europe west coast and also causes strengthening and eastward extension of the jet (Fig. 2.3d and 2.3f).

The two AR modes over the Atlantic also result in different regional impacts on precipitation. The first mode over the Atlantic is associated with widespread declines in precipitation over the North Atlantic, including large areas along the west coast of Europe and eastern Greenland. Significant decreases in extreme precipitation are only found over the high latitude regions of North Atlantic at around $70°N$. But significant increases in precipitation are found over regions at around $30°N$, especially over Iberian Peninsula (Fig. 2.4a). The Iberian Peninsula also tends to experience higher than normal extreme precipitation (Fig. 2.4c). Consistent with its AR anomaly pattern (Fig. 2.3b), the second mode tends to enhance both the mean and extreme precipitation over the Iberian Peninsula and Britain (Fig. 2.4b and 2.4d). Again, the results shown here are consistent with those based on the precipitation data from ERA-Interim (Fig. 2.A.3).

2.3.2 AMIP model evaluation

Before using the AMIP models to quantify the contributions of SST/sea ice forcing versus internal atmospheric variability to the interannual variability of the leading modes in AR

variability, we first evaluate their skills on simulating these modes shown in Figure 2.1 and 2.3. Figure 2.5a and 2.5b show the winter AR frequency climatology and AR variability defined as the standard deviation of winter AR frequency in observation and simulations, respectively. Overall, AMIP models can reproduce the climatology of AR distribution very well. They capture both the pattern and magnitude of the AR frequency over both the Atlantic and Pacific, except that the AR frequency over the AR maximum region in the Pacific is slightly underestimated. In terms of interannual variability, AMIP models reproduce both the spatial distribution and magnitude of the variability with high fidelity. They capture the maximum variability on the equatorward side of the climatological AR peak region. Decomposition of the AR variability in models shows that both the boundary-forced variability and the internally driven variability maximize over the equatorward side of the AR peak region (Fig. 2.5c and 2.5d), and that internally driven variability dominates over the boundary-forced variability at nearly all grid points. We also note that, for the leading AR modes, the percentage of variability explained by the boundary forcing can be greater than that for each grid point, which will be elaborated in section 2.4.

We next extract the leading modes of AR variability in the AMIP models using EOF analysis and evaluate how well models simulate the spatial structure of the observed leading modes using centered pattern correlation. Centered pattern correlation is the grid-by-grid spatial correlation between two anomaly spatial maps. The anomalies are computed by removing their own spatial mean from each map (centered). It measures the similarity of the spatial patterns between two maps. When performing EOF analysis on observations and simulations to extract the leading modes of the same field, the order of the leading modes in a model may not match those in observations. To resolve this problem, we apply the EOF swapping method (*Lee et al.*, 2019, 2021). For each ocean basin, we retain the first 3 leading modes identified in a model and calculate the pattern correlations between the first mode in observation and each of the 3 leading modes in the model. The mode in a model which has the highest correlation with the observed mode is then identified as the matching mode.

Similarly, to identify the corresponding second mode in a model, the pattern correlations between the observed second mode and each of the remaining 2 modes in the model are calculated. The simulated mode with the highest pattern correlation is identified as the second mode.

Figure 2.6 shows that AMIP models generally have high skills in reproducing the spatial structure of the observed modes, with the ensemble mean pattern correlations being 0.85, 0.69, 0.85 and 0.75 for the first and second modes in the Pacific and Atlantic, respectively. Models tend to simulate the first mode of each basin better compared to the second mode. Also, the box and whisker plots on the right show that the distribution for the 30-member ensemble, with one member from each of 30 AMIP models, is similar to that of the 40-member ensemble, with ten members from each of 4 AMIP models. This suggests that inter-member spread within one model is comparable to the inter-model spread, indicating that internal atmospheric variability is an important factor in causing the spread in skills, and that individual model biases play a less important role.

Moreover, the analysis on observation in section 2.3.1 has suggested that there is a tight relationship between the AR variability and circulation variability on the interannual timescale. That is, the PCs of the EOF modes derived from AR variability are strongly correlated with the corresponding PCs of the EOF modes derived from 850 mb zonal wind variability. Figure 2.7 shows that models are able to simulate this tight interannual relationship between AR variability and wind variability. The ensemble mean correlations for the PCs of the corresponding first and second AR/wind modes over the Pacific and Atlantic are 0.80, 0.69, 0.84 and 0.72, respectively. The observed correlations generally fall within the $25^{th} - 75^{th}$ percentile range of the inter-model spread, except for the second mode in the Atlantic which falls at the high end of the model spread.

In summary, the above results on the model evaluation suggest that AMIP models are capable of simulating the observed winter AR variability over the Northern hemisphere with high skills, justifying their uses to further investigate the roles of SST/sea ice forcing versus

internal atmospheric variability in driving the observed AR variability.

2.4 Internal atmospheric variability versus SST/sea ice forced variability

2.4.1 SVD modes of ARs and associated SST patterns

Having evaluated the EOF modes of individual models with the observed EOF modes, we next extract the SVD modes of ARs based on the interannual covariance between observation and models. This SVD analysis yields a pair of spatial patterns with the largest squared temporal covariances between observation and models. The SVD patterns for observation with the largest squared covariances resemble the observed EOF patterns that explain the largest percentages of AR variance (Figs. 2.1, 2.3 and 2.8), and the SVD patterns for models provide estimates for all the AMIP models.

Figure 2.8 shows that the SVD patterns of the AMIP models successfully reproduce the spatial structures in observation over both the Atlantic and Pacific, although there are minor differences between observation and simulations for the first mode over the Pacific and the second mode over the Atlantic. Specifically, for the first mode in the Pacific, models are able to capture the negative anomalies over the central north Pacific north of $306 \circ N$. They also produce a band of strong positive anomalies at the AR peak region. However, the positive anomalies in the ERA-Interim are tilted more northeastward and impinging toward the northwest US, while the positive anomalies in the AMIP models are more zonally oriented, making California as the regions mostly affected by this mode. For the second mode over the Atlantic, despite models being able to reproduce the tri-pole pattern with positive anomalies at the AR peak region and negative anomalies on both sides, the positive anomalies in the models shift southwestward compared to observation.

The SST anomaly patterns corresponding to these leading SVD modes are displayed in

Figure 2.9 by regressing the SST anomalies onto the standardized ECs of the observation and the ensemble mean EC of the AMIP models for the 35 winters. Over the Pacific, the first mode of AR variability is associated with an SST pattern which resembles the positive phase of ENSO (Fig. 2.9a and 2.9b). Indeed, the observed nino3.4 index is strongly correlated with the ensemble mean EC of the AMIP models at 0.76. Widespread of warm anomalies extend from the eastern equatorial Pacific and reach the western equatorial Pacific. The warm anomalies spread toward the extratropics along the eastern Pacific and reach the north Pacific above $40°N$. Encircled by the positive anomalies, negative SST anomalies originated from western equatorial Pacific extend northeastward and southeastward in the Northern and Southern Hemispheres, respectively. Significant positive SST anomalies are also found in the Indian Ocean. Moreover, the SST anomalies associated with the second AR mode also show positive anomalies over the equatorial eastern Pacific (Fig. 2.9c and 2.9d). However, compared to the pattern associated with the first mode, the positive anomalies are more confined zonally in observation (Fig. 2.9c), and both zonally and meridionally in models (Fig. 2.9d). The negative anomalies originating from the equatorial western Pacific extend more eastward and northward. This SST anomaly pattern over the Pacific bears strong resemblance to the North Pacific Mode (NPM) (*Deser and Blackmon*, 1995; *Park et al.*, 2012). Widespread positive anomalies are also found over the Indian Ocean and western Pacific along the East Asian coast. Further analysis shows that the SST patterns over the Pacific associated with the first and second modes of AR variability also resemble the first and second leading EOF modes of the observed interannual SST variability over the North Pacific (Fig. 2.A.4).

For the Atlantic AR modes (Fig. 2.9e, f, g, and h), the associated SST anomaly patterns over the Pacific are very similar to those associated with the AR modes of the Pacific, but with slightly smaller magnitude and shrinked areas with significant anomalies. Stronger and significant SST anomalies are found over the Atlantic, highlighting an important role that Atlantic SST plays in modulating the AR variability locally.

The results in Figure 2.9 also indicate that the SST patterns in observation tend to be less coherent and significant compared to the SST patterns obtained from simulations, and the differences are especially pronounced for the Atlantic modes (Fig. 2.9e and g). Since the SST patterns from simulations are obtained by regressing the SST anomalies onto the ensemble mean EC, these SST patterns are thus associated mostly with the forced AR variability. Therefore, the differences between SST patterns in observation and simulations imply a large fraction of internally driven variability contained in the observed ECs, especially for the modes in the Atlantic.

2.4.2 Relative roles of SST/sea ice forcing versus internal atmospheric variability in driving AR variability

We next quantify the roles of SST/sea ice forcing versus internal atmospheric variability in the leading modes of AR interannual variability using the coefficient of the determination (r^2) approach (Figure 2.10). Indeed, internal atmospheric variability plays an important role in driving the AR variability over both the Pacific and Atlantic as indicated by the large inter-model spread in the ECs. Over the Pacific, about half of the variance in the leading modes can be explained by the SST forced variability, but that fraction drops to about a quarter for the Atlantic modes, confirming that internal atmospheric variability indeed plays a more important role in driving the AR variability over the Atlantic.

Given such an important role internal atmospheric variability plays in the AR variability,can it alone drive the formation of the leading AR modes shown in Figure 2.8? To answer this question, we apply EOF analysis to the intra-ensemble AR anomalies based on model simulations. To obtain the intra-ensemble AR anomalies, for each model, we first removed their own winter AR frequency climatology from the winter AR frequency time series. After that, the ensemble mean anomalous winter AR frequency was calculated which represents the forced AR variability. This forced component was then removed from the anomalous winter AR frequency of each model to get the internally driven component. Finally, we

concatenated the internally driven components from all models together to obtain the intra-ensemble AR anomalies. Results from this analysis identify leading modes nearly identical to those based on the SVD analysis of the covariance between observation and models or the EOF of individual models or observation (compared Figures 2.1, 2.3, 2.8 and 2.A.5), suggesting that the leading modes forced by SST can also occur naturally due to internal atmospheric variability. These results are also consistent with *Ma et al.* (2021) in which they discover similar leading modes of AR variability by using an ensemble of models driven by the climatological annual cycle of SST from the Polar Amplification Model Intercomparison Project (PAMIP).

Given that both SST/sea ice forcing and internal atmospheric variability play such important roles in shaping the AR variability, their contributions to the magnitude of the total variance are further quantified. We estimate the total variance by calculating the variance of the ECs corresponding to the leading SVD modes during the 35 winters. The total variance of each mode in models is based on ECs across all models. Figure 2.11 indicates that AMIP models underestimate the variance for all modes, with the largest underestimate for the second Atlantic mode. We further estimate the magnitude of the forced variance in models by calculating the variance of the ensemble mean EC of each mode. The forced variance accounts for about half of the total variance for the Pacific modes, while that number drops to about 40% and 30% for the first and second Atlantic modes, respectively. These results further support that AR variability over the Atlantic is more strongly modulated by internal atmospheric variability compared to the Pacific AR variability.

Lastly, we investigate how much of the total observed variability in the AR EOF modes is regulated by the leading EOF modes of SST over each of the ocean basins by using the coefficient of determination (r^2) approach. The first SST mode over the Pacific associated with ENSO significantly correlates with both the first modes of the Pacific and Atlantic and explains about 30% and 17% of their observed total variance, respectively. The second SST mode over the Pacific, which resembles the NPM, exerts strong influences on the second

Pacific AR mode, and explains about half of the observed total variance of this mode. Moreover, we perform EOF analysis on the SST anomalies over the North Atlantic (Figure 2.A.6). The first mode shows a tri-pole pattern of SST anomalies over the North Atlantic, which resembles the SST anomaly pattern of the second AR mode over the Atlantic. Similar to the SST anomaly pattern of the first AR mode over the North Atlantic, the second mode in SST also shows a dipole pattern over the North Atlantic. Consequently, the leading modes of AR variability over the North Atlantic are also related to the leading SST modes over the North Atlantic. The first and second SST modes in the Atlantic explains about 20% of the observed total variance of the second and first modes of AR variability, respectively.

2.4.3 Tropical versus extratropical SST in driving the forced AR variability

Based on the SST patterns associated with the leading modes of AR variability (Figure 2.9), significant SST anomalies can be seen over both the tropical and extratropical oceans, suggesting both play roles in driving the forced AR variability. To better understand the relative roles of tropical SST versus extratropical SST in driving the forced AR variability, we analyze two additional ensembles based on CESM1. One ensemble with 10 members,termed "GOGA", is driven by observed SST globally. Another ensemble also with 10 members, termed "TOGA", is driven by observed SST only in the tropics. Despite their smaller ensemble size compared to the 30-member AMIP ensemble, they are still useful in providing an estimate on the relative roles of tropical SST versus extratropical SST in AR variability. The same combined SVD analysis is applied to the covariance matrix between observation and simulations based on GOGA.

Results show that GOGA is able to reproduce both the leading SVD modes of AR variability over the Pacific and the first mode over the Atlantic. The strengthening and eastward extension of ARs associated with the second mode over the Atlantic are too weak in the models (Fig. 2.A.7). Compared to the results based on the AMIP ensemble, the 10-member GOGA underestimates the fraction of forced variance in the first Pacific mode while

overestimating that in the second Atlantic mode (Fig. 2.12). The fraction of forced variance for the second Pacific mode and first Atlantic mode are consistent with those based on the AMIP ensemble. They explain about half and a quarter of the total variance, respectively, for the second Pacific mode and the first Atlantic mode. Consistent with the results based on the AMIP ensemble, AR variability in the Pacific is more strongly controlled by the SST variability compared to the AR variability in the Atlantic. For the forced variability, the role of the tropical SST variability dominates over the extratropical SST variability for both the leading modes over the Pacific, explaining about 77% and 71% of the total forced variability, respectively. Over the Atlantic, tropical SST explains about 49% and 56% of the total forced variability for the first and second mode, respectively, suggesting comparable role tropical SST versus extratropical SST plays in driving these modes.

2.5 Conclusions

A better understanding of the mechanisms controlling the interannual AR variability is crucial for water resource management and hazard warning (*Paltan et al.*, 2017; *Henn et al.*, 2020; *Dettinger*, 2011; *Ralph et al.*, 2006). In this study, we identify and characterize the leading modes of AR variability over both the Pacific and Atlantic during boreal winter, with distinct precipitation patterns and impacts over different coastal regions, similar to *Dong et al.* (2018) and *Li et al.* (2022). Over the Pacific, the first mode is characterized by a dipole structure with substantial enhanced AR frequency over the AR peak region and reduced AR activities further north (Fig. 2.1a). The second mode depicts a tri-pole pattern with a band of positive anomalies extended from west Pacific at about $306\circ N$ to northeast Pacific, accompanied by negative anomalies on both sides (Fig. 2.1b). The first AR mode in the Pacific significantly modulates precipitation along the U.S. west coast while the second mode mostly affects precipitation over the U.S. Northwest and British Columbia (Fig. 2.2). Over the Atlantic, the first mode represents the equatorward shift of the ARs, with significant impacts along the entire west coast of Europe, while the second mode represents

strengthening and eastward extension of the AR peak region, with the effects confined more toward the southern part of the west coast (Fig. 2.3a and b). It is worth mentioning that, given the strong correlation between the leading modes of AR variability and the corresponding leading modes of 850 mb zonal wind variability, the spatial patterns of the leading AR modes identified in this study do not depend on the AR detection algorithms used. Indeed, these leading modes of AR variability can also be identified in nearly all of the Tier 1 AR catalogues based on the global AR detection algorithms participated in the Atmospheric River Tracking Method Intercomparison Project (not shown; *Shields et al.* (2018)). As such, the AR modes identified here can serve as metrics to evaluate the AR variability in climate models.

We have quantified, perhaps for the first time, the relative roles of SST forcing versus internal atmospheric variability in driving the interannual variability of the leading AR modes by using a large ensemble of AMIP-type models participated in the CMIP6. We first show that the AMIP models have high skills in simulating many aspects of these modes, including their spatial structure and the strong coupling between circulation variability and AR variability.

Then, a combined SVD analysis using both observation and AMIP models is adopted to extract the leading modes of AR co-variability between observation and models. Based on the SVD analysis, the forced variability explains about half of and a quarter of the total variance for the leading AR modes over the Pacific and the Atlantic, respectively. These results suggest higher predictability of the AR variability over the Pacific compared to the Atlantic. The associated SST patterns for the leading modes over the Pacific bear marked resemblance to the corresponding leading modes of North Pacific SST, characterized by an ENSO-like (*Xiong and Ren*, 2021; *Kim et al.*, 2019) and an NPM-like (*Deser and Blackmon*, 1995; *Park et al.*, 2012) anomalous SST pattern, respectively. Further analysis reveals that these two Pacific SST modes also play some roles in the corresponding leading modes of Atlantic AR variability. Additionally, a model ensemble driven by observed SST only in the

tropical oceans is used to quantify the relative importance of tropical versus extratropical SST in exciting these leading modes of AR variability. Results show that tropical SST variability dominates over extratropical SST variability and contributes more to the total forced AR variability over the Pacific. Over the Atlantic, the tropical and extratropical SST play comparable roles in the formations of the leading modes of AR variability.

Our findings may have important implications for the interannual variations of boreal winter precipitation. While the SST variability modes, such as ENSO or NPM, provide some sources of predictability for the North American west coast, the predictability is limited by the internal variability of the atmosphere (*Teng and Branstator*, 2017; *Zhang et al.*, 2018; *Kumar and Chen*, 2017; *Dong et al.*, 2018; *Chen et al.*, 2018; *Deser et al.*, 2018; *Cash and Burls*, 2019), especially for the well-known failed 2016 winter rains in Southern California (*Zhang et al.*, 2018; *Patricola et al.*, 2020). *Dong et al.* (2018) estimates that about 80% of the interannual variability of winter precipitation in California is controlled by internal atmospheric variability, but we find that internal atmospheric variability only accounts for about half of the variability in the two Pacific AR modes. As both AR modes can influence the North American west coast (Fig. 2.2), this indicates that the winter precipitation related to the two AR modes may be more predictable. Our analysis also indicates that SST variability over the Pacific basin can influence the AR variability not only locally over the Pacific, but also remotely over the Atlantic (Fig. 2.9), similar to the remote influence of ENSO on NAO (*Li and Lau*, 2012; *Brönnimann*, 2007; *Zhang et al.*, 2019a). Moreover, the leading AR modes forced by SST can appear as the dominant pattern in the AR response to Arctic sea ice loss (*Ma et al.*, 2021) and also occur naturally due to internal atmospheric variability (Fig. 2.A.5). Further research is needed to better understand the mechanisms of internal atmospheric variability in driving AR variability at shorter timescales. This can potentially improve AR forecast at S2S timescale. Overall, the results presented in this study not only improve our physical understanding of the AR variability, but may also lead to better seasonal AR prediction over the densely populated regions, such as the North

American west coast and the Western Europe.

Acknowledgements. Weiming Ma and Gang Chen are supported by National Science Foundation Grants AGS-1832842 and NASA Grant 80NSS-C21K1522. We thank three anonymous reviewers for their constructive feedback that greatly improved the manuscript. The authors would like to acknowledge high-performance computing support from Cheyenne (https://doi.org/10.5065/D6RX99HX) provided by NCAR's Computational and Information Systems Laboratory, sponsored by the National Science Foundation.

2.6 Figures

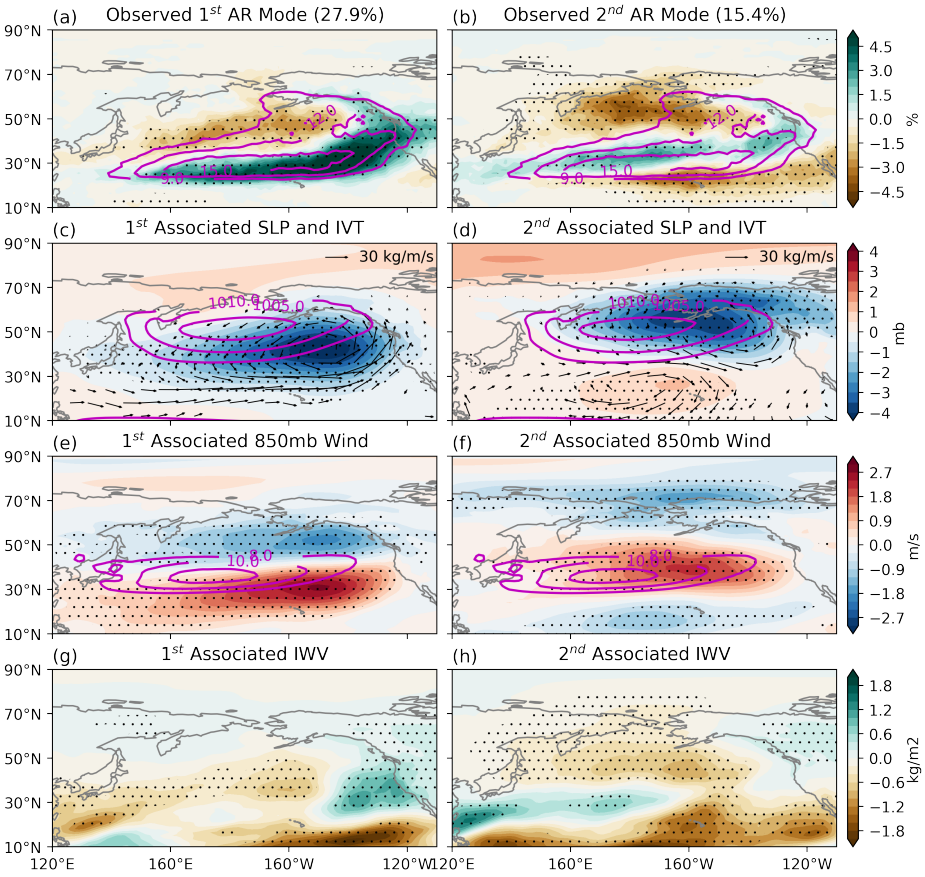

Figure 2.1: Observed AR frequency anomalies (a), (b), sea level pressure and IVT anomalies (c), (d), 850 mb zonal wind anomalies (e), (f), IWV anomalies (g), (h) associated with the first and second EOF modes of winter AR anomalies over the North Pacific, respectively. The values (i.e., 27.9% and 15.4%) in the title of (a) and (b) indicate the percentage of variance explained by each EOF. Patterns are the regression coefficients obtained by regressing their anomaly fields onto the respective standardized principal components (PCs) (i.e., linear regression between the time series of the anomaly fields and the time series of the standardized PCs). Solid contours in (a), (b), (c), (d), (e) and (f) indicate the climatology of the respective field. Shaded contours show the anomalies. Stippling indicates regions with anomalies significant at 95% confidence level based on Student's t test.

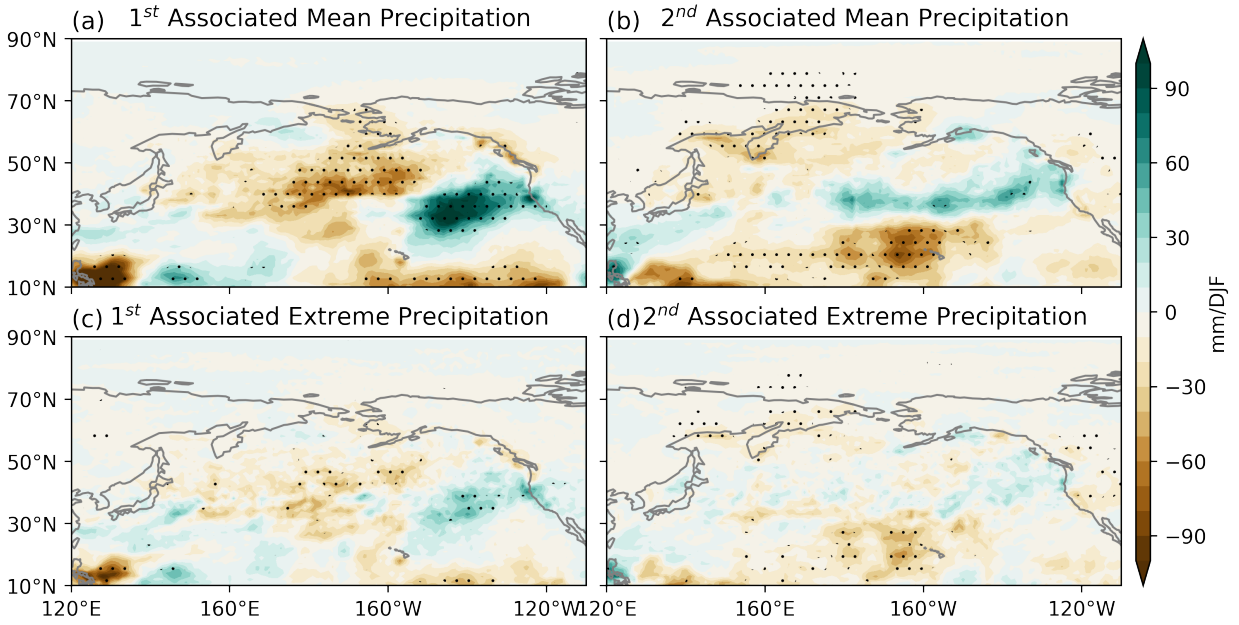

Figure 2.2: As in Figure 2.1, but for mean precipitation (a), (b) and extreme precipitation (c), (d) anomalies associated with the first and second EOF modes of winter mean AR anomalies over the North Pacific, respectively. Precipitation anomaly patterns are obtained by regressing their anomaly fields onto the respective standardized principal components (PCs) (i.e., linear regression between the time series of the precipitation anomaly fields and the time series of the standardized PCs). Stippling indicates regions with anomalies significant at 95% confidence level based on Student's t test.

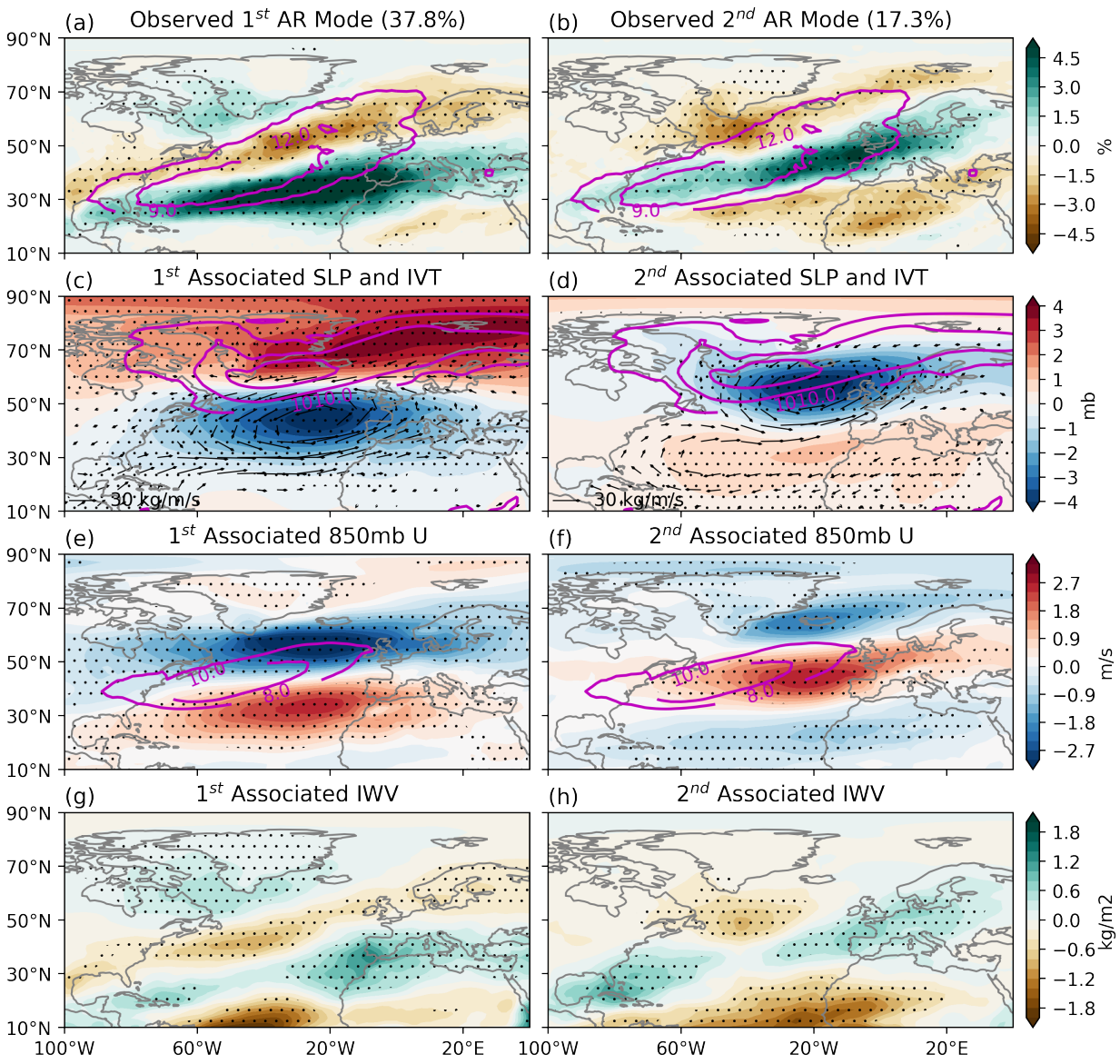

Figure 2.3: As in Figure 2.1, but for the North Atlantic: observed AR frequency anomalies (a), (b), sea level pressure and IVT anomalies (c), (d), 850 mb zonal wind anomalies (e), (f), IWV anomalies (g), (h) associated with the first and second EOF modes of winter AR anomalies, respectively. Patterns are obtained by regressing their anomaly fields onto the respective standardized principal components (PCs). Solid contours in (a), (b), (c), (d), (e) and (f) indicate the climatology. Shaded contours show the anomalies. Stippling indicates regions with anomalies significant at 95% confidence level based on Student's t test.

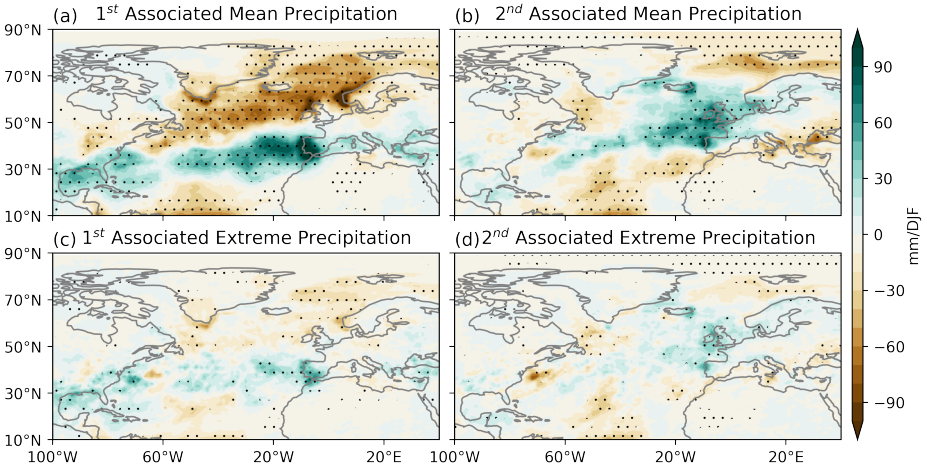

Figure 2.4: As in Figure 2.3, but for mean precipitation (a), (b) and extreme precipitation (c), (d) anomalies associated with the first and second EOF modes of winter AR anomalies over the North Atlantic, respectively. Patterns are obtained by regressing their anomaly fields onto the respective standardized principal components (PCs). Stippling indicates regions with anomalies significant at 95% confidence level based on Student's t test.

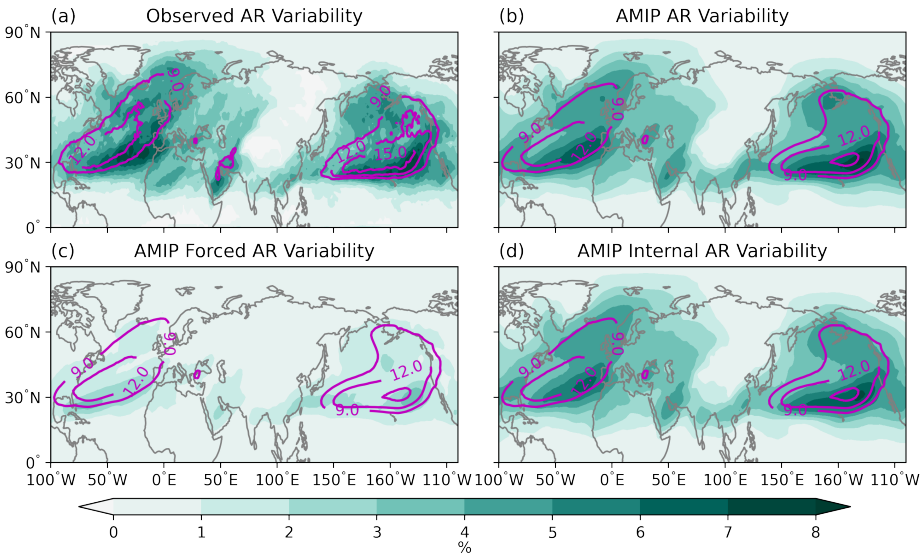

Figure 2.5: Observed (a) and simulated ensemble mean (b) AR climatology (solid contours) and variability (shaded contours). AR variability is defined as the standard deviation of the winter mean AR frequency. (c) and (d) show the forced and the internally driven components of the total variability in the AMIP models for each grid point. Forced variability is calculated as the standard deviation of the ensemble mean winter AR frequency across the 35 winters. Internally driven variability is estimated by the multi-year average of the standard deviations across all model anomalies relative to the ensemble mean (i.e. after removing the forced component).

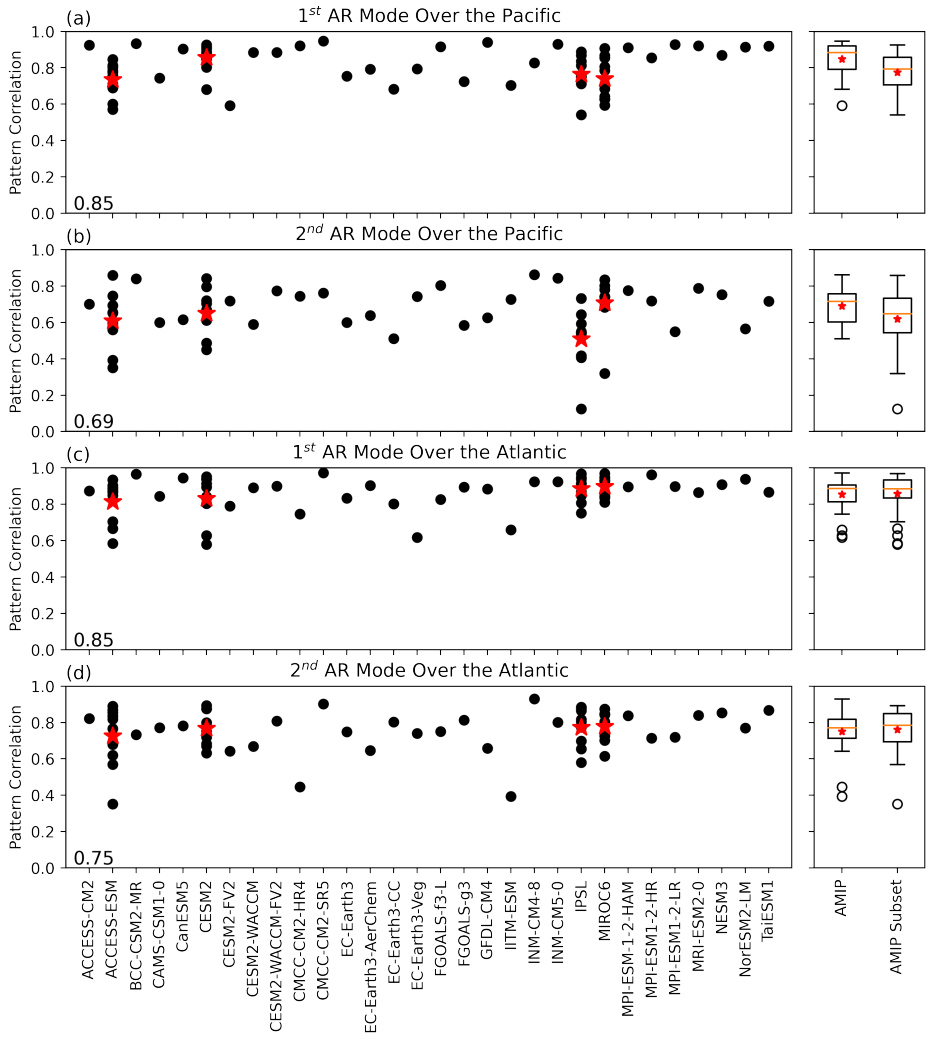

Figure 2.6: Centered pattern correlations between observation and simulations of the AR anomalies associated with the first (a), (c) and second (b), (d) EOF modes of AR variability over the North Pacific and North Atlantic, respectively. Values at the lower left corner indicate the ensemble mean pattern correlations. Four of the models (ACCESS-ESM, CESM2, IPSL and MIROC6) have ten members. Their ensemble means are indicated by a red star. The box and whisker plots on the right show the inter-model spreads of the pattern correlations for the 30-member AMIP ensemble with only the first member of each model("AMIP") and the 40-member ensemble from the four models which each has 10 members ("AMIP Subset"). The box shows the 25th and 75th percentile of the spread. The upper and lower whiskers are defined by the formula $75^{th}percentile + 1.5 \times (75^{th}percentile - 25^{th}percentile)$ and $25^{th}percentile - 1.5 \times (75^{th}percentile - 25^{th}percentile)$ respectively. Values outside of the whiskers are considered as outliers. The orange horizontal lines show the median while the red stars ensemble means.

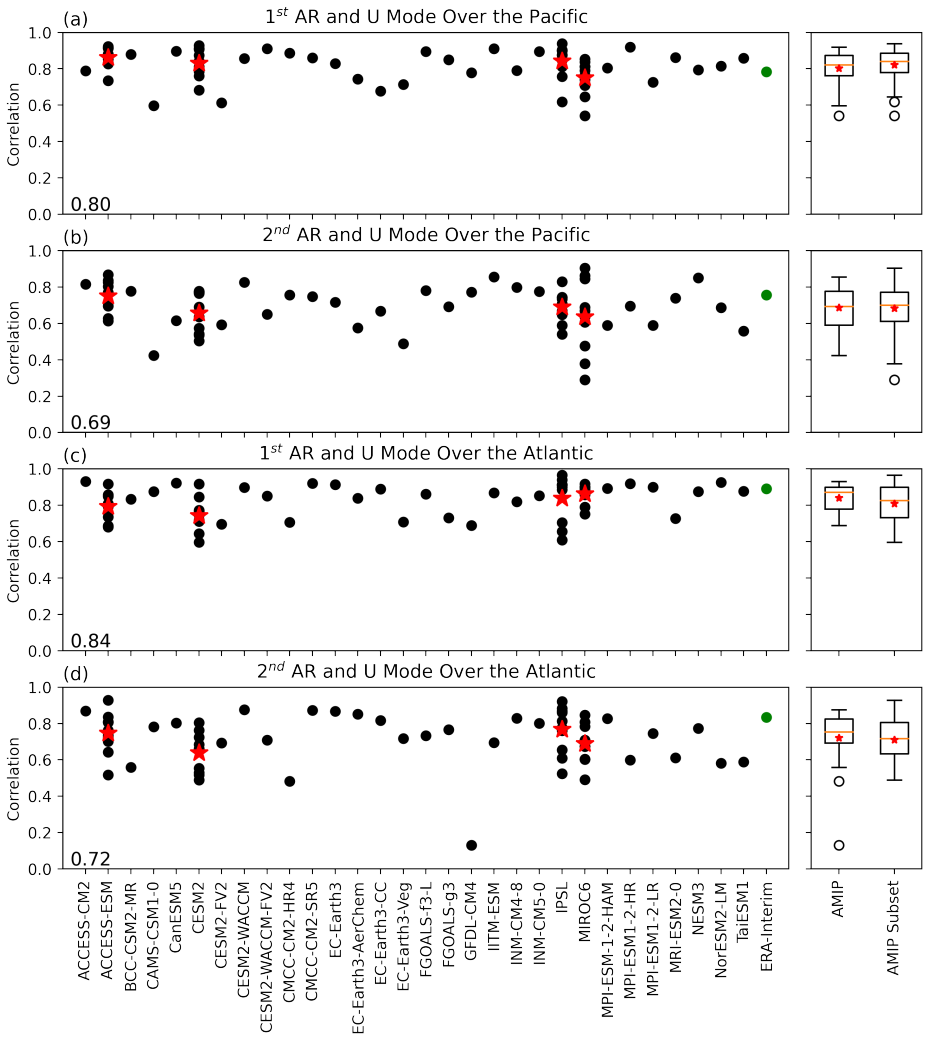

Figure 2.7: As in Fig. 2.6, for correlations between the principal components (PCs) associated with the EOF modes of AR anomalies and the corresponding PCs associated with EOF modes of 850 mb zonal wind anomalies for the first (a), (c) and second (b), (d) modes over the North Pacific and North Atlantic, respectively. Values at the lower left corner indicate the ensemble mean correlations. Four of the models (ACCESS-ESM, CESM2, IPSL and MIROC6) have ten members. Their ensemble means are indicated by a red star. Green dots represent the observed values. The box and whisker plots on the right show the inter-model spreads of the correlations for the 30-member AMIP ensemble ("AMIP") and the 40-member ensemble from the four models which each has 10 members ("AMIP Subset").

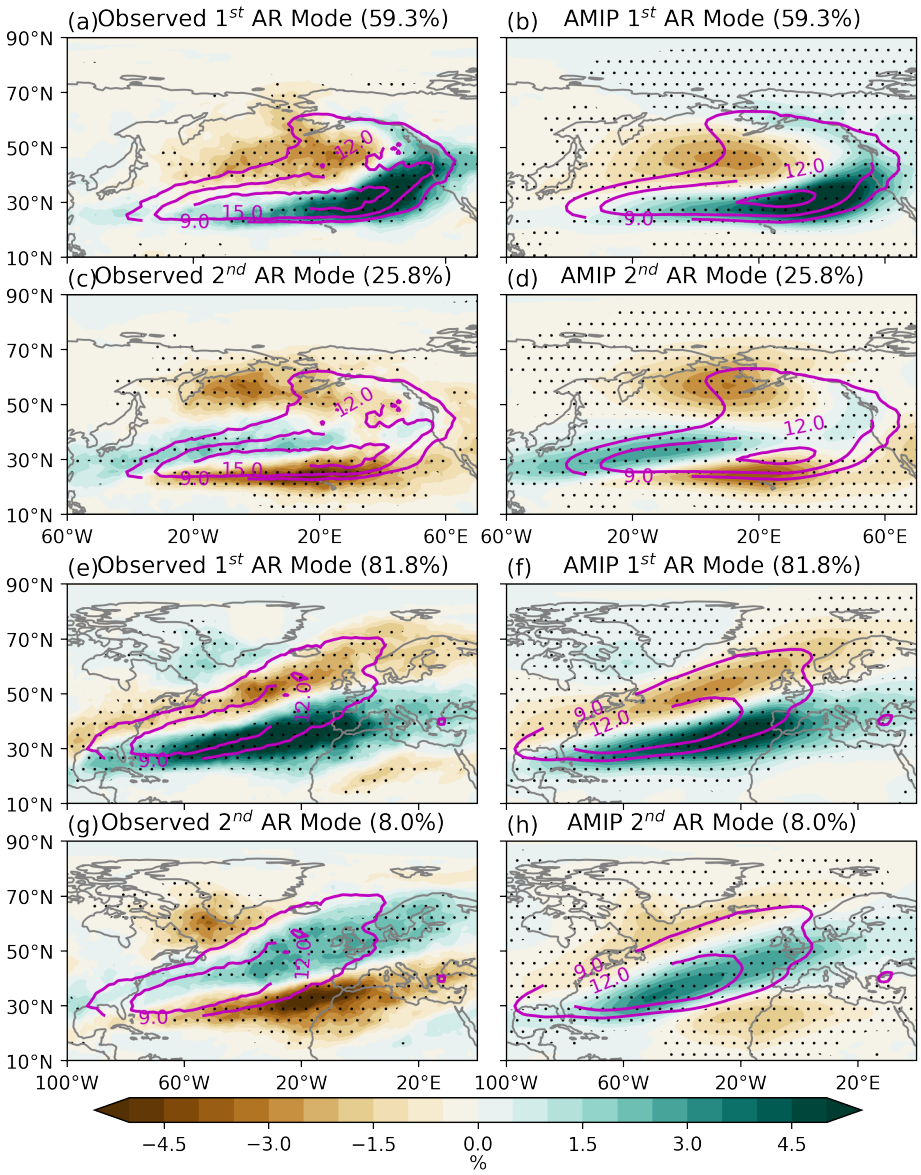

Figure 2.8: Leading modes of AR anomalies obtained from the SVD analysis of the covariance between observation and simulations. First (a), (b) and second (c), (d) modes of AR anomalies over the North Pacific. First (e), (f) and second (g), (h) modes of AR anomalies over the North Atlantic. Left and right panels display results from observation and simulations, respectively. The values in the title of each subpanel indicate the percentage of squared covariance explained by each SVD. Anomaly patterns in observation are obtained by regressing AR anomalies onto the standardized expansion coefficients (ECs) of 35 winters. Regressions in simulations are based on the 1050 winters across all ensemble members (30 members, each has 35 winters). Solid contours indicate climatology of winter AR frequency. Shaded contours represent anomalies. Stippling indicates regions with anomalies significant at the 95% confidence level based on Student's t test.

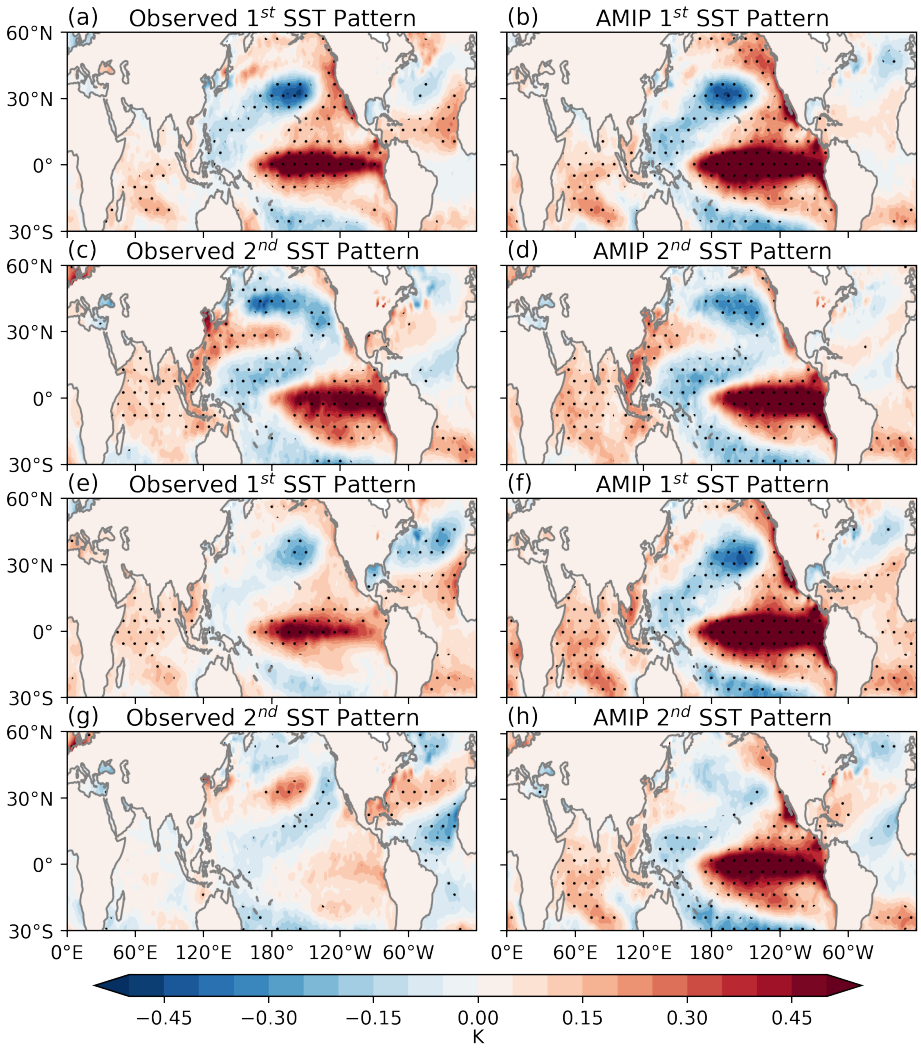

Figure 2.9: As in Fig. 2.8, but for SST anomalies associated with the leading modes of AR anomalies obtained from the SVD analysis of the covariance between observation and simulations. First (a), (b) and second (c), (d) modes of SST anomalies over the North Pacific. First (e), (f) and second (g), (h) modes of SST anomalies over the North Atlantic. Left and right panels show results from observation and simulations, respectively. Anomaly patterns in observation are obtained by regressing the SST anomalies onto the expansion coefficients (ECs) of the 35 winters. Anomalies in simulations are based on the ensemble mean EC. Stippling indicates regions with anomalies significant at the 95% confidence level based on Student's t test.

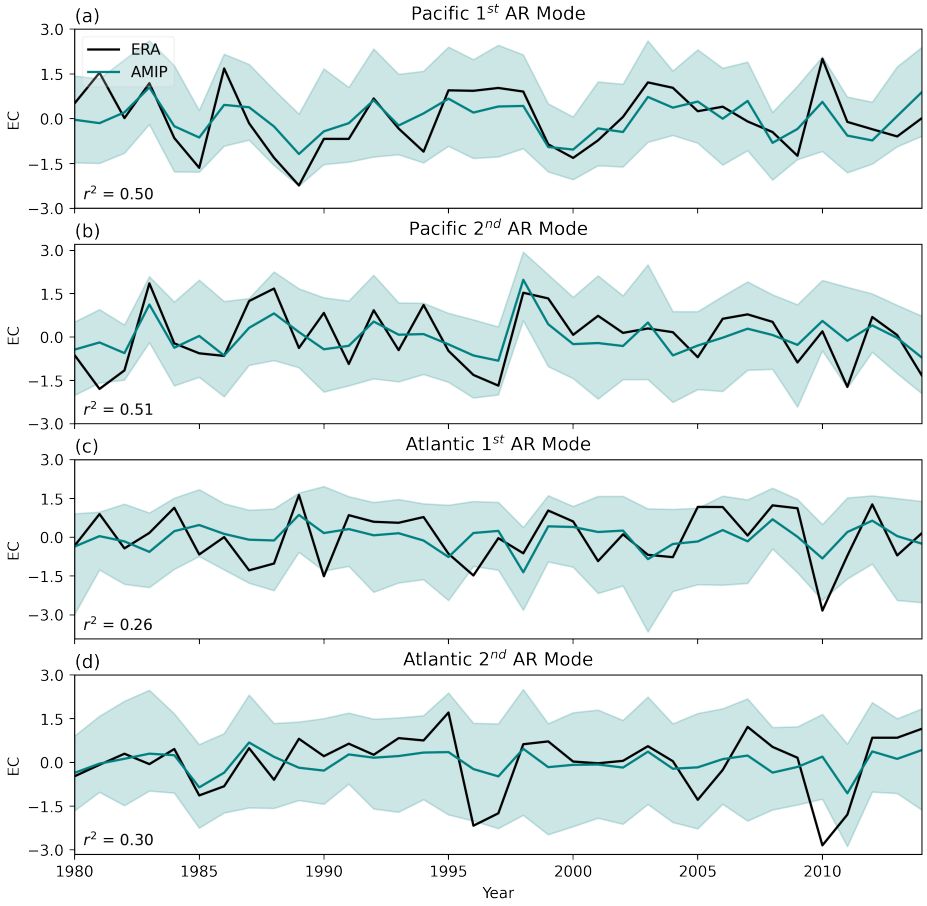

Figure 2.10: Expansion coefficients (ECs) for the first (a), (c) and second (b), (d) SVD modes of AR anomalies over the North Pacific and North Atlantic, respectively. Black and teal curves show ECs for the observation and ensemble mean EC for simulations, respectively. R2 between the observed ECs and the corresponding simulated ensemble mean EC are shown at the lower left corners of each panel. The shading shows the 2.5th and 97.5th percentile range of the model spread.

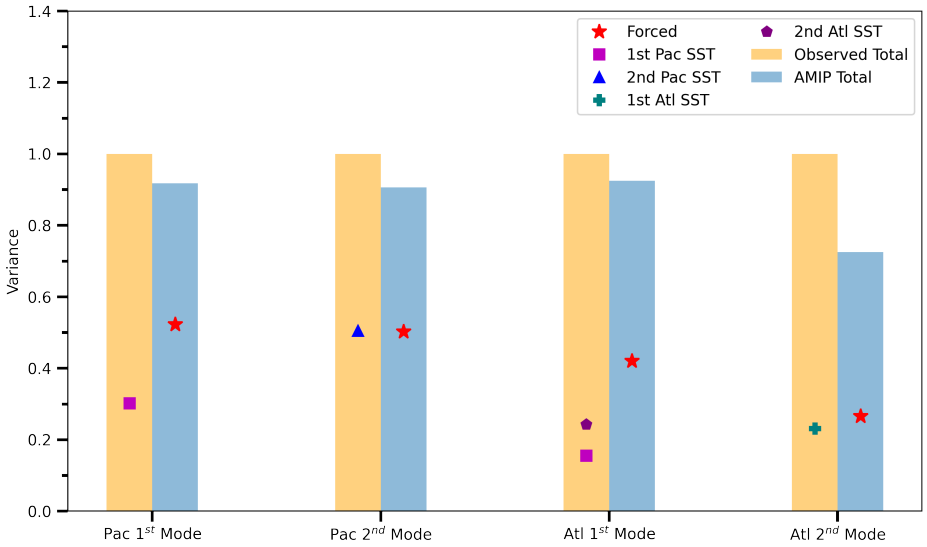

Figure 2.11: Magnitude of the total variance (yellow bars) in observation and simulations (blue bars). Red stars indicate the magnitude of the forced variance. Markers indicate the contributions of different SST modes to the total variance of the observed leading SVD modes of AR anomalies. The values for each mode are scaled by the observed total variance. See the text for more information on how the statistics shown in this figure are calculated.

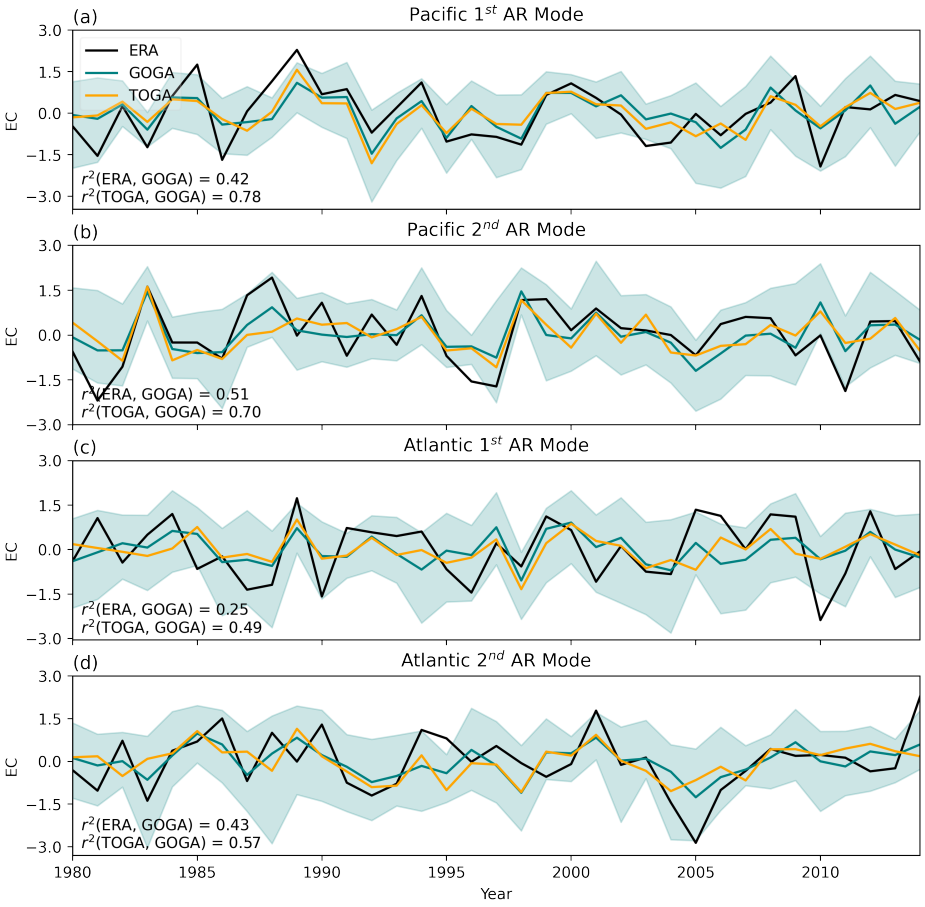

Figure 2.12: Same as Figure 2.10, but for the results based on the GOGA and TOGA ensembles.

Appendix

2.A Supplement

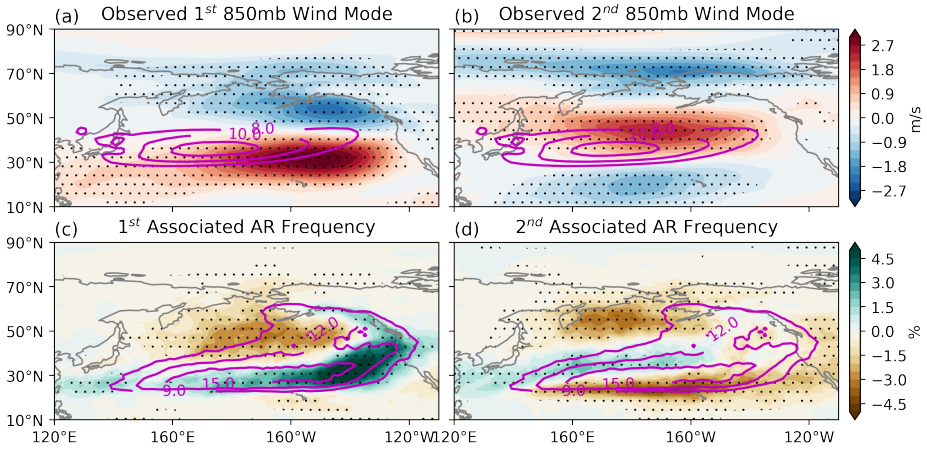

Figure 2.A.1: Observed 850 mb zonal wind anomalies (a), (b) and AR frequency anomalies (c), (d) associated with the first and second modes of winter 850 mb zonal wind anomalies over the North Pacific, respectively. Patterns are obtained by regressing their anomaly fields onto the respective standardized principal components (PCs). Solid contours indicate the climatology. Shaded contours show the anomalies. Stippling indicates regions with anomalies significant at 95% confidence level based on Student's t test.

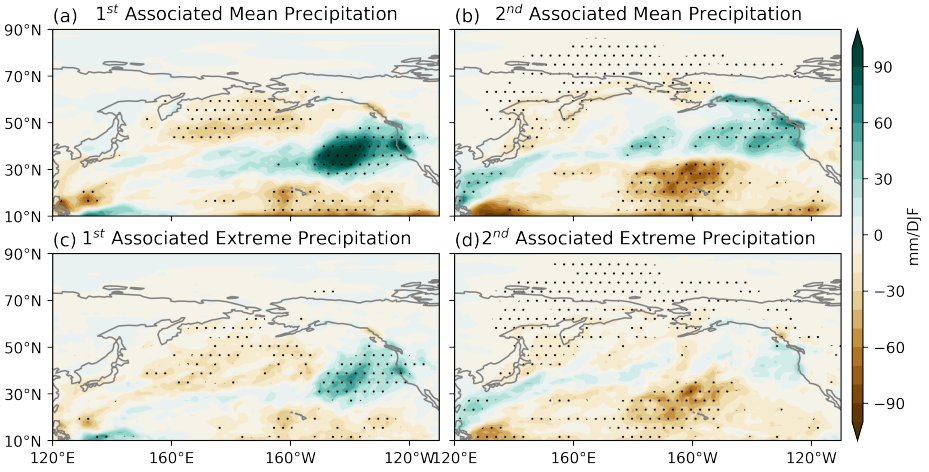

Figure 2.A.2: Same as Figure 2.2, but based on precipitation data from ERA-Interim.

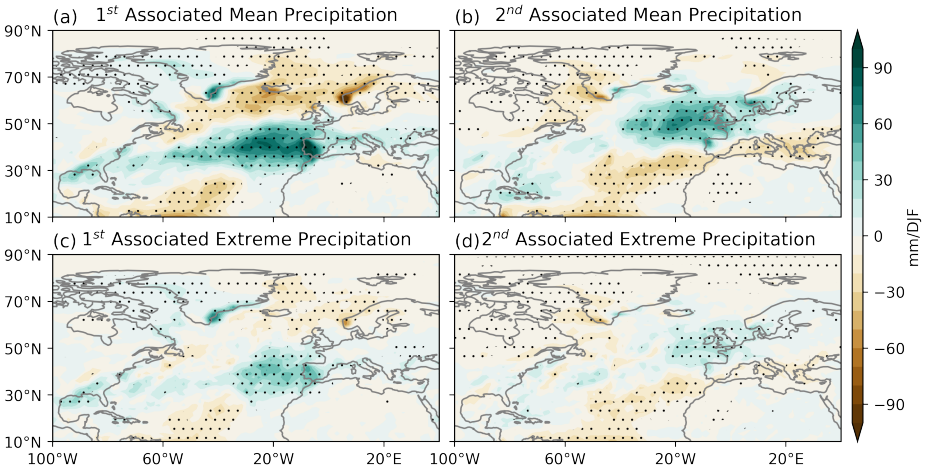

Figure 2.A.3: Same as Figure 2.4, but based on precipitation data from ERA-Interim.

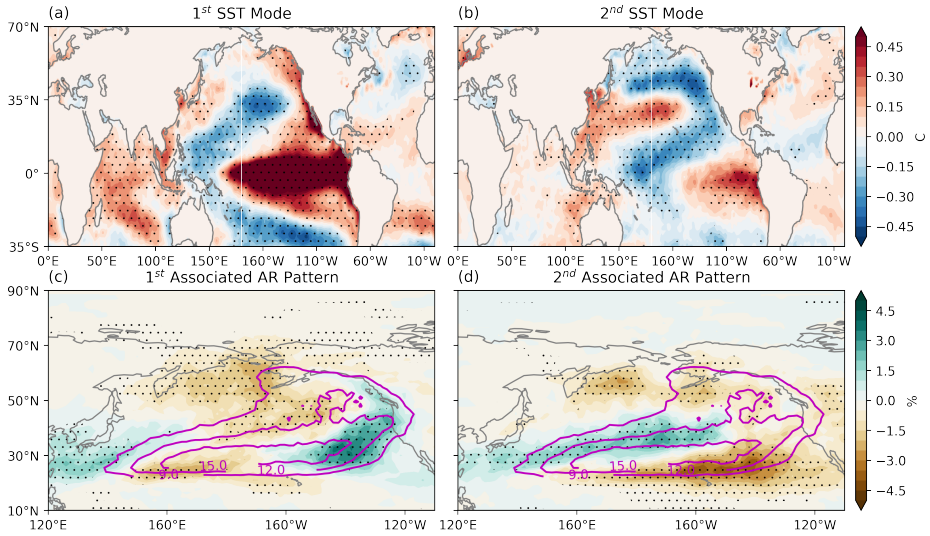

Figure 2.A.4: Observed SST anomalies (a), (b) and AR frequency anomalies (c), (d) associated with the first and second modes of winter SST anomalies over the Pacific ($30°S - 60°N, 120°E - 105°W$), respectively. Patterns are obtained by regressing their anomaly fields onto the respective standardized principal components (PCs). Solid contours in (c) and (d) indicate the climatology. Shaded contours show the anomalies. Stippling indicates regions with anomalies significant at 95% confidence level based on Student's t test.

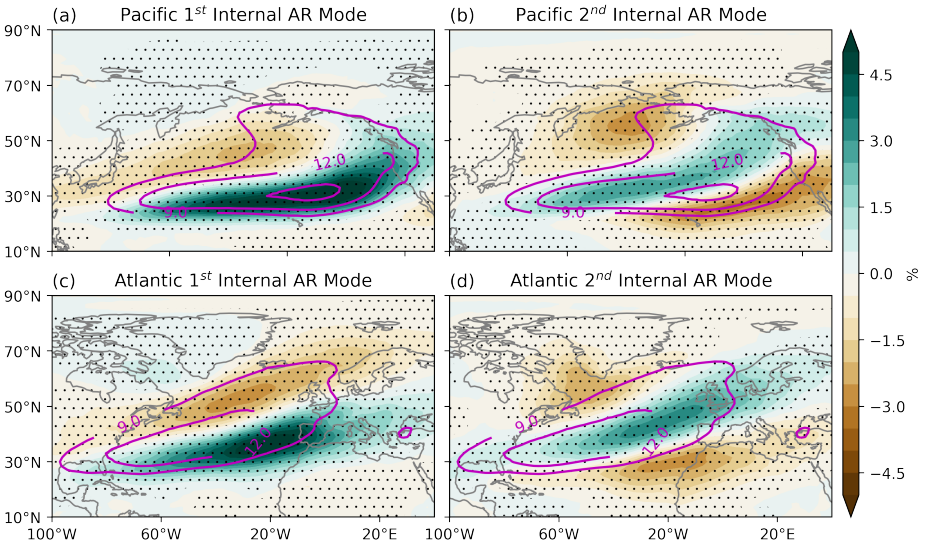

Figure 2.A.5: AR frequency anomalies associated with the first (a), (c) and second (b), (d) internal modes of AR anomalies over the North Pacific and North Atlantic, respectively. Patterns are obtained by regressing their anomaly fields onto the respective standardized principal components (PCs) across models. Solid contours indicate the climatology. Shaded contours show the anomalies. Stippling indicates regions with anomalies significant at 95% confidence level based on Student's t test.

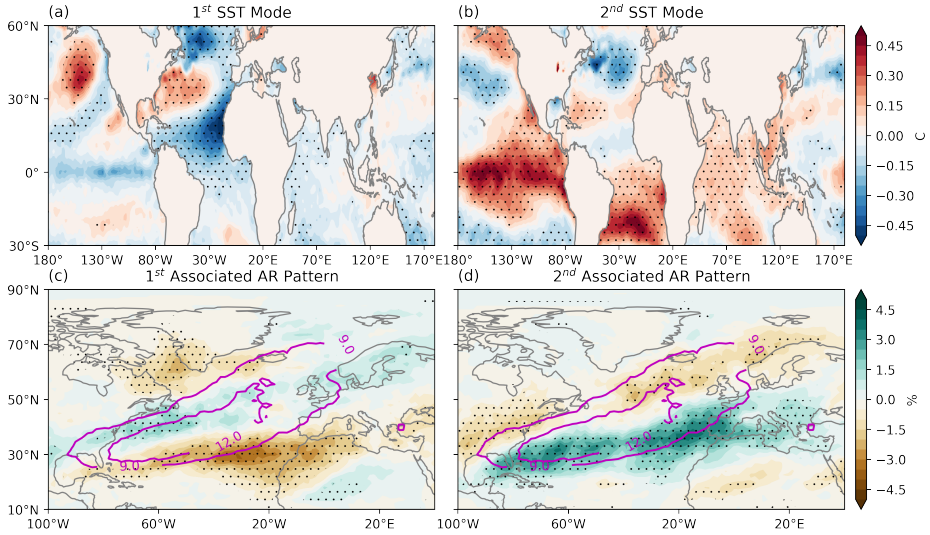

Figure 2.A.6: Observed SST anomalies (a), (b) and AR frequency anomalies (c), (d) associated with the first and second modes of winter SST anomalies over the Atlantic ($30°S - 65°N, 60°W - 0$), respectively. Patterns are obtained by regressing their anomaly fields onto the respective standardized principal components (PCs). Solid contours in (c) and (d) indicate the climatology. Shaded contours show the anomalies. Stippling indicates regions with anomalies significant at 95% confidence level based on Student's t test.

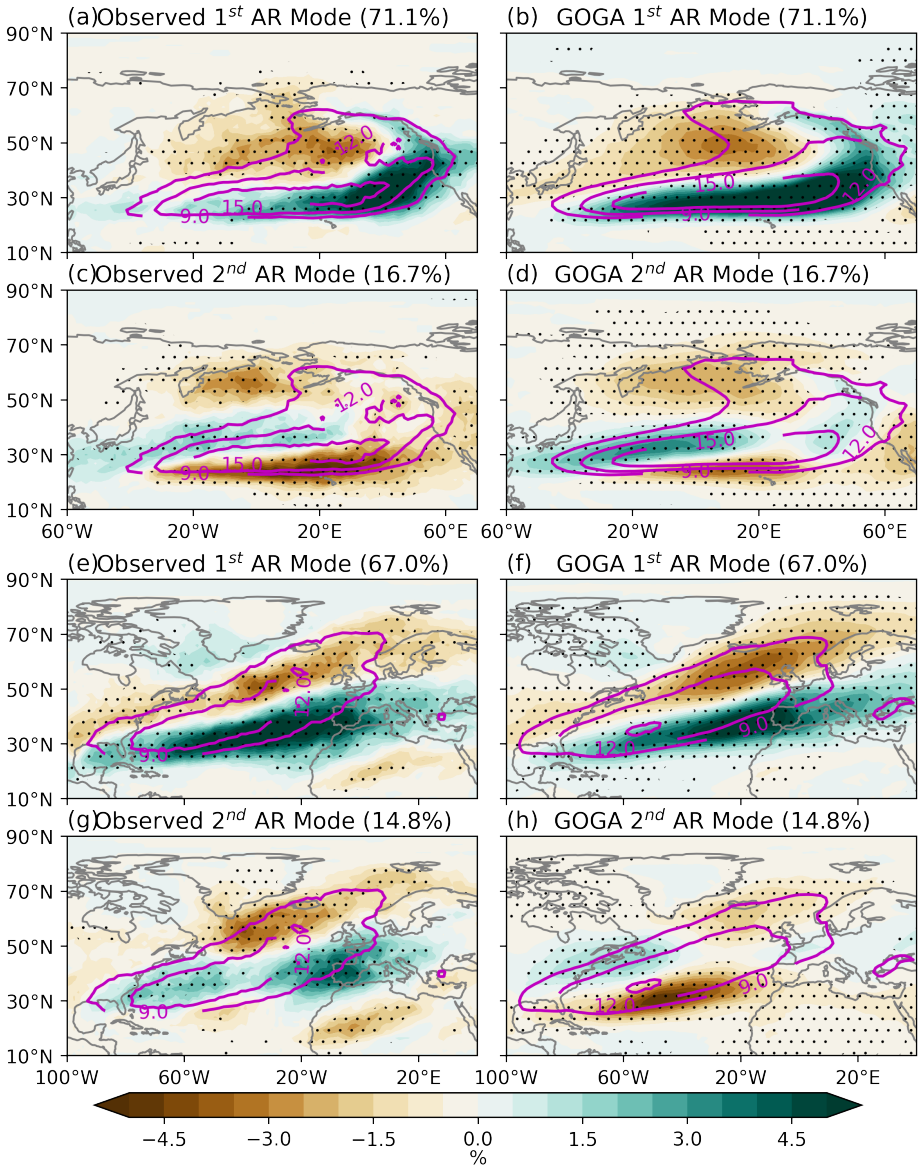

Figure 2.A.7: Same as Figure 2.9, but based on the SVD analysis between observation and the GOGA ensemble.

Table 2.A.1: The name, institution and horizontal resolution of the AMIP models used in this study.

Model	Institute	Horizontal Resolution (lat × lon)
ACCESS-CM2	CSIRO-ARCCSS	145 × 192
ACCESS-ESM1-5	CSIRO	145 × 192
BCC-CSM2-MR	BCC	160 × 320
CAMS-CSM1-0	CAMS	160 × 320
CanESM5	CCCma	64 × 128
CESM2	NCAR	192 × 288
CESM2-FV2	NCAR	96 × 144
CESM2-WACCM	NCAR	192 × 288
CESM2-WACCM-FV2	NCAR	96 × 144
CMCC-CM2-HR4	CMCC	192 × 288
CMCC-CM2-SR5	CMCC	192 × 288
EC-Earth3	EC-Earth-Consortium	256 × 512
EC-Earth3-AerChem	EC-Earth-Consortium	256 × 512
EC-Earth3-CC	EC-Earth-Consortium	256 × 512
EC-Earth3-Veg	EC-Earth-Consortium	256 × 512
FGOALS-f3-L	CAS	180 × 288
FGOALS-g3	CAS	80 × 180
GFDL-CM4	NOAA-GFDL	90 × 144
IITM-ESM	CCCR-IITM	94 × 192
INM-CM4-8	INM	120 × 180
INM-CM5-0	INM	120 × 180
IPSL-CM6A-LR	IPSL	143 × 144
MIROC6	MIROC	128 × 256
MPI-ESM1-2-HAM	HAMMOZ-Consortium	96 × 192
MPI-ESM1-2-HR	MPI-M	192 × 384
MPI-ESM1-2-LR	MPI-M	96 × 192
MRI-ESM2-0	MRI	160 × 320
NESM3	NUIST	96 × 192
NorESM2-LM	NCC	96 × 144
TaiESM1	AS-RCEC	192 × 288

CHAPTER 3

Poleward Shift of Atmospheric Rivers in the Southern Hemisphere in Recent Decades

[**Ma, W.**, Chen, G., Guan, B. (2020). Poleward Shift of Atmospheric Rivers in the Southern Hemisphere in Recent Decades. *Geophysical Research Letters*, 47(21), 1-11. https://doi.org/10.1029/2020GL089934]

Abstract

The atmospheric river (AR) frequency trends over the Southern Hemisphere are investigated using three reanalyses and two Community Earth System Model (CESM) ensembles. The results show that AR frequency has been increasing over the Southern Ocean and decreasing over lower latitudes in the past four decades and that ARs have been shifting poleward. While the observed trends are mostly driven by the poleward shift of the westerly jet, fully coupled CESM experiments indicate anthropogenic forcing would result in positive AR frequency trends over the Southern Ocean due mostly to moisture changes. The difference between the observed trends and anthropogenically driven trends can be largely reconciled by the atmosphere-only CESM simulations forced by observed sea surface temperatures: Sea surface temperature variability characteristic of the negative phase of the Interdecadal Pacific Oscillation strongly suppresses the moisture-driven trends while en-

hances the circulation-induced trends over the Southern Ocean, thus bringing the simulated trends into closer agreement with the observed trends.

3.1 Introduction

Atmospheric rivers (ARs), which are defined as corridors of enhanced integrated water vapor transport(IVT), are responsible for more than 90% of the poleward moisture transport at midlatitudes (*Zhu and Newell*, 1998). The regional impacts of ARs can be beneficial and/or detrimental. On the one hand, ARs are an important source of fresh water for many regions. In that regard, they contribute 30–60% of the annual total precipitation to many regions, such as the west coasts of North American and southern South America (*Dettinger*, 2011; *Guan et al.*, 2010; *Rutz and Steenburgh*, 2012; *Viale et al.*, 2018). ARs are also known as the "drought buster": 33–74% of the persistent droughts along the North American west coast from 1950 to 2010 were ended by the arrival of landfalling AR storms (*Dettinger*, 2013). On the other hand, a substantial fraction of the weather/water extremes over midlatitudes are related to having too many and/or too strong AR events, such as extreme precipitation (*Lamjiri et al.*, 2017; *Lavers and Villarini*, 2013),extreme surface winds (*Waliser and Guan*, 2017), and flooding (*Lavers et al.*, 2012; *Paltan et al.*, 2017; *Leung and Qian*, 2009; *Ralph et al.*, 2006). ARs' influence also extends beyond the midlatitudes (*Nash et al.*, 2018), with a linkage to anomalous snow accumulation and snow melt events over both the Arctic and Antarctic regions (*Baggett et al.*, 2016; *Gorodetskaya et al.*, 2014; *Hegyi and Taylor*, 2018; *Mattingly et al.*, 2018; *Wille et al.*, 2019). The presence of ARs in tropical areas is also starting to get recognized (*Thapa et al.*, 2018; *Yang et al.*, 2018). However, despite an increasingly large number of recent studies on ARs, particularly over western North America and Europe, the variability and trends of ARs in the Southern Hemisphere remain relatively understudied (*Payne et al.*, 2020).

Progress has also been made on understanding the historical and future changes in AR,

with a focus over the coastal regions that are vital to our adaptation planning for climate change. As IVT consists of both moisture and horizontal wind, the changes of ARs can be attributed to either changes in the moisture field, termed as thermodynamic change, or changes in the circulation, termed as dynamic change.Results from climate model simulations suggest that the future changes in ARs over many regions are dominated by an increase in atmospheric moisture content under climate warming (*Gao et al.*, 2015, 2016; *Payne and Magnusdottir*, 2015; *Warner et al.*, 2015) with a relatively uniform thermodynamic effect across the probability distribution of precipitation (*Ma et al.*, 2020a; *Norris et al.*, 2019a). In addition, ARs tend to occur in association with extratropical cyclones (*Eiras-Barca et al.*, 2018; *Zhang et al.*, 2019b), and thus, a meridional shift of the storm-steering westerly jet, as often found in observations and models in a changing climate (*Arblaster and Meehl*, 2006; *Chen and Held*, 2007; *Kushner et al.*, 2001; *Lee and Feldstein*, 2013; *Swart et al.*, 2015; *Thompson et al.*, 2011), may result in the shift of ARs in the same direction as the jet. Indeed, *Gao et al.* (2016) showed that future ARs making landfall over western Europe in Coupled Model Intercomparison Project Phase 5 (CMIP5) model projections will shift poleward as the westerly jet shifts poleward under global warming.

In the Southern Hemisphere, both observations and climate model simulations have shown that the westerly jet has been systemically shifting poleward in the past few decades (*Chen and Held*, 2007; *Solman and Orlanski*, 2014; *Swart et al.*, 2015). This poleward shift of the jet in observations is largely driven by anthropogenic forcing, with ozone depletion playing a larger role than greenhouse gas increases (*Arblaster and Meehl*, 2006; *Lee and Feldstein*, 2013; *Polvani et al.*, 2011; *Thompson et al.*, 2011). Besides anthropogenic forcing, the internal variability of the climate system, especially those originating from atmosphere-ocean coupling, can also modulate the jet trends in the Southern Hemisphere. On the interannual time scale, La Niña tends to shift the jet poleward, while the opposite is true during El Niño (*Chen et al.*, 2008; *Gong et al.*, 2013).On the interdecadal time scale, the negative phase of the Interdecadal Pacific Oscillation (IPO) is associated with the poleward shift of the jet

over southern Indian and southwestern Pacific Oceans during austral summer, which partly contributes to the observed poleward jet shift in the past four decades due to the negative trend in IPO from positive phase in 1979–1998 to negative phase in 1999–2013 (*Yang et al.*, 2020).

Given such a robust poleward shift of the westerly jet in observations and models, a natural question one may ask is whether ARs in the Southern Hemisphere have also been shifting poleward during this period,and if so, what roles anthropogenic forcing and internal variability have played in shaping this trend. To answer these questions, we will first examine the AR trends over the Southern Hemisphere in several reanalysis products. We will then investigate the role of anthropogenic forcing versus internal variability in driving the observed trends using results from two Community Earth System Model (CESM) ensembles. Finally,a new decomposition method will be presented to better understand the thermodynamic and dynamic contributions to the observed trends in ARs.

This paper is structured as follows. We will describe the data, AR detection algorithm, and the decomposition method in section 3.2. In section 3.3, the trends of ARs and the mechanisms driving the trends will be presented. Major findings will be summarized in section 3.4.

3.2 Data and Methods

3.2.1 Observation and Climate Model

We use three reanalysis products as the observation in this study, including the ECMWF Interim reanalysis(ERA-Interim) at the horizontal resolution of $1.5° \times 1.5°$ (*Dee et al.*, 2011), Version 2 of the National Aeronautics and Space Administration (NASA) Modern-Era Retrospective analysis for Research and Application (MERRA-2) at $0.5° \times 0.625°$ (*Gelaro et al.*, 2017), and the National Centers for Environmental Prediction-National Center for Atmospheric Research (NCEP-NCAR) reanalysis at $2.5° \times 2.5°$ (*Kalnay et al.*, 1996). Only data

at 00:00 UTC each day are used in our calculations. Using the daily mean of 6-hourly data will produce similar results (supporting information Figure 3.A.1). The horizontal wind and specific humidity at four levels are vertically integrated to calculate the IVT field (a detailed description on the IVT calculation is provided in the supporting information). For both ERA-Interim and NCEP-NCAR,the data used cover the period from 1979 to 2018 while for MERRA-2, 1980 to 2018. The daily precipitation from the Global Precipitation Climatology Project at $1^\circ \times 1^\circ$ is used to investigate the trends of AR-induced precipitation from 1997 to 2018 (*Huffman et al.*, 2001) and regridded to each of the reanalysis spatial resolution. All data sets are regridded to a common resolution of $1.5^\circ \times 1.5^\circ$ for calculating the multi-product observed mean. To test whether the results are sensitive to the precipitation data set used, we also performed the same analysis with daily precipitation from the Integrated Multi-satellite Retrievals for Global Precipitation Measurement data set covering the period from 2001 to 2018 (Huffman et al., 2019). The results are similar and will not change the conclusion of this paper (Figure 3.A.2).

We also analyze the daily mean output with spatial resolution of $0.9^\circ \times 1.25^\circ$ from two ensembles of CESM simulations for the mechanisms driving the observed trends. The horizontal wind and specific humidity at the same four levels as reanalyses are used to calculate the IVT. First, we use the fully coupled atmosphere-ocean simulations from the CESM Large Ensemble (LENS) (*Kay et al.*, 2015) which consists of 40 members. All members are driven by the observed historical forcing from 1920 to 2005, followed by the "business as usual" Representative Concentration Pathway 8.5 (RCP8.5) forcing from 2006 to 2100 (*Moss et al.*, 2010; *Taylor et al.*, 2012). We note that the RCP8.5 forcing after 2005 in the CESM ensembles is different from the reality. *Schwalm et al.* (2020) show that the total cumulative CO2 emission for 2005 to 2020 in RCP8.5 is in close agreement with the observed historical value in this period (within 1%), justifying the use of RCP8.5 forcing as the approximation to the reality. Ensemble spread is generated by applying a small perturbation to the initial atmospheric temperature fields. Since each member only differs in the initial condition, taking

the multi-model mean can effectively remove the internal variability and reveal the responses to anthropogenic forcing. Second, we examine a 10-member atmosphere-only ensemble from the same version of CESM, Version 1.1, forced by time-varying prescribed National Oceanic and Atmospheric Administration (NOAA) Extended Reconstruction Sea Surface Temperature, Version 4, and Hadley Centre Sea Ice, with other historical forcing identical to LENS except for the Stratospheric Processes and Their Role in Climate data set of the ozone forcing, termed as Global Ocean Global Atmosphere (GOGA). Since GOGA includes both the forced signal from radiative forcing and the observed internal variability from prescribed SST and Sea Ice in the coupled atmosphere-ocean system, the AR trends are expected to be more comparable with observations. While the ozone forcing in GOGA is slightly different from the one in LENS, *Schneider and Deser* (2018) showed that such difference in the ozone forcing has statistically insignificant effects on the trends of the Southern Hemisphere westerly jet over the satellite era. Given that the Whole Atmosphere Community Climate Model ozone data set used in LENS shows stronger ozone depletion (*Cionni et al.*, 2011), if the difference in ozone data set has any impacts on the results in the study, it would be an underestimate of the dynamic contribution to AR trends in GOGA. Note that despite the difference in the ensemble size and the period covered between LENS and GOGA, further analysis shows that the conclusion presented in this study is not sensitive to these differences (Figures 3.A.3–3.A.5).

3.2.2 AR Detection Algorithm and Dynamic Versus Thermodynamic Decomposition

The IVT-based global AR detection algorithm developed in *Guan and Waliser* (2015) is employed. A brief summary of the algorithm is provided here, and more detailed descriptions of the algorithm can be found in their study. In the first step of the algorithm, the seasonally and regionally dependent 85^{th} percentile of the IVT magnitude, or 100 kgm^1s^1, whichever is greater, is used as the intensity threshold to identify contiguous regions ("objects") with

elevated IVT. The identified objects will be discarded if (1) more than half of the grid cells have the direction of IVT deviating more than 45° from the object's mean IVT direction, that is, when IVT directions within an object are not coherent; (2) object-mean poleward IVT is less than 50 kgm^1s^1, that is, when the object does not have an appreciable mean poleward IVT component; or (3) direction of object-mean IVT deviates from the overall orientation of the shape of the object by more than 45°, that is, when IVT does not flow in the direction of the "river". Finally, only those objects with length greater than 2000 km and length-to-width ratio greater than 2 are retained as ARs. The IVT 85^{th} percentile is calculated by using the entire period of each individual data set. The grid points within each AR object are then used to compute AR frequency and AR-induced precipitation. The AR centroid latitude, poleward tip latitude, and landfall latitude are defined as in *Guan and Waliser* (2015).

In order to separate the dynamic and thermodynamic contributions to the AR trends, we create a hypothetical scenario of 6-hourly/daily IVT each year by a scaling method such that the annual mean specific humidity is made equal to its climatological value. More specifically, the specific humidity at each time step, each pressure level, and each grid cell is scaled with a factor of $\frac{q_c}{q_m}$, where q_c is the climatological specific humidity at the level and grid cell to which this factor applies and q_m is the annual mean specific humidity at the same level and grid cell for the given year. The climatological specific humidity is calculated by taking the average of the entire period of the data. By scaling the data this way, the interannual variability of the annual mean specific humidity is completely removed. Therefore, the effects of the background moisture interannual variability on AR frequency variability are suppressed. The IVT calculated with the scaled moisture field and the IVT 85^{th} percentile derived from the unscaled field are then used as input to the AR detection algorithm. The resulting AR trends from the scaled IVT with the annual mean moisture trends removed represent the dynamically driven component of the total trends, and the difference between the total trends and the dynamically driven trends represents the trends

driven by thermodynamic changes.

This scaling method assumes that the changes in annual mean moisture field represent the moisture changes associated with ARs that generally have much higher moisture content than the mean moisture field. This assumption is, at least partly, supported by recent studies on the thermodynamic change in precipitation intensity and accumulation ranging from mild to extreme recurrence intervals under climate warming, which indicates the fractional change in precipitation due solely to thermodynamic contribution is nearly uniform across the precipitation distribution (*Chen et al.*, 2019; *Ma et al.*, 2020a; *Norris et al.*, 2019a).Using a similar scaling approach to separate the dynamic and thermodynamic components in AR trends, *Gao et al.* (2015) concluded that their approach is only qualitatively accurate. We note that the scaling factor in our method herein is based on the mean specific humidity at each level and grid cell independently rather than based on the domain-averaged integrated water vapor as used in *Gao et al.* (2015). This leads to quantitatively more accurate results, because it accounts for not only the spatial variation between warm moist air in ARs and dry neighboring areas but also the vertical structure change in moisture under global warming due to the elevated warming in the upper troposphere.

3.3 Results

3.3.1 Spatial Distribution of AR Frequency Trends

The trends of AR frequency over the Southern Hemisphere are shown in Figure 3.5.1. In this study, AR frequency is defined as the fraction of time a grid cell experiences AR conditions in one year, and most ARs occur between $20°S$ and $60°S$. The most salient feature in the observed trends is the increase in AR frequency over almost the entire Southern Ocean. The magnitude of this positive trend varies among reanalyses, with the strongest trends occurring in NCEP-NCAR and the weakest trends in ERA-Interim (Figures 3.5.1g and 3.A.6), and thus, we present the spatial patterns using the single reanalysis from MERRA-2 and the

observed mean over NCEP-NCAR, MERRA-2, and ERA-Interim (Figures 3.5.1a and b). Despite difference in the magnitudes, all reanalyses show stronger trends over the Pacific sector compared to other ocean sectors. Over the Pacific Ocean, positive trends occur over western subtropical Pacific and extend southeastward into the higher latitudes, in contrast to a band of negative trend at lower latitudes extending from central tropical Pacific into central Chile which is consistent with the declines in precipitation over these regions in observation and model simulations (*Boisier et al.*, 2016). In the polar region off the coast of West Antarctica, a lack of trends or even weak negative trends are observed in MERRA-2 or the observed mean over three reanalyses. Over the Atlantic basin,regions with negative trends extend from the central basin at around $30°S$ southeastward into the Indian Ocean which may be linked to the "Day Zero" Cape Town drought in recent years (*Sousa et al.*, 2018).

To investigate the cause behind the observed trends, we first show that the ensemble mean from LENS, which represents the trends driven by anthropogenic forcing, produces significant positive trends nearly everywhere over the AR regions between $20°S$ and $60°S$, especially over the Southern Ocean (Figure 3.5.1c). This suggests that anthropogenic forcing plays a role in shaping the observed trends. However, unlike the observed trends, there is no significant negative trend over the lower latitude regions, and the strongest trends occur over the Indian and Atlantic sectors of the Southern Ocean, instead of the Pacific sector. Furthermore, the maximum of the positive trends occurs poleward of $60°S$ in LENS, while it occurs equatorward of $60°S$ in observations (Figure 3.5.1g). If CESM is perfect, these differences between observations and LENS indicate the influence of internal variability in the observed trends, such as decadal ocean-atmosphere modes. Indeed, the comparison of surface air temperature trends between LENS and GOGA (Figures 3.5.1e and f) reveals a rather uniform warming pattern in the Southern Hemisphere in LENS in contrast to GOGA which shows warming in the subtropics and cooling in the tropics and midlatitudes over the South Pacific similar to the IPO pattern (*Power et al.*, 1999; *Salinger et al.*, 2001; *Zhang et al.*,

1997). Driven by the observed SSTs, AR results from GOGA show higher consistency with observations: It successfully reproduces the negative trends over the eastern ocean along the subtropical boundary of climatological AR frequency peak regions; strongest positive trends also occur over the Pacific sector, and the weak negative trend off the coast of West Antarctica is apparent (Figure 3.5.1d). The maximum positive trend also occurs equatorward of $60°S$. These results indicate the importance of the IPO-like internal SST variability on modulating the AR decadal trends over the Southern Hemisphere.

3.3.2 AR-Induced Precipitation Trends

Given the positive trends in AR frequency over the Southern Ocean, it can be expected that the annual total AR-induced precipitation, defined as the precipitation engendered during AR conditions, would increase over these regions during the same period. Figure 3.5.2 shows the trends in annual total AR-induced precipitation after 1997 in observations (Figure 3.5.2a), GOGA (Figure 3.5.2c), and LENS (Figure 3.5.2e). Although the length of data is shorter due to the availability of this precipitation product only after 1997, the pattern of annual total AR-induced precipitation is consistent with the AR frequency trends in Figure 3.5.1. The AR-induced precipitation increases over the Southern Ocean with stronger trends in observations than in GOGA or LENS. While the trends over the Southern Ocean in LENS are relatively homogeneous, the trends in observations show some spatial heterogeneities with the strongest trends over the Pacific sector and weaker trends over other sectors. Over lower latitudes, the spatial pattern of the trends in GOGA and observations shows remarkable similarity over the Pacific basin: The positive trends over the central ocean along the subtropical boundary of AR frequency are sandwiched by negative trends over the western and eastern Pacific.

The annual total amount of precipitation induced by ARs over a region is determined by two factors: the AR frequency over the region and the average precipitation intensity induced by an AR event. Thus, the total trend in AR-induced precipitation is decomposed

into two parts: the trend due to changes in AR frequency by setting the annual mean AR-induced precipitation intensity as the climatological value and the trend due to interannual variability in AR-induced precipitation intensity by holding the annual AR frequency constant at the climatological level. The trends due to changes in AR frequency alone are shown in Figures 3.5.2b, d, and f for observations, GOGA, and LENS, respectively, and the trends due to changes in AR-induced precipitation intensity alone are displayed in Figure 3.A.7. By comparing the trends driven by AR frequency with the total trends, it is immediately apparent that the total trends are almost entirely driven by the trends in AR frequency in both GOGA and LENS. In observations, although the contribution from trends in AR-induced precipitation intensity is not negligible, AR frequency trends dominate the total trends.

3.3.3 Poleward Shift of ARs

The larger increase in AR frequency on the poleward flank of its climatological peak region (Figure 3.5.1) implies a poleward shift of AR events. Figure 3.5.3 shows the interannual variability of AR centroid latitude (Figure 3.5.3a), poleward tip latitude (Figure 3.5.3c), and landfall latitude (Figure 3.5.3e) averaged over all the events occurring between $20°S$ and $60°S$ for observations and models. For each individual data set, the interannual variabilities of the three measures of the AR latitudinal location are approximately correlated, indicating a systematic shift in AR location that is also consistent with the interannual changes in westerly jet latitude determined by the latitude of annual maximum zonal mean zonal wind at 850 hPa (Figure 3.5.3b). Although the ensemble means in AR latitude in LENS display little interannual variability, GOGA shows interannual variability very similar to those in the three reanalysis products, especially for centroid latitude, indicating the dominant role of SST variability on interannual variability rather than anthropogenic forcing. As summarized in Figure 3.5.3f, all three of these measures of the AR latitude indicate poleward shift of ARs with trends significant at the 95% confidence level in both observations and models; the only exception occurs with the centroid latitude in GOGA. This shift in AR latitude is

again consistent with the poleward shift in westerly jet latitude.

Different reanalysis products and models also exhibit some differences in the magnitude of latitudinal shift. While the AR centroid latitude simulated by LENS and GOGA is consistent with observations, model simulations produce an equatorward bias in both poleward tip latitude and landfall latitude (Figures 3.5.3c and 3.5.3e),in contrast to a poleward model bias in eddy-driven jet (Figure 3.5.3b). NCEP-NCAR displays the largest trends in AR latitude among the three reanalysis products, which is partly related to more ARs at lower latitudes around 1980 and more ARs at higher latitudes around 2010. The latitude of the eddy-driven jet in NCEP-NCAR, however, is comparable to the other two reanalyses. These differences may be related to discrepancies in moisture content (Figure 3.5.3d), as ARs are determined by IVT that combines both wind speed and moisture content. As greenhouse gas warming and Antarctic ozone depletion have different thermal finger-prints at the surface (*Lee and Feldstein*, 2013; *Thompson et al.*, 2011), the two may have different impacts on the dynamic and thermodynamic components of AR trends.

3.3.4 Thermodynamic and Dynamic Modulations on AR Trends

To gain a better mechanistic understanding for the AR trends over the Southern Hemisphere, we decompose the total trends into the component driven by changes in thermodynamics and the component driven by changes in dynamics. The results of this decomposition are shown in Figure 3.5.4. The observed trends in AR frequency are mostly driven by changes in circulation, with a larger increase on the poleward flank of climatological peak region (Figure 3.5.4a), consistent with the poleward shift in the westerly jet (Figure 3.5.4b).In contrast, the contribution from the changes in the moisture field is confined mostly within the Pacific basin (Figure 3.5.4b), with an increase in AR frequency over the western Pacific and a decrease over the eastern Pacific in the subtropics, in line with the trends in surface air temperature (Figure 3.5.1f). These basic patterns in observed trends are reasonably simulated by GOGA, supporting the observed AR trends in the reanalysis products.

Decomposition from LENS, however, suggests that the increases in moisture will dominate the AR trends and cause nearly uniform increases over the entire Southern Ocean, consistent with the spatially uniform trends in surface air temperature. The trends in circulation play a secondary role, causing slight decreases over the regions around $30°S$ and slight increases over the regions around $60°S$. As discussed earlier, the ensemble mean trends in LENS represent anthropogenically forced signals, and the difference between LENS and GOGA can be mostly attributed to differences in SST resulting from the IPO-like internal variability in the coupled atmosphere-ocean system.

The difference of the thermodynamically and dynamically driven trends between GOGA and LENS are shown in Figures 3.5.4g and 3.5.4h, respectively. Figure 3.5.4g indicates that the enhanced positive trends over the Pacific sector are at least partly driven by circulation changes due to the negative IPO-like trend (Figure 3.5.1f), consistent with the IPO going from positive phase in 1979–1998 to negative phase in 1999–2013, contributing to a poleward shift in the westerly jet (*Yang et al.*, 2020). In addition, the negative IPO-like SST trend drives widespread drying in the moisture field except wetting in the subtropical region(Figure 3.A.8) which also results in widespread decline in AR frequency over the entire Southern Ocean. Therefore, the resulted AR poleward shift in GOGA is weaker than the shift simulated by LENS (Figure 3.5.3).

3.4 Conclusions

We investigated the trends of AR frequency over the Southern Hemisphere in observations and climate models over the past four decades. During this period, the observed AR frequency has been increasing over the Southern Ocean and decreasing at lower latitude regions at around $30°S$. Consistent with this trend pattern, AR events have been systematically shifting poleward, at a rate of 0.24°, 0.27°, and 0.72° latitude per decade for the AR centroid, poleward tip, and landfall location, respectively, consistent with the poleward shift of

the westerly jet by 0.30° latitude per decade (*Swart et al.*, 2015; *Yang et al.*, 2020). The annual total precipitation induced by ARs has also been increasing over the Southern Ocean due mostly to the increases in AR frequency over the regions.

Results from two CESM ensembles suggest that, although anthropogenic forcing can drive positive AR frequency trends over the Southern Ocean in recent decades, the observed trends are strongly modulated by negative IPO-like internal variability in sea surface temperature that is characterized as warming in the sub-tropics and cooling in the tropics and midlatitudes over the South Pacific (Figure 3.5.1f). Decomposing the total trends into the thermodynamic and dynamic components reveals that the observed trends are largely driven by changes in the circulation (Figure 3.5.4a) and that the thermodynamic contribution confines mostly within the Pacific basin (Figure 3.5.4b). In the coupled model simulations of LENS, however, the thermodynamic effects dominate over the dynamic effects and cause nearly uniform positive trends over the Southern Ocean (Figure 3.5.4f). The difference in observations and LENS is largely explained by the negative IPO-like sur-face warming in the GOGA simulations forced by observed changes in SSTs, which drives a poleward shift in the westerly jet (*Yang et al.*, 2020) as well as widespread declines in AR frequency over the Southern Ocean associated with surface cooling (Figure 3.5.4h).

Acknowledgements. Weiming Ma and Gang Chen are supported by National Science Foundation Grants AGS-1742178 and1608775. We would like to acknowledge high-performance computing support from Cheyenne (https://doi.org/10.5065/D6RX99HX) provided by NCAR's Computational and Information Systems Laboratory,sponsored by the National Science Foundation. We thank two anonymous reviewers for their comments that helped improve this manuscript.

3.5 Figures

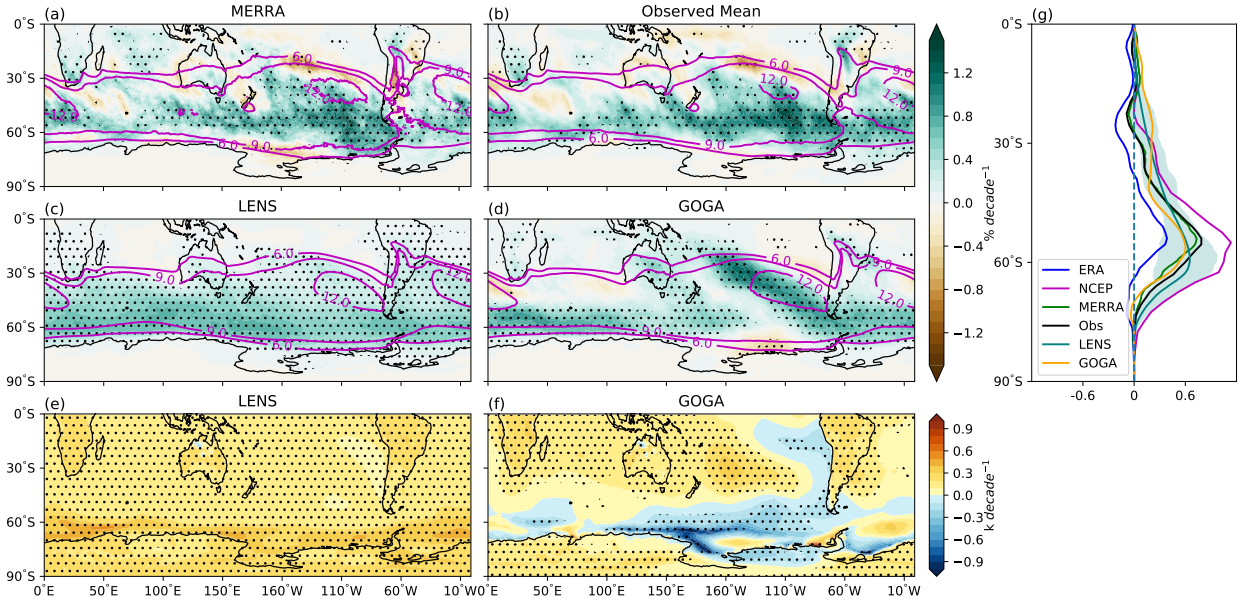

Figure 3.5.1: Spatial distribution of climatology (solid contours) and trends (color shading) for AR frequency in MERRA-2 (a), observed mean (b), LENS (c),and GOGA (d) over the period of 1979–2018 (except for MERRA-2 over 1980–2018 and GOGA over 1979–2015). (e) and (f) show the surface air temperature trends from 1979–2018 in LENS and from 1979–2015 in GOGA, respectively. The zonal mean of AR frequency trend is shown in (g) with shading showing the 5th and 95th percentiles of the intermember spread in LENS. The observed mean is the average of the three reanalysis products. Details of the ensemble simulations in LENS and GOGA are described in section 3.2.1. Stippling in (a)–(f) indicates regions with trends significant at the 95% confidence level based on two-tailed Student's t test and after accounting for lag-1 auto-correlation.

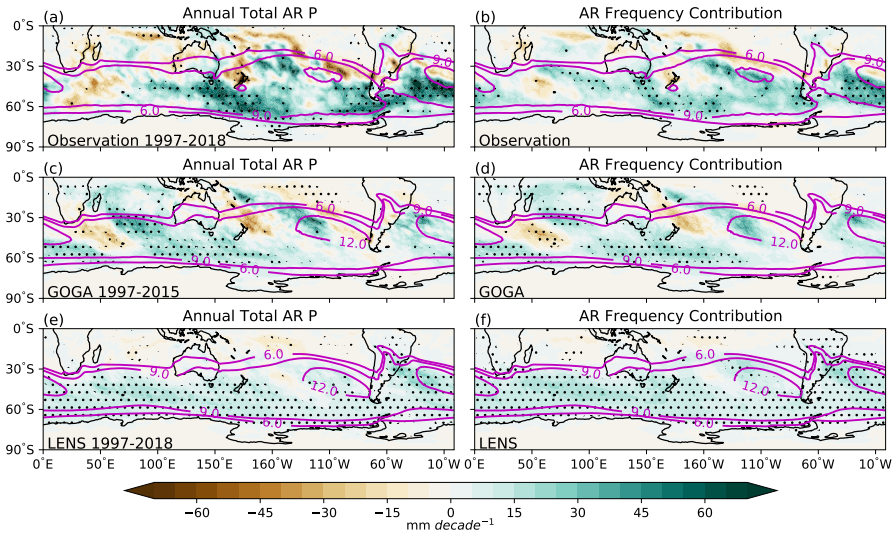

Figure 3.5.2: Trends of annual total AR-induced precipitation in observation mean (a), GOGA (c), and LENS (e). (b), (d), and (f) show the contribution to the total trends from the trends in AR frequency alone for observation, GOGA, and LENS, respectively. Observations and LENS are analyzed over the period of 1997–2018 and GOGA over 1997–2015. Solid contours show the climatology of AR frequency. Stippling indicates regions with trends significant at the 95% confidence level based on two-tailed Student's t test and after accounting for lag-1 auto-correlation.

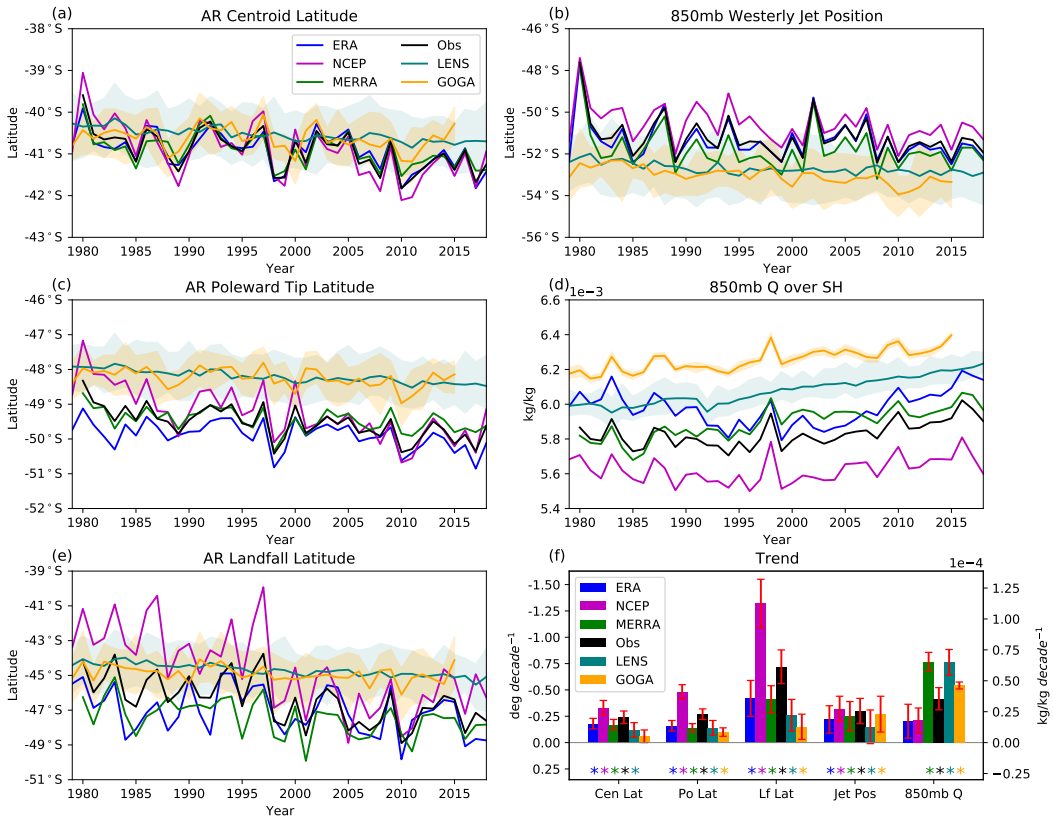

Figure 3.5.3: Interannual variability in AR latitude, westerly jet latitude, and lower-level moisture content in the Southern Hemisphere: mean AR centroid latitude(a), AR poleward tip latitude (c), AR landfall latitude (e), westerly jet latitude at 850 mb (b), and mean specific humidity at 850 mb (d). The mean AR statistics are averaged over all the events occurring between 20°S and 60°S. The linear trends of AR centroid latitude ("Cen Lat"), poleward tip latitude ("Po Lat"),landfall latitude ("Lf Lat"), westerly jet position ("Jet Pos"), and 850 mb specific humidity ("850mb Q") are summarized in (f). Red error bars indicate the standard error of the trends in observations and the standard deviation of intermember spread in GOGA and LENS. Asterisk indicates trends which are significant at the 95% confidence level based on Student's t test and after accounting for lag-1 auto-correlation.

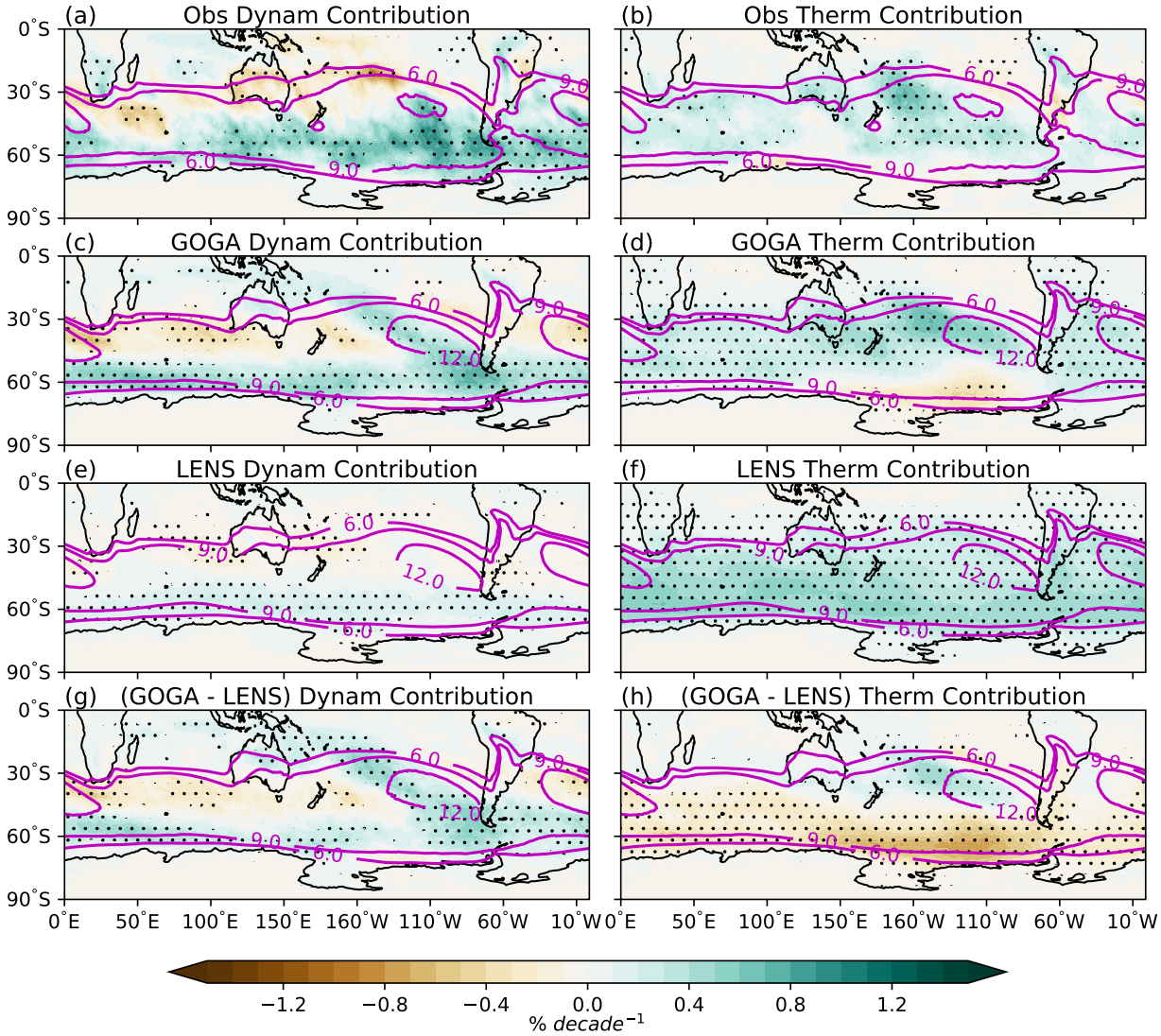

Figure 3.5.4: Dynamic and thermodynamic decompositions of AR frequency trends (color shading) for observations (a, b), GOGA (c, d), and LENS (e, f). (g) and (h)show the difference of the dynamic and thermodynamic components between GOGA and LENS, respectively. Solid contours show the climatology of AR frequency. Stippling indicates regions with trends significant at the 95% confidence level based on two-tailed Student's t test and after accounting for lag-1 autocorrelation.

Appendix

3.A Supplement

Text 3.A1 The horizontal winds and specific humidity at the near surface level, 850 mb, 500 mb and 200 mb (300 mb for NCEP-NCAR which doesn't have specific humidity archived above 300 mb) are vertically integrated to calculate the IVT as:

$$IVT = \frac{1}{g} \int_{sfc}^{200mb} qU dp$$

where g is gravitational acceleration, q is specific humidity, U is the horizontal wind and dp is the pressure difference between neiboring pressure levels. The lowest model level is treated as the near surface level except for specific humidity in NCEP-NCAR which doesn't provide data at lowest model levels. In NCEP-NCAR, 2 meter specific humidity and winds at 0.995 sigma level (near surface) are used in place of near surface data. Since the atmospheric pressure near the surface can be smaller than 850 mb (even 1-5 mb smaller than 500 mb under extremely rare conditions in the Northern Hemisphere), to compute IVT, the surface pressure is first compared with 850 mb for a given grid cell at a given time step. If the surface pressure is greater than 850 mb, IVT is calculated using data at all four levels. Ortherwise, IVT is calculated using data only at the near surface level, 500 mb and the 200 mb. Surface pressure used in reanalyses is at 00:00 UTC, as are other reanalyses variables used. For CESM ensembles, monthly surface pressure is used because daily surface pressure is not available. Since the daily surface pressure at a given location usually varies by only few millibar from day to day, monthly mean surface pressure can serve as a good approximation for the daily surface pressure for the days within that month.

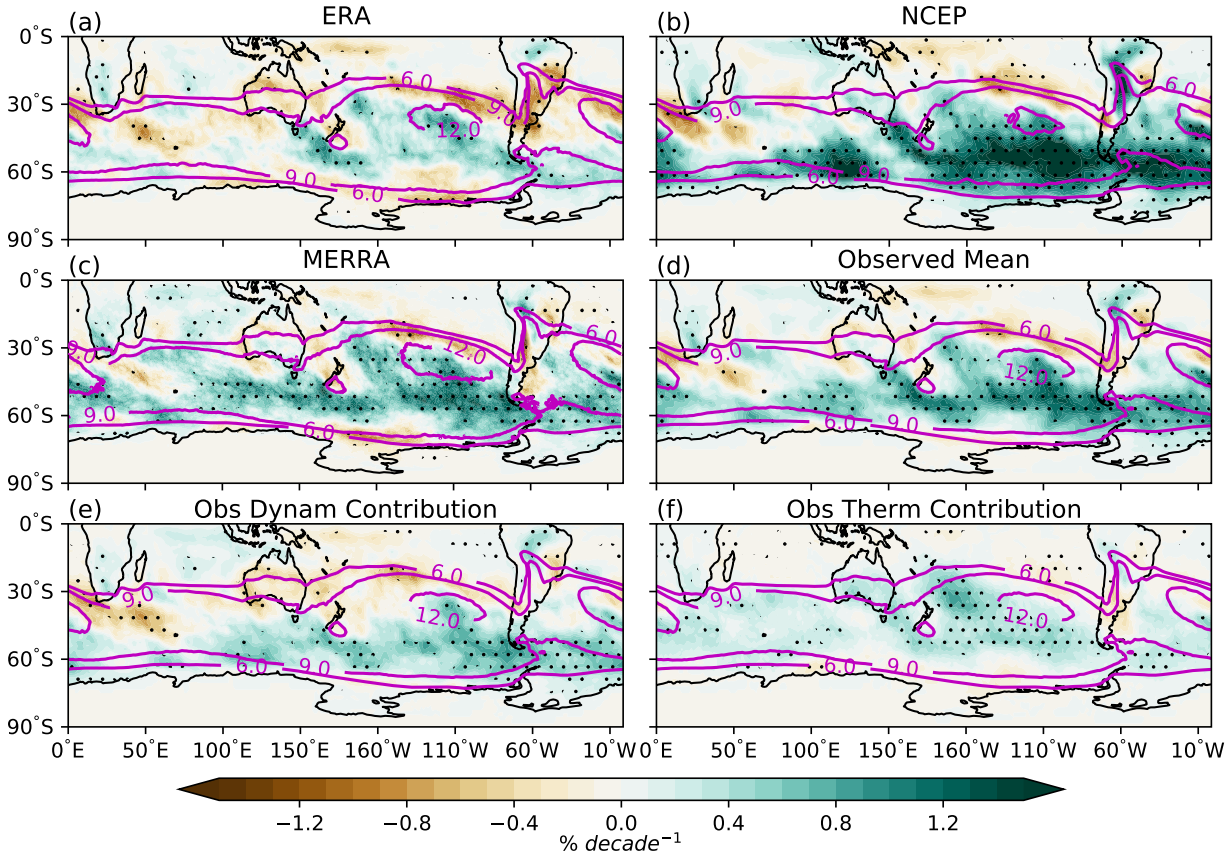

Figure 3.A.1: Spatial distribution of the climatology (solid contours) and trends (color shading) of AR frequency calculated with daily mean of 6-hourly data in ERA-Interim (a), NCEP-NCAR (b), MERRA-2 (c), and the mean of the three reanalyses (d). The observed mean dynamic and thermodynamic contribution to the total trends are shown in (e) and (f), respectively. Stippling indicates regions with trends significant at the 95% confidence level based on two-tailed Student's t test and after accounting for lag-1 autocorrelation.

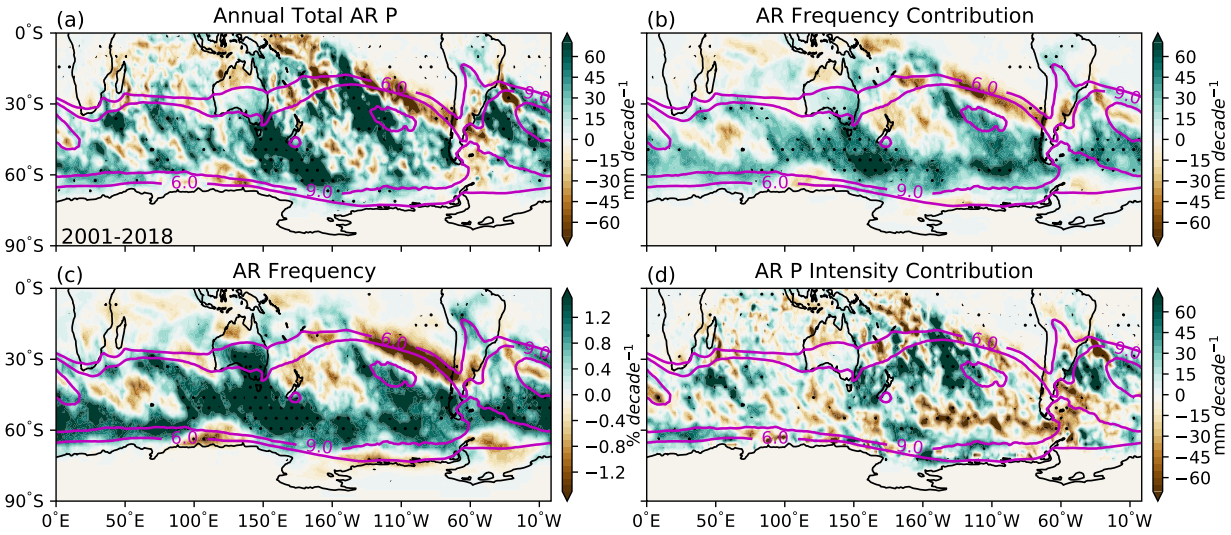

Figure 3.A.2: Observed AR-induced precipitation trends from 2001 to 2018 calculated from IMERG. Trends in annual total AR-induced precipitation (a), contribution to the total trends from the trends in AR frequency (b), trends in AR frequency (c), and the contribution to the total trends from the trends in AR-induced precipitation intensity (d). Solid contours show the climatology of AR frequency. Stippling indicates regions with trends significant at the 95% confidence level based on two-tailed Student's t test and after accounting for lag-1 autocorrelation.

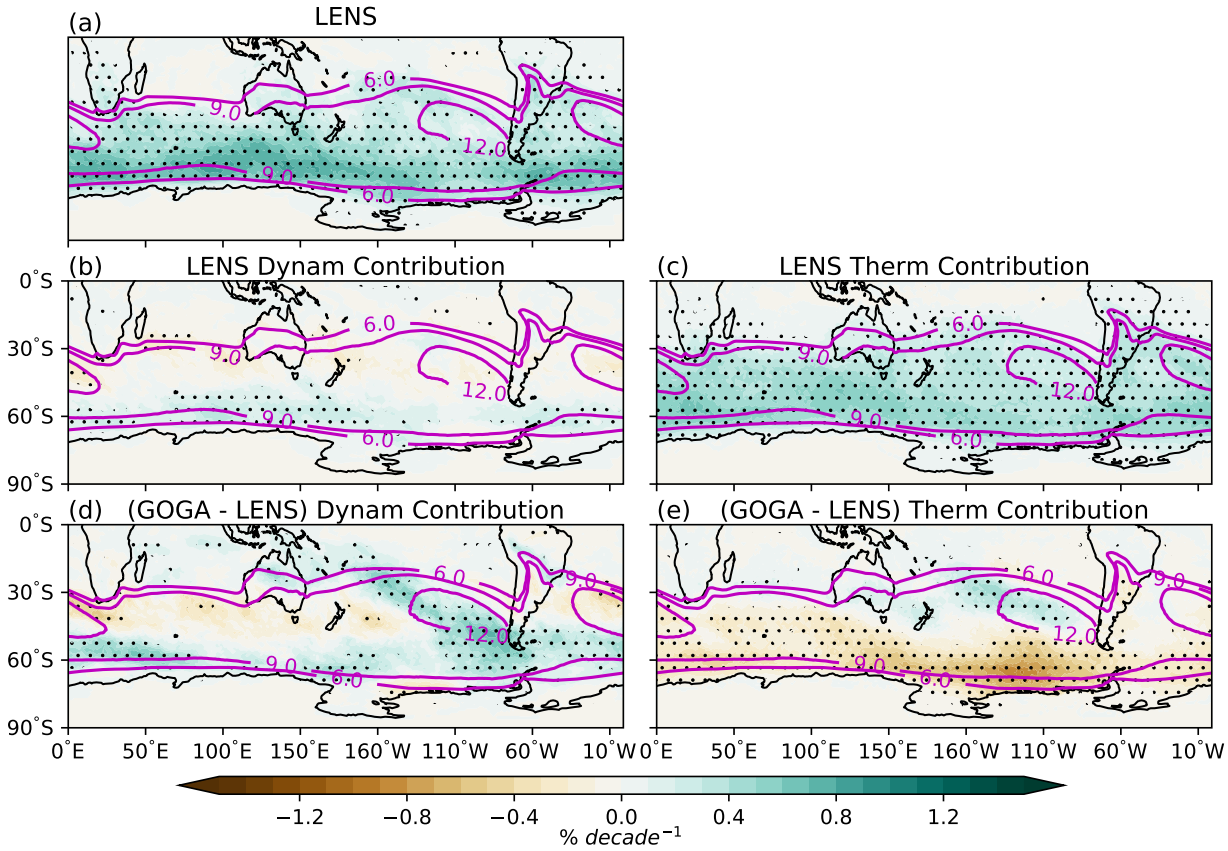

Figure 3.A.3: Trends in AR frequency in LENS calculated with results from the first 10 members. Shown are the total trends (a), trends due to dynamic contribution (b), trends due to thermodynamic contribution (c), the difference in trends due to dynamic contribution between GOGA and LENS (d), and the difference in trends due to thermodynamic contribution between GOGA and LENS (e). Solid contours show the climatology of AR frequency. Stippling indicates regions with trends significant at the 95% confidence level based on two-tailed Student's t test and after accounting for lag-1 autocorrelation.

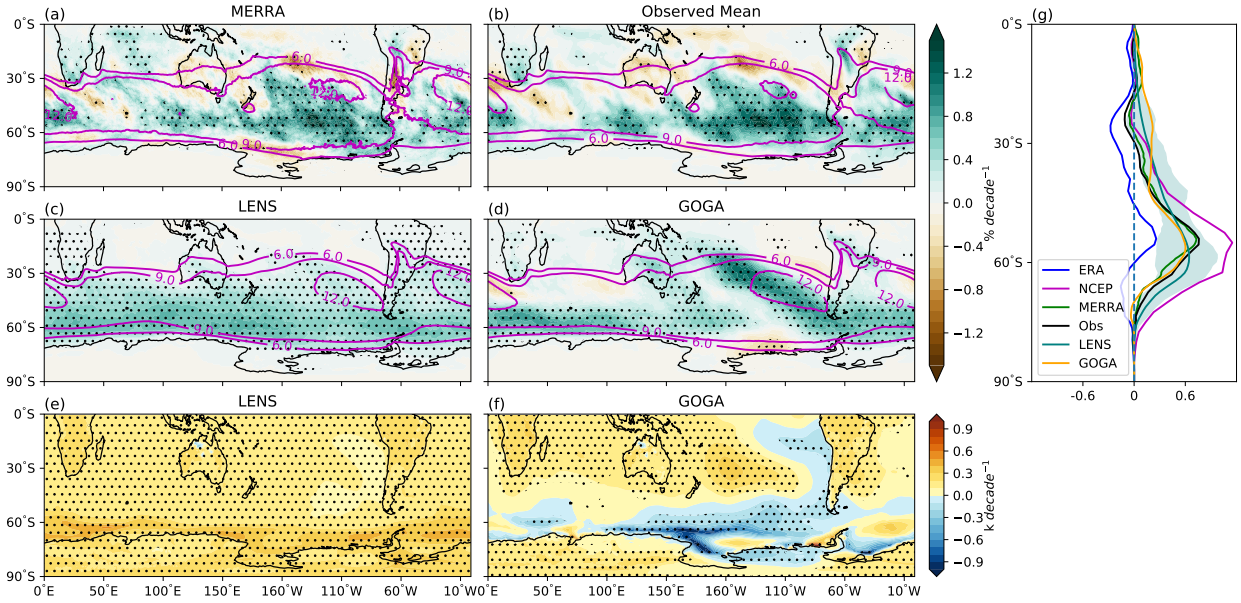

Figure 3.A.4: Same as Figure 3.5.1 but covering the period from 1979 to 2015 (for MERRA-2, 1980 to 2015).

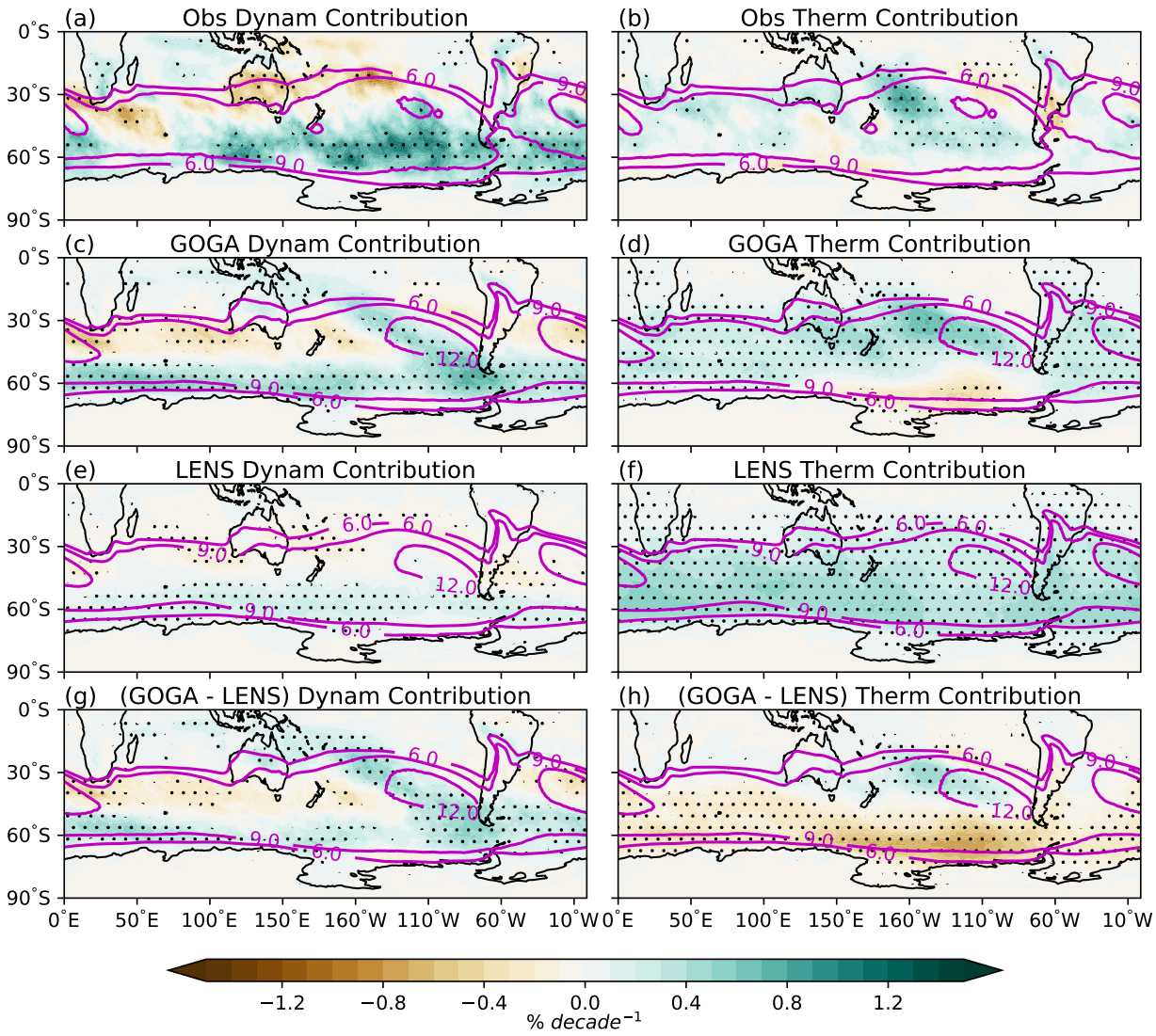

Figure 3.A.5: Same as Figure 3.5.4 but covering the period from 1979 to 2015 (for MERRA-2, 1980 to 2015).

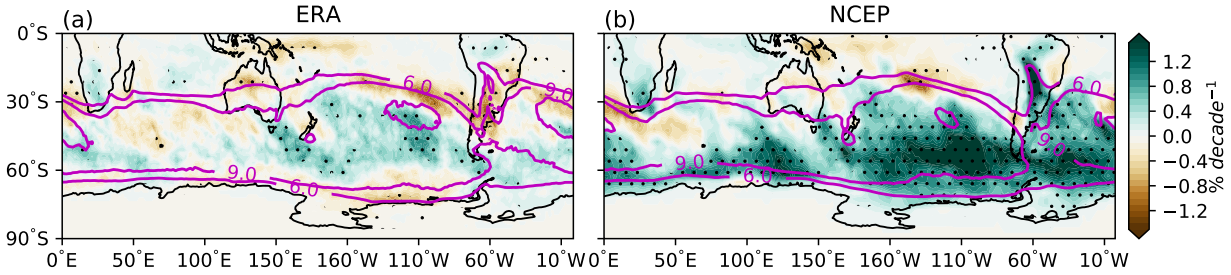

Figure 3.A.6: AR frequency trends in ERA-Interim (a) and NCEP-NCAR (b). Solid contours show the climatology of AR frequency. Stippling indicates regions with trends significant at the 95% confidence level based on two-tailed Student's t test and after accounting for lag-1 autocorrelation.

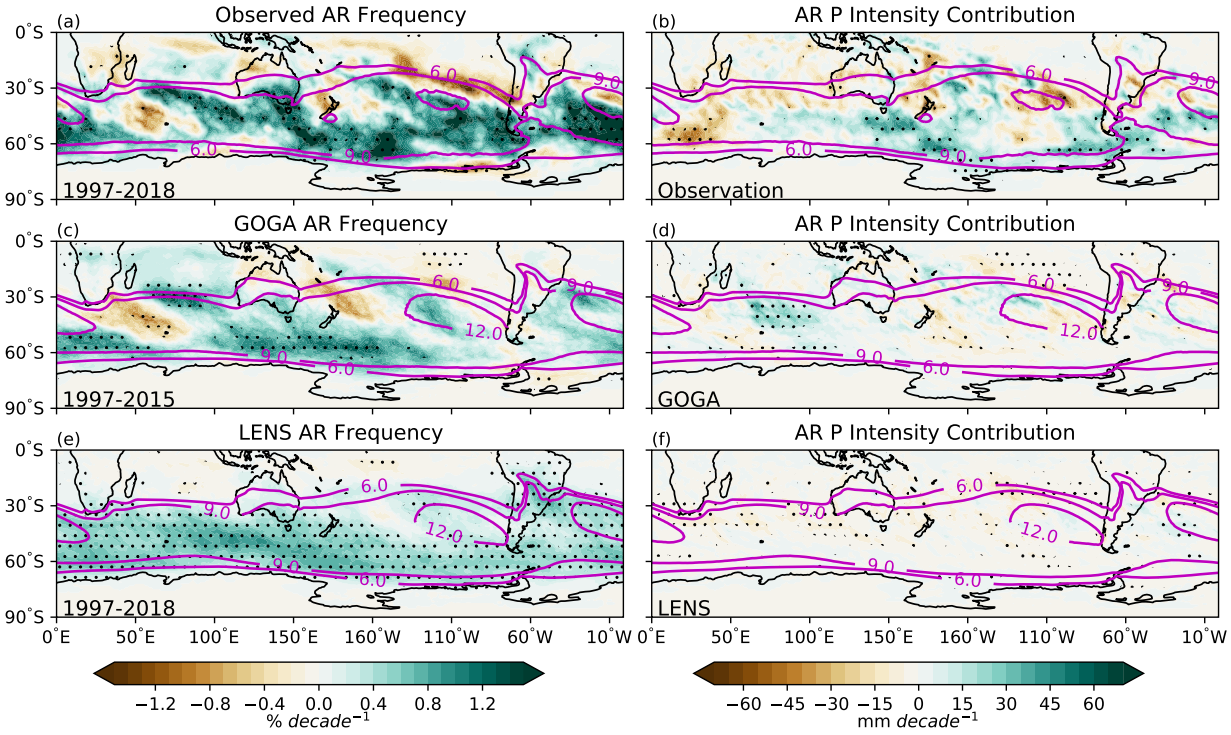

Figure 3.A.7: Trends of AR frequency in the observational mean (a), GOGA (c) and LENS (e). (b), (d) and (f) show the contribution to the total AR-induced precipitation trends from the trends in AR-induced precipitation intensity alone for observation, GOGA and LENS, respectively. Observations and LENS are analyzed over the period of 1997-2018, and GOGA over 1997-2015. Solid contours show the climatology of AR frequency. Stippling indicates regions with trends significant at the 95% confidence level based on two-tailed Student's t test and after accounting for lag-1 autocorrelation.

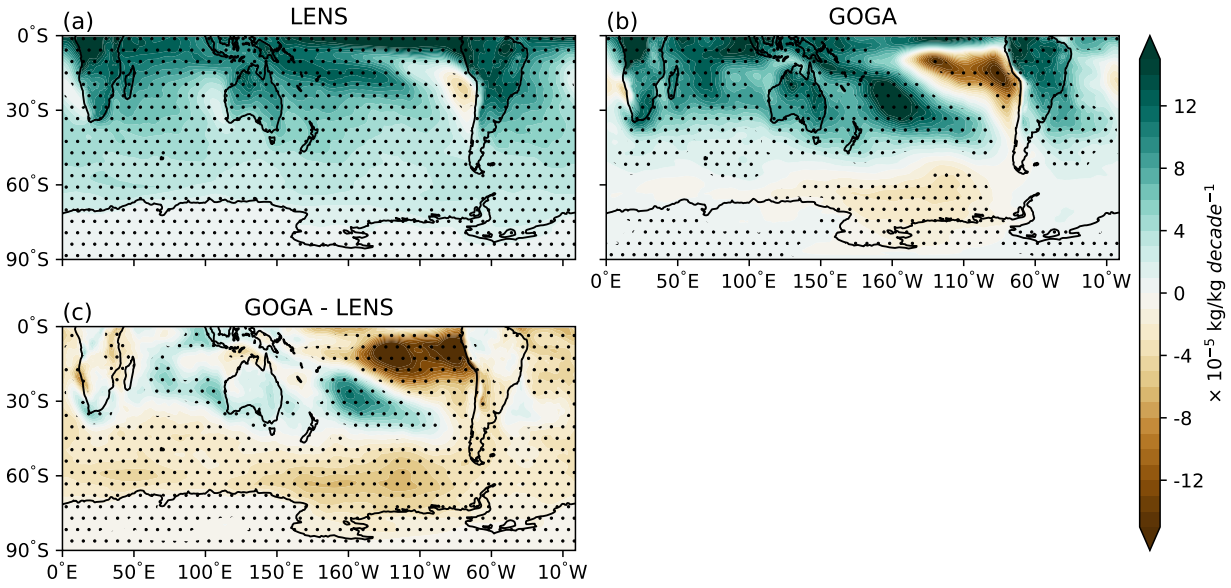

Figure 3.A.8: Ensemble mean trends in 850 mb specific humidity for LENS from 1979-2018 (a) and GOGA from 1979-2015 (b). (c) shows the difference between (b) and (a). Stippling indicates regions with trends significant at the 95% confidence level based on two-tailed Student's t test and after accounting for lag-1 autocorrelation.

CHAPTER 4

Atmospheric River Response to Arctic Sea Ice Loss in the Polar Amplification Model Intercomparison Project

[**Ma, W.**, Chen, G., Peings, Y., Alviz, N. (2021). Atmospheric River Response to Arctic Sea Ice Loss in the Polar Amplification Model Intercomparison Project. *Geophysical Research Letters*, 1-12. https://doi.org/10.1029/2021gl094883]

Abstract

The atmospheric river (AR) response to Arctic sea ice loss in the Northern hemisphere winter is investigated using simulations from the Polar Amplification Model Intercomparison Project. Results have shown that the midlatitude responses are dominated by dynamic effects. Poleward of around $60°N$, the dynamic and thermodynamic effects cancel each other, resulting in relatively small responses. The response uncertainty can be characterized by leading uncertainty modes, with the responses over the Pacific and Atlantic projecting onto the northeastward extension and equatorward shift mode, respectively. In addition, the responses seem to be mean state-dependent: under the same forcing, models with more poleward-located climatological ARs tend to show stronger equatorward shifts over the At-

lantic; over the Pacific, models with more westward-located climatological AR core tend to show stronger northeastward extensions. These relationships highlight the importance of improving the AR climatology representation on reducing the response uncertainty to Arctic sea ice loss.

4.1 Introduction

Due to the increase of atmospheric greenhouse gases, Arctic has been warming faster than the rest of the globe, and Arctic sea ice has also been declining rapidly. It has been hypothesized that Arctic sea ice loss can influence climate in the midlatitudes through alteration of the large-scale circulation (e.g., *Blackport and Screen* (2019); *Cohen et al.* (2014); *Cvijanovic et al.* (2017); *Kug et al.* (2015); *Liu et al.* (2012); *Peings and Magnusdottir* (2014); *Screen et al.* (2018a,b)).The loss of sea ice over the Arctic is accompanied with enhanced near-surface warming, which reduces the equator-to-pole temperature gradient. A weaker equator-to-pole temperature gradient may slow down the westerly winds and amplify Rossby waves and associated midlatitude weather extremes (e.g., *Cohen et al.* (2014)). However, this is a debated mechanism due to low consistency and robustness of the midlatitude atmospheric response to Arctic sea ice loss (*Barnes and Polvani*, 2013; *Blackport and Screen*, 2020; *Cohen et al.*, 2020; *Peings et al.*, 2021). How midlatitude climate and extreme weather events respond to Arctic sea ice loss is an area of active research. The goal of the article is to quantify how atmospheric rivers (ARs), a type of midlatitude extreme weather, respond to Arctic sea ice loss in a large, coordinated set of atmosphere-only simulations under identical sea ice forcing.

Despite only covering about 10% of the Earth's circumference at midlatitudes a any given time, ARs are responsible for more than 90% of the poleward moisture transport at these latitudes (*Zhu and Newell*, 1998). Studies have found that ARs are important suppliers of fresh water to many regions around the globe (*Dettinger*, 2011; *Rutz and Steenburgh*, 2012;

Viale et al., 2018). For example, ARs contribute up to 50% of the annual precipitation over California (*Dettinger*, 2011). While ARs can deliver much-needed rainfall in periods of drought, they are also the culprits behind many extreme weather events, such as extreme precipitation (*Gao et al.*, 2016; *Lamjiri et al.*, 2017; *Lavers and Villarini*, 2013; *Ma et al.*, 2020a; *Norris et al.*, 2019a), extreme wind events (*Waliser and Guan*, 2017) and flooding (*Lavers et al.*, 2012; *Paltan et al.*, 2017; *Ralph et al.*, 2006; *Leung and Qian*, 2009). Besides their influence in the midlatitudes, ARs also play an important role in shaping the polar climate (*Baggett et al.*, 2016; *Francis et al.*, 2020; *Nash et al.*, 2018; *Wang et al.*, 2020; *Wille et al.*, 2019; *Yang and Magnusdottir*, 2017). For example, *Francis et al.* (2020) found that ARs influence the formation of Polynyas, which are large and persistent areas of open water and thin ice in thick sea ice-covered areas, of the Southern Ocean. With ARs shifting toward higher latitudes over the Southern Hemisphere in recent decades, it is expected that ARs may exert a stronger influence on the climate of Antarctica (*Ma et al.*, 2020b).

Meanwhile, ARs are strongly influenced by the variability of both the large-scale circulation and moisture field (*Gao et al.*, 2015; *Payne et al.*, 2020; *Tan et al.*, 2020; *Zavadoff and Kirtman*, 2020). Therefore, Arctic sea ice loss may be capable of influencing AR variability in midlatitudes. Yet how ARs are going to respond to Arctic sea ice loss remains unknown. Endorsed by the Coupled Model Intercomparison Project Phase 6 (CMIP6; *Eyring et al.* (2016)), the Polar Amplification Model Intercomparison Project (PAMIP) provides a guideline for running coordinated multi-model sea ice loss experiments (*Smith et al.*, 2019). PAMIP provides an unprecedented opportunity to study how Arctic sea ice loss influences ARs. Using data from PAMIP, we seek to understand how ARs in the Northern hemisphere winter respond to Arctic sea ice loss, partitioning the response in a dynamical and a thermodynamical contribution. We also investigate uncertainties associated with the AR response to Arctic sea ice loss, using the spread in the multi-model ensemble.

4.2 Data and Methods

4.2.1 PAMIP Experiments

Two sets of experiments from PAMIP are used to investigate how ARs respond to Arctic sea ice loss: "pdSST-piArcSIC" (piArcSIC) and "pdSST-futArcSIC" (futArcSIC). These experiments are atmosphere-only time slice experiments initialized with conditions from April 1^{st}, 2000. Each experiment is run for 14 months with the first 2 months discarded as spin-up. Both experiments are driven by the same present-day sea surface temperature (SST) condition which is based on the 1979–2008 climatology from the Hadley Center Sea Ice and SST data set (*Rayner et al.*, 2003). These two experiments differ only in the Arctic sea ice concentration. piArcSIC is driven by pre-industrial sea ice conditions derived from a multi-model ensemble of CMIP5 (*Taylor et al.*, 2012) pre-industrial control runs. futArcSIC is forced by sea ice conditions constructed using an ensemble of CMIP5 RCP8.5 scenario, that corresponds to an estimate of Arctic sea ice under $2°C$ global warming in these runs. More details on the PAMIP experimental design can be found in *Smith et al.* (2019). Throughout this manuscript, the response to sea ice loss is calculated by taking the difference between futArcSIC and piArcSIC. The nine models that are included in the PAMIP database at the time of this study are used (See Table 4.A.1 in the Supplementary for more Information). Each model experiment consists of 100 ensemble members. Daily specific humidity, zonal wind, and meridional wind at 1,000, 850, 700, and 500 mb from these models and the ECMWF Interim reanalysis (ERA-Interim; *Dee et al.* (2011)) are used to calculate the integrated water vapor transport (IVT) which is then used for AR detection.

4.2.2 AR Detection Algorithm and the Dynamical Vs. Thermodynamical Decomposition

We use the *Guan and Waliser* (2015) AR detection Algorithm. This algorithm is an IVT-based global AR detection algorithm. Many criteria are employed in this algorithm to detect

ARs. We will outline some of the key criteria here, and a full description of the algorithm can be found in *Guan and Waliser* (2015). The algorithm first identifies contiguous regions ("object") of elevated IVT with the regionally and seasonally dependent 85^{th} percentile IVT intensity. The 85^{th} percentile IVT threshold is calculated based on overlapping 5 month windows, so for a given month at a given location, the threshold is derived over all time steps during the five months centered on that month over the entire period covered by the data set. To ensure coherence of the object, the algorithm requires at least more than half of the grid cells within the object to have mean IVT direction deviating less than 45° within the mean object IVT direction. Since ARs play a critical role for the poleward moisture transport, the object means poleward IVT is required to be greater than 50 kg/m/s. Lastly, the object should be longer than 2000 km and with length to width ratio greater than 2. We calculate the IVT threshold separately for each model. The IVT threshold is derived from the piArcSIC experiment and used for both the piArcSIC and futArcSIC experiments for AR detection.

We are interested in the AR response during December, January, and February (DJF) which is the active AR season in the Northern hemisphere. To quantify the dynamical and thermodynamical contributions to the AR response, a scaling method which was previously used in *Ma et al.* (2020b) is employed in this study. To obtain the dynamical contribution, the DJF moisture in futArcSIC is scaled so that the DJF mean moisture field in futArcSIC is equal to that of piArcSIC in DJF. More specifically, the DJF specific humidity of futArcSIC at each time step, level, and grid is scaled by the ratio $\frac{Q_{pi}}{Q_{fut}}$, where Q_{pi} and Q_{fut} are the DJF mean specific humidity for the piArcSIC and futArcSIC, respectively, for the level and grid to which this scaling applies. The scaled moisture field is then combined with the futArcSIC wind field to calculate the scaled IVT which would be subsequently used with the IVT threshold derived from piArcSIC for AR detection. By scaling the futArcSIC DJF moisture field "back" to the piArcSIC DJF moisture field, any change in the AR statistics detected with the scaled IVT field can be treated as the response due to the change in wind field,

namely, the dynamical contribution. Similarly, to obtain the thermodynamical contribution, the DJF moisture field in piArcSIC is scaled by the ratio $\frac{Q_{fut}}{Q_{pi}}$. The scaled moisture field is then combined with the piArcSIC wind field to calculate the scaled IVT field which will be used for AR detection. Strong moisture/surface air temperature gradients are created at the edge of the strong sea ice loss regions. These strong surface air temperature gradients would modify the wind fields, thus influencing ARs. In conventional dynamic/thermodynamic decomposition, such effects are usually treated as the interaction between the dynamic and thermodynamic. However, the scaling method used in this study is only able to decompose the changes into the dynamic and thermodynamic components, thus not able to account for this kind of covariance between moisture and wind. The linearity of the method can be tested by comparing the sum of the dynamical and thermodynamical effects with the combined effect.

4.3 Results

4.3.1 Multi-Model Ensemble Mean Response to Sea Ice Loss

The ensemble mean response of AR frequency is shown in Figure 4.5.1a. In this study, AR frequency is defined as the fraction of time a grid point experiences AR condition. Under sea ice loss, the strongest anomalies in AR are found in the climatological AR peak regions, namely, the Pacific and the Atlantic basins. The AR response over both the Pacific and the Atlantic exhibits a tri-pole pattern. Over the Pacific, ARs increase between $30°N$ and $40°N$ and decrease on both sides of this band of enhanced AR frequency. This tri-pole pattern in AR response results in enhanced AR frequency over the Northwest United States (US) and reduced AR frequency over both the Southwest US and Alaska. The drying over Southwest US, including California, is consistent with *Cvijanovic et al.* (2017) who found that Arctic sea ice loss can induce drying over California in a coupled model. In contrast, over the Atlantic, AR frequency is reduced between $40°N$ and $60°N$, with enhanced AR frequency

on both sides. This pattern leads to enhanced AR frequency over the Iberian Peninsula and drying over Northwest Europe. Note that a significant decrease in AR activity also occurs over central Eurasia.

To better understand the mechanisms behind the multi-model mean AR response, we decompose the total response into a dynamical (Figure 4.5.1c) and thermodynamical (Figure 4.5.1d) contribution. Over the Pacific, the dynamically induced AR response exhibits a tri-pole pattern similar to the total response, except that the reduced AR frequency in higher latitudes around $60°N$ is more pronounced than the total response shown in Figure 4.5.1a. Over the Atlantic, the changes in zonal wind induce a dipolar response in AR frequency, with widespread reduction in AR frequency in high latitudes, and enhanced AR frequency at around $30°N$. The reduced AR frequency over central Eurasia is dynamically induced. The dynamical response in ARs is consistent with changes in the 850 mb zonal wind (Figure 4.5.1e). In response to sea ice loss, zonal wind weakens everywhere around $60°N$ and strengthens at lower latitudes. Over the Pacific, the strengthening of the jet occurs mostly over the jet exit region, resulting in the northeastward extension of the jet, consistent with the findings of *Ronalds et al.* (2020). Over the Atlantic, the weakening and strengthening of zonal wind occur on the poleward and equatorward sides of the jet, resulting in an equatorward shift of the jet. Such equatorward shift of the jet in response to sea ice loss has also been reported in many sea ice loss studies (e.g., *Deser et al.* (2010); *Peings and Magnusdottir* (2014); *Screen et al.* (2013, 2018a,b). The thermodynamical contribution is mostly confined to the high latitudes above $50°N$ (Figure 4.5.1d). It enhances ARs nearly everywhere, especially over the northern Atlantic and Barents-Kara sea regions. This is consistent with a moistening of the Arctic lower troposphere with sea ice loss (*Deser et al.* (2015); Figures 4.5.1f and 4.A.1). Arctic sea ice loss also appears to drive a weak drying of lower latitude areas. However, this drying is only statistically significant off the coast of the Southwest US. Overall, the decomposition suggests that over the regions poleward of around $60°N$, the dynamical and thermodynamical contributions are opposite in sign and tend to

cancel each other, resulting in a relatively small net response there. In the midlatitudes, the response is mostly controlled by the dynamical changes. Our decomposition method nearly reproduces the total response, with only a slight overestimate of the positive response over the Barents-Kara seas, corroborating the validity of the method (Figure 4.5.1b).

4.3.2 Uncertainty in Responses

The atmospheric response to Arctic sea ice loss over the midlatitudes is highly uncertain, possibly due to model deficiency, but mostly due to small signal-to-noise ratio of the induced changes (*Cohen et al.*, 2020; *Peings et al.*, 2021). Despite significant signals emerging in the ensemble mean, these signals are relatively small compared to the noise, as defined from the standard deviation of interannual variability in DJF AR frequency (Figure 4.A.2). Over the AR peak regions of the Atlantic and Pacific, the amplitude of the mean response only ranges from 10% to 20% of the noise and reaches a maximum of about 30% over the Barents-Kara Seas. Besides this small signal-to-noise ratio in the response, considerable inter-model spread exists. As shown in Figure 4.A.3, while most of the models seem to be able to produce the tri-pole patterns shown in the ensemble mean over both basins, the magnitude and position of the tri-pole patterns vary across models. Further analysis suggests that the inter-model spread is mostly caused by model uncertainty in the zonal wind response, i.e., the dynamical responses (Figures 4.A.4 and 4.A.6). In contrast, the thermodynamical response is quite robust across models (Figures 4.A.5 and 4.A.6).

In order to explore reasons for multi-model spread, we apply an empirical orthogonal function (EOF) analysis to obtain the principal spatial patterns of uncertainty in the AR response (*Langenbrunner et al.*, 2015). We first regrid all the model responses on a common grid of $0.9^\circ \times 1.25^\circ$, then concatenate the response in each member (900 in total, 9 models, each with 100 members). These EOF analyses are performed across the ensemble member dimension, instead of the conventional time dimension. Since the response uncertainty in each ensemble member is dominated by internal variability, the EOF patterns obtained this

way will mostly reflect the uncertainty in the response due to internal variability. We focus on the Pacific and the Atlantic basins. Following *Barnes and Polvani* (2013), the Pacific and Atlantic are defined as the regions from 0° to 90°N and 135°E to 125°W, from 0° to 90°N and 60°W to 0°, respectively. To test the robustness of the results, we also varied these boundaries by a few degrees in either direction. The results are not sensitive to small variations in these boundaries.

As shown in Figure 4.5.2, the first mode of uncertainty over the Pacific, which explains 25.5% of the uncertainty, describes the inter-member disagreement in the strengthening over the AR core regions and the weakening over the poleward side of the core regions (Figure 4.5.2a). The associated uncertainty pattern in zonal wind, which is obtained by regressing the wind anomalies onto the standardized principal component (PC), shows the uncertainty in both the strengthening and meridional shift of the jet (Figure 4.5.2c). The second uncertainty mode which explains 13.0% of the uncertainty represents the uncertainty in the narrowing of the AR maximum regions and their northeastward extension. The associated wind pattern mostly reflects the uncertainty in the northeastward extension of the jet. Over the Atlantic, the first uncertainty mode shows a meridional shift of the ARs, which explains about 29.6% of the uncertainty. Accordingly, the associated pattern in zonal wind shows the meridional shift of the jet. The second mode describes the uncertainty in the strengthening and eastward extension of the AR maximum regions. It explains about 14.6% of the uncertainty. The associated wind pattern reflects the uncertainty in the strengthening and eastward extension of the jet (Figure 4.5.2h).

We also perform the same EOF analysis on the responses of the 850 mb zonal wind (Figure 4.A.7). The results show that the first mode over the Pacific and the first two modes over the Atlantic have spatial patterns that are very similar to the corresponding wind patterns obtained from the EOF analyses on the AR response (Compared Figures 4.A.7a, 4.A.7e, 4.A.7f to Figures 4.5.2c, 4.5.2g and 4.5.2h). Indeed, the correlation between the PCs of the first AR mode and the first wind mode over the Pacific, the first AR mode and the

first wind mode over the Atlantic, the second AR mode and the second wind mode over the Atlantic are 0.83, 0.86 and 0.75, respectively. Since the uncertainty in the AR response results from uncertainties in the zonal wind and moisture responses, these high correlations suggest that these three AR uncertainty modes are largely driven by the corresponding zonal wind uncertainty modes. However, the correlation between the second AR mode and the second wind mode over the Pacific is 0.52 which is slightly weaker than the correlation (0.59) between the second AR mode and the third wind mode (Figure 4.A.8a). This suggests that both the second and third modes of zonal wind variability may play a role in driving the second uncertainty AR mode over the Pacific.

In the above analyses, we show the uncertainty patterns of the response due to internal variability. However, the response uncertainty can also arise from model differences. To understand the pattern of uncertainty associated with model differences, we perform the same EOF analyses on the ensemble mean AR responses of individual models. Note that *Peings et al.* (2021) shows that 100 members may be not enough to suppress all the internal variability in these PAMIP experiments. Therefore, the EOF modes obtained this way may still contain a substantial influence of internal variability. Nevertheless, performing EOF analysis on the ensemble mean response of individual models can still give us an estimate for the uncertainty due to model differences. Instead of concatenating the response of individual members together, we concatenate the ensemble mean responses of individual models. Despite having only nine models, the dominant mode of uncertainty over the Pacific and the first two modes of uncertainty over the Atlantic (Figure 4.A.9) largely resemble those due to internal variability (Figure 4.5.2), though the magnitude is smaller, and the spatial patterns are noisier due to a smaller sample size. Over the Pacific, the first uncertainty mode due to model difference (Figure 4.A.9a) mostly describe uncertainty in the strengthening of the AR peak regions. In addition, it also reflects the uncertainty in the northeastward extension. Indeed, its associated wind pattern shows the uncertainty in both the meridional shift and strengthening of the jet, especially over the jet exit regions (Figure 4.A.9c). Unlike

the second AR mode due to internal variability (Figure 4.5.2b) which shows a narrowing and northeastward extension of the AR peak regions, the second mode of model difference (Figure 4.A.9b) is quite similar to the first mode, but shifted southeastward, making it project more strongly onto the meridional shift mode. Over the Atlantic, the first and second uncertainty modes due to model differences (Figures 4.A.9e and 4.A.9f) are the same as those due to internal variability, i.e., they show a meridional shift and a strengthening/eastward extension of ARs, respectively.

4.3.3 Potential Emergent Constraints

Combining the results from the multi-model mean responses (Figure 4.5.1) and the uncertainty modes (Figure 4.5.2), one can see that the mean AR response projects onto leading modes of uncertainty over both the Pacific and the Atlantic (Figure 4.5.3). For example, the mean AR response over the Pacific projects preferentially onto the second uncertainty mode which represents the northeastward extension of ARs. Over the Atlantic, the mean AR response projects strongly onto the first uncertainty mode which is associated with the meridional shift of ARs. Similarly, the mean 850 mb zonal wind response over the Atlantic also projects onto the uncertainty mode associated with the meridional shift of the winds. The mean zonal wind response over the Pacific, which represents the northeastward extension of the jet, shows no clear preference as to which modes it projects onto. Since these leading modes of uncertainty are mostly driven by internal variability, this implies that they should also represent the leading modes of unforced variability in ARs and the 850 mb zonal winds. Indeed, an EOF analysis of interannual variability in DJF AR frequency and DJF 850 mb zonal winds across all 900 members in the piArcSIC experiment produces leading modes of variability nearly identical to those shown in Figures 4.5.2 and 4.A.7 (not shown). These results suggest that the response to sea ice loss projects onto natural modes of variability.

Under global warming, generally climate models project a robust poleward shift of the eddy-driven jets over both the Atlantic and Southern Hemisphere (*Barnes and Polvani*,

2013). Some studies further show that this poleward shift is related to the mean jet state: namely, models with an equatorward-biased climatological jet tend to produce a more poleward shift under global warming (*Barnes and Hartmann*, 2010; *Kidston and Gerber*, 2010). *Barnes and Hartmann* (2010) explain such state dependency by invoking the eddy-mean flow feedback. Since wave breaking can lead to eddy momentum flux divergence and thus weakening of the jet, they argue that the poleward shift of the jet, equivalently, the strengthening of the winds on the poleward side of the jet, is sustained by suppressing wave breaking on the poleward side of the jet. However, due to the sphericity of the earth, the poleward wave breaking is suppressed for a jet that is located nearer to the pole in climatology. *Burrows et al.* (2017) further examines this relationship in a set of idealized model simulations and confirms the importance of subtropical eddy mixing for the persistence of eddy-driven jet under a range of climate forcings, including tropical and Arctic forcings. *Chen et al.* (2020) showed that the eddy-driven jet changes under different forcings experience similar circulation feedback in spite of the direction of jet shift. As a result, it is expected that poleward biased jets tend to shift less poleward under climate warming, and equatorward biased jets shift less equatorward under Arctic warming. Given such state dependency in the jet responses to warming, one may ask if the AR response to sea ice loss also exhibits similar state dependency.

Over the Pacific, since the AR response is characterized by a northeastward extension of ARs, we explore whether the degree of extension is related to the climatological AR core longitude. We define AR core longitude as the longitude where the meridionally averaged AR frequency between $20°N$ and $50°N$ is maximum over the Pacific. Indeed, as shown in Figure 4.5.4a, models with a climatological AR core located more westward tend to produce a stronger positive response over the AR extension regions defined as the regions between $30°N$ and $50°N$ and $180°E$ and $230°W$ (blue box in Figure 4.5.1e). Similarly, their responses also tend to project more strongly onto the second uncertainty mode over the Pacific which is associated with the northeastward extension (Figure 4.5.4c). Over the Atlantic, the degree of

AR equatorward shift under sea ice loss seems to depend on the latitude of the climatological AR peak regions, which is defined as the latitude of maximum zonally averaged AR frequency between $60°W$ and $0°$ (Figure 4.5.4b). Models with climatological AR peak regions located over higher latitudes tend to exhibit stronger equatorward shifts and their responses also tend to project more strongly onto the first uncertainty mode which represents the meridional shift of ARs (Figure 4.5.4d). Moreover, such relations between the AR response and the AR basic state in the models also exist for the westerly jet (Figure 4.A.10), though the relationships are weaker. Over the Pacific, models with a more westward-located climatological jet core tend to simulate a stronger northeastward extension. Over the Atlantic, the westerly jet also tends to shift further equatorward in the models that have a more poleward-located climatological jet.

The results presented in this section suggest a potential emergent constraint for the AR response to sea ice loss: given that the AR response appears to depend on the modeled AR climatology, we may be able to use the observed AR climatology to constrain the spread in modeled AR climatology, and thus narrow the spread in the AR response under sea ice loss (*Hall et al.*, 2019). Following such constraints, observations indicate that the AR peak regions over the Pacific and Atlantic will extend northeastward and shift equatorward under Arctic sea ice loss, respectively (Figure 4.5.4). However, the limited number of models used in this study prevent us from reaching a definite conclusion. More models are needed to test the robustness of such relationships between mean state and response. Idealized experiments similar to *Burrows et al.* (2017) could also be conducted to investigate physical mechanisms behind such emergent constraints.

4.4 Conclusions

The response of DJF AR frequency to prescribed $+2°C$ global warming-equivalent Arctic sea ice loss has been investigated using a set of atmosphere-only simulations from the PAMIP

ensemble. Under Arctic sea ice loss, over the Pacific, it is found that ARs extend northeastward and occur closer to the North American west coast. Over the Atlantic, ARs shift equatorward. The AR response in midlatitudes is mostly governed by the changes in dynamics. Above about $60°N$, the weakening of the zonal wind tends to reduce AR frequency while the moistening of the atmosphere due to sea ice loss tends to enhance AR frequency. These two effects cancel each other, leading to relatively small negative response over the Pacific sector and positive response over the Atlantic sector.

Inter-model spread in the AR responses is mostly due to the spread in the zonal wind response, with the response in the moisture field being quite consistent across models. We further found that the response uncertainty due to internal variability and model differences resemble modes of internal variability. The uncertainty modes over the Pacific describe uncertainty in the strengthening or weakening of the AR core and northeastward extension of ARs. Over the Atlantic, they represent the uncertainty in the meridional shift and eastward extension of ARs. While the patterns of the leading uncertainty modes due to internal variability resemble those due to model differences, their magnitudes are substantially larger (compare Figures 4.5.2 and 4.A.9). This suggests that internal variability plays a much larger role than model difference in uncertainties, so that a large ensemble of simulations is required to robustly address the signal-to-noise ratio problem. Analyses of additional 200 members of the SC-WACCM4 experiments (not shown) indicates that the noise associated with internal variability is not completely suppressed in the ensemble mean of the 100 member ensemble, consistent with *Peings et al.* (2021), and thus more than 100 members are needed to suppress the noise due to internal variability. In addition, the future sea ice loss scenario used here corresponds to $2°C$ warming of the global mean surface air temperature. Different sea ice loss scenarios under stronger warming will also help to strengthen the signal, thus the signal-to-noise ratio. Finally, the noisy patterns shown in the uncertainty modes due to model differences also indicate that more models are need-ed to better understand the uncertainty due to model differences.

Potential emergent constraints between the AR basic state and the AR response were also explored. Over the Pacific, we found that models with a more westward-located climatological AR core tend to simulate a greater northeastward extension under Arctic sea ice loss. Over the Atlantic, stronger equatorward shifts in response to sea ice loss tend to occur in models that have a more poleward climatological peak of AR activity. Together, these results and the observed AR statistics suggest that Arctic sea ice loss promotes a northeastward extension of ARs over the North Pacific, and an equatorward shift over the North Atlantic. However, the limited number of models used in this study prevent us from making a definite conclusion. Future works using more models with identical sea ice loss forcing are thus needed to test and quantify the robustness of the relationships found in this study. These potential emergent constraints also suggest that it is important to improve the representation of AR climatology in models for AR projection studies. Such improvements can be achieved by increasing model spatial resolution. For example, using the Community Earth System Model version 1.3 (CESM1.3; *Chang et al.* (2020)), shows that CESM1.3 with higher spatial resolution can simulate more realistic AR characteristics compared to the version with lower resolution. Given the high correlation between the westerly jet and ARs, additional improvements on AR climatology can be obtained by better representation of the jet characteristics, such as mean jet position and strength, in models.

Under climate warming, other factors than Arctic sea ice loss (e.g., tropical SST increases or ocean-atmosphere coupling) can also contribute to the changes in ARs. For example, while the loss of Arctic sea ice shifts ARs equatorward over the Atlantic, the tropical upper tropospheric warming induces an opposite response by shifting the westerly jet poleward (*Barnes and Screen*, 2015; *Butler et al.*, 2010; *Chen et al.*, 2020; *Shaw et al.*, 2016). Considering only the dynamic effect, the robust poleward shift of the westerly jet over the Atlantic under warming suggests that the influences of tropical upper tropospheric warming will dominate over that from the Arctic sea ice loss and shift ARs poleward. However, both Arctic sea ice loss and tropical upper tropospheric warming will also modify the moisture field in their way

and thus exert different thermodynamic influences on the AR distribution. Furthermore, the influences of Arctic sea ice loss on ARs and the influences of the tropical upper tropospheric warming on ARs may not be linearly additive, they may interact in some nonlinear ways. Taking these factors together, this "tug-of-war" between Arctic warming and tropical upper tropospheric warming makes AR response to warming uncertain. In this study, we isolate the effects of Arctic sea ice loss on AR changes with two sets of PAMIP experiments which differ only in Arctic sea ice conditions. Future works using PAMIP experiments that include SST changes alone or both Arctic sea ice loss and SST changes with/without ocean-atmosphere coupling are needed to better understand the importance of this "tug-of-war" on ARs.

Acknowledgements. The authors thank Rosie Eade at Met Office for the use of the HadGEM3 data, Lantao Sun at Colorado State University for the use of the CESM2 data and Guillaume Gastineau at Institut Pierre Simon Laplace for the use of the IPSL-CM6A data. Weiming Ma and Gang Chen are supported by National Science Foundation Grants AGS-1832842 and NASA Grant 80NSS-C21K1522. Yannick Peings is supported by Department of Energy (DOE) Grant DE-SC0019407. This research used resources of the National Energy Research Scientific Computing Center (NERSC), a U.S. Department of Energy Office of Science User Facility located at Lawrence Berkeley National Labora-tory, operated under Contract No. DE-AC02-05CH11231. The authors would like to acknowledge high-performance computing support from Cheyenne (https://doi.org/10.5065/D6RX99HX) provided by NCAR's Computational and Information Systems Laboratory, sponsored by the National Science Foundation.

4.5 Figures

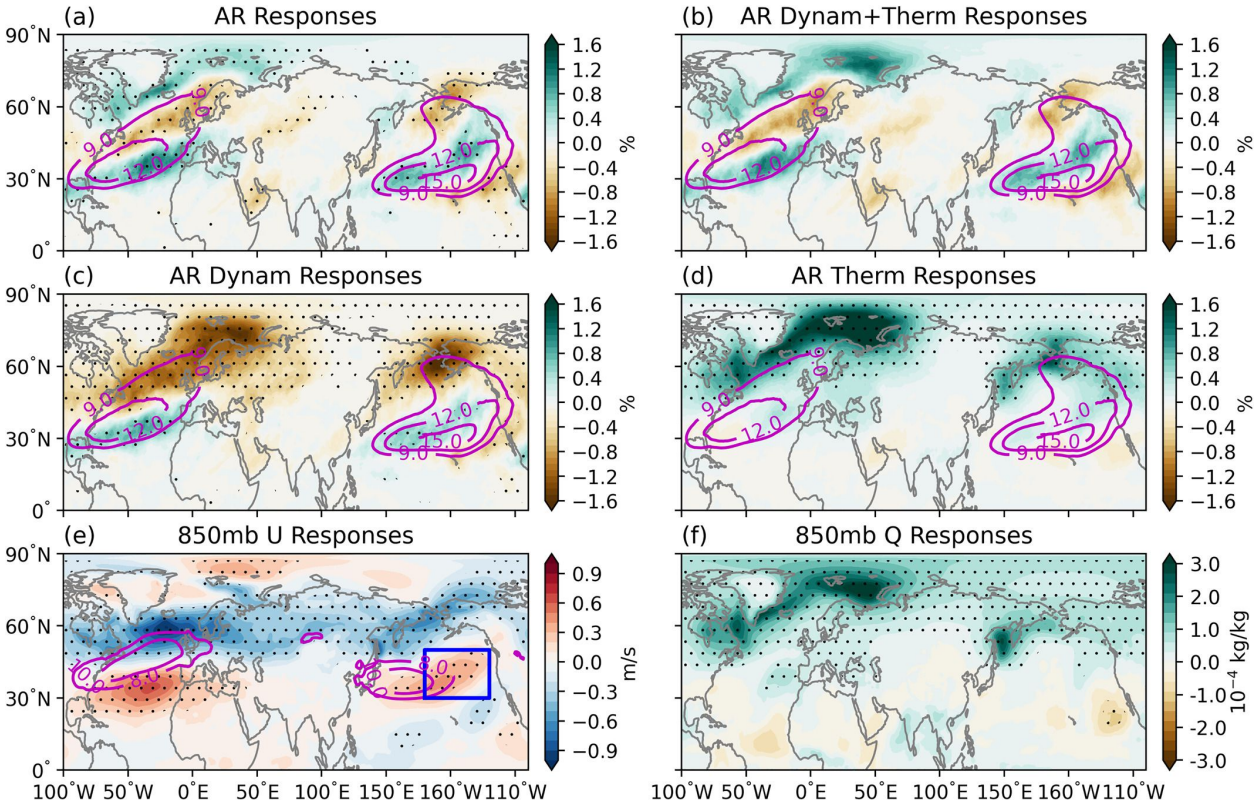

Figure 4.5.1: The multi-model ensemble-mean total (a), dynamical (c), and thermodynamical (d) responses of AR frequency to Arctic sea ice loss. (b) shows the sum of (c and d). The ensemble-mean response of the 850 mb zonal wind and 850 mb specific humidity are shown in (e and f), respectively. The shaded contours show the responses, and the solid contours show the climatology. Stippling indicates regions with anomalies significant at the 95% confidence level based on a Student's t test. The blue square in (e) indicates the region of northeastward extension in AR over the Pacific.

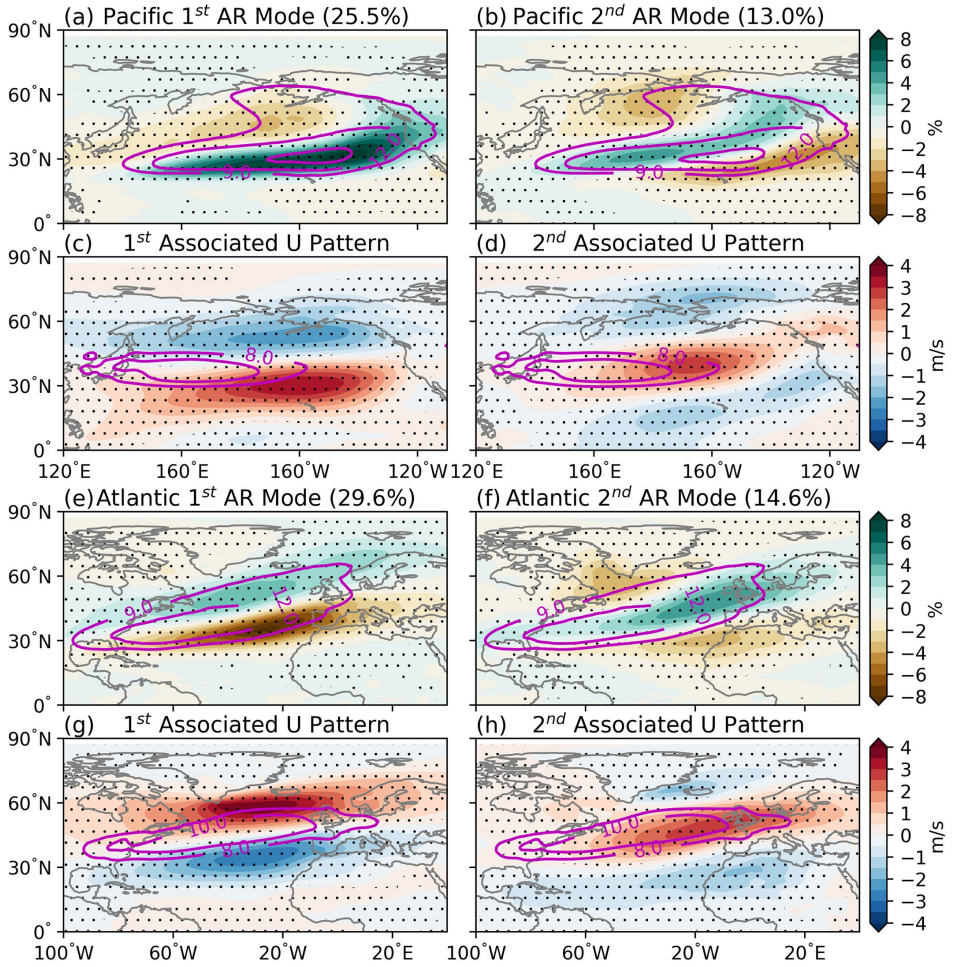

Figure 4.5.2: The first (a) and second (b) uncertainty modes in AR frequency response over the Pacific. (c and d) are the associated 850 mb zonal wind response patterns. (e – h) are similar to (a – d), but for the Atlantic. The shaded contours show the uncertainty patterns while the solid contours indicate the climatology. Values inside parentheses indicate the fraction of variance explained by each mode. Stippling indicates regions where the uncertainty patterns are significant at the 95% confidence level based on Student's t test.

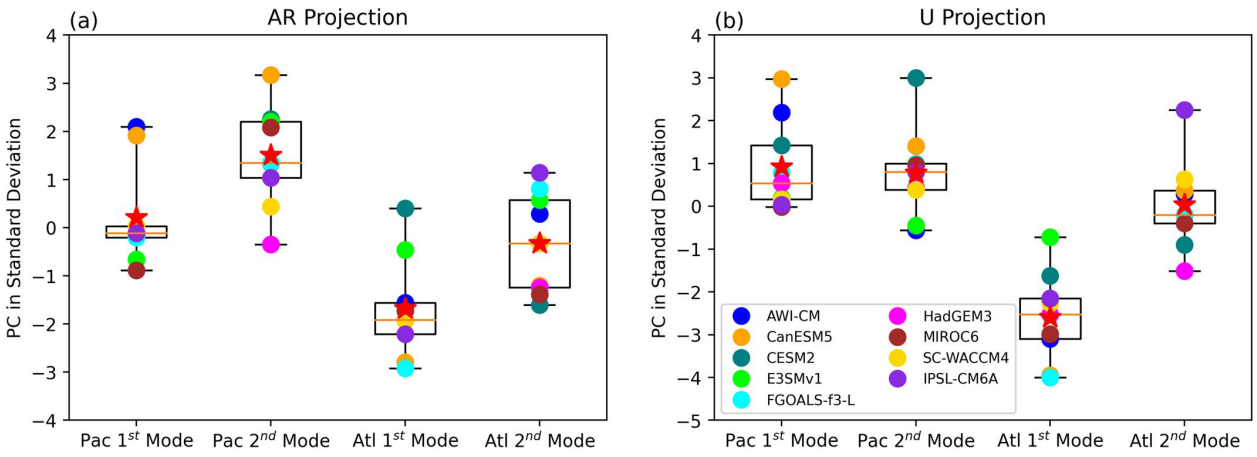

Figure 4.5.3: The responses of AR frequency (a) and 850 mb zonal wind (b), as projected onto their leading uncertainty modes. The box shows the 25th and 75th percentile of the inter-model spread. The caps show the maximum and minimum. Star and the horizontal line show the multi-model ensemble mean and median, respectively.

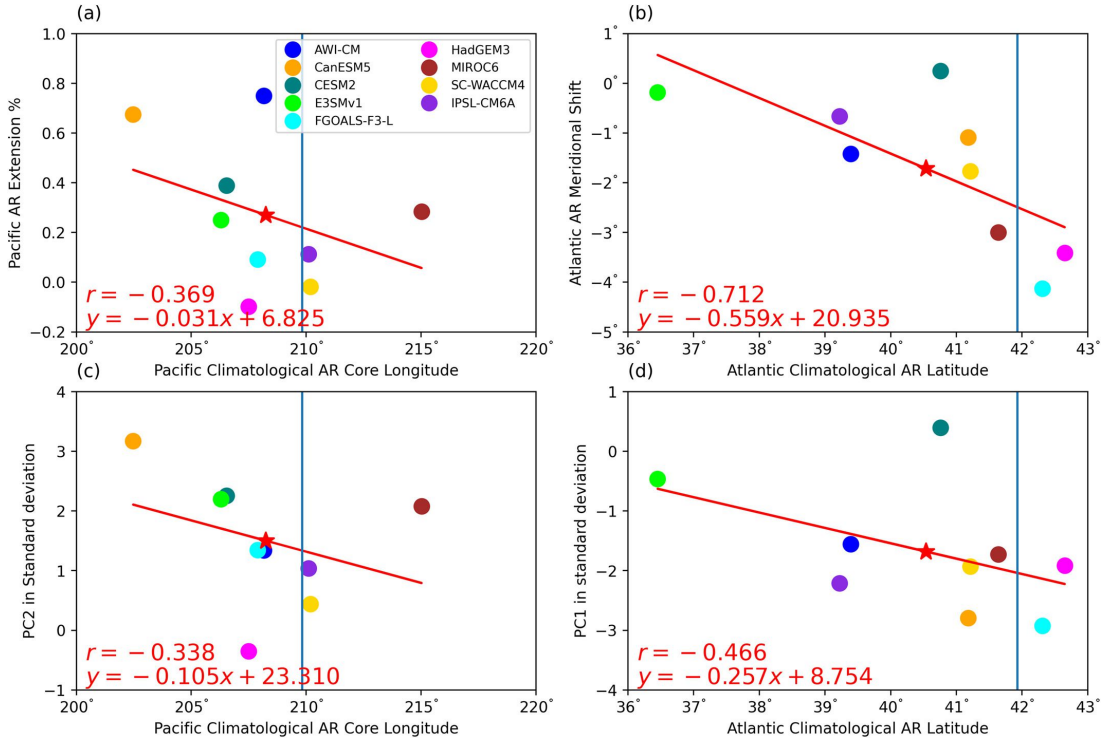

Figure 4.5.4: The climatological AR core longitude vs. AR extension over the Pacific (a). The climatological AR latitude vs. AR meridional shift over the Atlantic (b). The climatological AR core longitude vs. the projection of AR response onto the 2nd AR uncertainty mode over the Pacific (c). The climatological AR latitude vs. the projection of AR response onto the 1st AR uncertainty mode over the Atlantic (d). The red line shows the least squares regression line, with equations and correlations listed on the bottom left. The star shows the multi-model ensemble mean. Observed AR core longitude and AR latitude from ERA-Interim are indicated by the blue vertical line. See Section 4.2.1 for the definition of AR core longitude, AR extension, AR latitude, and AR meridional shift.

4.A Supplement

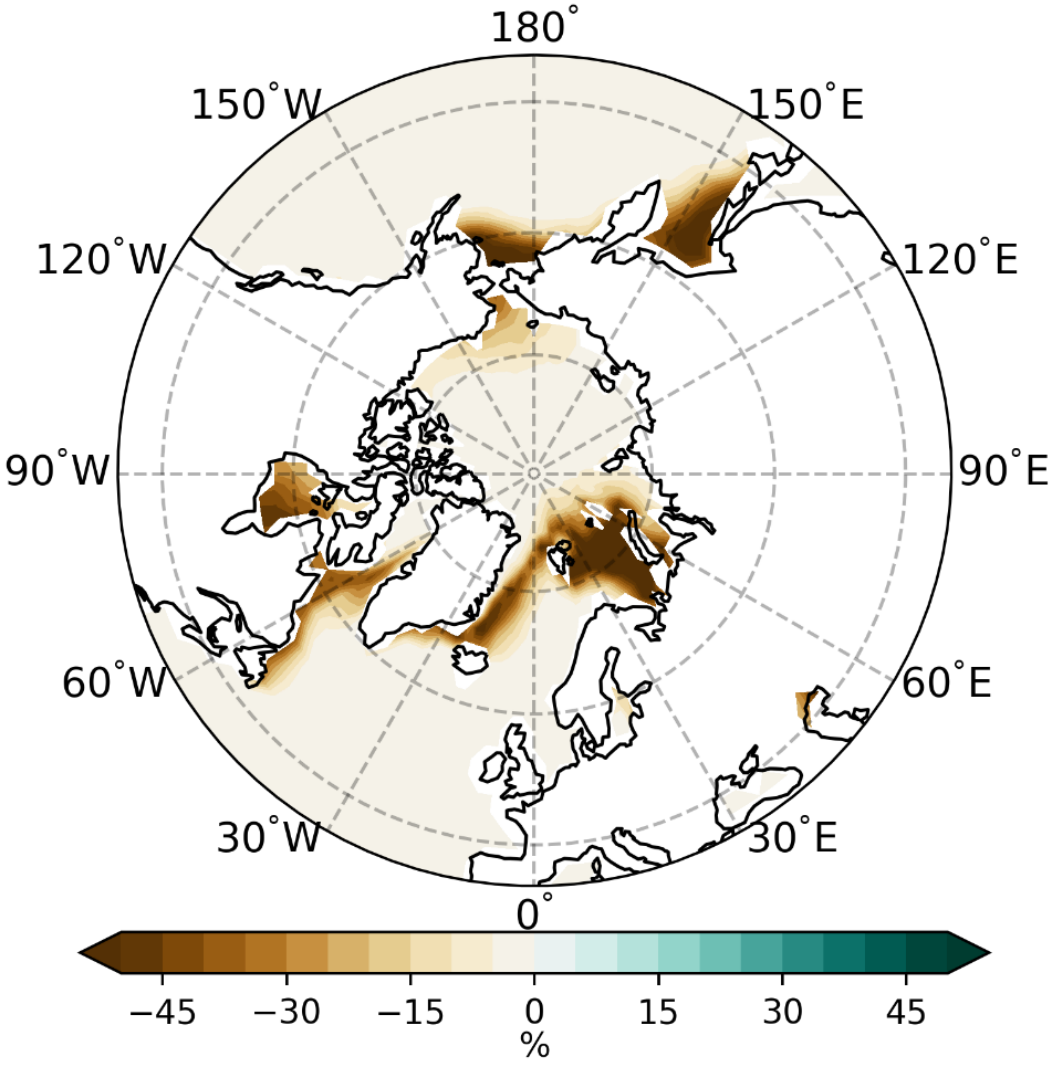

Figure 4.A.1: DJF sea ice concentration anomalies imposed in futArcSIC relative to pi-ArcSIC.

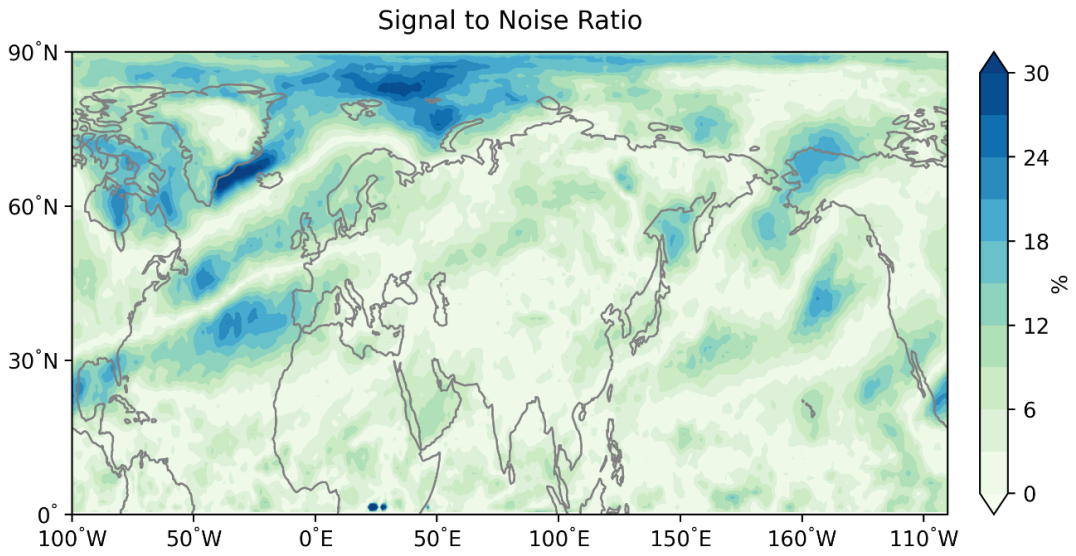

Figure 4.A.2: The spatial distribution of the signal-to-noise ratio of the mean AR response. The signal is defined as the ensemble mean AR frequency response of all 900 members while the noise is defined as the standard deviation of the DJF AR frequency interannual variability in piArcSIC across 900 members.

Table 4.A.1: Model Information

Model	Institute	Resolution (lat × lon)
AWI-CM	Alfred Wegener Institute	$0.93^\circ \times 0.94^\circ$
CanESM5	Canadian Centre for Climate Modelling and Analysis	$2.8^\circ \times 2.8^\circ$
CESM2	National Center for Atmospheric Research	$0.9^\circ \times 1.25^\circ$
E3SMv1	Department of Energy	$2.5^\circ \times 2.5^\circ$
FGOALS-f3-L	Chinese Academy of Sciences	$1^\circ \times 1.25^\circ$
HadGEM3	Met Office UK Hadley Centre	$0.8^\circ \times 0.5^\circ$
MIROC6	Center for Climate System Research/University of Tokyo/Japan Agency for Marine-Earth Science and Technology/National Institute for Environmental Studies	$1.4^\circ \times 1.4^\circ$
SC-WACCM4	National Center for Atmospheric Research	$2.5^\circ \times 1.9^\circ$
IPSL-CM6A	Institut Pierre Simon Laplace	$1.3^\circ \times 2.5^\circ$

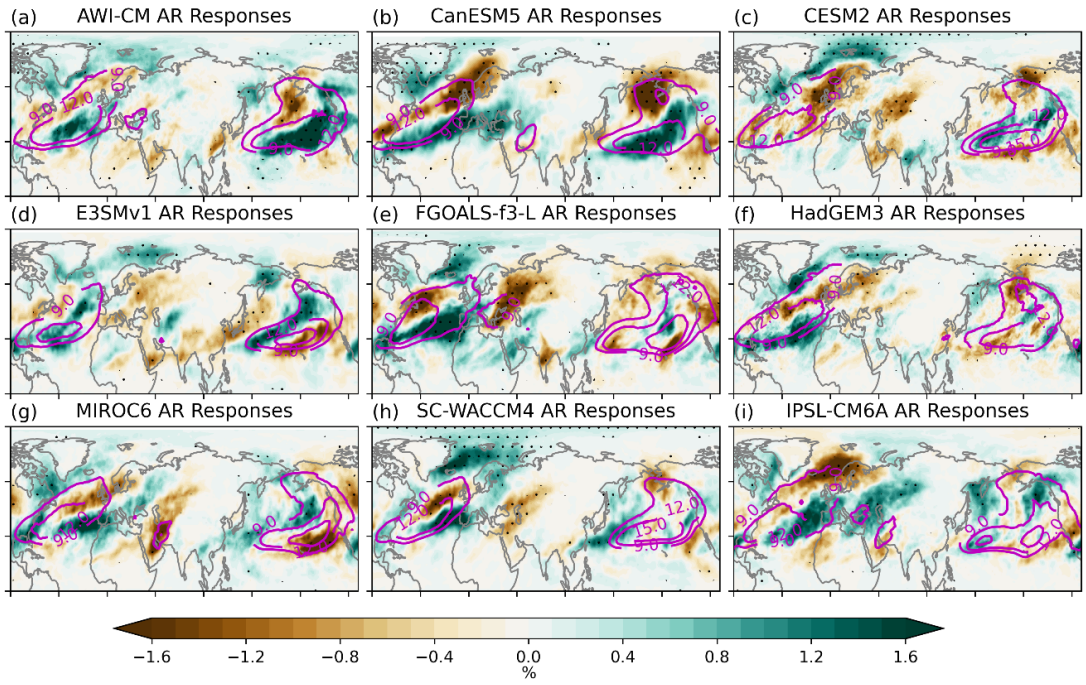

Figure 4.A.3: DJF AR responses in individual models. Responses are shown in shaded contours and the climatology is shown in magenta contours. Stippling indicates regions with responses significant at the 95% confidence level based on a Student's t test.

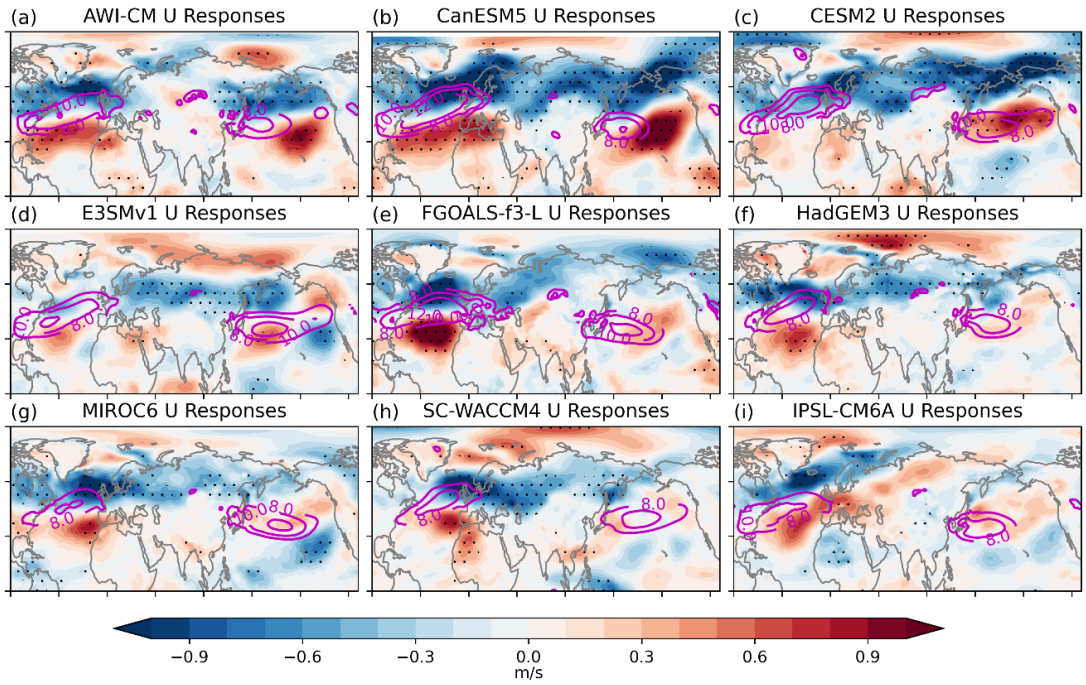

Figure 4.A.4: DJF 850mb zonal wind responses in individual models. Responses are shown in shaded contours and the climatology is shown in magenta contours. Stippling indicates regions with responses significant at the 95% confidence level based on a Student's t test.

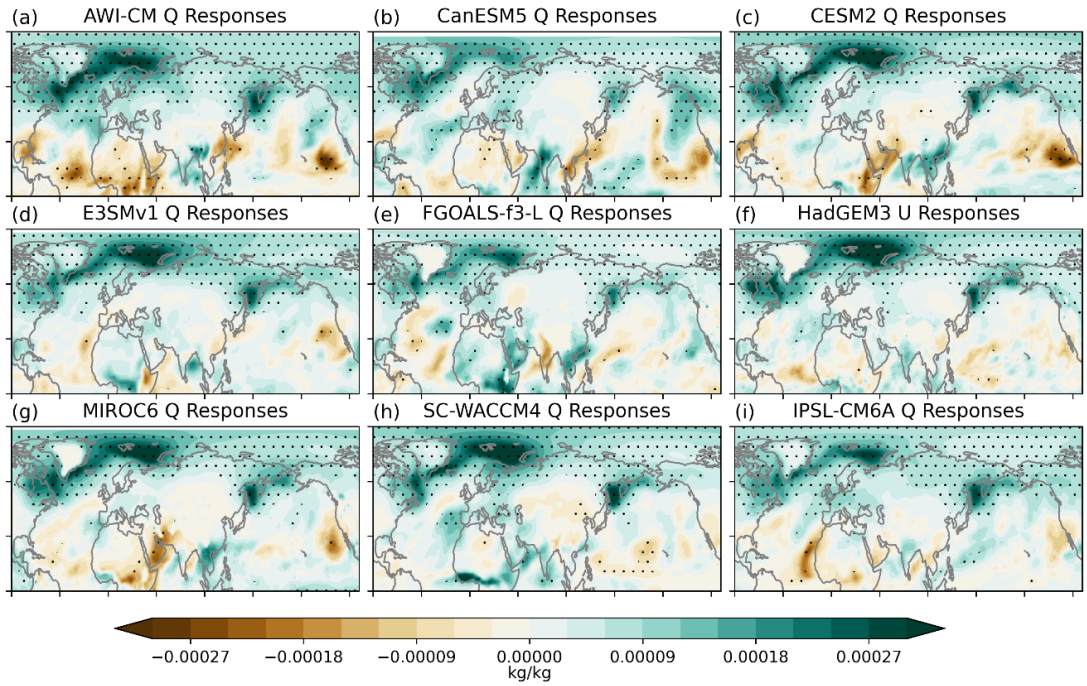

Figure 4.A.5: DJF 850mb specific humidity responses in individual model. Stippling indicates regions with responses significant at the 95% confidence level based on a Student's t test.

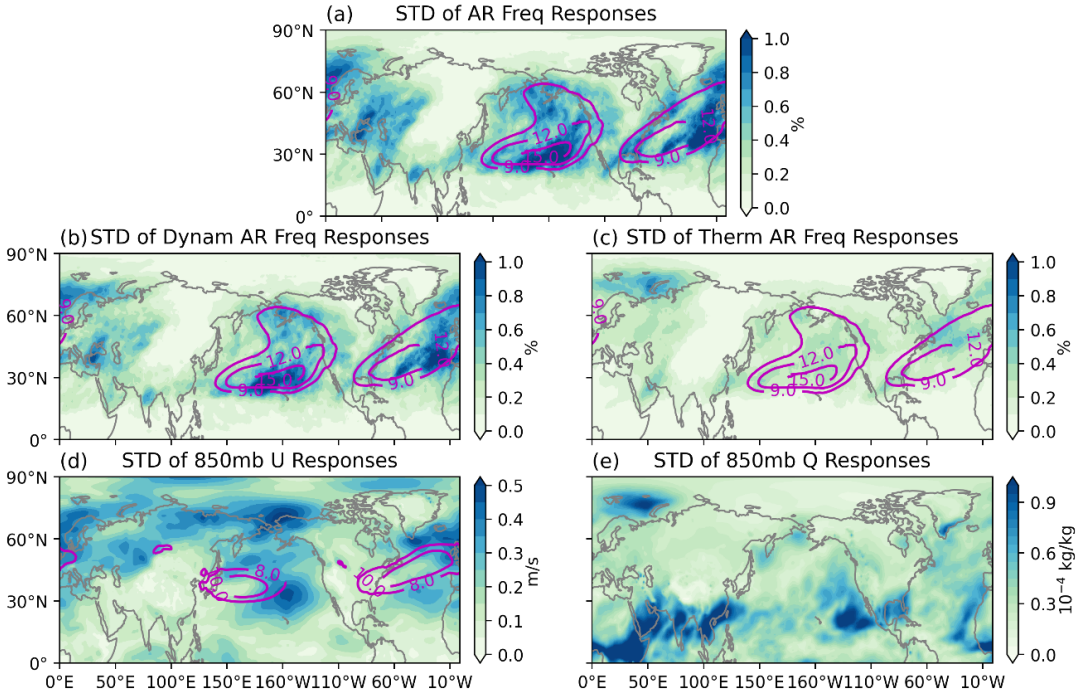

Figure 4.A.6: Inter-model spread of the total AR responses (a), dynamic component of the AR responses (b) and thermodynamic component of the AR responses (c). (d) and (e) show the inter-model spread in the 850 mb zonal wind responses and the 850 mb specific humidity responses, respectively. Inter-model spread is quantified as the standard deviation of the responses across models (shaded contours). Solid contours show the climatology.

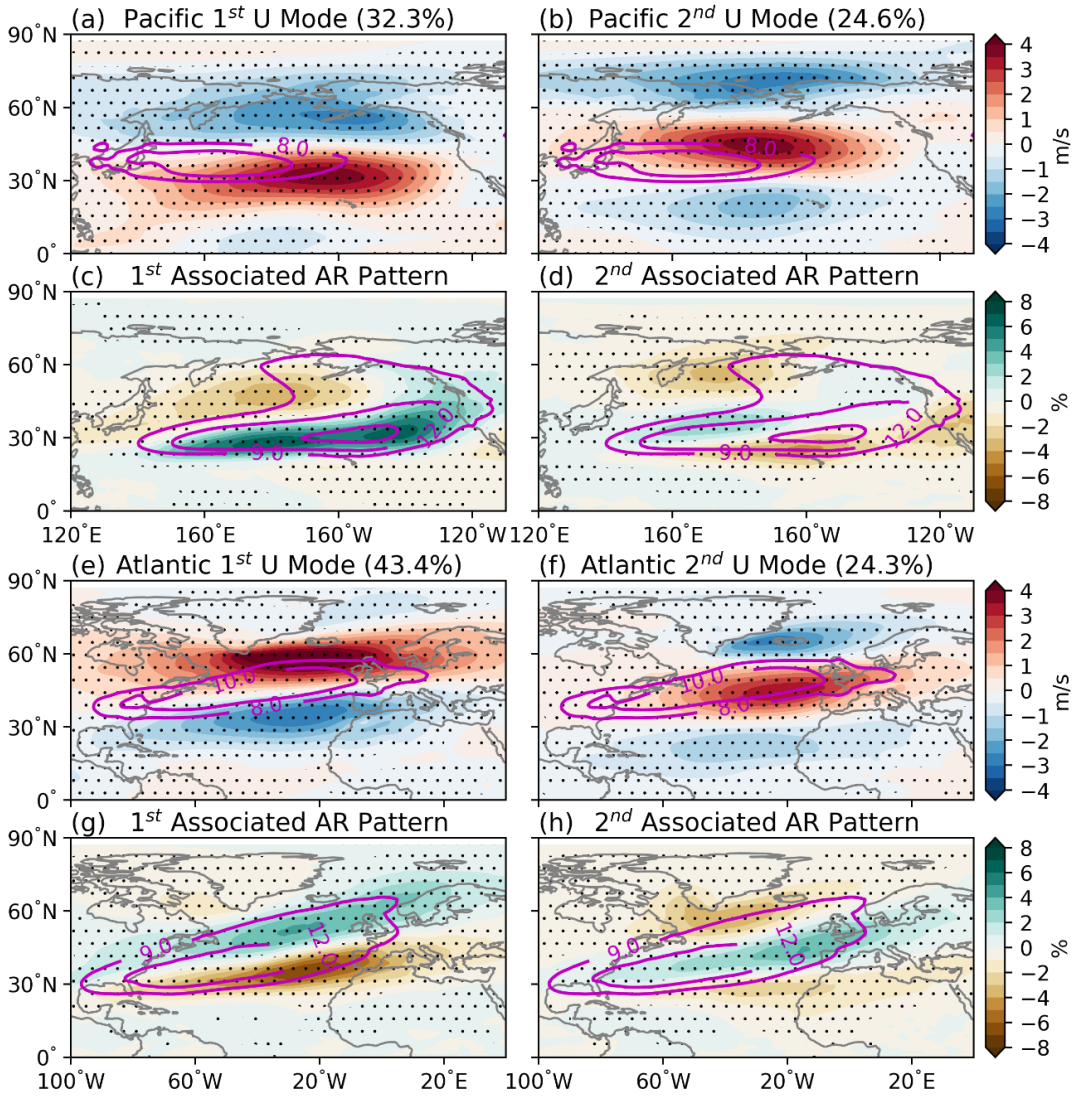

Figure 4.A.7: The first (a) and second (b) uncertainty modes in 850mb zonal wind responses over Pacific. (c) and (d) are the associated AR frequency response patterns. (e)-(h) are similar to (a)-(d), but for the Atlantic. The shaded contours show the uncertainty patterns while the solid contours climatology. Values inside parentheses indicate the fraction of variance explained by each mode. Stippling indicates regions significant at the 95% level.

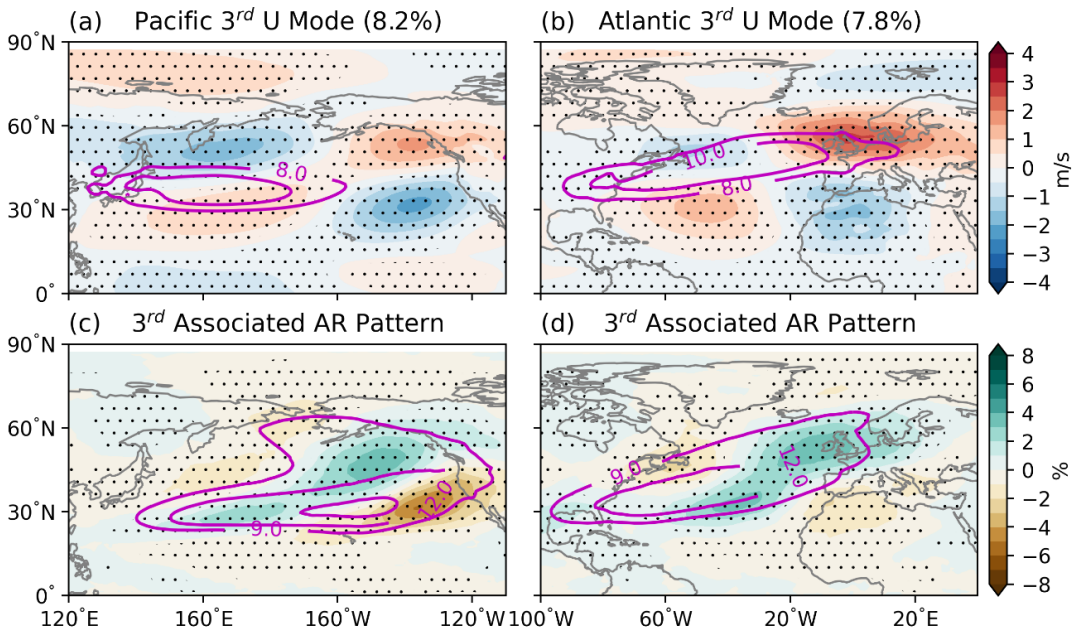

Figure 4.A.8: Same as figure 4.A.6, but for the third uncertainty mode in 850mb zonal wind.

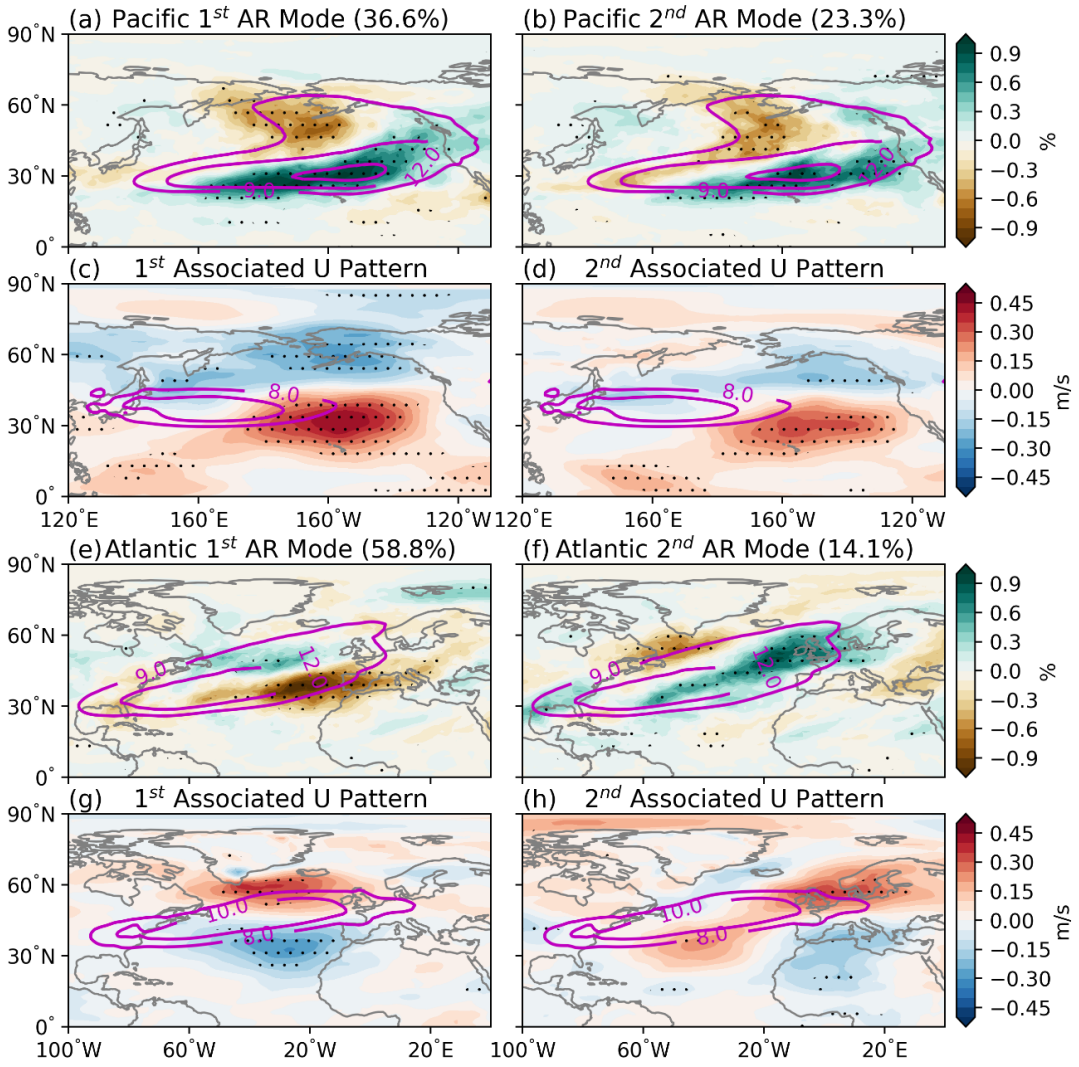

Figure 4.A.9: The first (a) and second (b) uncertainty modes due to model differences in AR frequency response over Pacific. (c) and (d) are the associated 850mb zonal wind response patterns. (e)-(h) are similar to (a)-(d), but for the Atlantic. The shaded contours show the uncertainty patterns while the solid contours climatology. Values inside parentheses indicate the fraction of variance explained by each mode. Stippling indicates regions significant at the 95% level.

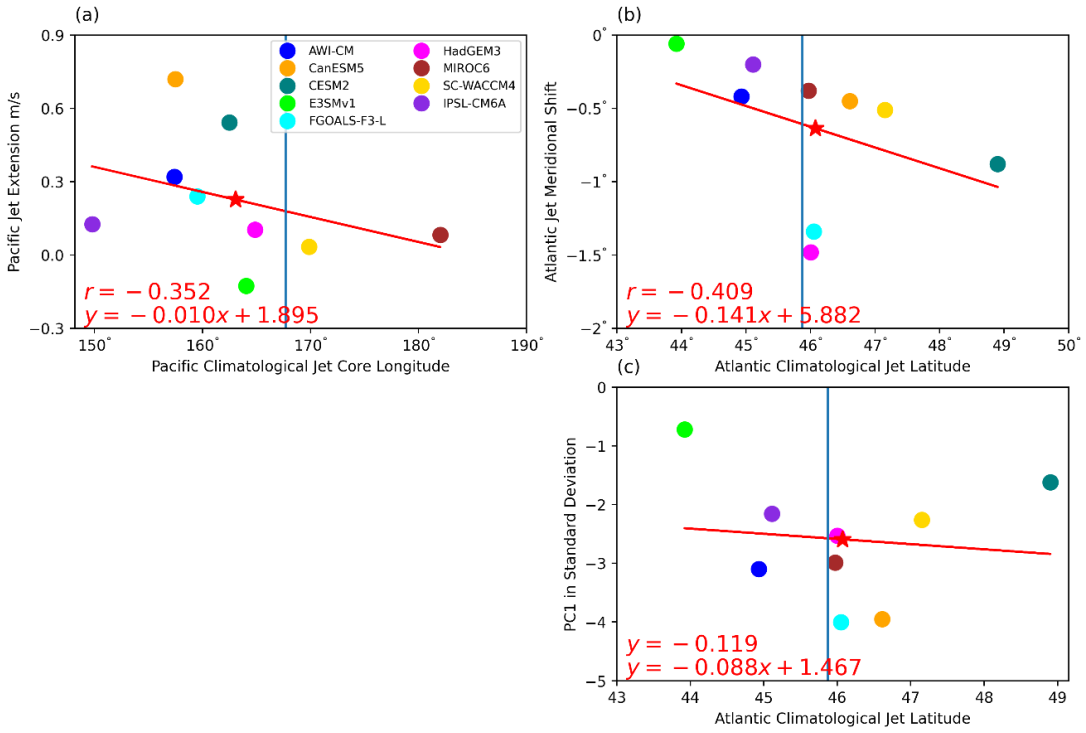

Figure 4.A.10: The climatological jet core longitude versus jet extension over Pacific (a). The climatological jet latitude versus jet meridional shift over Atlantic (b). The climatological jet latitude versus the projection of jet responses onto the 1st wind uncertainty mode over Atlantic (c). The red line shows the least squares regression line, with equations and correlations listed on the bottom left. The star shows the ensemble mean. Observed jet core longitude and jet latitude from ERA-Interim show in the blue vertical line. See section 4.2.1 for the definition of jet core longitude, jet extension, jet latitude and jet meridional shift.

CHAPTER 5

Projected Changes to Extreme Precipitation Along North American West Coast From the CESM Large Ensemble

[**Ma, W.**, Norris, J., Chen, G. (2020). Projected Changes to Extreme Precipitation Along North American West Coast From the CESM Large Ensemble. *Geophysical Research Letters*, 47(1), 1-10. https://doi.org/10.1029/2019GL086038]

Abstract Precipitation events along the North American (NA) west coast are strongly modulated by atmospheric rivers, yet the mechanisms of their influences on the probability distributions of precipitation events are not well studied. Simulations from the Community Earth System Model (CESM)large ensemble under global warming are investigated using a moisture budget conditioned onto precipitation events for the recurrence intervals ranging from 0.1 to 50 years. In the midlatitudes, the increases in precipitation intensity and accumulation for all events over the NA west coast are predominantly controlled by moisture increases. In contrast, changes in the subtropical precipitation distributions in southwestern NA are associated with moisture increases and duration decreases for all events, with additional dynamical amplification for the heaviest precipitation events. These interpreta-

tions from the conditional moisture budget are more consistent with future projection of atmospheric rivers than the conventional mean and transient decomposition of the moisture budget.

5.1 Introduction

Among the regions with high hydrologic sensitivity to global warming, the North American (NA) westcoast, due to its dense population, has received substantial attention. The hydroclimate over NA westcoast is strongly modulated by atmospheric river (AR) variation (*Ralph et al.*, 2006; *Leung and Qian*, 2009; *Waliser and Guan*, 2017). In a warming climate, ARs are expected to increase significantly in both frequency and intensity due mostly to the higher moisture content in a warmer atmosphere (*Gao et al.*, 2015; *Hagos et al.*, 2016; *Payne and Magnusdottir*, 2015; *Lu et al.*, 2018; *Warner et al.*, 2015). While the studies on ARs have offered a comprehensive understanding on the changes in integrated water vapor transport under global warming, the mechanisms for their influences on the probability distributions of precipitation events are not well studied. In contrast, there is mounting evidence for global hydrological cycle intensification under global warming. Changes to the mean precipitation generally follow the"wet-get-wetter, dry-get-drier"mechanisms (*Chou and Neelin*, 2004; *Held and Soden*, 2006). For extreme precipitation, climate models project substantial increases over most of the globe (*Emori and Brown*, 2005; *Norris et al.*, 2019a; *Pfahl et al.*, 2017). This paper will examine to what extent these paradigms of global hydrological cycle intensification are related to the regional precipitation changes associated with ARs along the NA west coast.

It has been shown that changes to the mean precipitation minus evaporation (P - E) over NA under global warming can be understood by changes to the moisture flux convergence by the mean flow and transient eddies, respectively (*Seager et al.*, 2014; *Ting et al.*, 2018). Given that ARs are sporadic, should AR activities change significantly in the future, then one

may expect the changes in moisture flux convergence b ytransient eddies to, if not dominate, at least play an important role in the future changes in mean P - E along the NA west coast. However, an evaluation of the moisture budget by *Seager et al.* (2014) suggests that the future increases in cold season mean P - E over western NA, where ARs typically make landfall, will be mostly controlled by the changes in moisture flux convergence by the mean flow, while the changes in moisture flux convergence by transient eddies are negligible. These findings appear to be inconsistent with the studies on AR projection. Here we will analyze the moisture budget conditioned on precipitation events so as to reconcile the projected moisture transport dominated by the mean flow with the projected AR intensification over the NA west coast.

Previous studies have also suggested that the increases in extreme precipitation in a warming climate generate more latent heat release in the upper troposphere and remove atmospheric moisture at a rate faster than the replenishment by surface evaporation (*Dai et al.*, 2020; *Giorgi et al.*, 2011; *Thackeray et al.*, 2018; *Trenberth et al.*, 2003). This indicates that future extreme precipitation events are more effective in drying out and stabilizing the atmosphere, resulting in decreases in the strength and frequency of the light-moderate precipitation. So one may ask if such changes will occur along the NA west coast, and if so, what will be the mechanisms driving these changes? To address these questions, we analyze the moisture budget for precipitation across a range of recurrence intervals along the NA west coast from $20°N$ to $60°N$. We will study precipitation measured as both instantaneous rate and accumulation sizes. We study accumulation because, if one is concerned with the societal impacts of future precipitation changes, accumulation, defined as the amount of precipitation integrated through the event, is probably a more relevant quantity. For example, a high accumulation event with short duration will likely result in flooding. To ascertain the mechanisms driving these projected changes, we also decompose the changes into dynamic and thermodynamic contributions for both intensity and accumulation, with an extra contribution from duration for accumulation.

This paper is structured as follows. We will briefly describe the data and methodology in section 5.2. In section 5.3, the results for precipitation intensity as a function of recurrence interval will first be presented,followed by those for accumulations. Major conclusions will be presented in section 5.4.

5.2 Data and Methods

We use 6-hourly data from the CESM large ensemble (*Kay et al.*, 2015). The current climate is evaluated over the period from 1990 to 2005. The future climate is from 2071 to 2080 under RCP8.5 scenario. We chose these two periods because they are the only periods for which 6-hourly data are archived in the CESM large ensemble. We also experimented with just using the 10-year period for the recent climate to match the length of the future climate, and the precipitation probability distributions are not sensitive to the period chosen because both climates consist of 40 members. The projected changes are taken as the difference between these two climates. Each member of the large ensemble differs only in initial conditions. Therefore, the differences between ensemble members are solely due to internal variability of the climate system and the ensemble mean can be treated as the response to external forcing.

5.2.1 Recurrence Intervals for Precipitation Intensity and Accumulation Size

We are interested in extreme events. To compare extreme precipitation intensification with changes in light-moderate precipitation, we analyze the events above the 0.1-year recurrence interval. Recurrence interval is the expected value of the period between exceedances of a given precipitation intensity or accumulation size.The bins of recurrence interval are determined by the following formula:

$$e_i = 50^{-0.6+0.2i} \; for \; i = 0, 1, ..., 8$$

where e_i denotes the number of years for the i^{th} recurrence interval. This formula is designed to account for a balance between the number of bins and the sample size within each bin, generating a list of nine recurrence intervals ranging from about 0.1 to 50 years. To calculate either the precipitation intensity or the accumulation size associated with each recurrence interval, the data set is first sorted in ascending order. The value for the e_i-year recurrence interval for a climate of Y years is calculated by taking the average between the"$first_i$"th and the"$last_i$"th elements of the time series in ascending order, where $first_i = Y/50^{0.6+0.2(i0.5)}$ and $last_i = Y/50^{0.6+0.2(i+0.5)}$. This approach implies that the i^{th} recurrence interval is calculated by averaging over the probability distribution between the $(i1/2)th$ and $(i + 1/2)th$ recurrence intervals.

Following *Norris et al.* (2019b), an accumulation event is defined as the integral of consecutive time slices with precipitation rate greater than 0.5 mm/h: The beginning of the event occurs when precipitation rate becomes $>$ 0.5 mm/hr with the previous time step $<$ 0.5 mm/hr. Once the precipitation rate falls below this threshold, the event is considered to be over. An example of accumulation is shown in Figure 5.5.1 with total accumulation of 104 mm over 36 hr.

The largest recurrence interval in this study is 50 years. Therefore, a data set with length on the order of at least several hundred years is required to smooth out the noise and obtain robust results for high recurrence interval events. To generate such a data set, aggregation was performed on the original data set. We first aggregate all 40 members to generate a single time series for each grid point for both the current and future climate, respectively. To make the spatial maps smoother, the time series is further aggregated over 3×3 grid points surrounding each grid point to generate a single time series of 5760 years for the current climate (16 years $\times$ 40 members $\times$ 9 grid points) and 3600 years for the future climate (10 years $\times$ 40 members $\times$ 9 grid points). Again, the precipitation distributions are not sensitive to the use of 16 or 10 years for the present climate.

Realistically simulating the hydrological cycle over regions with complex terrain, such

as the NA west coast,requires models to have high spatial resolution (*Dulière et al.*, 2011; *Leung and Qian*, 2003). In this study, we defined the NA west coast as ten rectangular boxes immediately off the coast between $20°N$ and $60°N$, as shown in Figure 5.5.1a, which captures the large-scale precipitation features but is unable to describe the fine-scale characteristics associated with coastlines or orography. Each box consists of 15 grid points (three in the zonal direction and five in the meridional direction), with the upper three and/or lower three grid points overlapping with the adjacent box. As for the spatial maps described above, aggregation is performed on the original data set within each box.

5.2.2 Conditional Moisture Budget

The conditional moisture budget equation is used to study what controls the projected changes in extreme precipitation events. Our methods closely follow those in *Chen et al.* (2019) and *Norris et al.* (2019a), who analyzed the moisture budget conditionally averaged onto percentiles of precipitation intensity, and *Norris et al.* (2019a), who analyzed recurrence intervals of precipitation accumulations. A brief description is as follows.

The moisture budget of the atmosphere over a grid point is (*Seager and Henderson*, 2013)

$$P - E = \frac{-1}{g}\nabla \cdot \int_0^{p_s} vqdp - \frac{1}{g}\frac{\partial}{\partial t}\int_0^{p_s} qdp \tag{5.1}$$

where P is precipitation, E is evaporation estimated from the surface latent heat flux divided by the latent heat of vaporization,v is the horizontal wind vector,q is the water vapor mixing ratio, p_s is the surface pressure, and g is the gravitational acceleration. Defining the dry-air mass convergence, C_k at the k_{th} model level as $C_k = \frac{1}{g}\nabla \cdot (V_k dp_k)$, and denoting the mass-weighted vertical integral of some variable X as $\{X\} = \frac{1}{g}\sum_k (X_k dp_k)$, where X_k is X on the k^{th} model level and dp_k is the pressure difference between the base and top of the k^{th} model level, equation 5.1 can be written as

$$P - E = \sum_k (q_k C_k) - v \cdot \nabla q - \frac{\partial}{\partial t}\{q\} \tag{5.2}$$

where the first term on the right-hand side represents the effect of horizontal mass convergence or vertical moisture transport by mass continuity, the second term is the horizontal advection and the third term is the moisture storage.

It has been shown that, for extreme events, evaporation is negligible, horizontal advection, and storage tend to cancel each other to some degree, resulting in vertical transport dominating the budget (*Chen et al.*, 2019; *Norris et al.*, 2019a). After conditioning the budget onto thee-year recurrence interval of precipitation and neglecting the covariance between q_k and C_k, the moisture budget becomes

$$\bar{P}^e \approx \sum_k \bar{q_k}^e \bar{C_k}^e \tag{5.3}$$

Similarly, for precipitation accumulation

$$\bar{P_{acc}}^e \approx \bar{D}^e \sum_k \bar{q_k}^e \bar{C_k}^e \tag{5.4}$$

where D is the duration of the events and the overbar denotes the event-mean for events in the e_i-year recurrence interval bin.

From 5.3 and neglecting the second order term $\sum_k \delta\bar{q_k}^e \delta\bar{C_k}^e$, the projected changes of precipitation intensity can be approximated by

$$\delta\bar{P}^e \approx \sum_k \bar{q_k}^e \delta\bar{C_k}^e + \sum_k \bar{C_k}^e \delta\bar{q_k}^e \tag{5.5}$$

Equation 5.5 states that the future changes in extreme precipitation intensity are due to circulation (dynamic) changes exerting on the current climate moisture and moisture (thermodynamic) changes acting on the current climate circulation. Similarly, 5.4 can be decomposed into

$$\delta \bar{P_{acc}}^{e} \approx \delta(\bar{D}^{e}) \sum_{k} \bar{q_k}^{e} \bar{C_k}^{e} + \bar{D}^{e} \sum_{k} \bar{q_k}^{e} \delta \bar{C_k}^{e} + \bar{D}^{e} \sum_{k} \bar{C_k}^{e} \delta \bar{q_k}^{e} \tag{5.6}$$

Beside thermodynamic and dynamic effects, duration changes (first term on the right-hand side) can also affect the precipitation accumulation. Together, equations 5.5 and 5.6 allow us to quantify how various factors contribute to the total changes in precipitation intensity and accumulation over different recurrence intervals, respectively.

5.3 Results

5.3.1 Spatial Distribution of Projected Changes in Extreme Precipitation

We first present changes to the spatial patterns of P - E for the climatological mean, 1- and 50-year recurrence intervals under global warming, in comparison with those for precipitation accumulations over rainfall events. One of the most notable features for PE is the maximum precipitation along the coastal regions due to orographic enhancement, not just for the mean, but also for extreme events (top row of Figure 5.5.2). The change in mean PE along the NA west coast under global warming is characterized by a north-south dipole, with wetting from central California northward and drying southward (Figure 5.5.2a), which is consistent with the"wet-get-wetter, dry-get-drier" paradigm. The largest increase occurs along the coastal regions where historical PE is also a local maximum. This north-south dipole in the PE changes also applies to the 1-year event (Figure 5.5.2b), but with positive changes occurring over a larger area. In the 50-year recurrence interval, PE increases everywhere with substantial increases occurring near the coast in the lower latitude regions (Figure 5.5.2c). Note for extreme events, the contribution from evaporation is negligible.

Comparing with the changes in mean P - E (Figure 5.5.2a), negative mean precipitation intensity changes occur over a smaller area at the lower latitude regions (Figure 5.5.2d), because the mean evaporation is intensified everywhere. Interestingly, the north-south dipole

pattern also shows up for the events with 1-year recurrence interval (Figure 5.5.2e): a decrease in accumulation over the subtropics and an increase over the midlatitudes, especially along the coastal regions. Like the changes for P - E, accumulation also increases nearly everywhere for the 50-year recurrence interval events. And the largest increases also occur along the coastal regions, especially the lower latitude coastal regions. All these results indicate that extreme precipitation is likely to increase nearly everywhere, even in the subtropics with reduced mean P - E. In the next two subsections, we will focus on the region of NA west coast, where the largest signals are found and precipitation changes are mostly influenced by ARs. In particular, we will explain the opposite signed changes between extreme and mean precipitation as the result of the changes in atmospheric circulation.

5.3.2 Changes of P - E as a Function of Recurrence Interval Along NA West Coast

To investigate the future changes of P - E and the associated driving mechanisms along the NA west coast,we first show that, to a very large degree, P - E (Figure 5.5.3a, contours) can be balanced by the moisture flux convergence minus moisture storage across different recurrence intervals, which we will refer to as the total moisture budget (Figure 5.5.3b, contours). The total moisture budget captures the climatology of P - E reasonably well. Despite a slight underestimate of its magnitude, the total moisture budget correctly captures the corresponding latitudes for the local P - E maximum and minimum. Similar to the climatology, the changes in total moisture budget under global warming reflect the changes in P - E very well except for events above the 10-year recurrence interval over midlatitudes where the changes in the total moisture budget tend to be slightly larger than the changes in P - E (Figures 5.5.3a and b, colors). Overall, P - E increases for all recurrence intervals over midlatitudes. Over subtropics, P - E increases substantially for the most extreme events and decreases slightly for the light-moderate events.

Further analysis shows that the vertical moisture transport dominates the total moisture

budget (Figure 5.5.3c): It nearly accounts for all the P - E climatology over subtropics and contributes to more than half of the P - E climatology over midlatitudes. Nevertheless, the changes in the vertical moisture transport under global warming capture the changes of both patterns and magnitude in P - E very well. Therefore, decomposing the changes of this term into thermodynamic and dynamic components (whose sum is approximately equal to vertical moisture transport) can help us better understand the mechanisms driving the projected changes in P - E. Over subtropics, the changes in circulation (dynamic) amplify P - E for extreme events while dampening those with relatively small recurrence interval (Figure 5.5.3d). On the other hand, such dynamic modulation of P - E changes is negligible over midlatitudes. This appears to be consistent with the dynamic amplification due to latent heating in extreme precipitation over regions with relatively high surface temperature (*Nie et al.*, 2018). Moreover, the increases in moisture content (thermodynamic) contribute positively everywhere for all events above the 0.1-year recurrence interval (Figure 5.5.3e). Applying Clausius-Clapeyron (CC) scaling (7%/K) to the vertical moisture transport based on the changes in local mean surface temperature, we almost reproduce the thermodynamic contribution in Figure 5.5.3f. This indicates that the changes in extreme PE in the midlatitudes will approximately follow the CC scaling in the future, whereas, due to dynamic changes, extreme PE in the subtropics will experience super CC scaling, with a weakening in light-moderate events.

While we have considered a broad range of extreme precipitation, our results are consistent with the projected increases in both AR frequency and intensity due mostly to the higher moisture content in a warmer atmosphere, with an additional dynamical contribution in low latitudes (*Payne and Magnusdottir*, 2015).Previous studies on the global hydrological cycle have found that the future changes in midlatitude extreme P - E along the NA west coast will be dominated by the thermodynamic effects (*Emori and Brown*, 2005; *Norris et al.*, 2019a; *Pfahl et al.*, 2017), which are consistent with our results. Furthermore, we also demonstrate that the increases in moisture scale well with the changes in mean surface

temperature for all events above the 0.1-year recurrence interval. This, however, seems to yield a different picture from *Seager et al.* (2014) who showed the changes to mean P - E in the winter half year are mostly contributed by the mean flow moisture flux convergence while the moisture flux convergence by transient eddies plays a negligible role (Figure 3h in *Seager et al.* (2014)). The monthly mean flow is averaged over both precipitating and non-precipitating days, which is likely to include many non-AR days, and changes to the mean flow can influence both AR days and non-AR days. In contrast, the conditional moisture budget gives an intuitive explanation similar to the diagnostics of ARs, as the moisture transport is averaged only over precipitating days of a given precipitation intensity.

5.3.3 Changes of Precipitation Accumulations as a Function of Recurrence Interval

We next move to the projected changes to accumulations over precipitation events. Like instantaneous rate,the moisture budget for accumulation is closed very well. As shown in Figures 5.5.4a and 5.5.4b, precipitation can be balanced by the sum of moisture flux convergence and evaporation, minus moisture storage for both climatology and projected changes. With global warming, accumulation size increases for all recurrence intervals over midlatitudes. For events at a particular recurrence interval, the magnitude of the changes tends to increase with latitude. Over the subtropics, accumulation sizes increase for events larger than the 10-year recurrence interval and decrease for events below it. Overall, the pattern of the changes for accumulation is consistent with that of the instantaneous rate, implying that the results for precipitation intensity in section 5.3.2 apply throughout extreme events.

Figure 5.5.4c shows that vertical moisture transport dominates the total moisture budget for accumulation,similar to the results for precipitation intensity (Figure 5.5.3): It captures the precipitation accumulation climatology very well over subtropics and contributes to most of the climatology over midlatitudes. To a large degree, the changes in precipitation accumu-

lation can be explained by the changes in the vertical moisture transport (Figure 5.5.4c). It captures the uniform wetting for all recurrence interval over midlatitudes. Over subtropics, its changes are also very similar to the changes in precipitation accumulation,with wetting for large recurrence intervals and drying for relatively small recurrence intervals.Moreover, decomposing the changes in vertical moisture transport reveals that the contribution from the dynamic component occurs mostly over subtropics (Figure 5.5.4d). It increases accumulation sizes for recurrence intervals greater than 10 years and decreases those below this recurrence interval. The thermodynamic component contributes positively to accumulation everywhere for all recurrence intervals, with the greatest contribution for events with very large recurrence intervals over lower latitude regions and regions centered around $42^{\circ}N$ (Figure 5.5.4e). Scaling the changes in vertical transport by the changes in surface temperature according to the CC relation (7%/K) almost reproduces the contribution made by the thermodynamic component. Finally, if changes in accumulation are only controlled by the thermodynamic and dynamic components, the mechanisms driving the changes in accumulation are nearly the same as those driving the changes in precipitation intensity. However, duration is also an important factor in determining the changes in accumulation. The decreases in duration reduce accumulation for events over subtropics while having negligible effects on the accumulation over midlatitudes (Figure 5.5.4g).

In summary, the changes in midlatitude accumulations follow the CC scaling, while in the subtropics, the change in dynamics, thermodynamics, and duration combine to increase the accumulation for large recurrence intervals and reduce the accumulation for relatively small recurrence intervals.

5.4 Conclusions

We investigated the projected changes of P - E (in term of instantaneous rate) and precipitation accumulation (over rainfall events) along the NA west coast for recurrence intervals

ranging from 0.1 to 50 years. Under warming, both P - E and precipitation accumulation increase in the midlatitudes ($30°N$ to $60°N$) for all recurrence intervals. In the subtropics ($20°N$ to $30°N$), projected changes of both P - E and precipitation accumulation demonstrate very similar behaviors: decreases for events at the relatively small recurrence intervals and increases for those at the very large recurrence intervals. Moreover, the thermodynamic component contributes positively everywhere for all recurrence intervals. And it is responsible for almost all of the wetting in the midlatitudes. We also show that the thermodynamic contribution can be predicted by the changes in local mean surface temperature by assuming moisture increases approximately by 7% per degree warming (i.e., the CC scaling). The influence of the dynamic change is confined mostly in the subtropics: it amplifies precipitation for the very large recurrence intervals and dampens those with relatively small recurrence intervals. The decreases in duration reduce the accumulation sizes for all recurrence intervals in the subtropics while the duration remains nearly unchanged for all midlatitude events. The intensification in largest accumulations in the presence of a drying mean climate in southwestern NA poses a major challenge to local water management.

Previous studies have found that most of the extreme P - E events along the NA west coast are associated with ARs, which are projected to intensify over this region (*Dong et al.*, 2018; *Waliser and Guan*, 2017). Our results are consistent with the projected increases in both AR frequency and intensity due mostly to the higher moisture content in a warmer atmosphere, with additional dynamical contribution in low latitudes (*Payne and Magnusdottir*, 2015). This, however, seems to yield a different picture from *Seager et al.* (2014) who showed the changes to mean P - E in the winter half year are mostly contributed by the mean flow moisture flux convergence. We note the conventional decomposition into mean and transient components would give the monthly mean flow averaged over both precipitating and non-precipitating days, which is likely to include many non-AR days. In contrast, the conditional moisture budget is averaged only over precipitating days of given intensity, which gives an explanation more consistent with the event-based diagnostics of ARs.

Acknowledgements. The authors are supported by Department of Energy Grant DE-SC0016117 and National Science Foundation Grant AGS-1742178. We would like to acknowledge high-performance computing support from Cheyenne (https://doi.org/10.5065/D6RX99HX) provided by NCAR's Computational and Information Systems Laboratory, sponsored by the National Science Foundation. Data from CESM large ensemble can be found online (http://www.cesm.ucar.edu/projects/community-projects/LENS/data-sets.html).

5.5 Figures

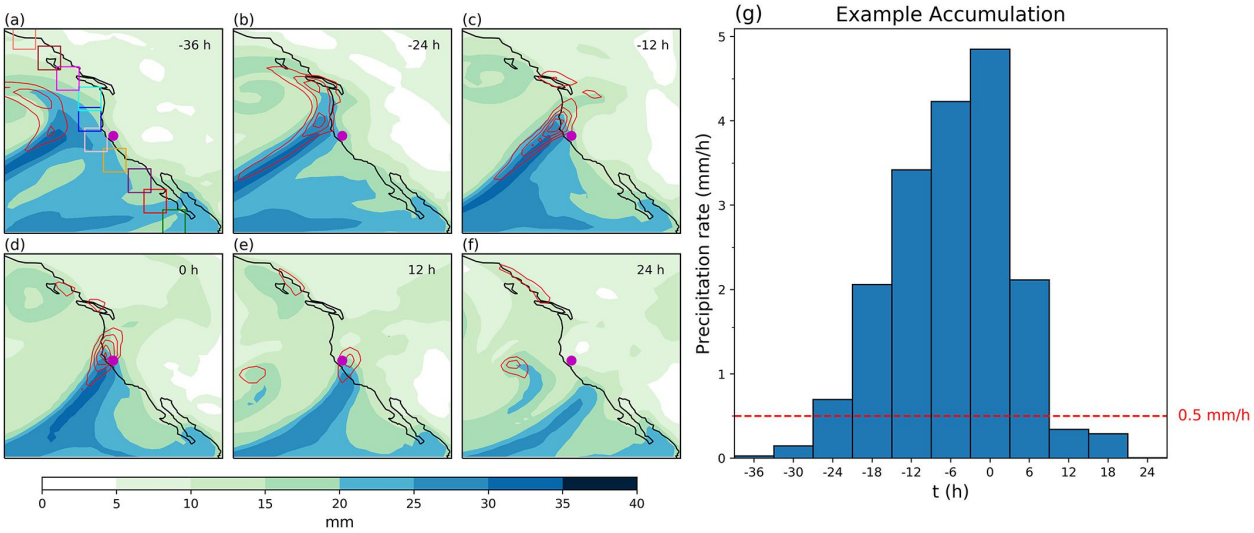

Figure 5.5.1: An example showing the evolution of an atmospheric river event in the CESM large ensemble simulation. The left panel shows the spatial distribution of the precipitable water (shaded contours) and precipitation (red solid contours, starting from 1 mm/hr with an interval of 1 mm/hr) evolving with time.The right panel shows the 6-hourly precipitation amounts recorded over a particular grid point (magenta dot) associated with this event. The 10 colored boxes in the gridded panels are the grids used to defined NA west coast.

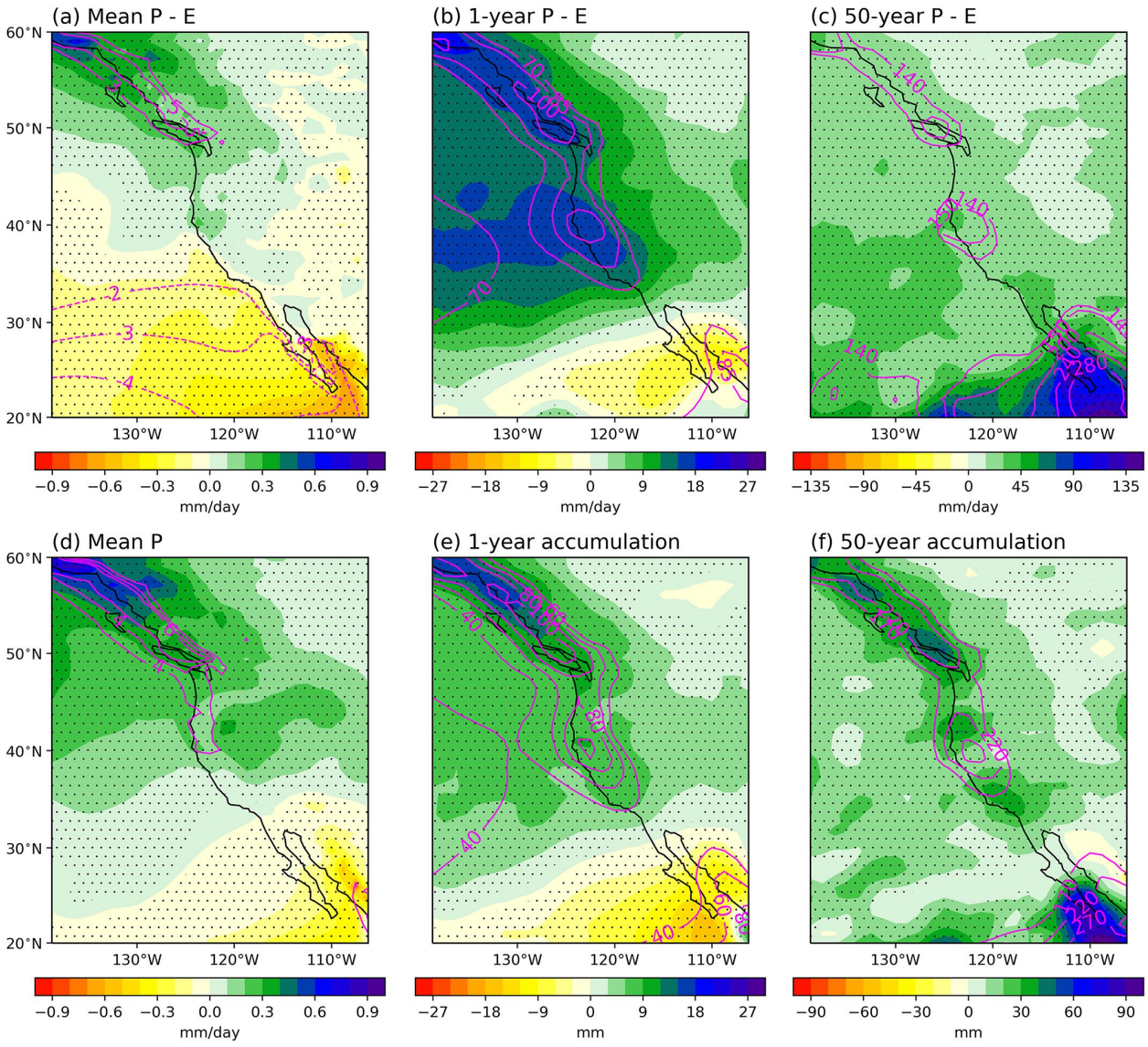

Figure 5.5.2: Spatial distribution of climatology (solid contours) and projected changes (shaded contours) for P - E (a–c) and precipitation accumulation (d–f) over western NA, for (a, d) climatological mean, (b, e) events of 1-year recurrence interval, and (c, f) 50-year recurrence interval. The present climate is evaluated over the period of 1990–2005 in the CESM large ensemble. The projected changes are based on the difference between the future climate (2071 – 2080) and present climate. Both climatology and projected changes have the same unit. Stippling indicates regions where $> 80\%$ of the bootstrap replications agree on the sign of the change.

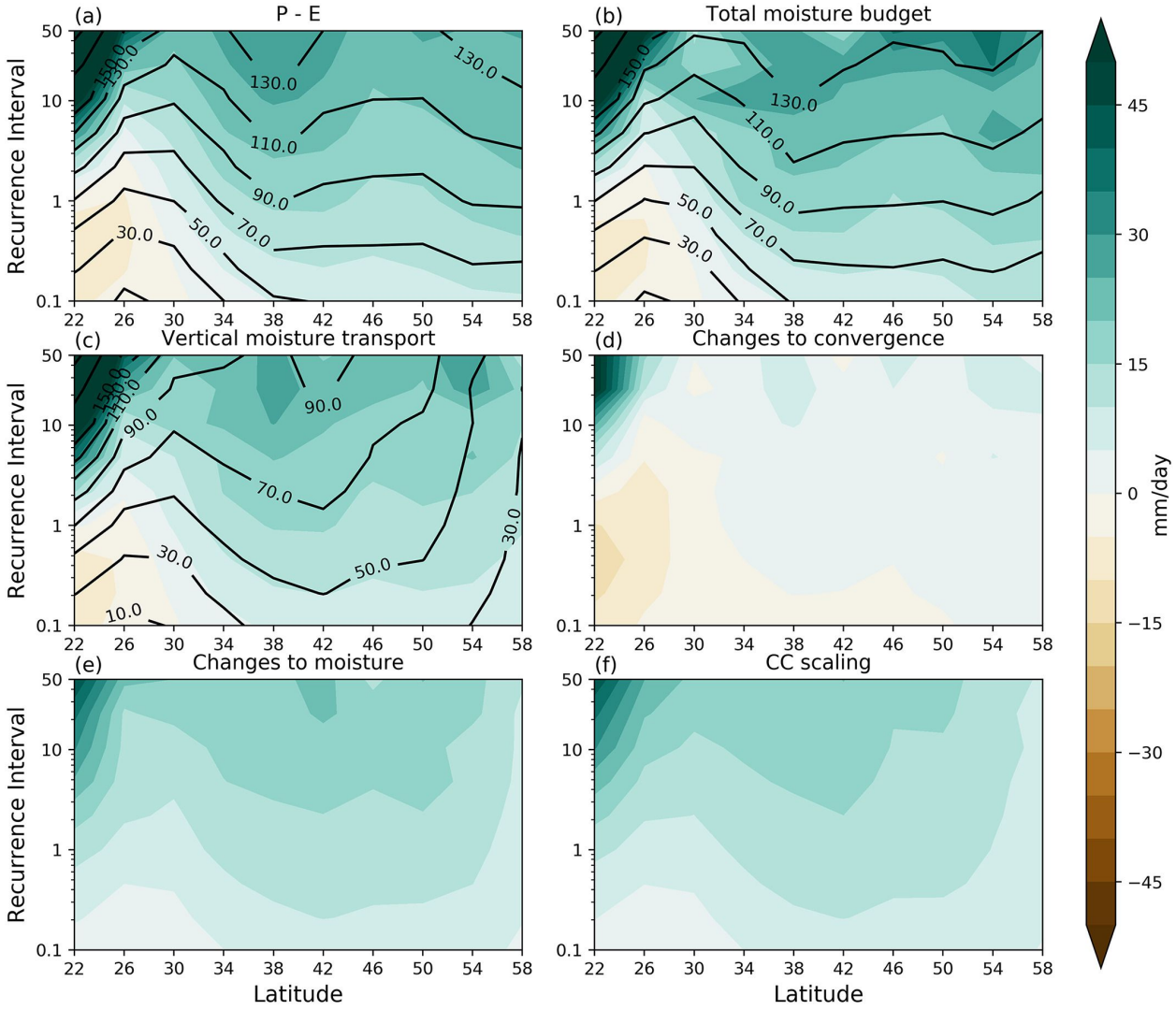

Figure 5.5.3: Climatology (solid contours) and projected changes (shaded contours) of P - E and various moisture budget terms contributing to P - E over NA west coast as function of recurrence interval. Individual panels are (a) P - E,(b) total moisture budget (moisture flux convergence minus moisture storage), (c) vertical moisture transport, (d) dynamic component, (e) thermodynamic component, and (f) CC scaling. See equations 5.1 and 5.5 for details.

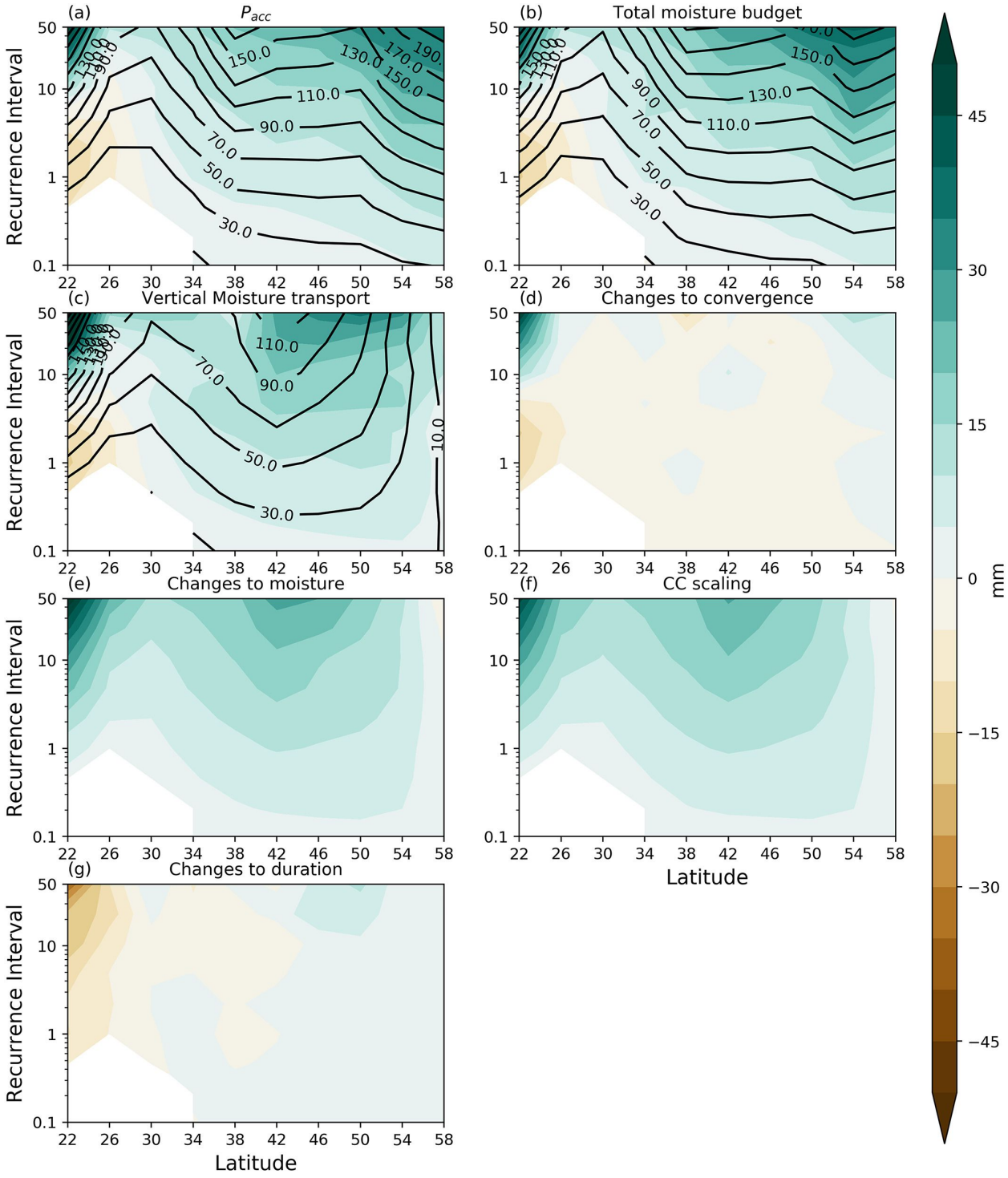

Figure 5.5.4: Climatology (solid contours) and projected changes (shaded contours) of precipitation accumulation and various moisture budget terms contributing to precipitation accumulation along the NA west coast as a function of recurrence interval. Individual panels are (a) precipitation, (b) total moisture budget, (c) vertical moisture transport, (d)dynamic component, (e) thermodynamic component, (f) CC scaling, and (g) duration changes. See equations (1) and (6)for details. Bins with more than 10% non-precipitating events are set as missing values and shown as blank in the figure.

Appendix

5.A Supplement

Text S1 We used bootstrapping methods to establish significance for the projected changes in the gridded figures. There are 100 bootstrap replications in total. Random sampling with replacement is used to choose each member to form a replication with 40 members for both the current and future climates. Once a replication is created, the analysis described in the Data and Methods section are repeated to calculated the projected changes of various quantities. If at least 80% of the replications agree on the sign of the change, significance is said to be established.

Text S2 Most of the extreme precipitation events along the NA west coast are induced by ARs which transport tropical and subtropical sourced moisture into the coast (Waliser Guan, 2017). Besides the resultant vertical moisture transport along the transport pathway, this suggests that horizontal advection may play an important role in the moisture budget along the NA west coast for extreme events. Indeed, our analysis shows that horizontal advection dominates the mean budget in both the climatology and future changes (Fig. S1 and S2). For extreme events, it is the second most important term in the climatological budget. Together with vertical moisture transport, it accounts for almost the full moisture budget for the climatology of extreme events. In term of changes, horizontal advection is slightly negative while the storage term is slightly positive (Fig. S2 and S3). To some extent, these two terms cancel each other, resulting in the changes in precipitation intensity being almost entirely due to changes in vertical moisture transport (Chen et al., 2019; Norris et al., 2019b). For accumulation, both the changes in evaporation and storage term are negligible for all recurrence intervals along the NA west coast (Fig. S4). The change in horizontal advection is also negligible except for events with very large recurrence intervals over high latitudes (50N to 60N) where the changes are slightly positive. Therefore, like the changes

in P - E, the changes in vertical moisture transport under global warming account for most of the changes in precipitation accumulation. Based on the above results, decomposing the vertical moisture transport gives a mechanistic explanation for precipitation changes along the NA west coast.

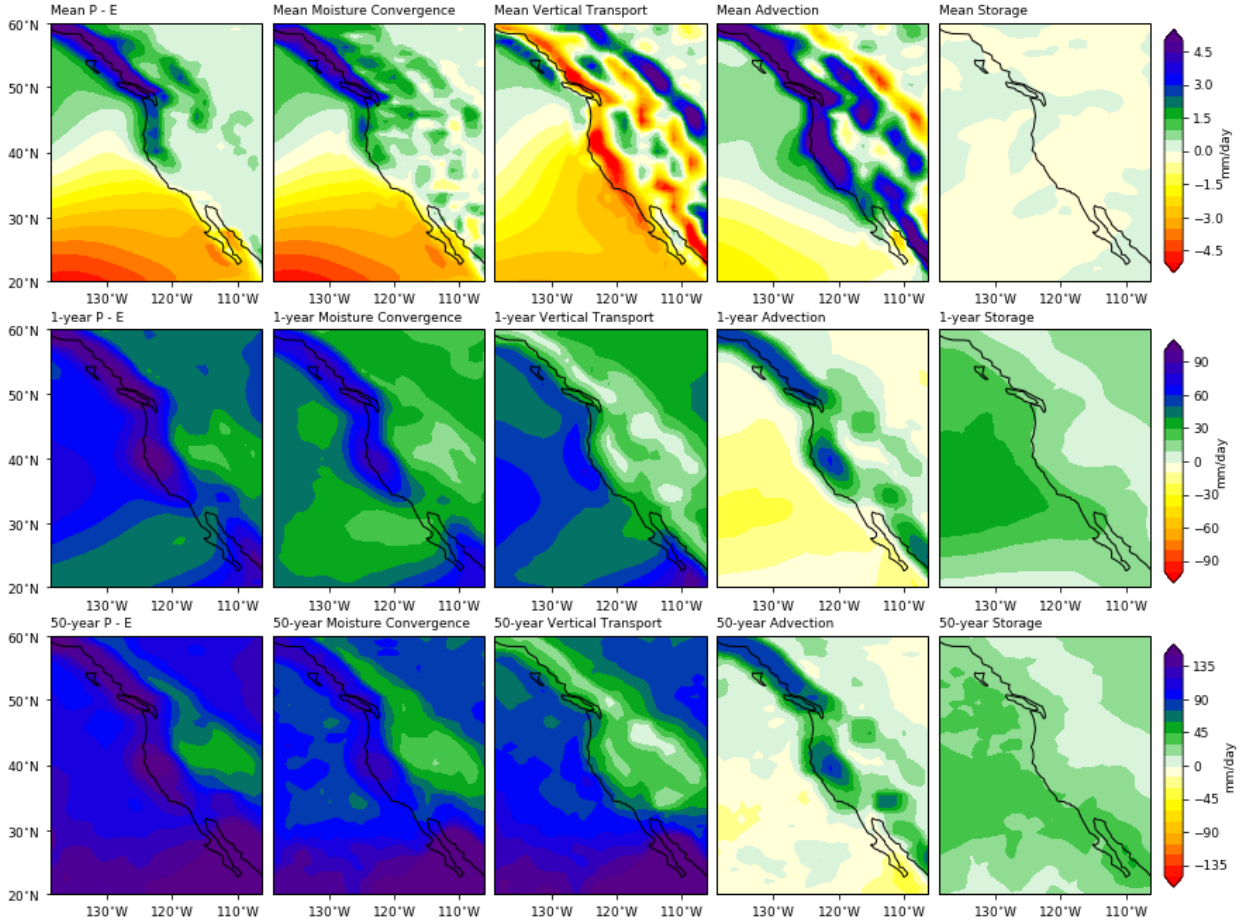

Figure 5.A.1: Mean (1st row), 1-year (2nd row) and 50-year (3rd row) recurrence interval Climatology of various terms in the moisture budget for instantaneous rate.

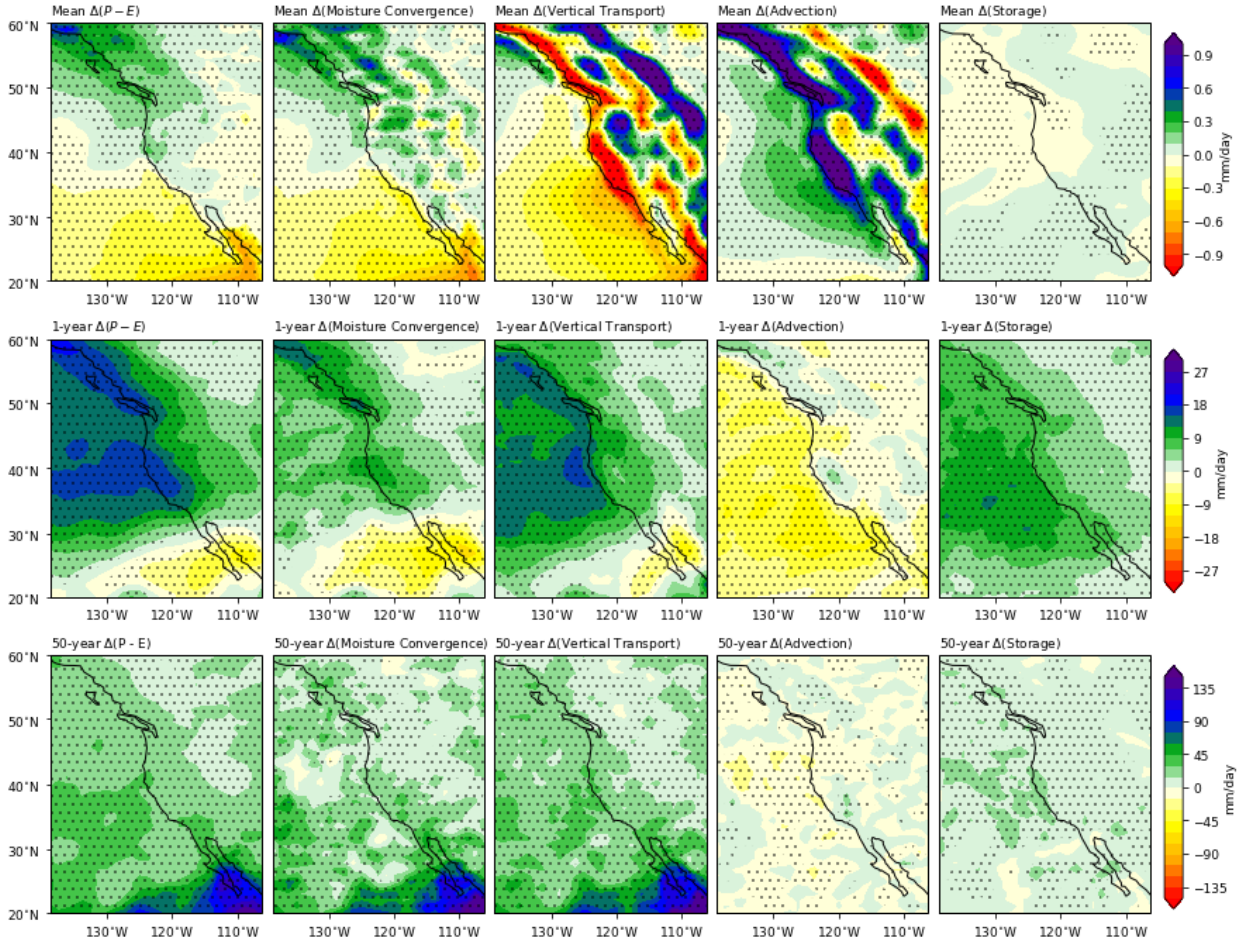

Figure 5.A.2: Mean (1st row), 1-year (2nd row) and 50-year (3rd row) recurrence interval projected changes of various terms in the moisture budget for instantaneous rate. Stippling indicates regions where $> 80\%$ of the bootstrap replications agree on the sign of the change.

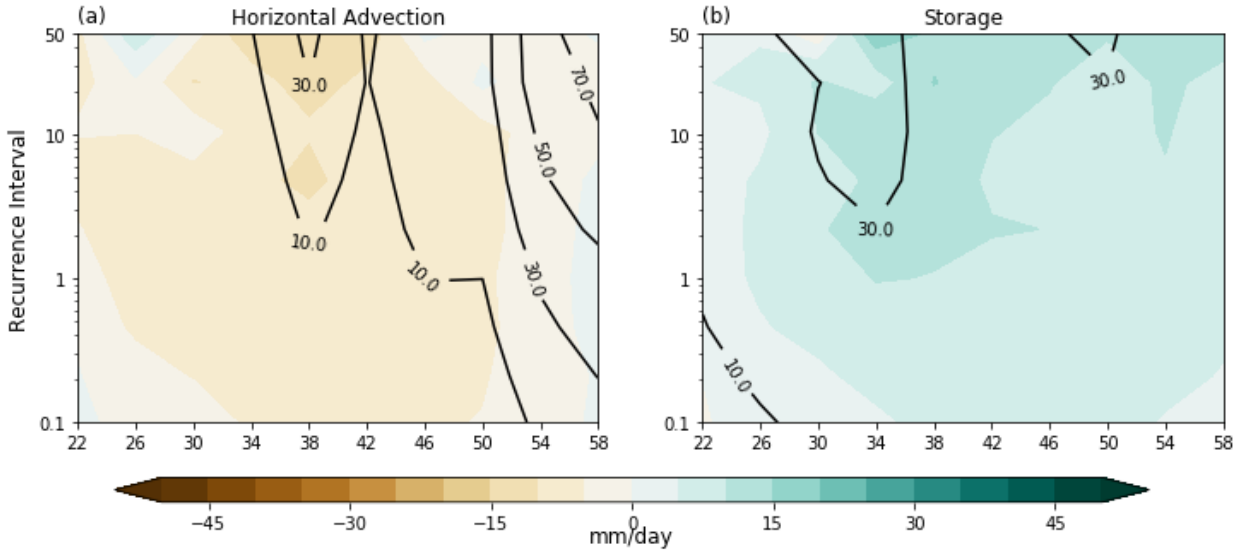

Figure 5.A.3: Climatology (solid contours) and projected changes (shaded contours) of horizontal advection (left) and storage (right) for instantaneous rate along NA west coast as a function of recurrence interval.

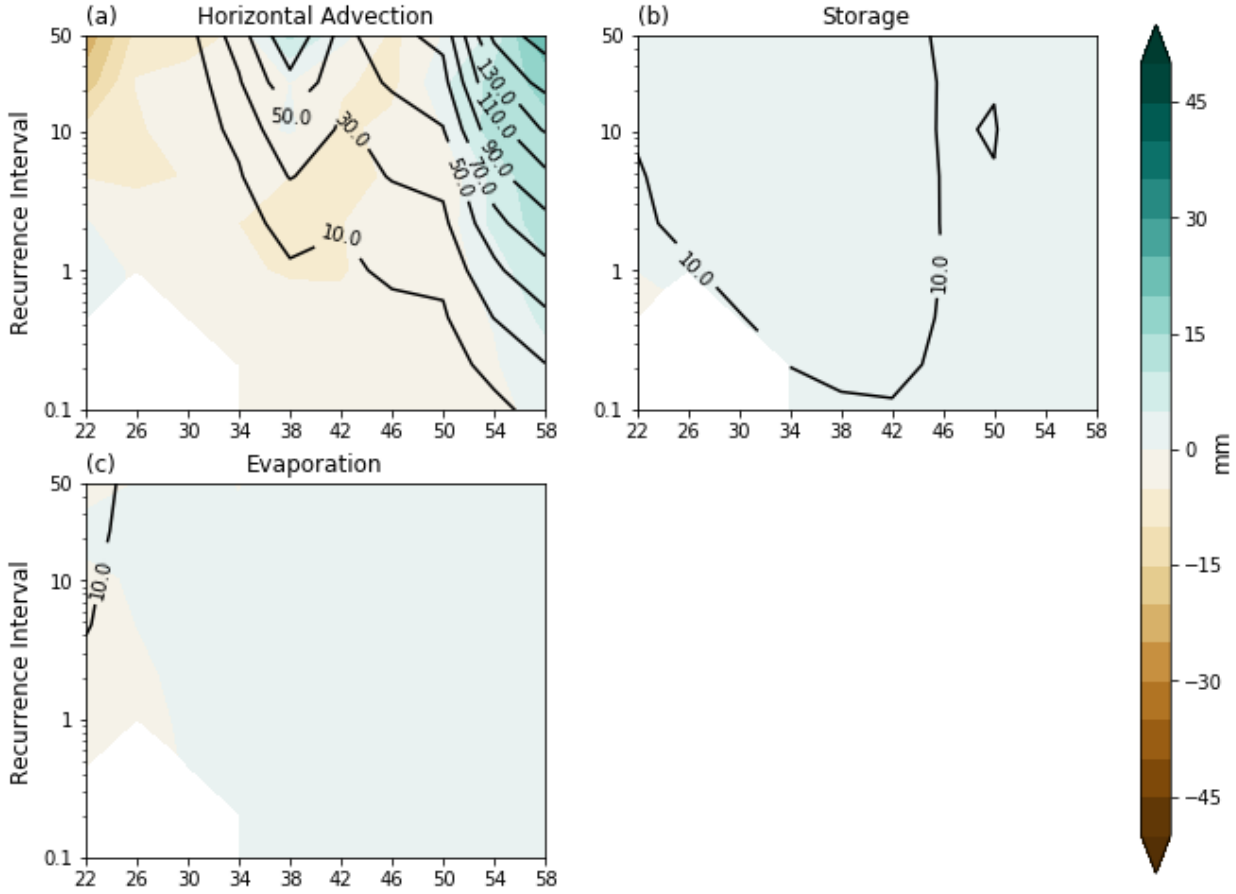

Figure 5.A.4: Climatology (solid contours) and projected changes (shaded contours) of horizontal advection (upper left), storage (upper right) and evaporation (lower left) for accumulation along NA west coast as a function of recurrence interval.

CHAPTER 6

Evaluating the Representations of Atmospheric Rivers and Their Associated Precipitation in Reanalyses with Satellite Observations

[**Ma, W.**, Chen, G., and Su, H., Guan, B, and Shields, C., Evaluating the Representations of Atmospheric Rivers and Their Associated Precipitation in Reanalyses with Satellite Observations, in preparation.]

Abstract

Atmospheric rivers (ARs) are filaments of enhanced horizontal moisture transport in the atmosphere. Due to their prominent role in the meridional moisture transport and regional weather extremes, ARs have been studied extensively in recent years. Yet, how well reanalyses are in representing ARs and their associated precipitation remains largely unknown. In this study, we developed an AR detection algorithm specifically for satellite observations (AIRS/AMSU) based on moisture and the geostrophic winds derived from 3D geopotential height field. This algorithm enables us to develop the first global AR catalogue based solely on satellite observations. The satellite-based AR catalogue is then combined with the satellite-based precipitation (IMERG) to evaluate the representations of AR and

AR-induced precipitation in reanalysis products. Our results show that the spreads in AR frequency and AR length distribution are generally small across datasets, while the spread in AR width is relatively larger. In terms of the AR-induced precipitation, both AR-induced mean and extreme precipitation are too weak nearly everywhere in reanalyses. However, all reanalyses tend to precipitate too often under AR conditions, especially over low latitude regions. This finding is consistent with the "drizzling" bias which has plagued generations of climate models. Overall, the findings uncovered in this study can help to improve the AR representation in reanalyses as well as climate models.

6.1 Introduction

Characterized by filaments of enhanced moisture transport in the atmosphere, atmospheric rivers (ARs) play a critical role in the global hydrological cycle. Despite only covering a very small fraction of the earth's circumference, an early study revealed that ARs contribute more than 90% of the poleward moisture transport over midlatitudes (*Zhu and Newell*, 1998). At the regional scale, depending on their strength and duration (*Ralph et al.*, 2019), ARs can exert either beneficial or detrimental impacts upon landfall. It has been shown that ARs are important freshwater suppliers to many coastal regions around the world and can serve as effective drought busters (*Dettinger*, 2011, 2013; *Rutz and Steenburgh*, 2012; *Viale et al.*, 2018). For example, it has been estimated that up to half of the annual precipitation over California is delivered by ARs (*Dettinger*, 2011). Meanwhile, intense ARs making landfall usually lead to a wide range of weather hazards, such as wind and precipitation extremes, and flooding (*Chen and Kumar*, 2018; *Henn et al.*, 2020; *Lamjiri et al.*, 2017; *Lavers and Villarini*, 2013; *Ma et al.*, 2020a; *Paltan et al.*, 2017; *Ralph et al.*, 2006; *Waliser and Guan*, 2017). In recent years, studies on ARs' roles in affecting sea ice variability (*Hegyi and Taylor*, 2018; *Wang et al.*, 2020; *Woods and Caballero*, 2016) and ice shelf stability (*Djoumna and Holland*, 2021; *Mattingly et al.*, 2018; *Wille et al.*, 2022, 2019) have been increasing rapidly.

Reanalysis products have long been used as observations in AR studies. Yet, reanalyses are not obtained by direct observations. Instead, they are produced by models which are constrained by observations through data assimilation. Therefore, reanalyses can only be treated as proxies of observations. Furthermore, since reanalyses are model-based "observations", it can be expected that each reanalysis would have its own biases intrinsic to the model used to produce it. However, most AR studies, which use reanalyses as observations, usually assume that ARs in reanalyses are representative of the true observation. Given the imperfection of the models used to produce these reanalyses, such a simple assumption is questionable. So far, studies on the intercomparison between reanalyses and observations of the AR representations are very limited, which hinders our confidence in the ability of reanalyses in representing ARs. By evaluating six AR events in reanalyses against aircraft observations, *Ralph et al.* (2012) concluded that Climate Forecast System Reanalysis (CFSR) (*Saha et al.*, 2010), Modern-Era Retrospective analysis for Research and Applications (MERRA) (*Rienecker et al.*, 2011) and European Centre for Medium-Range Weather Forecasts (ECMWF) interim reanalysis (ERAI) (*Dee et al.*, 2011) exhibit comparable skills in representing the characteristics of these six ARs. They also have better performance compared to National Centers for Environmental Prediction (NCEP) -National Center for Atmospheric Research (NCAR) Reanalysis I (NCEP R1) (*Kalnay et al.*, 1996), Tropospheric Chemistry Reanalysis (TCR) (*Miyazaki et al.*, 2012) and North American Regional Reanalysis (NARR) (*Mesinger et al.*, 2006). Expanding the sample size to 21 AR events, *Guan and Waliser* (2017) found that, compared to dropsonde observations, ERAI and MERRA, Version 2 (MERRA-2) (*Gelaro et al.*, 2017) have a mean error of -2% and -8% in AR width, respectively, and +3% and -1% in total integrated water vapor transport, respectively. Using MERRA2, ECMWF Reanalysis Version 5 (ERA5) (*Hersbach et al.*, 2020) and Japanese 55-year Reanalysis (JRA-55) (*Kobayashi et al.*, 2015), a recent study from the Atmospheric River Tracking Method Intercomparison Project (ARTMIP) (*Shields et al.*, 2018) found that ARs tend to get detected more frequently in MERRA2 due to its higher climatological IVT.

ARs in ERA5 tend to be narrower due to its finer spatial resolution (*Collow et al.*, 2022). It's immediately apparent that the above studies either evaluate AR representations using a small sample size or only using few reanalyses. In addition, these studies only examine the representation of AR characteristics, such as AR frequency and AR intensity, in reanalyses. How AR-induced precipitation is represented in reanalyses remains mostly unexplored.

Besides reanalyses, satellite observations have also been frequently used to characterize ARs and their associated precipitation (*Arabzadeh et al.*, 2020; *Cannon et al.*, 2017, 2020; *Matrosov*, 2013; *Neiman et al.*, 2008a,b; *Ralph et al.*, 2004; *Wick et al.*, 2012). Integrated water vapor (IWV) from the Special Sensor Microwave Imager (SSM/I) (*Hollinger et al.*, 1990) has been widely used to understand AR characteristics. For example, by compositing the IWV from SSM/I of 312 AR events over the eastern North Pacific, *Ralph et al.* (2004) found that, on average, the IWV magnitude and width of a typical AR is about 2.81 cm and 388 km, respectively. Focusing on landfalling ARs along the western North America from 1997 to 2005, *Neiman et al.* (2008b) used the IWV from SSM/I to investigate AR seasonality and landfall orientation. They found that warm season ARs tend to occur in the North while cool season ARs tend to occur in the South. Winter landfalling ARs tend to extend northeastward from the tropical eastern Pacific while summer landfalling ARs tend to be more zonally oriented. Besides AR characteristics, AR-induced precipitation has also been studied using satellite observations. For example, using radar reflectivity profiles from the Global Precipitation Measurement Dual-Frequency Precipitation Radar (GPM-DPR), *Cannon et al.* (2020) showed that both stratiform and convective precipitation are abundant in ARs and AR-induced precipitation is usually triggered by forced ascent in the vicinity of a cold front in frontogenetic environments. These satellite-based studies have improved our understanding in ARs. However, most of these studies focus on ARs occurring over the eastern North Pacific while a global satellite-based AR study is lacking. Furthermore, since 3D satellite observed wind field is currently not available, these studies usually detect ARs by adopting a simple IWV threshold of 2 cm and requiring the detected object to

be longer than 2000 km and narrower than 1000 km (*Neiman et al.*, 2008b; *Ralph et al.*, 2004; *Wick et al.*, 2012). However, ARs are defined as enhanced moisture transport in the atmosphere. Detecting ARs using only the moisture field would inevitably run the risk of detecting filamentary features which resemble ARs, but are associated with weak moisture transport. Furthermore, variability in ARs at different time scale can controlled by both the variability in the circulation and moisture (*Gao et al.*, 2015; *Ma et al.*, 2020b, 2021; *Ma and Chen*, 2022; *Payne et al.*, 2020; *Zhang et al.*, 2021). For example, at the interannual time scale, it has been shown that AR variability is predominantly controlled by circulation variability (*Ma and Chen*, 2022). While at decadal time scale, either circulation (*Ma et al.*, 2020b) or moisture (*Zhang et al.*, 2021) can dominate the AR variability. Using only IWV in the AR detection can generate AR variability which only reflect the variability in the moisture field, but not necessary the variability in the circulation field. Therefore, further improvements are needed in the methods used to detect ARs in satellite observations by incorporating the wind component.

Given the limitations in the previous AR studies discussed above, the goals of this study are threefold: i) improve previous AR detection methods for satellite observations by incorporating satellite-based wind information, ii) perform a comprehensive intercomparison of AR representations between seven reanalyses, which are commonly used in AR community, and satellite observation, iii) evaluate AR precipitation in reanalyses against precipitation from satellite observation. The structure of this paper is organized as follows: section 6.2 describes the reanalyses and satellite data used, as well as the approach used to detect ARs in satellite data. Major results will be presented in section 6.3. A brief conclusion and discussion will be provided in section 6.4.

6.2 Data and Methods

6.2.1 Satellite Data and Reanalyses

IWV from SSM/I has been widely used in AR studies. However, the spatial coverage of SSM/I is confined over oceans while observations over lands, which are most relevant for AR impacts, are not available. To circumvent this issue, IWV from the combined retrievals of the Atmospheric Infrared Sounder (AIRS) and the Advanced Microwave Sounding Unit (AMSU) onboarded NASA's Aqua platform is used in this study (hereafter AIRS/AMSU) (AIRS Science Team/Joao Teixeira, 2013). The AIRS/AMSU dataset has a global coverage with spatial resolution of $1^\circ \times 1^\circ$ and daily temporal resolution. Observations made each day consist of an ascending orbit and a descending orbit. We take the average of these two orbits to obtain a more smooth field which is representative of the daily mean. Due to the limited swath width of the satellite observations, gaps with no observation exist between swathes. While averaging the ascending orbit and descending orbit to create the daily mean can effectively remove most of these swath gaps, small gaps remain over subtropical regions after this procedure. We fill in these small gaps using the "poisson_grid_fill" function from NCL. Note that the results presented in this study would not be affected by whether these small gaps are being filled or not. Geopotential height at 925, 850, 700 and 600 mb levels are also obtained from AIRS/AMSU and processed in the same way as the IWV field (see section 6.2.2 for the use of this variable in our study). Observed precipitation is based on the Integrated Muti-SatellitE Retrievals for GPM (IMERG) Version 6 Final Run. This satellite-based precipitation dataset has been widely used in previous studies for mid-latitude weather systems, such as cyclones and atmospheric rivers (*Arabzadeh et al.*, 2020; *Naud et al.*, 2020). Constrained by the temporal coverage of AIRS/AMSU, the study period of this work is from 08/31/2002 to 09/24/2016.

Seven reanalyses, which have been widely used in AR studies, are employed here: they are MERRA-2, ERA5, ERAI, JRA-55, CFSR, NCEP/Department of Energy (DOE) Re-

analysis II (NCEP R2) (*Kanamitsu et al.*, 2002) and the NCEP R1. These datasets have varied temporal resolution. Data at 00 and 12 UTC are averaged to obtain the daily mean. We also tried calculating the daily mean using data at 00, 06, 12 and 18 UTC. The results presented in this study are not sensitive to how the daily mean is calculated (not shown). Both IWV and geopotential height are bilinearly interpolated to a common resolution of $1^\circ \times 1^\circ$ before analysis. The precipitation fields from reanalyses also have varied temporal resolution. Some datasets provide the analysis field while others provide the forecast field. Precipitation data are thus processed accordingly to obtain the daily mean. More specifically, daily precipitation from MERRA2 and ERA5 is calculated by aggregating hourly total precipitation. Daily precipitation in ERAI is calculated by summing the 12-hour forecasted accumulated precipitation initialized at 00 and 12 UTC. Daily precipitation in JRA-55 is calculated from the forecasted precipitation rate initialized at 00, 06, 12 and 18 UTC with steps of 3 and 6 hours. Daily precipitation in CFSR is calculated by aggregating the 6-hour forecasted accumulated precipitation initialized at 00, 06, 12 and 18 UTC. For NCEP R1 and NCEP R2, mean daily precipitation rate is available for direct download. All reanalysis-based precipitation data and IMERG are regridded to a common $1^\circ \times 1^\circ$ resolution using the nearest neighborhood method before analysis.

6.2.2 AR Detection Method

As has been discussed above, AR detections for satellite data usually rely only on the IWV because satellite-based 3D wind field is not available. To introduce wind information into the AR detection, we derive geostrophic winds from the geopotential height at 925, 850, 700 and 600 mb levels. Outside of the deep tropics, geostrophic winds at these levels are found to correlate strongly with the actual winds with correlation coefficients close to one (not shown). Geostrophic winds at these four levels are then vertically averaged to obtain the weighted vertical average geostrophic winds. The IVT based on the weighted vertical average geostrophic winds, which we will call the geostrophic IVT (GIVT), is then calculated

by:

$$GIVT = \sqrt{(IWV \times < U_g >)^2 + (IWV \times < V_g >)^2}$$

where U_g and V_g are the geostrophic zonal wind and geostrophic meridional wind, respectively. The angle bracket denotes the weighted vertical average. We find that the GIVT can serve as a good proxy for the actual IVT in terms of magnitude. As demonstrated in Figures 6.5.1a and 6.5.1b, the snapshot of the GIVT shown is nearly identical to the snapshot of actual IVT. Filaments of enhanced IVT in the actual IVT field can also be found in the GIVT field. Minor differences between these two fields only exist in the magnitude: GIVT tends to slightly overestimate the magnitude of the actual IVT, especially over regions with enhanced IVT. Indeed, as shown in Figure 6.5.2a, which plots the joint probability distribution function (PDF) of the actual IVT versus GIVT in ERA5 for year 2003, most of the points fall along the one-to-one line, indicating the good correspondence between the GIVT and the actual IVT. As IVT increases, slightly more points are located above the one-to-one line than those located below it. This corroborates our observation based on Figures 1a and 1b that GIVT tends to be slightly stronger than the actual IVT over enhanced IVT regions. As we will show later, such a slight overestimate of the IVT magnitude by the GIVT has negligible effect on the ARs detected due to the percentile-based threshold adopted by the AR detection algorithm (ARDT) used in this study.

The ARDT used in this study is based on the IVT-based *Guan and Waliser* (2015) algorithm, with modifications so that GIVT can be directly used as input. This ARDT is a global algorithm which has been widely used in AR studies (*Arabzadeh et al.*, 2020; *Espinoza et al.*, 2018; *Ionita et al.*, 2020; *Kim et al.*, 2021; *Nash et al.*, 2018). Notable criteria adopted by this ARDT are listed here. Readers are referred to *Guan and Waliser* (2015) for a detailed description of the algorithm. In the first step of the detection, a seasonally and regionally dependent 85^{th} percentile of the IVT magnitude, or 100 kg/m/s, whichever is greater, is used as the intensity threshold. The detected "objects" are then further filtered by three IVT

direction criteria. The detected "object" will be filtered if 1) more than half of the grid cells have IVT deviating more than 45° from the object's mean IVT (the coherence criterion), 2) mean poleward meridional IVT is less than 50 kg/m/s (the meridional IVT criterion) and 3) direction of object-mean IVT deviates from the overall orientation of the object's shape by more than 45° (the consistency criterion). Objects which pass these IVT direction criteria are subjected to further geometrical screening. The final detected ARs should be longer than 2000 kg and with length/width ratio greater than two.

To test the sensitivity of the algorithm to the input variables, in the first step, we used both the IVT and GIVT from ERA5 as input to the original *Guan and Waliser* (2015) ARDT. The AR frequency, which is defined as the fraction of time a grid cell experiences AR conditions, based on GIVT is very similar to that based on the IVT (Figure 6.A.1). Enhanced AR frequency is found over the mid-latitude storm track regions. However, compared to the AR frequency based on the IVT, results based on the GIVT underestimate AR frequency over mid-latitude regions and overestimate it over the subtropics. We then removed the three IVT direction criteria one at a time, and tested the sensitivity of the modified algorithm to the input variables. We found that removing either the coherence criterion or the consistency criterion has very little effects on the AR frequency. The differences between the IVT-based AR frequency and the GIVT-based AR frequency persist. However, once we removed the meridional IVT criterion, the differences between the IVT-based AR frequency and the GIVT-based AR frequency mostly vanish. Meanwhile, the magnitude of the AR frequency also increases nearly everywhere. These results imply that there are likely large differences in the magnitude of the meridional IVT between the IVT and GIVT. Given the results found in the sensitivity experiments, we removed the three IVT direction criteria of the original algorithm in our modified algorithm. After these three IVT direction criteria are removed, AR frequency increases nearly everywhere and its distribution becomes more uniform (Figure 6.A.1i).

Besides removing these three criteria, two additional minor modifications are also made

to the algorithm. We found that the modified algorithm tends to detect more ARs over the Northern Hemisphere continents during boreal summer. To partially alleviate this problem, instead of calculating the IVT threshold for a particular month using all the time steps from the five month centered on that month over the study period, we only use the time steps from that month in the modified algorithm. Furthermore, previous studies have found that the *Guan and Waliser* (2015) algorithm occasionally pick up tropical disturbances as ARs (*Lora et al.*, 2020; *Zhou et al.*, 2021b). To alleviate this problem, we impose that, if the detected object which has all its area located within 30°N/S will be filtered out. This criterion mostly affects ARs within 30°N/S and it reduces the magnitude of AR frequency over these regions. We want to emphasize that the conclusions presented in this study are not sensitive to whether these two criteria are adopted or not (not shown). In summary, our modified algorithm based on the *Guan and Waliser* (2015) ARDT detects ARs with enhanced IVT/GIVT relative to its background state, length greater than 2000 km and length/width ratio greater than two.

Due partly to the low sampling frequency in satellite observations, the geostrophic winds derived from the geopotential height tend to be noisier compared to the smoother fields in reanalyses. Since geostrophic winds are derived based on the gradient of the geopotential height. These noises in the geopotential height results in the derived geostrophic winds being too strong compared to the geostrophic winds in reanalyses. We applied a simple bias correction to the satellite weighted vertical average geostrophic wind speed so that the satellite mean wind speed over midlatitudes is equal to that in ERA5 (see text S1 in the supplementary for details on how the bias correction is carried out). We found that these noises in the geostrophic wind field in satellite data can also increase the "false negative" rate for AR detection. In other words, features which are detected as ARs in reanalyses are occasionally not picked up as ARs in satellite data. To resolve this problem, Gaussian smoothing was applied to the bias-corrected weighted vertical average geostrophic wind speed of the satellite data. We adjusted the size of the smoothing kernel by varying the

sigma parameter ranging from 1 to 6 in an increment of 0.5. We found that, when the sigma is too small, the field is not smoothed enough. This results in the "false negative" rate remaining high. However, when we set the sigma too large, the field is smoothed out too much. This effect can cause some filaments of enhanced IVT to be smoothed out and thus potentially get filtered out during the detection process. We set the sigma to be three in this study because the field is neither smoothed out too much nor not smoothed enough when the sigma is three. This smoothing on the geostrophic wind field of AIRS/AMSU tends to slightly enhanced the weak GIVT values while weaken the strong GIVT value (Figures 6.5.1c and 6.5.2b). Since the ARDT used in this study use a percentile-based threshold, the smoothing is expected to have very minor effects on the ARs detected (compare Figure 6.5.1f with 6.5.1d and 6.5.1e). In addition, the AR frequency difference between ERA5 and AIRS/AMSU is also small when sigma is set to three. These two additional operations on the satellite data are based on the assumption that ERA5 is better representative of the true observation. Whether such an assumption is valid or not is not a concern in this study, both satellite data and reanalyses have their own biases in representing ARs which remain largely unknown. The purpose of this study is not to treat satellite data as the true observation and evaluate the biases in reanalyses relative to satellite observations. Instead, our goal is to demonstrate the feasibility of including wind information for AR detection in satellite data and also comprehensively investigate the spread among reanalyses. Therefore, the assumption we made in this study is justifiable.

6.3 Results

6.3.1 AR Frequency and Characteristics

Figure 6.5.3a shows the annual AR frequency distribution in AIRS/AMSU. Enhanced AR frequency is observed over the mid-latitude oceans. Unlike the AR frequency distribution obtained from other global ARDTs that participated in the ARTMIP (Figure 6.A.2), the

AR frequency distribution in Figure 6.5.3a is spatially more uniform, and substantially more ARs are detected over lands. It has been shown by previous studies that these features in the AR frequency distribution are unique to the *Guan and Waliser* (2015) algorithm due mostly to the relative threshold adopted by the algorithm (*Rutz et al.*, 2019; *Shields et al.*, 2018). Since our algorithm is modified from the (*Guan and Waliser*, 2015) ARDT, it's thus expected that the AR frequency distribution based on our algorithm shares many similarities to that based on the *Guan and Waliser* (2015) algorithm (Figure 6.A.2). The spatial patterns of the AR frequency difference between reanalyses and AIRS/AMSU are very similar across reanalyses: the differences over the storm track regions, where ARs are most active, are generally small. Reanalyses tend to have fewer ARs over the subtropical regions while having more ARs over the higher latitudes poleward of 60°N/S, especially near the coast of Antarctica. Reanalyses also tend to have slightly more ARs over the high latitude land regions over the Northern Hemisphere. Compared to AIRS/AMSU, all reanalyses simulate more ARs around the dateline. This is caused by the discontinuity in the observed fields in AIRS/AMSU which can occasionally prevent the detection of ARs over the region. In AIRS/AMSU, observations start at the dateline and progress westward. This results in the data west of the dateline is farthest apart in time from those east of the dateline and lead to the formation of discontinuity over the region in AIRS/AMSU. For the zonal mean figures shown below, regions around dateline ($\pm 10°$) will be excluded from the calculations. In addition, pressure levels at 925 and 850 mb are used in the derivation of the geostrophic winds. This can result in unrealistic AR statistics over topographies. Therefore, regions with climatological surface pressure less than 850 mb (based on ERA5) are also excluded in the calculations of zonal mean. The spreads among the reanalyses are small, with NCEP R1 and NCEP R2 have slightly higher AR frequency, suggesting that all reanalyses have similar performance in representing the AR frequency distribution (Figures, 6.5.3c, d and e).

AR frequency is controlled by both the size and the number of the detected ARs. Fig-

ure 6.5.4a shows that the PDFs of the AR length are consistent across different datasets. Compared to the AR length in reanalyses, ARs in AIRS/AMSU is slightly longer. There is a larger spread in the AR width distribution (Figure 6.5.4b). In particular, the ARs in MERRA2 are the narrowest. Consistent with the narrowest ARs in MERRA2, ARs in MERRA2 also have the smallest area (Figure 6.5.4c) and largest length/width ratio (Figure 6.5.4d). The total number of ARs in MERRA2 during the study period is more than other datasets (Figure 6.5.4a). This suggests that MERRA2 tends to simulate more ARs, but with smaller AR size. These two effects in MERRA2 compensate each other and result in the AR frequency comparable to those in other reanalyses. NCEP R1, NCEP R2 and to a lesser extent CFSR have larger AR size due to the larger AR width in these datasets, but fewer ARs detected. Consequently, the length/width ratio in these three datasets are smallest and AR frequencies in NCEP R1 and NCEP R2 are higher compared to other reanalyses (Figures 6.5.3c, d and e).

6.3.2 AR Strength

AR GIVT is defined as the GIVT under AR conditions. As shown in Figure 6.5.5a, enhanced AR GIVT occurs over the storm track regions. Unlike AR frequency, the spatial distribution of AR GIVT is less uniform and exhibits more spatial variation, with enhanced AR GIVT concentrated in smaller regions of the storm tracks. Compared to the magnitude of the AR GIVT over oceans, AR GIVT over lands is substantially weaker. In terms of the differences between reanalyses and AIRS/AMSU, the differences in the spatial distribution of AR GIVT between reanalyses and AIRS/AMSU are quite similar across reanalyses (Figures 6.5.5b, c, d and e). Reanalyses show stronger AR GIVT over the midlatitudes, especially the storm track regions. Weaker GIVT can be found over subtropical regions. Since the geostrophic wind in AIRS/AMSU is bias-corrected based on that in ERA5, the differences in AR GIVT between reanalyses and AIRS/AMSU should not be treated as biases in reanalyses. Over the Northern Hemisphere, MERRA2, NCEP R1 and NCEP R2 tend to have stronger AR

GIVT. Over the Southern Ocean, AR GIVT in NCEP R1 and NCEP R2 are substantially stronger than those in other reanalyses. The spread among these five reanalyses is relatively small, though the AR GIVT in MERRA2 is slightly stronger, consistent with the stronger IVT magnitude in MERRA2 found in *Collow et al.* (2022). It is not surprising that we also find that the results of the AR GIVT are consistent with those of the climatological mean GIVT (Figure 6.A.3), suggesting that differences in AR GIVT among datasets are mostly due to the differences in the climatological mean GIVT.

The differences in the AR GIVT can be caused by the differences in AR IWV and AR geostrophic wind magnitude. Figure 6.5.6a shows the AR IWV in AIRS/AMSU. Enhanced AR IWV mostly occurs over the subtropical regions equatorward of 30°N/S. Poleward of 30°N/S, AR IWV decreases rapidly. Compared to the AR IWV over oceans, AR IWV over lands is substantially weaker. Compared to the AR IWV in AIRS/AMSU, reanalyses simulate stronger AR IWV over midlatitudes poleward of 30°N/S and weaker AR IWV can be found equatorward of 30°N/S. This spatial pattern in the difference is shared by all reanalyses (Figures 6.5.6b, c, d and e). Over the Northern Hemisphere, the spread among all reanalyses is relatively small, with the AR IWV in NCEP R1 and NCEP R2 being slightly stronger than those in other reanalyses. Over the Southern Ocean, the AR IWV in NCEP R1 and NCEP R2 is substantially stronger than those in the other five reanalyses, which is consistent with the results in AR GIVT. Similar to GIVT, the results of the AR IWV are also reflective of the results in the climatological mean IWV (Figure 6.A.4). Since there is no bias correction applied to the IWV field, although unlikely, if the IWV in AIRS/AMSU represents the true observation, the results presented here suggest that all reanalyses have a wet bias over the midlatitudes and a dry bias over the subtropics. The wet bias over midlatitudes is strongest in NCEP R1 and NCEP R2. Compared to NCEP R1 and NCEP R2, the wet bias in CFSR, which is the third-generation reanalysis from NCEP, is greatly alleviated. Similarly, compared to ERAI, ERA5, which is the latest generation of reanalysis from ECMWF, also sees improvements in the wet bias. These results show that there are

improvements in simulating the IWV across generations of reanalysis products.

Figure 6.5.7a shows the AR geostrophic wind magnitude, unlike the pattern in the AR IWV, enhanced AR wind is found over the regions poleward of 30°N/S. This suggests that the enhanced AR GIVT shown in Figure 6.5.5a is dominated by IWV over the subtropics, but wind over midlatitudes. AR wind over the Southern Hemisphere is stronger compared to that over the Northern Hemisphere. Enhanced wind can also be found along the coastal regions of Antarctica. The enhanced wind over these regions is likely unrealistic, which may be caused by the presence of topography. Compared to the AR wind in AIRS/AMSU, reanalyses overestimate the wind magnitude over the midlatitude Southern Ocean while substantially underestimating it along the coastal regions of Antarctica. Such a large difference between reanalyses and AIRS/AMSU over these regions likely indicates that the wind over these regions in AIRS/AMSU is biased high. Weaker wind in reanalyses can be found over subtropical regions and regions at around 60°N. Unlike the AR IWV field, the spread in the AR wind among reanalyses is small (Figures 6.5.7c, d and e), indicating higher skills for reanalyses in simulating the wind field. Note that the AR wind in the AIRS/AMSU shown here has been bias-corrected by the wind filed in ERA5. The differences between reanalyses and AIRS/AMSU thus should not be treated as biases in reanalyses. Again, the results in the AR wind are also consistent with the results in the climatological mean wind (Figure 6.A.5).

6.3.3 AR Precipitation

It has been well documented that ARs are associated with enhanced precipitation (*Arabzadeh et al.*, 2020; *Gao et al.*, 2016; *Lavers and Villarini*, 2013). It's also quite common that reanalysis-based precipitation is directly used in AR studies (*Gao et al.*, 2016; *Kim et al.*, 2022; *Maclennan et al.*, 2022; *Pasquier et al.*, 2019). Yet, reanalysis-based precipitation is not directly constrained by observations. Their performance against observed precipitation thus requires further evaluation. In this section, we will focus on AR precipitation which

is defined as the precipitation that falls within the AR footprints. Figure 6.5.8a shows the mean AR precipitation intensity. Over the Northern Hemisphere, enhanced AR precipitation occurs over the poleward flank of the AR active regions over both the North Pacific and North Atlantic. Intense AR precipitation can be observed extending from the southwest of the ocean basin into the northeast of the ocean basin. There is a discontinuity between the western North Pacific and the eastern North Pacific. The intensity west of the dateline is much weaker than that over east of the dateline. The exact cause of this discontinuity is unclear. However, after manual examinations of the identified ARs and the precipitation field, there seems to be a time lag between the AR footprints detected from AIRS/AMSU and the precipitation systems in IMERG: the precipitation systems tend to locate east/northeast (ahead) of the AR footprints. This spatial mismatch between the AR footprints and the precipitation systems likely contributes to the abnormally weak AR precipitation over this region. Therefore, we will exclude this region from the following analysis and discussion, as well as in the zonal mean calculations followed.

Over the Southern Hemisphere, consistent with *Collow et al.* (2022), strong AR precipitation occurs over the South Pacific and South Atlantic while AR precipitation over the South Indian Ocean is relatively weak. Compared to the AR precipitation over oceans, AR precipitation over lands is much weaker, except over some coastal regions. Reanalyses underestimate the AR precipitation over regions with strong AR precipitation intensity, such as the northeast North Pacific, North Atlantic poleward of 50°N, western subtropics over the South Pacific and Southern Ocean Poleward of around 40°S. The differences between reanalyses and satellite observation are relatively small over regions between 30°N/S and 40[∘N/S in both hemispheres. The biases over lands are smaller compared to those over oceans, likely due to the smaller AR precipitation intensity over lands. AR precipitation intensity is weakest in NCEP R1 while the spread among the other six reanalyses is generally small.

As shown in Figure 6.5.9a, ARs contribute substantially to the annual total precipitation.

Over many of the oceanic and coastal regions, AR precipitation can account for up to half of the annual total precipitation. The contribution of ARs to total precipitation over lands is spatially more heterogeneous. For example, ARs can contribute up to half of the annual precipitation over regions, such as Australia and North Africa. At the same time, East Aisa only receives 10-30% of its annual precipitation from ARs. Compared to observation, reanalyses generally underestimate ARs' contribution to the total precipitation over oceans, especially over regions equatorward of 30°N/S and poleward of 50°N/S. Smaller differences between reanalyses and satellite observation can be found over regions between 30°N/S and 40°N/S. Over lands, depending on regions, ARs in reanalyses can contribute more to the total precipitation, such as over Australia and East Asia. At the same time, they can also underestimate ARs' contribution to the total precipitation over regions such as northern North America and South Africa. The spread across reanalyses is generally small. However, over the Northern Hemisphere and equatorward of about 30°S over the Southern Hemisphere, NCEP R1 simulates the lowest contribution to total precipitation by ARs while CFSR produces the lowest contribution to total precipitation by ARs over oceans poleward of 30°S over the Southern Hemisphere.

It has been shown by previous studies that ARs play an even more important role in extreme precipitation compared to mean precipitation (*Arabzadeh et al.*, 2020; *Gao et al.*, 2016). Defined as the 95^{th} percentile intensity of all the AR precipitation, AR extreme precipitation intensifies substantially (Fig. 6.5.10a) compared to AR mean precipitation (Fig. 6.5.8a). Over regions, such as the western South Pacific subtropics, northwest of South Atlantic and southwest of North Atlantic, the intensity of AR extreme precipitation can exceed 60 mm/day. Over the Southern Ocean, the spatial pattern of the AR extreme precipitation intensity is very similar to the AR mean precipitation intensity, with very strong intensity observed over the South Pacific and South Atlantic. The intensity over the South Indian Ocean is substantially weaker. Over the Northern Hemisphere oceans, enhanced AR extreme precipitation can be observed over the entire ocean basins of the

North Pacific and North Atlantic, except over the southeast ocean basins. Enhanced AR extreme precipitation can also be found over the west coast of North America and Chile due to orographic lifting, as well as in eastern North America and South America. The spatial patterns of the difference between reanalyses and satellite observation are similar to those for the differences in AR mean precipitation between reanalyses and satellite observation. The AR extreme precipitation in reanalyses is substantially weaker than the satellite observation nearly everywhere (Figure 6.5.10b). The largest underestimate occurs over the subtropical oceans and regions poleward of 50°N/S. The differences over lands are smaller compared to the differences over oceans due likely to the weaker AR extreme precipitation over lands. The magnitude of the AR extreme precipitation is weakest in NCEP R1, followed by ERAI. The spread of the other five reanalyses is generally small (Figures 6.5.10c, d and e). There is an improvement in simulating AR precipitation intensity from NCEP R1 to NCEP R2 and CFSR. Similar improvement can also be found from ERAI to ERA5.

For a grid point, we define an extreme precipitation threshold as the 95^{th} percentile of all precipitation with intensity greater than 0.01 m/day. The total extreme precipitation for a grid point is then calculated by summing all the daily precipitation with intensity greater than or equals to this extreme precipitation threshold. As shown in Figure 6.5.11a, ARs contribute strongly to the total extreme precipitation. While the spatial pattern of the fractional contribution to extreme precipitation by ARs is very similar to the spatial pattern in the fractional contribution to mean precipitation by ARs (Figure 6.5.9a), compared to the 30-50% in the fractional contribution to mean precipitation, ARs account for 50-70% of the total extreme precipitation over most of the oceanic regions. Unlike the fractional contribution to mean precipitation which shows the largest fraction at around 30°N/S, the spatial pattern in the fractional contribution to extreme precipitation is spatially more uniform over oceans. Over lands, large fractional contribution can be found over the west coast of North America, Chile, South Africa, over eastern North America, eastern South America, Australia, and interestingly North Africa. In contrast to the differences in the fractional

contribution to mean precipitation which shows strong underestimates by reanalyses nearly everywhere, the differences in fractional contribution to extreme precipitation are smaller. Underestimates by reanalyses can be found over regions poleward of 50°N/S and some regions over the subtropics. Over midlatitudes and many land regions, ARs in reanalyses tend to contribute slightly more to the total extreme precipitation. Compared to other reanalyses, NCEP R1, NCEP R2, and CFSR tend to simulate a smaller fraction of extreme precipitation contributed by ARs, especially over oceans.

It has been well documented that climate models tend to suffer the so-called "drizzling" bias in which models tend to rain too frequently and too lightly (*Chen et al.*, 2021; *Dai*, 2006). To investigate whether this problem is also present in AR precipitation, we define a metric called AR precipitation frequency. There is no guarantee that precipitation must occur when a grid point is experiencing AR conditions. We thus define AR precipitation frequency as the fraction of AR days a grid point experiences noticeable precipitation. Noticeable precipitation is defined as those with daily precipitation greater than or equal to 0.5 mm/day. We tried varied thresholds ranging from 0.1 mm/day to 2 mm/day. The conclusions presented here are not sensitive to the threshold used (not shown). As shown in Figure 6.5.12a, over most of the mid-latitude regions, more than 80% of the AR days are associated with noticeable precipitation. This suggests that our algorithm is able to effectively identify precipitating systems with enhanced moisture transport. Smaller AR precipitation frequency is generally found over lands and subtropical regions, suggesting that ARs are usually less efficient in generating precipitation over these regions. Compared to observation, except for NCEP R1 and NCEP R2, ARs in reanalyses tend to precipitate too often, especially over subtropics equatorward of 30°N/S, which is consistent with previous studies showing that "drizzling" bias is most severe over lower latitude regions (*Chen et al.*, 2021; *Dai*, 2006). Other regions which also suffer this problem include regions poleward of 50°S, Eurasia, west coast of North America and South America. Interestingly, this "drizzling" bias is greatly alleviated poleward of about 30[∘N over North Pacific and North Atlantic, as well as over

the Southern Ocean between about 30°S to 40⌈∘S. Surprisingly, the AR precipitation frequency in NCEP R1 and R2 is more comparable to the satellite observation, especially over the Southern Ocean. In these two reanalyses, ARs precipitate even less often compared to observation over regions between 30°N and 50°N and the subtropics of the Southern Hemisphere. The reasons for the improvement in the AR-related "drizzling" bias in these two older generation reanalyses is unknown and warrant further studies.

6.4 Conclusions and Discussion

Satellite observations and reanalyses have been indispensable in AR studies. However, previous AR studies using satellite data usually detect ARs based only on the IWV while studies using reanalyses usually make the assumption that reanalyses are representative of the true observation (*Matrosov*, 2013; *Neiman et al.*, 2008b; *Ralph et al.*, 2004; *Wick et al.*, 2012). In this study, we improve previous satellite-based AR studies by incorporating wind into the AR detection. Low-level geostrophic winds deriving from the geopotential height are combined with the IWV to obtain the GIVT. We demonstrate that GIVT can serve as a good proxy for IVT in terms of magnitude. By removing the three IVT direction criteria in the *Guan and Waliser* (2015) algorithm, namely the coherence criterion, the meridional IVT criterion and the consistency criterion, we show that the AR frequency based on the GIVT and that based on the IVT are nearly identical. The modified ARDT is then applied to the GIVT from the satellite observation AIRS/AMSU and seven commonly used reanalyses: MERRA2, ERA5, ERAI, JRA-55. CFSR. NCEP R1 and NCEP R2. We find that all datasets show high agreement on simulating the AR frequency. Given that the IWV and wind field in reanalyses are strongly constrained by satellite observations, this result should be expected: a weather system which is present in satellite observations should also be present in reanalyses. While the spread in AR length across datasets is relatively small, larger spread in the AR width can be found across datasets. Consequently, the spread in width leads to the spreads in the AR area and AR length/width ratio. Compared to other

datasets, MERRA2 tends to simulate narrower and more ARs while CFSR, NCEP R1 and NCEP R2 tend to simulate broader and fewer ARs. Compared to ARs in satellite observation, ARs in reanalyses have stronger GIVT over midlatitudes. The spread in the AR GIVT among reanalyses is mostly caused by the spead in AR IWV while the spread in AR wind magnitude is small. Compared to satellite observation, ARs in reanalyses are too wet over midlatitudes and dry over subtropics. We find that there are improvements in simulating the IWV field from NCEP R1, NCEP R2 to CFSR, and from ERAI to ERA5.

Unlike IWV and winds in reanalyses which are heavily constrained by observations, precipitation in reanalyses is produced by the models without any direct constraints. Larger biases are thus can be expected to be found in reanalysis-based precipitation. We evaluate the AR-induced precipitation in reanalyses against that based on IMERG. We reveal systematic biases in the reanalysis-based AR precipitation characteristics. Specifically, we find that reanalyses systematically underestimate both the mean and extreme AR precipitation intensity over oceans, with the strongest underestimates found in NCEP R1. Consequently, the fractional contributions to both the mean and extreme precipitation by ARs are all underestimated by reanalyses. It has long been known that climate models suffer the so-called "drizzling" bias problem. Namely, models tend to rain too often and too lightly. Defining AR precipitation frequency as the fraction of AR days a grid point experiences noticeable precipitation, we discover that ARs in reanalyses tend to rain too often, especially over the lower latitude regions. Combined with the weak biases in the AR precipitation intensity, we demonstrate that the "drizzling" bias also exists for AR precipitation in reanalyses. These findings question the direct uses of reanalysis-based precipitation in AR studies.

Studies have shown that the statistics of ARs and AR precipitation are sensitive to the ARDT used (*Collow et al.*, 2022; *Rutz et al.*, 2019; *Shields et al.*, 2018). In this study, we employed the modified ARDT based on *Guan and Waliser* (2015) to demonstrate the feasibility of using GIVT for detecting ARs. In this regard, this study thus also serves as proof of concept. We have demonstrated that GIVT can be a good proxy for IVT given that

the direction of GIVT/IVT is not considered. Therefore, as long as the IVT-based ARDT doesn't have any IVT direction criteria, GIVT can be used readily as input to the algorithm and produce AR statistics comparable to those based on IVT. As has been shown (Figure 6.A.2), the AR statistics based on the *Guan and Waliser* (2015) are quite different from those based on other ARDTs. It can thus be expected that the results presented in this study are somewhat algorithm-dependent. For example, we show in this study that there is a high agreement among datasets on the AR frequency. However, this is mostly due to the percentile-based threshold used in our ARDT. It can be expected that reanalyses with larger climatological GIVT would have larger AR frequency if an absolute threshold is used. Nevertheless, since an identical ARDT is consistently applied to all datasets, the results regarding the spreads among datasets in this study should be more robust.

As a product obtained from both infrared (AIRS) and microwave (AMSU) sensors, the retrieval quality of AIRS/AMSU under cloudy condition degrades rapidly, the sampling frequency under cloudy regions, such as the ITCZ and mid-latitude regions, is lower than that over the clear regions, such as the subtropics and some land regions. Furthermore, the Aqua satellite on which the AIRS and AMSU sensors board is in a Sun-synchronous polar orbit, both AIRS and AMSU can only sample the atmosphere twice daily at low latitude regions and thus cannot adequately resolve the diurnal cycle. These sampling issues can result in biases in the satellite observations (*Tian et al.*, 2013). Given these factors, the results based on AIRS/AMSU should not be treated as true observation and the differences between AIRS/AMSU and other reanalyses also should not be viewed as the biases in reanalyses. Instead, the spreads among datasets should be simply viewed as observed uncertainties. Smaller spread of a quantity thus gives us more confidence in the ability of reanalyses and satellite observations in representing the true observation of that quantity and vice versa. In this sense, we have more confidence in the reanalyses and satellite observation's ability in representing AR frequency, AR length and AR wind magnitude while our confidence in the AR width and AR IWV representations is lower.

While potential biases exist in the IWV and geostrophic wind field from AIRS/AMSU, it's also possible that the satellite-based precipitation product IMERG also contains biases. Evaluations on the performance of IMERG against other ground observations and remotely sensed products have shown varied results (*Pradhan et al.*, 2022). Whether IMERG has better performance than other observed precipitation products remains inconclusive. However, IMERG is produced by merging the precipitation estimates with highest quality from passive microwave sensors and infrared sensors. It thus can be regarded as the state-of-the-art observational precipitation product. Compared to IMERG, it has been well known that models have troubles in simulating the precipitation realistically. It thus can be expected that the IMERG precipitation is closer to the true observation compared to reanalysis-based precipitation. The differences between IMERG-based AR precipitation and reanalysis-based AR precipitation can also be viewed as the biases in reanalyses. Furthermore, a previous study (*Naud et al.*, 2020), which uses IMERG to evaluate the modeled precipitation in Oceanic extratropical cyclones, found that IMERG-based cyclone precipitation is stronger over the warm sector of the cyclone compared to other model- and reanalysis-based cyclone precipitation. Given that ARs are usually located over the warm sector of the cyclone, this result adds further confidence in the findings presented in this study.

In this study, we have provided a proof of concept for the feasibility of detecting ARs in satellite observations using both the moisture and wind information. As the quality of the satellite observations continues to improve, the methodology presented here can be applied to other satellite observations to develop observed AR statistics. We have also conducted a comprehensive intercomparison between reanalyses and satellite observations and among reanalyses on their skills in representing AR characteristic and AR related precipitation. Our findings provide better guidance on the direct uses of reanalyses and reanalysis-based precipitation in future AR studies. The satellite-based AR statistics and AR precipitation developed in this study can also be used to evaluate the climate models' skills in representing ARs and AR precipitation. Such evaluation will be conducted in a future study.

Acknowledgements. Weiming Ma and Gang Chen are supported by National Science Foundation Grants AGS-1832842 and NASA Grant 80NSS-C21K1522.

6.5 Figures

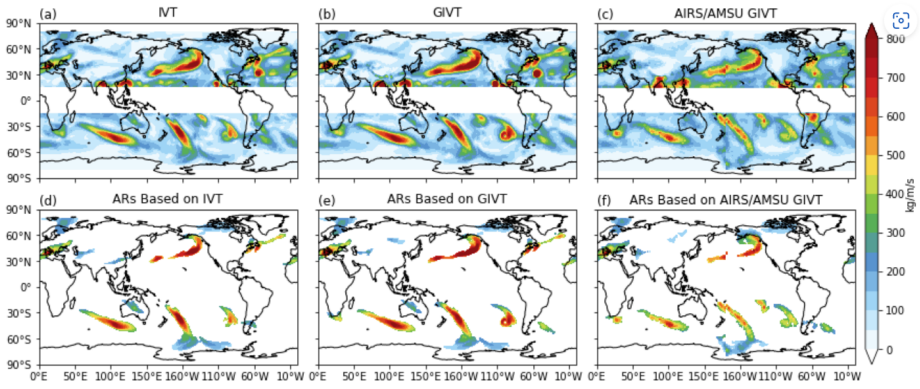

Figure 6.5.1: A snapshot of the IVT (a) and GIVT (b) in ERA5. (c) is showing the same snapshot of GIVT, but from AIRS/AMSU. Corresponding ARs detected by the modified algorithm are shown in (d). (e), and (f), respectively.

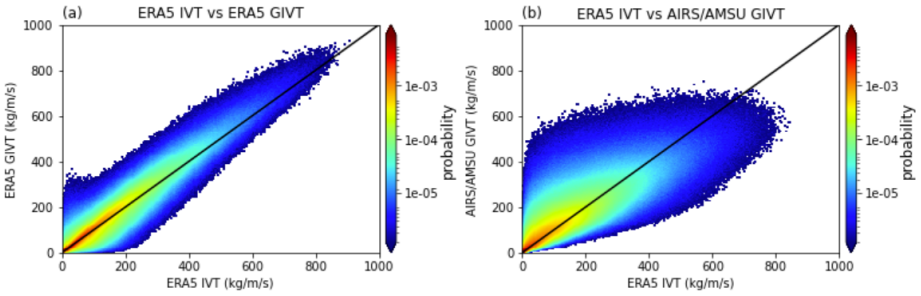

Figure 6.5.2: Joint probability distribution function of IVT versus GIVT in ERA5 (a) and IVT from ERA5 versus smoothed GIVT from AIRS/AMSU (b). Note that the colorbars are in logarithmic scale.

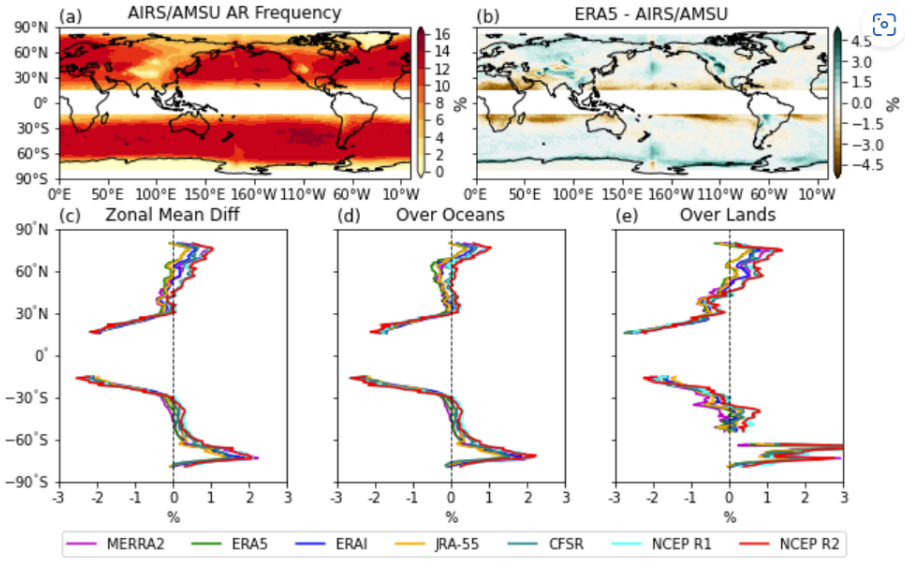

Figure 6.5.3: AR frequency detected by the modified algorithm based on AIRS/AMSU (a). AR frequency difference between ERA5 and AIRS/AMSU (b). The differences between the zonal mean AR frequency in reanalysis products and AIRS/AMSU. (d) and (e) are the same as (c), but for the zonal mean differences over oceans and lands, respectively.

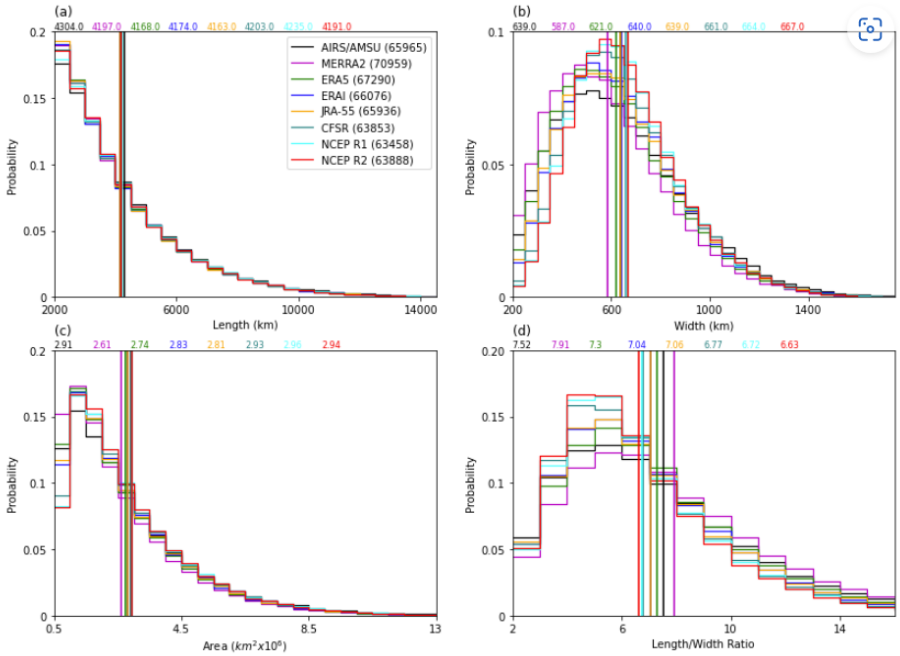

Figure 6.5.4: Probability distribution functions of AR length (a), width (b), area (c), and length/width ratio (d) for all reanalyses and AIRS/AMSU. The numbers inside the parentheses in (a) indicate the total number of ARs detected during the study period.

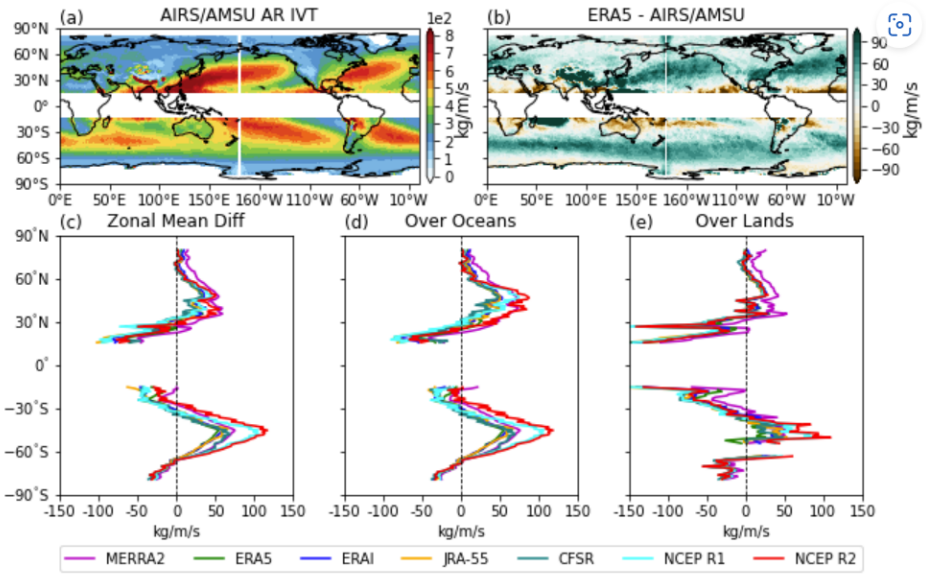

Figure 6.5.5: AR GIVT in AIRS/AMSU (a). AR GIVT difference between ERA5 and AIRS/AMSU (b). The differences between zonal mean AR GIVT in reanalyses and AIRS/AMSU (c). (d) and (e) are the same as (c), but for the zonal mean AR IVT over oceans and lands, respectively.

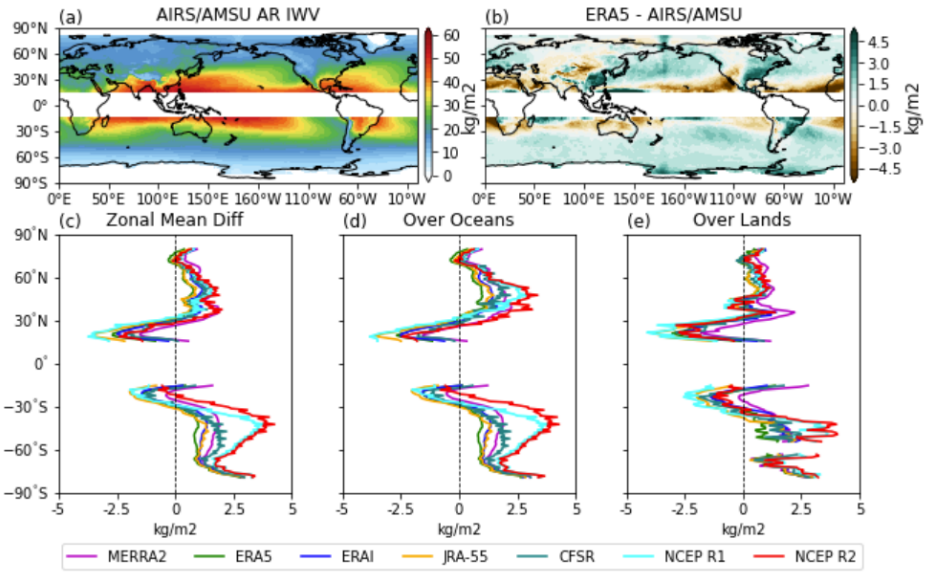

Figure 6.5.6: AR IWV in AIRS/AMSU (a). AR IWV difference between ERA5 and AIRS/AMSU (b). The differences between zonal mean AR IWV in reanalyses and AIRS/AMSU (c). (d) and (e) are the same as (c), but for the zonal mean AR IWV over oceans and lands, respectively.

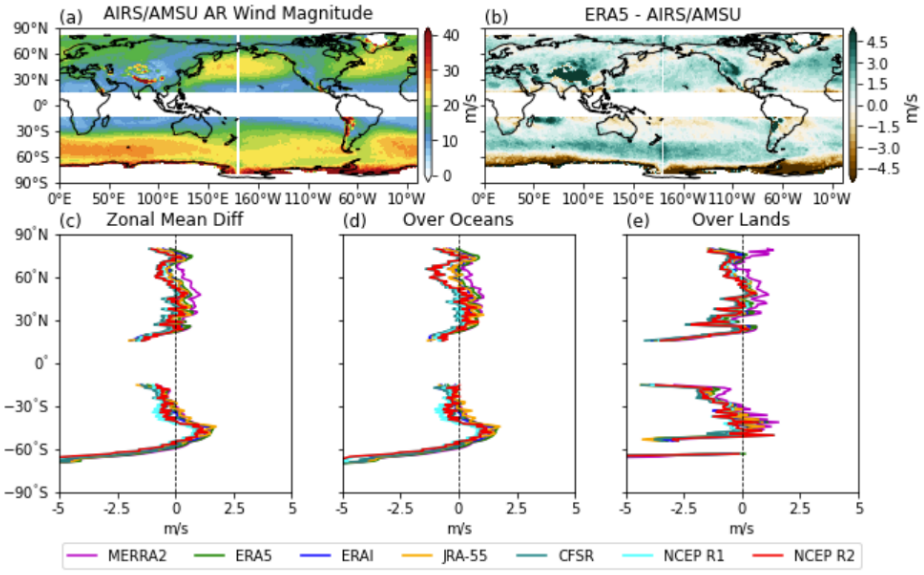

Figure 6.5.7: AR geostrophic wind magnitude in AIRS/AMSU (a). AR geostrophic wind magnitude difference between ERA5 and AIRS/AMSU (b). The differences between zonal mean AR geostrophic wind magnitude in reanalyses and AIRS/AMSU (c). (d) and (e) are the same as (c), but for the zonal mean AR geostrophic wind magnitude over oceans and lands, respectively.

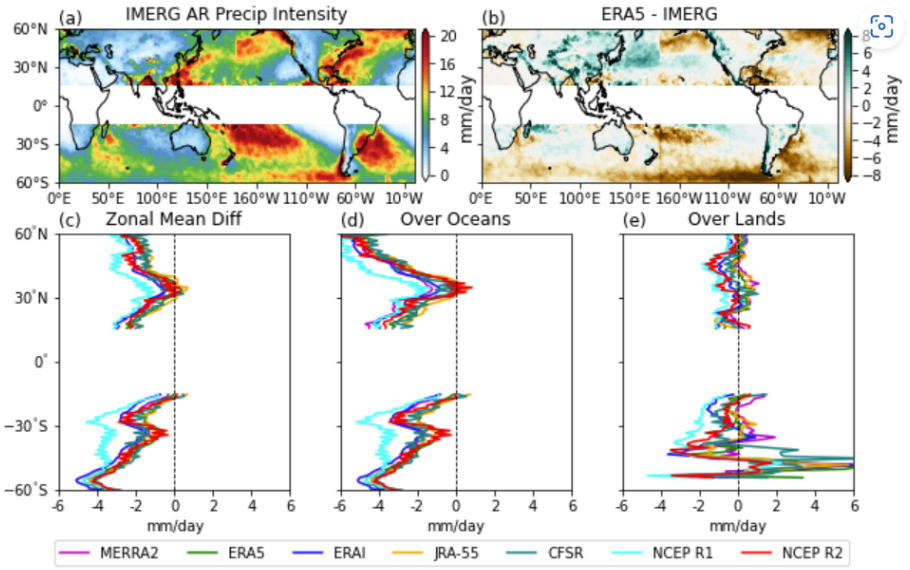

Figure 6.5.8: AR precipitation intensity in IMERG (a). AR precipitation intensity difference between ERA5 and IMERG (b). The differences between zonal mean AR precipitation intensity in reanalyses and IMERG (c). (d) and (e) are the same as (c), but for the zonal mean AR precipitation intensity over oceans and lands, respectively.

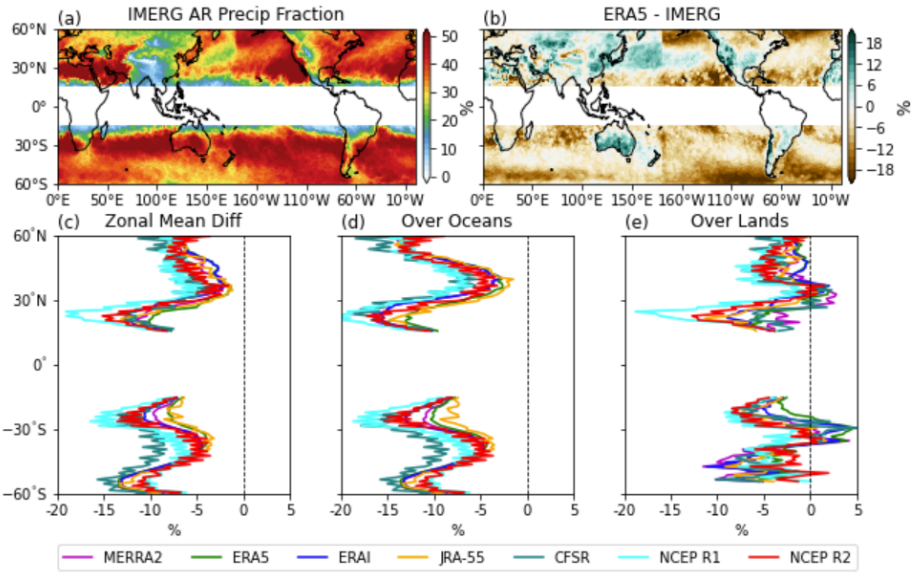

Figure 6.5.9: AR precipitation fraction in IMERG (a). AR precipitation fraction difference between ERA5 and IMERG (b). The differences between zonal mean AR precipitation fraction in reanalyses and IMERG (c). (d) and (e) are the same as (c), but for the zonal mean AR precipitation fraction over oceans and lands, respectively.

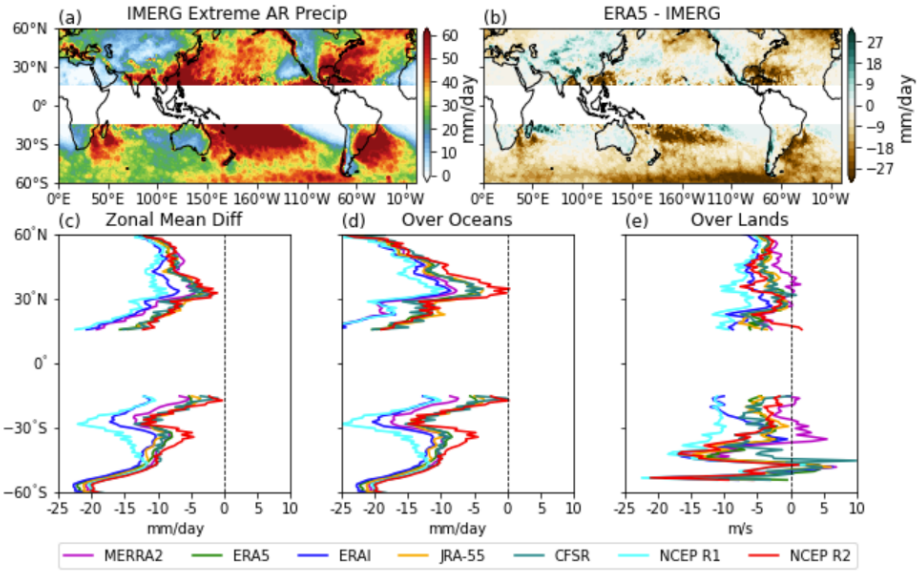

Figure 6.5.10: Extreme AR precipitation intensity in IMERG (a). Extreme AR precipitation intensity difference between ERA5 and IMERG (b). The differences between zonal mean extreme AR precipitation intensity in reanalyses and IMERG (c). (d) and (e) are the same as (c), but for the zonal mean extreme AR precipitation intensity over oceans and lands, respectively.

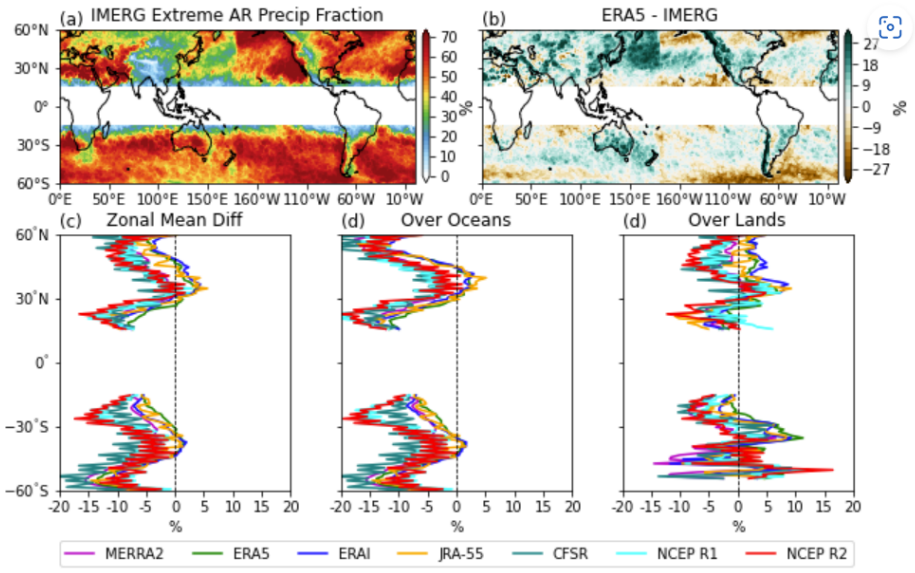

Figure 6.5.11: Extreme AR precipitation fraction in IMERG (a). Extreme AR precipitation fraction difference between ERA5 and IMERG (b). The differences between zonal mean extreme AR precipitation fraction in reanalyses and IMERG (c). (d) and (e) are the same as (c), but for the zonal mean extreme AR precipitation fraction over oceans and lands, respectively.

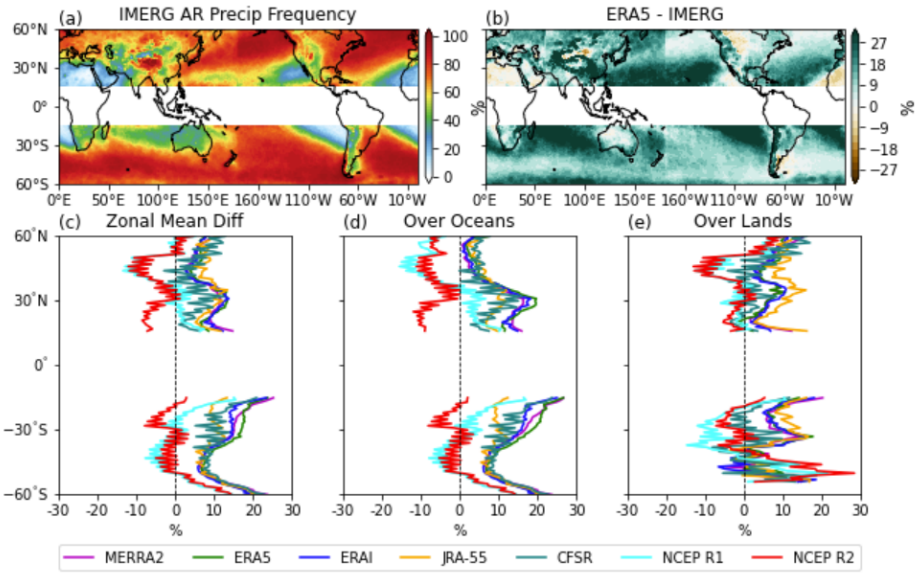

Figure 6.5.12: AR precipitation frequency in IMERG (a). AR precipitation frequency difference between ERA5 and IMERG (b). The differences between zonal mean AR precipitation frequency in reanalyses and IMERG (c). (d) and (e) are the same as (c), but for the zonal mean AR precipitation frequency over oceans and lands, respectively.

Appendix

6.A Supplement

Text S1 Due to the presence of the noises in the geopotential height field in AIRS/AMSU, the derived geostrophic winds are too strong compared to those derived from reanalyses. To alleviate this problem, a bias correction procedure was applied to the geostrophic wind magnitude in AIRS/AMSU. More specifically, the climatological mean geostrophic wind magnitude over mid-latitude oceans from 30°N/S to 60°N/S in ERA5 was regressed onto the unsmoothed climatological mean geostrophic wind magnitude over mid-latitude oceans from 30°N/S to 60°N/S in AIRS/AMSU. The obtained regression coefficient and intercept were then applied to the geostrophic wind magnitude in AIRS/AMSU. This bias correction procedure would correct the mean in AIRS/AMSU so that the mean geostrophic wind magnitude over mid-latitude oceans from 30°N/S to 60°N/S in AIRS/AMSU would equal to that in ERA5. Since the AR detection algorithm used in this study adopts a percentile-based threshold, such bias correction on the geostrophic wind magnitude would not affect the ARs detected.

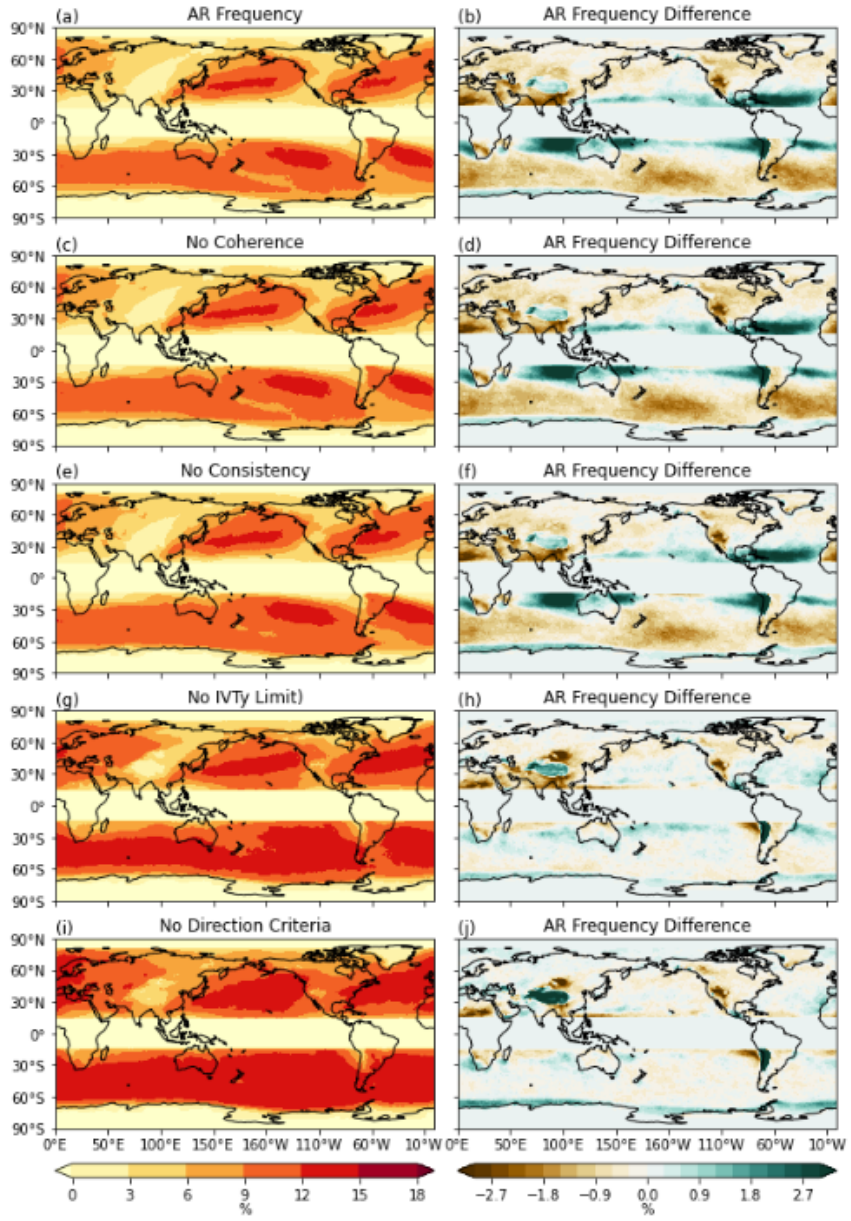

Figure 6.A.1: AR frequency distribution based on GIVT using the original *Guan and Waliser* (2015) algorithm (a), the original algorithm but with the coherence criterion removed (c), the original algorithm but with the consistency criterion removed (e), the original algorithm but with the meridional IVT criterion removed (g), the original algorithm but with all three IVT direction criteria removed (i). (b), (d), (f), (h) and (j) are showing the AR frequency differences between those based on GIVT and those based on IVT (GIVT – IVT) using the corresponding modified algorithms. See the main text for more information on the IVT direction criteria used in the original algorithm.

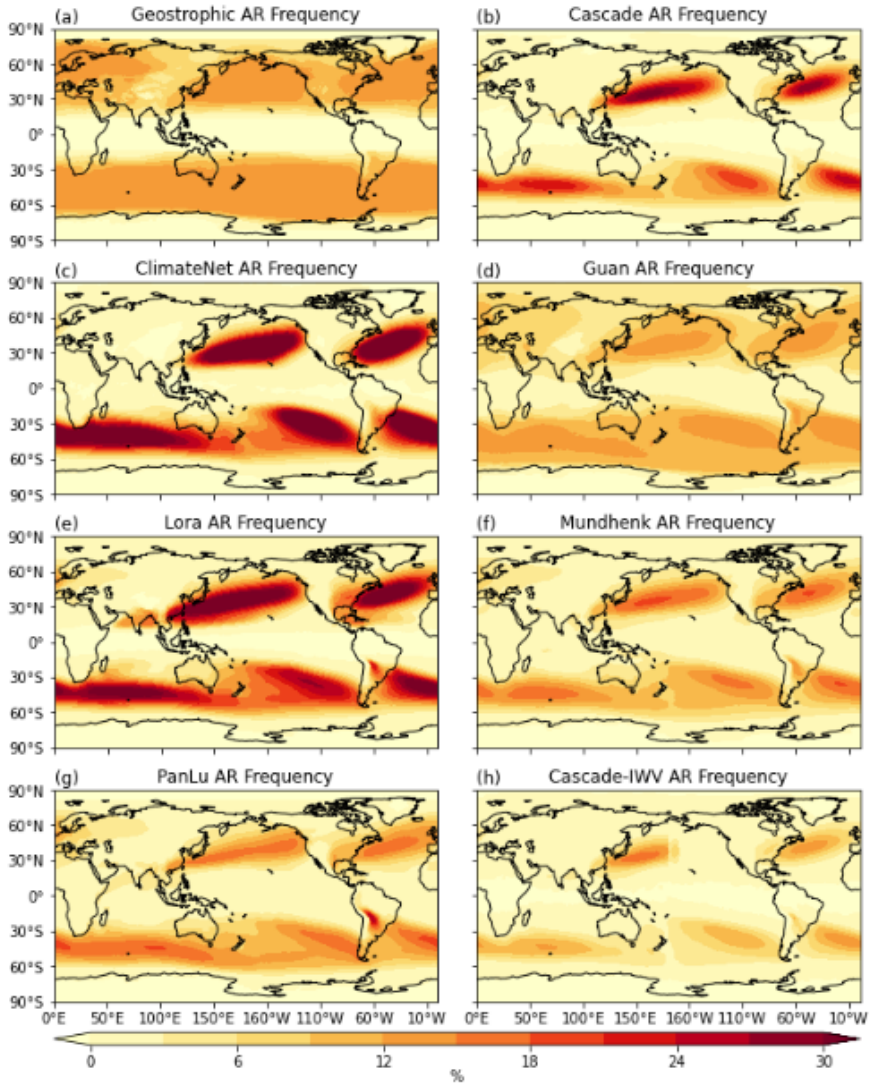

Figure 6.A.2: Annual AR frequency based on the AR detection algorithm for satellite data and seven global AR detection algorithms participated in the ARTMIP. All panels are based the the 6-hourly data from MERRA2.

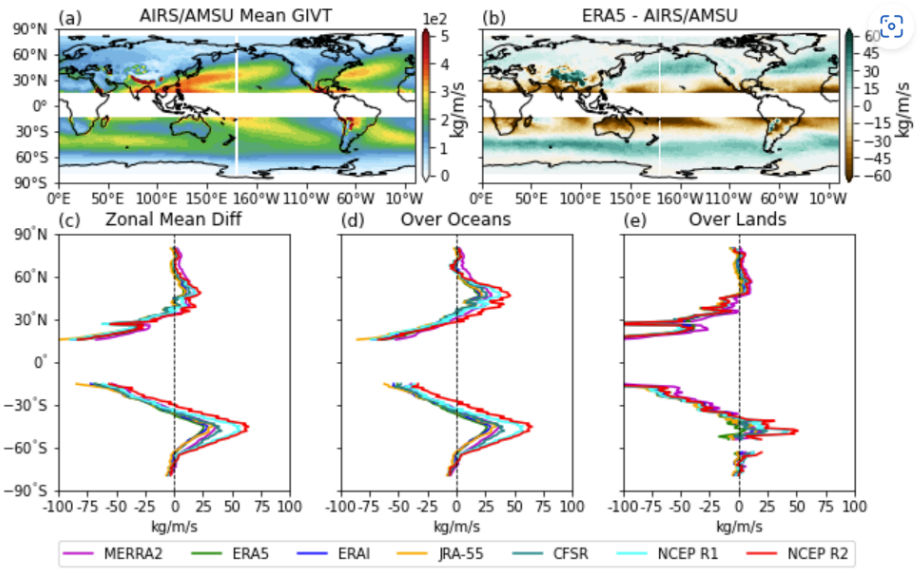

Figure 6.A.3: Climatological mean GIVT in AIRS/AMSU (a). Climatological mean GIVT difference between ERA5 and AIRS/AMSU (b). The differences between climatological zonal mean GIVT in reanalyses and AIRS/AMSU (c). (d) and (e) are the same as (c), but for the climatological zonal mean GIVT over oceans and lands, respectively.

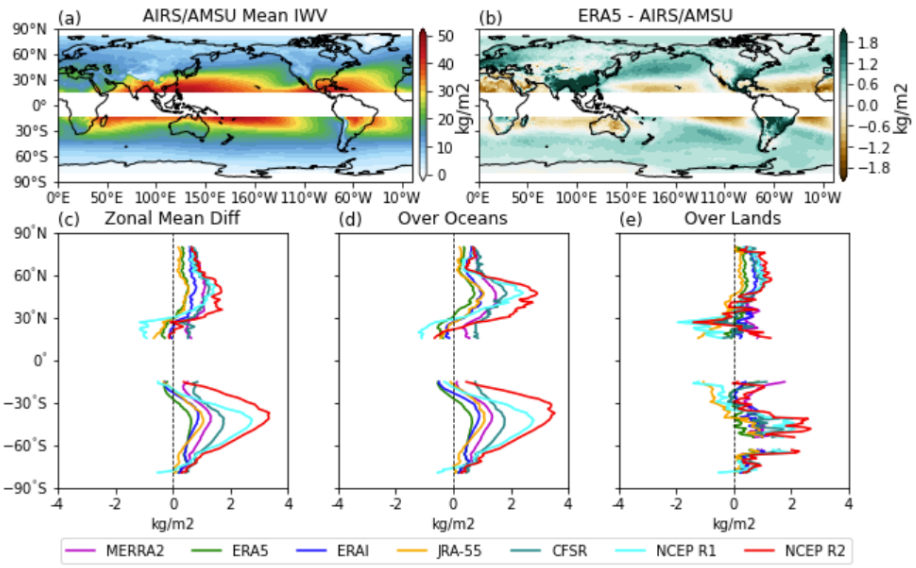

Figure 6.A.4: Climatological mean IWV in AIRS/AMSU (a). Climatological mean IWV difference between ERA5 and AIRS/AMSU (b). The differences between climatological zonal mean IWV in reanalyses and AIRS/AMSU (c). (d) and (e) are the same as (c), but for the climatological zonal mean IWV over oceans and lands, respectively.

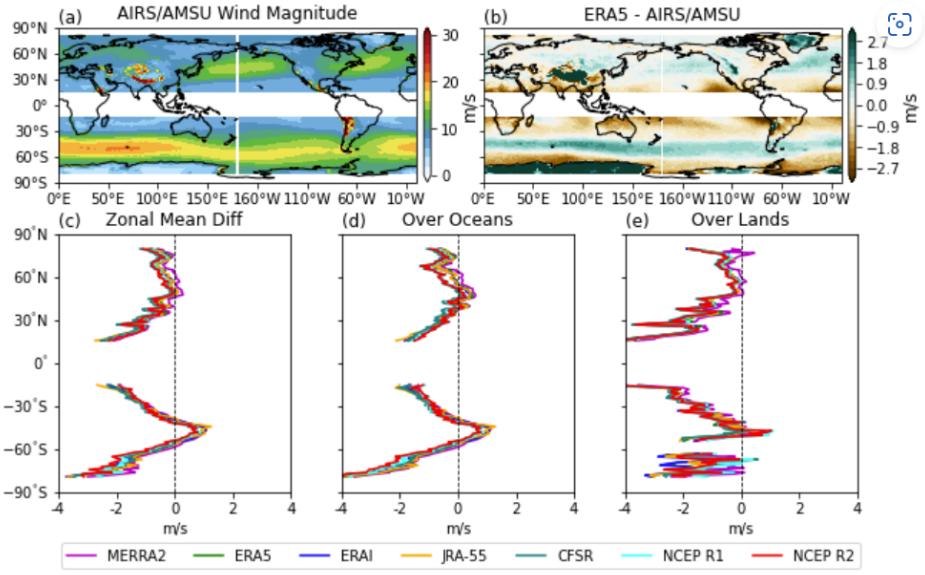

Figure 6.A.5: Climatological mean geostrophic wind speed in AIRS/AMSU (a). Climatological mean geostrophic wind speed difference between ERA5 and AIRS/AMSU (b). The differences between climatological zonal mean geostrophic wind speed in reanalyses and AIRS/AMSU (c). (d) and (e) are the same as (c), but for the climatological zonal mean geostrophic wind speed over oceans and lands, respectively.

CHAPTER 7

Final conclusions and future work

7.1 Final conclusions

Atmospheric rivers (ARs) are long and narrow bands of intense water vapor transport in the atmosphere. Despite occupying only small portion of the atmosphere at any given time, these filamentary features play a key role in the meridional moisture transport as well as exert profound impacts on regional hydrological climate. An earlier study reveals that at least 90% of the poleward atmospheric moisture transport is delivered by ARs (*Zhu and Newell*, 1998). On regional scale, depending on their strength and duration, ARs can be either beneficial or detrimental (*Ralph et al.*, 2019). On one hand, ARs contribute significantly to the annual total precipitation for many regions around the world (*Dettinger*, 2011; *Rutz and Steenburgh*, 2012; *Viale et al.*, 2018). ARs are also identified as an effective mechanism for terminating persistent droughts and have been termed "drought busters" (*Dettinger*, 2013). On the other hand, extreme AR events have been found behind many of the weather hazards, such as extreme precipitation (*Chen et al.*, 2018; *Lavers and Villarini*, 2013; *Ma et al.*, 2020a), floods (*Dettinger*, 2011; *Henn et al.*, 2020; *Paltan et al.*, 2017) and wind extremes (*Waliser and Guan*, 2017). In recent years, it is increasingly recognized that ARs can have strong influence on the polar climate, such as inducing sea ice loss (*Hegyi and Taylor*, 2018; *Wang et al.*, 2020; *Woods and Caballero*, 2016) and affecting ice shelf stability (*Djoumna and Holland*, 2021; *Mattingly et al.*, 2018; *Wille et al.*, 2022).

Given such important roles ARs play in our climate system, a better understanding on the factors controlling AR variability on different time scales would be especially beneficial in

improving the AR predictability. On the interannual time scale, El Nino Southern Oscillation (ENSO) has been shown to exert strong control on the AR variability along the North American West Coast, with its influence dependent on the ENSO flavors (*Kim et al.*, 2019). On the longer time scale, the variability of ARs depends strongly on the anthropogenic forcing but is also confounded by the decadal internal variability (*Dong et al.*, 2021; *Ma et al.*, 2020b). Regardless of the time scale considered, AR variability arises from two different sources, namely, the variability in circulation and the variability in the moisture. For example, it has been shown that ARs' response to anthropogenic warming is predominantly controlled by the moisture change (*Zhang et al.*, 2021).

Despite efforts have been made in studying the role of SST, such as that associated with ENSO, in modulating interannual AR variability, how internal variability can confound the effects of SST remains unexplored. On the longer time scale, attempts have been made to look at the relative roles of dynamic factor versus thermodynamic factor in determining the future AR response (*Gao et al.*, 2015; *Payne et al.*, 2020; *Zhang et al.*, 2021). However, besides decomposing the total AR response uncertainty into the dynamic versus thermodynamic components, AR response can be influenced by the responses in different parts of the climate system. Notably, two anthropogenically driven processes play key roles in causing the AR response uncertainty: namely, the warming of the tropical upper troposphere, which drives the poleward shift of the westerly jet, and the amplified warming of the polar regions, which drives the equatorward shift of the westerly jet. How each of these individual process influences AR response remains unknown. Besides AR uncertainty, the mechanisms concerning the AR-induced precipitation receive less attention. Further studies are thus needed to better understand how AR precipitation, especially AR extreme precipitation, is going to respond to warming. In addition, investigating the mechanisms driving AR variability relies heavily on reanalyses which have long been served as proxies of observations. Yet, how well these reanalyses in representing ARs and AR precipitation are unknown. The reason for that is because global AR statistics derived directly from observations are not available. In

this dissertation, I will address the research gaps listed above in the following chapters.

In Chapter 2, we first identify and characterize the leading modes of winter AR frequency variability over the North Pacific and North Atlantic in reanalysis. We then demonstrate that the atmospheric global climate models from the Coupled Model Intercomparison Project phase 6 (CMIP6) can simulate these leading modes with high skill. Using a combined singular value decomposition (SVD) method, we systematically quantify the relative roles of SST/sea ice and internal variability in driving the interannual variability of the identified leading modes. We find that SST/sea ice forcing can explain about half and a quarter of the observed variance for the leading modes over the North Pacific and North Atlantic, respectively. These results highlight the more predictable nature of the AR variability over the North Pacific and improve our understanding on the AR variability and the associated mechanisms over the Northern Hemisphere.

In Chapter 3, we investigate the trend of ARs in the Southern Hemisphere. We find that ARs have been shifting poleward in the Southern Hemisphere over the past four decades. We then develop a simple scaling method which allows us to decompose the total trend into a dynamic and a thermodynamic component. We show that the observed trend is mostly driven by the poleward shift of the westerly jet while the trend in the moisture field plays relatively minor role. Using two large ensembles based on the Community Earth System Model (CESM) (*Kay et al.*, 2015), one fully coupled and another one with prescribed SST/sea ice, we demonstrate the combined roles of anthropogenic forcing and interdecadal internal variability in driving the observed AR trend. The findings of this study have important implications and suggest that internal variability on the interdecadal time scale must be taken into account when studying AR response to future warming.

In Chapter 4, we focus on the impacts of Arctic Amplification and its associated sea ice loss on the variability of ARs over the Northern Hemisphere. Using nine models participated in the Polar Amplification Model Intercomparison Project (PAMIP) (*Smith et al.*, 2019), we find that, in response to Arctic sea ice loss, ARs extend northeastward over the North

Pacific and shift equatorward over the North Atlantic. We also investigate the relative roles of dynamic versus thermodynamic components, as well as those of the internal variability versus model difference in driving the AR response uncertainty. Potential emergent constraints are also explored which may help to reduce the AR response uncertainty. In this study, we investigate an important source of certainty in AR response to anthropogenic warming. These findings provide us a more complete understanding on AR response to warming.

In Chapter 5, instead of the AR characteristics, we shift our focus to the AR-induced extreme precipitation with recurrence interval ranging from 0.1 year to 50 years along the North American West Coast. We find that, under a warming climate, AR extreme precipitation intensifies nearly everywhere. Using a moisture budget approach, we show that the intensification of extreme precipitation over the midlatitudes is predominantly driven by the increases in atmospheric moisture, namely the thermodynamic component. Over the subtropics, while the thermodynamic component still contributes positively to AR extreme precipitation, the dynamical changes suppress the light to moderate precipitation while enhancing the most extreme precipitation substantially. This work elucidates the mechanisms driving the intensification of AR-induced extreme precipitation along the North American West Coast and has important implications for water resource management and infrastructure planning for the regions.

In Chapter 6, we develop a novel method to detect ARs in satellite observation using both the integrated water vapor (IWV) and geostrophic winds derived from geopotential height. Using data from the Atmospheric Infrared Sounder (AIRS) and the Advanced Microwave Sounding Unit (AMSU) (AIRS/AMSU), we generate a set of satellite-based global AR statistics. These satellite-based AR statistics are then used to evaluate the representation of ARs and AR precipitation in seven commonly used reanalyses. We find that reanalyses are consistent with satellite observations in the AR frequency distribution. However, ARs in reanalyses tend to precipitate too often and too lightly. In this study, for the first time, we detect ARs in satellite observations using not only the IWV, but also the wind information.

These results can also provide us more guidance on the uses of reanalyses in future AR studies.

7.2 Future work

Results of Chapter 4 are based on atmosphere-only models, it has been suggested that the signals in the response to Arctic sea ice loss are stronger in coupled models (*Deser et al.*, 2015). Furthermore, how tropical upper tropospheric warming, which is also major source of AR response uncertainty, would influence ARs remains unknown. In Chapter 6, we evaluate the performance of seven commonly used reanalyses in simulating ARs and AR precipitation. Climate models are also used extensively in AR studies, especially in future AR studies. Therefore, it's important to understand how well climate models can simulate ARs. Given these considerations, in future works, I will seek to address the following questions:

1. Is the AR response to Arctic sea ice loss sensitive to whether the ocean-atmosphere coupling is enabled? If yes, how does the response differ in coupled simulations?

2. How do ARs respond to tropical upper tropospheric warming? What are the major mechanisms controlling the response uncertainty?

3. How well do climate models participated in CMIP6 simulate the AR characteristics and AR precipitation? Can increasing model spatial resolution lead to better performance?

Addressing these questions in future works will lead to better understanding in AR variability at long time scale as well as improve our confidence in the models' ability to project future changes in ARs.

Bibliography

Arabzadeh, A., M. R. Ehsani, B. Guan, S. Heflin, and A. Behrangi (2020), Global intercomparison of atmospheric rivers precipitation in remote sensing and reanalysis products, *Journal of Geophysical Research: Atmospheres*, *125*(21), e2020JD033,021.

Arblaster, J. M., and G. A. Meehl (2006), Contributions of external forcings to southern annular mode trends, *Journal of climate*, *19*(12), 2896–2905.

Baggett, C., S. Lee, and S. Feldstein (2016), An investigation of the presence of atmospheric rivers over the north pacific during planetary-scale wave life cycles and their role in arctic warming, *Journal of the Atmospheric Sciences*, *73*(11), 4329–4347.

Baggett, C. F., E. A. Barnes, E. D. Maloney, and B. D. Mundhenk (2017), Advancing atmospheric river forecasts into subseasonal-to-seasonal time scales, *Geophysical Research Letters*, *44*(14), 7528–7536.

Barnes, E. A., and D. L. Hartmann (2010), Testing a theory for the effect of latitude on the persistence of eddy-driven jets using cmip3 simulations, *Geophysical Research Letters*, *37*(15).

Barnes, E. A., and L. Polvani (2013), Response of the midlatitude jets, and of their variability, to increased greenhouse gases in the cmip5 models, *Journal of Climate*, *26*(18), 7117–7135.

Barnes, E. A., and J. A. Screen (2015), The impact of arctic warming on the midlatitude jet-stream: Can it? has it? will it?, *Wiley Interdisciplinary Reviews: Climate Change*, *6*(3), 277–286.

Blackport, R., and J. A. Screen (2019), Influence of arctic sea ice loss in autumn compared to that in winter on the atmospheric circulation, *Geophysical Research Letters*, *46*(4), 2213–2221.

Blackport, R., and J. A. Screen (2020), Insignificant effect of arctic amplification on the amplitude of midlatitude atmospheric waves, *Science advances*, *6*(8), eaay2880.

Boisier, J. P., R. Rondanelli, R. D. Garreaud, and F. Muñoz (2016), Anthropogenic and natural contributions to the southeast pacific precipitation decline and recent megadrought in central chile, *Geophysical Research Letters*, *43*(1), 413–421.

Bond, N. A., M. F. Cronin, H. Freeland, and N. Mantua (2015), Causes and impacts of the 2014 warm anomaly in the ne pacific, *Geophysical Research Letters*, *42*(9), 3414–3420.

Bozkurt, D., O. Sen, Y. Ezber, B. Guan, M. Viale, and F. Caglar (2021), Influence of african atmospheric rivers on precipitation and snowmelt in the near east's highlands, *Journal of Geophysical Research: Atmospheres*, *126*(4), e2020JD033,646.

Bretherton, C. S., C. Smith, and J. M. Wallace (1992), An intercomparison of methods for finding coupled patterns in climate data, *Journal of climate*, *5*(6), 541–560.

Brönnimann, S. (2007), Impact of el niño–southern oscillation on european climate, *Reviews of Geophysics*, *45*(3).

Burrows, D. A., G. Chen, and L. Sun (2017), Barotropic and baroclinic eddy feedbacks in the midlatitude jet variability and responses to climate change–like thermal forcings, *Journal of the Atmospheric Sciences*, *74*(1), 111–132.

Butler, A. H., D. W. Thompson, and R. Heikes (2010), The steady-state atmospheric circulation response to climate change–like thermal forcings in a simple general circulation model, *Journal of Climate*, *23*(13), 3474–3496.

Cannon, F., F. M. Ralph, A. M. Wilson, and D. P. Lettenmaier (2017), Gpm satellite radar measurements of precipitation and freezing level in atmospheric rivers: Comparison with ground-based radars and reanalyses, *Journal of Geophysical Research: Atmospheres*, *122*(23), 12–747.

Cannon, F., J. M. Cordeira, C. W. Hecht, J. R. Norris, A. Michaelis, R. Demirdjian, and F. M. Ralph (2020), Gpm satellite radar observations of precipitation mechanisms in atmospheric rivers, *Monthly Weather Review*, *148*(4), 1449–1463.

Cash, B. A., and N. J. Burls (2019), Predictable and unpredictable aspects of us west coast rainfall and el niño: Understanding the 2015/16 event, *Journal of Climate*, *32*(10), 2843–2868.

Chang, P., S. Zhang, G. Danabasoglu, S. G. Yeager, H. Fu, H. Wang, F. S. Castruccio, Y. Chen, J. Edwards, D. Fu, et al. (2020), An unprecedented set of high-resolution earth system simulations for understanding multiscale interactions in climate variability and change, *Journal of Advances in Modeling Earth Systems*, *12*(12), e2020MS002,298.

Chen, D., A. Dai, and A. Hall (2021), The convective-to-total precipitation ratio and the "drizzling" bias in climate models, *Journal of Geophysical Research: Atmospheres*, *126*(16), e2020JD034,198.

Chen, G., and I. M. Held (2007), Phase speed spectra and the recent poleward shift of southern hemisphere surface westerlies, *Geophysical Research Letters*, *34*(21).

Chen, G., J. Lu, and D. M. Frierson (2008), Phase speed spectra and the latitude of surface westerlies: Interannual variability and global warming trend, *Journal of Climate*, *21*(22), 5942–5959.

Chen, G., J. Norris, J. D. Neelin, J. Lu, L. R. Leung, and K. Sakaguchi (2019), Thermodynamic and dynamic mechanisms for hydrological cycle intensification over the full probability distribution of precipitation events, *Journal of the Atmospheric Sciences*, *76*(2), 497–516.

Chen, G., P. Zhang, and J. Lu (2020), Sensitivity of the latitude of the westerly jet stream to climate forcing, *Geophysical Research Letters*, *47*(4), e2019GL086,563.

Chen, M., and A. Kumar (2018), Winter 2015/16 atmospheric and precipitation anomalies over north america: El niño response and the role of noise, *Monthly Weather Review*, *146*(3), 909–927.

Chen, X., L. R. Leung, Y. Gao, Y. Liu, M. Wigmosta, and M. Richmond (2018), Predictability of extreme precipitation in western us watersheds based on atmospheric river occurrence, intensity, and duration, *Geophysical Research Letters*, *45*(21), 11–693.

Chou, C., and J. D. Neelin (2004), Mechanisms of global warming impacts on regional tropical precipitation, *Journal of climate*, *17*(13), 2688–2701.

Cionni, I., V. Eyring, J.-F. Lamarque, W. Randel, D. Stevenson, F. Wu, G. Bodeker, T. Shepherd, D. Shindell, and D. Waugh (2011), Ozone database in support of cmip5 simulations: results and corresponding radiative forcing, *Atmospheric Chemistry and Physics*, *11*(21), 11,267–11,292.

Cohen, J., J. A. Screen, J. C. Furtado, M. Barlow, D. Whittleston, D. Coumou, J. Francis, K. Dethloff, D. Entekhabi, J. Overland, et al. (2014), Recent arctic amplification and extreme mid-latitude weather, *Nature geoscience*, *7*(9), 627–637.

Cohen, J., X. Zhang, J. Francis, T. Jung, R. Kwok, J. Overland, T. Ballinger, U. Bhatt, H. Chen, D. Coumou, et al. (2020), Divergent consensuses on arctic amplification influence on midlatitude severe winter weather, *Nature Climate Change*, *10*(1), 20–29.

Collow, A. M., C. A. Shields, B. Guan, S. Kim, J. Lora, E. McClenny, K. Nardi, A. Payne, K. Reid, E. Shearer, et al. (2022), An overview of artmip's tier 2 reanalysis intercomparison: Uncertainty in the detection of atmospheric rivers and their associated precipitation, *Journal of Geophysical Research: Atmospheres*, *127*(8), e2021JD036,155.

Cvijanovic, I., B. D. Santer, C. Bonfils, D. D. Lucas, J. C. Chiang, and S. Zimmerman (2017), Future loss of arctic sea-ice cover could drive a substantial decrease in california's rainfall, *Nature communications*, *8*(1), 1–10.

Dai, A. (2006), Precipitation characteristics in eighteen coupled climate models, *Journal of climate*, *19*(18), 4605–4630.

Dai, A., R. M. Rasmussen, C. Liu, K. Ikeda, and A. F. Prein (2020), A new mechanism for warm-season precipitation response to global warming based on convection-permitting simulations, *Climate Dynamics*, *55*(1), 343–368.

Dee, D. P., S. M. Uppala, A. J. Simmons, P. Berrisford, P. Poli, S. Kobayashi, U. Andrae, M. Balmaseda, G. Balsamo, d. P. Bauer, et al. (2011), The era-interim reanalysis: Configuration and performance of the data assimilation system, *Quarterly Journal of the royal meteorological society*, *137*(656), 553–597.

Deser, C., and M. L. Blackmon (1995), On the relationship between tropical and north pacific sea surface temperature variations, *Journal of Climate*, pp. 1677–1680.

Deser, C., R. Tomas, M. Alexander, and D. Lawrence (2010), The seasonal atmospheric response to projected arctic sea ice loss in the late twenty-first century, *Journal of Climate*, *23*(2), 333–351.

Deser, C., R. A. Tomas, and L. Sun (2015), The role of ocean–atmosphere coupling in the zonal-mean atmospheric response to arctic sea ice loss, *Journal of Climate*, *28*(6), 2168–2186.

Deser, C., I. R. Simpson, A. S. Phillips, and K. A. McKinnon (2018), How well do we know enso's climate impacts over north america, and how do we evaluate models accordingly?, *Journal of Climate*, *31*(13), 4991–5014.

Dettinger, M. (2011), Climate change, atmospheric rivers, and floods in california–a multimodel analysis of storm frequency and magnitude changes 1, *JAWRA Journal of the American Water Resources Association*, *47*(3), 514–523.

Dettinger, M. D. (2013), Atmospheric rivers as drought busters on the us west coast, *Journal of Hydrometeorology*, *14*(6), 1721–1732.

Djoumna, G., and D. Holland (2021), Atmospheric rivers, warm air intrusions, and surface radiation balance in the amundsen sea embayment, *Journal of Geophysical Research: Atmospheres*, *126*(13), e2020JD034,119.

Dong, L., L. R. Leung, F. Song, and J. Lu (2018), Roles of sst versus internal atmospheric variability in winter extreme precipitation variability along the us west coast, *Journal of Climate*, *31*(19), 8039–8058.

Dong, L., L. R. Leung, F. Song, and J. Lu (2021), Uncertainty in el niño-like warming and california precipitation changes linked by the interdecadal pacific oscillation, *Nature communications*, *12*(1), 1–10.

Dulière, V., Y. Zhang, and E. P. Salathe Jr (2011), Extreme precipitation and temperature over the us pacific northwest: A comparison between observations, reanalysis data, and regional models, *Journal of Climate*, *24*(7), 1950–1964.

Eiras-Barca, J., A. M. Ramos, J. G. Pinto, R. M. Trigo, M. L. Liberato, and G. Miguez-Macho (2018), The concurrence of atmospheric rivers and explosive cyclogenesis in the north atlantic and north pacific basins, *Earth System Dynamics*, *9*(1), 91–102.

Emori, S., and S. Brown (2005), Dynamic and thermodynamic changes in mean and extreme precipitation under changed climate, *Geophysical Research Letters*, *32*(17).

Espinoza, V., D. E. Waliser, B. Guan, D. A. Lavers, and F. M. Ralph (2018), Global analysis of climate change projection effects on atmospheric rivers, *Geophysical Research Letters*, *45*(9), 4299–4308.

Eyring, V., S. Bony, G. A. Meehl, C. A. Senior, B. Stevens, R. J. Stouffer, and K. E. Taylor (2016), Overview of the coupled model intercomparison project phase 6 (cmip6) experimental design and organization, *Geoscientific Model Development*, *9*(5), 1937–1958.

Francis, D., K. S. Mattingly, M. Temimi, R. Massom, and P. Heil (2020), On the crucial role of atmospheric rivers in the two major weddell polynya events in 1973 and 2017 in antarctica, *Science advances*, *6*(46), eabc2695.

Gao, Y., J. Lu, L. R. Leung, Q. Yang, S. Hagos, and Y. Qian (2015), Dynamical and thermodynamical modulations on future changes of landfalling atmospheric rivers over western north america, *Geophysical Research Letters*, *42*(17), 7179–7186.

Gao, Y., J. Lu, and L. R. Leung (2016), Uncertainties in projecting future changes in atmospheric rivers and their impacts on heavy precipitation over europe, *Journal of Climate*, *29*(18), 6711–6726.

Gelaro, R., W. McCarty, M. J. Suárez, R. Todling, A. Molod, L. Takacs, C. A. Randles, A. Darmenov, M. G. Bosilovich, R. Reichle, et al. (2017), The modern-era retrospective analysis for research and applications, version 2 (merra-2), *Journal of climate*, *30*(14), 5419–5454.

Gershunov, A., T. Shulgina, F. M. Ralph, D. A. Lavers, and J. J. Rutz (2017), Assessing the climate-scale variability of atmospheric rivers affecting western north america, *Geophysical Research Letters*, *44*(15), 7900–7908.

Giorgi, F., E.-S. Im, E. Coppola, N. Diffenbaugh, X. Gao, L. Mariotti, and Y. Shi (2011), Higher hydroclimatic intensity with global warming, *Journal of Climate*, *24*(20), 5309–5324.

Gong, T., S. B. Feldstein, and D. Luo (2013), A simple gcm study on the relationship between enso and the southern annular mode, *Journal of the atmospheric sciences*, *70*(6), 1821–1832.

Gorodetskaya, I. V., M. Tsukernik, K. Claes, M. F. Ralph, W. D. Neff, and N. P. Van Lipzig (2014), The role of atmospheric rivers in anomalous snow accumulation in east antarctica, *Geophysical Research Letters*, *41*(17), 6199–6206.

Guan, B., and D. E. Waliser (2015), Detection of atmospheric rivers: Evaluation and application of an algorithm for global studies, *Journal of Geophysical Research: Atmospheres*, *120*(24), 12,514–12,535.

Guan, B., and D. E. Waliser (2017), Atmospheric rivers in 20 year weather and climate simulations: A multimodel, global evaluation, *Journal of Geophysical Research: Atmospheres*, *122*(11), 5556–5581.

Guan, B., N. P. Molotch, D. E. Waliser, E. J. Fetzer, and P. J. Neiman (2010), Extreme snowfall events linked to atmospheric rivers and surface air temperature via satellite measurements, *Geophysical Research Letters*, *37*(20).

Guan, B., D. E. Waliser, N. P. Molotch, E. J. Fetzer, and P. J. Neiman (2012), Does the madden–julian oscillation influence wintertime atmospheric rivers and snowpack in the sierra nevada?, *Monthly Weather Review*, *140*(2), 325–342.

Guan, B., D. E. Waliser, F. M. Ralph, E. J. Fetzer, and P. J. Neiman (2016), Hydrometeorological characteristics of rain-on-snow events associated with atmospheric rivers, *Geophysical research letters*, *43*(6), 2964–2973.

Guirguis, K., A. Gershunov, T. Shulgina, R. E. Clemesha, and F. M. Ralph (2019), Atmospheric rivers impacting northern california and their modulation by a variable climate, *Climate dynamics*, *52*(11), 6569–6583.

Hagos, S. M., L. R. Leung, J.-H. Yoon, J. Lu, and Y. Gao (2016), A projection of changes in landfalling atmospheric river frequency and extreme precipitation over western north america from the large ensemble cesm simulations, *Geophysical Research Letters*, *43*(3), 1357–1363.

Hall, A., P. Cox, C. Huntingford, and S. Klein (2019), Progressing emergent constraints on future climate change, *Nature Climate Change*, *9*(4), 269–278.

Hegyi, B. M., and P. C. Taylor (2018), The unprecedented 2016–2017 arctic sea ice growth season: The crucial role of atmospheric rivers and longwave fluxes, *Geophysical research letters*, *45*(10), 5204–5212.

Held, I. M., and B. J. Soden (2006), Robust responses of the hydrological cycle to global warming, *Journal of climate*, *19*(21), 5686–5699.

Henn, B., K. N. Musselman, L. Lestak, F. M. Ralph, and N. P. Molotch (2020), Extreme runoff generation from atmospheric river driven snowmelt during the 2017 oroville dam spillways incident, *Geophysical Research Letters*, *47*(14), e2020GL088,189.

Hersbach, H., B. Bell, P. Berrisford, S. Hirahara, A. Horányi, J. Muñoz-Sabater, J. Nicolas, C. Peubey, R. Radu, D. Schepers, et al. (2020), The era5 global reanalysis, *Quarterly Journal of the Royal Meteorological Society*, *146*(730), 1999–2049.

Hollinger, J. P., J. L. Peirce, and G. A. Poe (1990), Ssm/i instrument evaluation, *IEEE Transactions on Geoscience and Remote sensing*, *28*(5), 781–790.

Huffman, G. J., R. F. Adler, M. M. Morrissey, D. T. Bolvin, S. Curtis, R. Joyce, B. McGavock, and J. Susskind (2001), Global precipitation at one-degree daily resolution from multisatellite observations, *Journal of hydrometeorology*, *2*(1), 36–50.

Hurrell, J. W., Y. Kushnir, G. Ottersen, and M. Visbeck (2003), An overview of the north atlantic oscillation, *Geophysical Monograph-American Geophysical Union*, *134*, 1–36.

Ionita, M., V. Nagavciuc, and B. Guan (2020), Rivers in the sky, flooding on the ground: the role of atmospheric rivers in inland flooding in central europe, *Hydrology and Earth System Sciences*, *24*(11), 5125–5147.

Kalnay, E., M. Kanamitsu, R. Kistler, W. Collins, D. Deaven, L. Gandin, M. Iredell, S. Saha, G. White, J. Woollen, et al. (1996), The ncep/ncar 40-year reanalysis project, *Bulletin of the American meteorological Society*, *77*(3), 437–472.

Kanamitsu, M., W. Ebisuzaki, J. Woollen, S.-K. Yang, J. Hnilo, M. Fiorino, and G. Potter (2002), Ncep–doe amip-ii reanalysis (r-2), *Bulletin of the American Meteorological Society*, *83*(11), 1631–1644.

Kay, J. E., C. Deser, A. Phillips, A. Mai, C. Hannay, G. Strand, J. M. Arblaster, S. Bates, G. Danabasoglu, J. Edwards, et al. (2015), The community earth system model (cesm) large ensemble project: A community resource for studying climate change in the presence of internal climate variability, *Bulletin of the American Meteorological Society*, *96*(8), 1333–1349.

Kidston, J., and E. Gerber (2010), Intermodel variability of the poleward shift of the austral jet stream in the cmip3 integrations linked to biases in 20th century climatology, *Geophysical Research Letters*, *37*(9).

Kim, H.-M., Y. Zhou, and M. A. Alexander (2019), Changes in atmospheric rivers and moisture transport over the northeast pacific and western north america in response to enso diversity, *Climate Dynamics*, *52*(12), 7375–7388.

Kim, J., H. Moon, B. Guan, D. E. Waliser, J. Choi, T.-Y. Gu, and Y.-H. Byun (2021), Precipitation characteristics related to atmospheric rivers in east asia, *International Journal of Climatology*, *41*, E2244–E2257.

Kim, S., L. R. Leung, B. Guan, and J. C. Chiang (2022), Atmospheric river representation in the energy exascale earth system model (e3sm) version 1.0, *Geoscientific Model Development*, *15*(14), 5461–5480.

Kobayashi, S., Y. Ota, Y. Harada, A. Ebita, M. Moriya, H. Onoda, K. Onogi, H. Kamahori, C. Kobayashi, H. Endo, et al. (2015), The jra-55 reanalysis: General specifications and basic characteristics, *Journal of the Meteorological Society of Japan. Ser. II*, *93*(1), 5–48.

Kug, J.-S., J.-H. Jeong, Y.-S. Jang, B.-M. Kim, C. K. Folland, S.-K. Min, and S.-W. Son

(2015), Two distinct influences of arctic warming on cold winters over north america and east asia, *Nature Geoscience*, *8*(10), 759–762.

Kumar, A., and M. Chen (2017), What is the variability in us west coast winter precipitation during strong el niño events?, *Climate Dynamics*, *49*(7), 2789–2802.

Kushner, P. J., I. M. Held, and T. L. Delworth (2001), Southern hemisphere atmospheric circulation response to global warming, *Journal of Climate*, *14*(10), 2238–2249.

Lamjiri, M. A., M. D. Dettinger, F. M. Ralph, and B. Guan (2017), Hourly storm characteristics along the us west coast: Role of atmospheric rivers in extreme precipitation, *Geophysical Research Letters*, *44*(13), 7020–7028.

Langenbrunner, B., J. D. Neelin, B. R. Lintner, and B. T. Anderson (2015), Patterns of precipitation change and climatological uncertainty among cmip5 models, with a focus on the midlatitude pacific storm track, *Journal of Climate*, *28*(19), 7857–7872.

Lavers, D. A., and G. Villarini (2013), The nexus between atmospheric rivers and extreme precipitation across europe, *Geophysical Research Letters*, *40*(12), 3259–3264.

Lavers, D. A., and G. Villarini (2015), The contribution of atmospheric rivers to precipitation in europe and the united states, *Journal of Hydrology*, *522*, 382–390.

Lavers, D. A., G. Villarini, R. P. Allan, E. F. Wood, and A. J. Wade (2012), The detection of atmospheric rivers in atmospheric reanalyses and their links to british winter floods and the large-scale climatic circulation, *Journal of Geophysical Research: Atmospheres*, *117*(D20).

Lee, J., K. R. Sperber, P. J. Gleckler, C. J. Bonfils, and K. E. Taylor (2019), Quantifying the agreement between observed and simulated extratropical modes of interannual variability, *Climate Dynamics*, *52*(7), 4057–4089.

Lee, J., K. R. Sperber, P. J. Gleckler, K. E. Taylor, and C. J. Bonfils (2021), Benchmarking performance changes in the simulation of extratropical modes of variability across cmip generations, *Journal of Climate*, *34*(17), 6945–6969.

Lee, S., and S. B. Feldstein (2013), Detecting ozone-and greenhouse gas–driven wind trends with observational data, *Science*, *339*(6119), 563–567.

Leung, L. R., and Y. Qian (2003), The sensitivity of precipitation and snowpack simulations to model resolution via nesting in regions of complex terrain, *Journal of Hydrometeorology*, *4*(6), 1025–1043.

Leung, L. R., and Y. Qian (2009), Atmospheric rivers induced heavy precipitation and flooding in the western us simulated by the wrf regional climate model, *Geophysical research letters*, *36*(3).

Li, C., W. Mei, and Y. Kamae (2022), Variability and predictability of cold-season north atlantic atmospheric river occurrence frequency in a set of high-resolution atmospheric simulations, *Climate Dynamics*, *58*(9), 2485–2500.

Li, Y., and N.-C. Lau (2012), Impact of enso on the atmospheric variability over the north atlantic in late winter—role of transient eddies, *Journal of Climate*, *25*(1), 320–342.

Liu, J., J. A. Curry, H. Wang, M. Song, and R. M. Horton (2012), Impact of declining arctic sea ice on winter snowfall, *Proceedings of the National Academy of Sciences*, *109*(11), 4074–4079.

Lora, J. M., C. Shields, and J. Rutz (2020), Consensus and disagreement in atmospheric river detection: Artmip global catalogues, *Geophysical Research Letters*, *47*(20), e2020GL089,302.

Lu, J., D. Xue, Y. Gao, G. Chen, L. Leung, and P. Staten (2018), Enhanced hydrological extremes in the western united states under global warming through the lens of water vapor wave activity, *npj Climate and Atmospheric Science*, *1*(1), 1–9.

Ma, W., and G. Chen (2022), What controls the interannual variability of the boreal winter atmospheric river activities over the northern hemisphere?, *Journal of Climate*, pp. 1–39.

Ma, W., J. Norris, and G. Chen (2020a), Projected changes to extreme precipitation along north american west coast from the cesm large ensemble, *Geophysical Research Letters*, *47*(1), e2019GL086,038.

Ma, W., G. Chen, and B. Guan (2020b), Poleward shift of atmospheric rivers in the southern hemisphere in recent decades, *Geophysical Research Letters*, *47*(21), e2020GL089,934.

Ma, W., G. Chen, Y. Peings, and N. Alviz (2021), Atmospheric river response to arctic sea ice loss in the polar amplification model intercomparison project, *Geophysical Research Letters*, *48*(20), e2021GL094,883.

Maclennan, M. L., J. T. Lenaerts, C. Shields, and J. D. Wille (2022), Contribution of atmospheric rivers to antarctic precipitation, *Geophysical research letters*, p. e2022GL100585.

Matrosov, S. Y. (2013), Characteristics of landfalling atmospheric rivers inferred from satellite observations over the eastern north pacific ocean, *Monthly Weather Review*, *141*(11), 3757–3768.

Mattingly, K., T. Mote, and X. Fettweis (2018), Atmospheric river impacts on greenland ice sheet surface mass balance, *Journal of Geophysical Research: Atmospheres*, *123*(16), 8538–8560.

McGowan, H., K. Borthwick, A. Schwartz, J. N. Callow, S. Bilish, and S. Browning (2021), Atmospheric rivers: An overlooked threat to the marginal snowpack of the australian alps, *Journal of Hydrometeorology*, *22*(10), 2521–2532.

Mesinger, F., G. DiMego, E. Kalnay, K. Mitchell, P. C. Shafran, W. Ebisuzaki, D. Jović, J. Woollen, E. Rogers, E. H. Berbery, et al. (2006), North american regional reanalysis, *Bulletin of the American Meteorological Society*, *87*(3), 343–360.

Miyazaki, K., H. Eskes, K. Sudo, M. Takigawa, M. Van Weele, and K. Boersma (2012), Simultaneous assimilation of satellite no 2, o 3, co, and hno 3 data for the analysis of tropospheric chemical composition and emissions, *Atmospheric Chemistry and Physics*, *12*(20), 9545–9579.

Mori, M., Y. Kosaka, M. Watanabe, H. Nakamura, and M. Kimoto (2019), A reconciled estimate of the influence of arctic sea-ice loss on recent eurasian cooling, *Nature Climate Change*, *9*(2), 123–129.

Moss, R. H., J. A. Edmonds, K. A. Hibbard, M. R. Manning, S. K. Rose, D. P. Van Vuuren, T. R. Carter, S. Emori, M. Kainuma, T. Kram, et al. (2010), The next generation of scenarios for climate change research and assessment, *Nature*, *463*(7282), 747–756.

Mundhenk, B. D., E. A. Barnes, E. D. Maloney, and C. F. Baggett (2018), Skillful empirical subseasonal prediction of landfalling atmospheric river activity using the madden–julian oscillation and quasi-biennial oscillation, *NPJ Climate and Atmospheric Science*, *1*(1), 1–7.

Nash, D., D. Waliser, B. Guan, H. Ye, and F. M. Ralph (2018), The role of atmospheric rivers in extratropical and polar hydroclimate, *Journal of Geophysical Research: Atmospheres*, *123*(13), 6804–6821.

Naud, C. M., J. Jeyaratnam, J. F. Booth, M. Zhao, and A. Gettelman (2020), Evaluation of modeled precipitation in oceanic extratropical cyclones using imerg, *Journal of Climate*, *33*(1), 95–113.

Neiman, P. J., F. M. Ralph, G. A. Wick, Y.-H. Kuo, T.-K. Wee, Z. Ma, G. H. Taylor, and M. D. Dettinger (2008a), Diagnosis of an intense atmospheric river impacting the pacific northwest: Storm summary and offshore vertical structure observed with cosmic satellite retrievals, *Monthly Weather Review*, *136*(11), 4398–4420.

Neiman, P. J., F. M. Ralph, G. A. Wick, J. D. Lundquist, and M. D. Dettinger (2008b), Meteorological characteristics and overland precipitation impacts of atmospheric rivers affecting the west coast of north america based on eight years of ssm/i satellite observations, *Journal of Hydrometeorology*, *9*(1), 22–47.

Nie, J., A. H. Sobel, D. A. Shaevitz, and S. Wang (2018), Dynamic amplification of extreme precipitation sensitivity, *Proceedings of the National Academy of Sciences*, *115*(38), 9467–9472.

Norris, J., G. Chen, and J. D. Neelin (2019a), Thermodynamic versus dynamic controls on extreme precipitation in a warming climate from the community earth system model large ensemble, *Journal of Climate*, *32*(4), 1025–1045.

Norris, J., G. Chen, and J. D. Neelin (2019b), Changes in frequency of large precipitation accumulations over land in a warming climate from the cesm large ensemble: The roles of moisture, circulation, and duration, *Journal of Climate*, *32*(17), 5397–5416.

Paltan, H., D. Waliser, W. H. Lim, B. Guan, D. Yamazaki, R. Pant, and S. Dadson (2017), Global floods and water availability driven by atmospheric rivers, *Geophysical Research Letters*, *44*(20), 10–387.

Park, J.-Y., S.-W. Yeh, and J.-S. Kug (2012), Revisited relationship between tropical and north pacific sea surface temperature variations, *Geophysical Research Letters*, *39*(2).

Pasquier, J., S. Pfahl, and C. M. Grams (2019), Modulation of atmospheric river occurrence and associated precipitation extremes in the north atlantic region by european weather regimes, *Geophysical Research Letters*, *46*(2), 1014–1023.

Patricola, C. M., J. P. O'Brien, M. D. Risser, A. M. Rhoades, T. A. O'Brien, P. A. Ullrich, D. A. Stone, and W. D. Collins (2020), Maximizing enso as a source of western us hydroclimate predictability, *Climate Dynamics*, *54*(1), 351–372.

Payne, A. E., and G. Magnusdottir (2015), An evaluation of atmospheric rivers over the north pacific in cmip5 and their response to warming under rcp 8.5, *Journal of Geophysical Research: Atmospheres*, *120*(21), 11–173.

Payne, A. E., M.-E. Demory, L. R. Leung, A. M. Ramos, C. A. Shields, J. J. Rutz, N. Siler, G. Villarini, A. Hall, and F. M. Ralph (2020), Responses and impacts of atmospheric rivers to climate change, *Nature Reviews Earth & Environment*, *1*(3), 143–157.

Peings, Y., and G. Magnusdottir (2014), Response of the wintertime northern hemisphere atmospheric circulation to current and projected arctic sea ice decline: A numerical study with cam5, *Journal of Climate*, *27*(1), 244–264.

Peings, Y., Z. M. Labe, and G. Magnusdottir (2021), Are 100 ensemble members enough to capture the remote atmospheric response to+ 2° c arctic sea ice loss?, *Journal of Climate*, *34*(10), 3751–3769.

Pfahl, S., P. A. O'Gorman, and E. M. Fischer (2017), Understanding the regional pattern of projected future changes in extreme precipitation, *Nature Climate Change*, *7*(6), 423–427.

Polvani, L. M., D. W. Waugh, G. J. Correa, and S.-W. Son (2011), Stratospheric ozone depletion: The main driver of twentieth-century atmospheric circulation changes in the southern hemisphere, *Journal of Climate*, *24*(3), 795–812.

Power, S., T. Casey, C. Folland, A. Colman, and V. Mehta (1999), Inter-decadal modulation of the impact of enso on australia, *Climate dynamics*, *15*(5), 319–324.

Pradhan, R. K., Y. Markonis, M. R. V. Godoy, A. Villalba-Pradas, K. M. Andreadis, E. I. Nikolopoulos, S. M. Papalexiou, A. Rahim, F. J. Tapiador, and M. Hanel (2022), Review of gpm imerg performance: A global perspective, *Remote Sensing of Environment*, *268*, 112,754.

Ralph, F., G. Wick, P. Neiman, B. Moore, J. Spackman, M. Hughes, F. Yong, and T. Hock (2012), Atmospheric rivers in reanalysis products: A six-event comparison with aircraft

observations of water vapor transport, in *Extended abstracts, wcrp reanalysis conf., silver spring, md.*

Ralph, F. M., P. J. Neiman, and G. A. Wick (2004), Satellite and caljet aircraft observations of atmospheric rivers over the eastern north pacific ocean during the winter of 1997/98, *Monthly Weather Review*, *132*(7), 1721–1745.

Ralph, F. M., P. J. Neiman, G. A. Wick, S. I. Gutman, M. D. Dettinger, D. R. Cayan, and A. B. White (2006), Flooding on california's russian river: Role of atmospheric rivers, *Geophysical Research Letters*, *33*(13).

Ralph, F. M., J. J. Rutz, J. M. Cordeira, M. Dettinger, M. Anderson, D. Reynolds, L. J. Schick, and C. Smallcomb (2019), A scale to characterize the strength and impacts of atmospheric rivers, *Bulletin of the American Meteorological Society*, *100*(2), 269–289.

Rayner, N., D. E. Parker, E. Horton, C. K. Folland, L. V. Alexander, D. Rowell, E. C. Kent, and A. Kaplan (2003), Global analyses of sea surface temperature, sea ice, and night marine air temperature since the late nineteenth century, *Journal of Geophysical Research: Atmospheres*, *108*(D14).

Rienecker, M. M., M. J. Suarez, R. Gelaro, R. Todling, J. Bacmeister, E. Liu, M. G. Bosilovich, S. D. Schubert, L. Takacs, G.-K. Kim, et al. (2011), Merra: Nasa's modern-era retrospective analysis for research and applications, *Journal of climate*, *24*(14), 3624–3648.

Rogers, J. C. (1981), The north pacific oscillation, *Journal of Climatology*, *1*(1), 39–57.

Ronalds, B., E. A. Barnes, R. Eade, Y. Peings, and M. Sigmond (2020), North pacific zonal wind response to sea ice loss in the polar amplification model intercomparison project and its downstream implications, *Climate Dynamics*, *55*(7), 1779–1792.

Rutz, J. J., and W. J. Steenburgh (2012), Quantifying the role of atmospheric rivers in the interior western united states, *Atmospheric Science Letters*, *13*(4), 257–261.

Rutz, J. J., C. A. Shields, J. M. Lora, A. E. Payne, B. Guan, P. Ullrich, T. O'brien, L. R. Leung, F. M. Ralph, M. Wehner, et al. (2019), The atmospheric river tracking method intercomparison project (artmip): quantifying uncertainties in atmospheric river climatology, *Journal of Geophysical Research: Atmospheres*, *124*(24), 13,777–13,802.

Saha, S., S. Moorthi, H.-L. Pan, X. Wu, J. Wang, S. Nadiga, P. Tripp, R. Kistler, J. Woollen, D. Behringer, et al. (2010), The ncep climate forecast system reanalysis, *Bulletin of the American Meteorological Society*, *91*(8), 1015–1058.

Salinger, M., J. Renwick, and A. Mullan (2001), Interdecadal pacific oscillation and south pacific climate, *International journal of climatology: a journal of the Royal Meteorological Society*, *21*(14), 1705–1721.

Schneider, D. P., and C. Deser (2018), Tropically driven and externally forced patterns of antarctic sea ice change: Reconciling observed and modeled trends, *Climate Dynamics*, *50*(11), 4599–4618.

Schwalm, C. R., S. Glendon, and P. B. Duffy (2020), Rcp8. 5 tracks cumulative co2 emissions, *Proceedings of the National Academy of Sciences*, *117*(33), 19,656–19,657.

Screen, J. A., I. Simmonds, C. Deser, and R. Tomas (2013), The atmospheric response to three decades of observed arctic sea ice loss, *Journal of climate*, *26*(4), 1230–1248.

Screen, J. A., C. Deser, D. M. Smith, X. Zhang, R. Blackport, P. J. Kushner, T. Oudar, K. E. McCusker, and L. Sun (2018a), Consistency and discrepancy in the atmospheric response to arctic sea-ice loss across climate models, *Nature Geoscience*, *11*(3), 155–163.

Screen, J. A., T. J. Bracegirdle, and I. Simmonds (2018b), Polar climate change as manifest in atmospheric circulation, *Current Climate Change Reports*, *4*(4), 383–395.

Seager, R., and N. Henderson (2013), Diagnostic computation of moisture budgets in the era-interim reanalysis with reference to analysis of cmip-archived atmospheric model data, *Journal of Climate*, *26*(20), 7876–7901.

Seager, R., D. Neelin, I. Simpson, H. Liu, N. Henderson, T. Shaw, Y. Kushnir, M. Ting, and B. Cook (2014), Dynamical and thermodynamical causes of large-scale changes in the hydrological cycle over north america in response to global warming, *Journal of Climate*, *27*(20), 7921–7948.

Shaw, T., M. Baldwin, E. A. Barnes, R. Caballero, C. Garfinkel, Y.-T. Hwang, C. Li, P. O'gorman, G. Rivière, I. Simpson, et al. (2016), Storm track processes and the opposing influences of climate change, *Nature Geoscience*, *9*(9), 656–664.

Shields, C. A., J. J. Rutz, L.-Y. Leung, F. M. Ralph, M. Wehner, B. Kawzenuk, J. M. Lora, E. McClenny, T. Osborne, A. E. Payne, et al. (2018), Atmospheric river tracking method intercomparison project (artmip): project goals and experimental design, *Geoscientific Model Development*, *11*(6), 2455–2474.

Smith, D. M., J. A. Screen, C. Deser, J. Cohen, J. C. Fyfe, J. García-Serrano, T. Jung, V. Kattsov, D. Matei, R. Msadek, et al. (2019), The polar amplification model intercomparison project (pamip) contribution to cmip6: investigating the causes and consequences of polar amplification, *Geoscientific Model Development*, *12*(3), 1139–1164.

Solman, S. A., and I. Orlanski (2014), Poleward shift and change of frontal activity in the southern hemisphere over the last 40 years, *Journal of the Atmospheric Sciences*, *71*(2), 539–552.

Sousa, P. M., R. C. Blamey, C. J. Reason, A. M. Ramos, and R. M. Trigo (2018), The 'day zero'cape town drought and the poleward migration of moisture corridors, *Environmental Research Letters*, *13*(12), 124,025.

Swart, N. C., J. C. Fyfe, N. Gillett, and G. J. Marshall (2015), Comparing trends in the southern annular mode and surface westerly jet, *Journal of Climate*, *28*(22), 8840–8859.

Tan, Y., F. Zwiers, S. Yang, C. Li, and K. Deng (2020), The role of circulation and its

changes in present and future atmospheric rivers over western north america, *Journal of Climate*, *33*(4), 1261–1281.

Taylor, K. E., R. J. Stouffer, and G. A. Meehl (2012), An overview of cmip5 and the experiment design, *Bulletin of the American meteorological Society*, *93*(4), 485–498.

Teng, H., and G. Branstator (2017), Causes of extreme ridges that induce california droughts, *Journal of Climate*, *30*(4), 1477–1492.

Thackeray, C. W., A. M. DeAngelis, A. Hall, D. L. Swain, and X. Qu (2018), On the connection between global hydrologic sensitivity and regional wet extremes, *Geophysical Research Letters*, *45*(20), 11–343.

Thapa, K., T. A. Endreny, and C. R. Ferguson (2018), Atmospheric rivers carry nonmonsoon extreme precipitation into nepal, *Journal of Geophysical Research: Atmospheres*, *123*(11), 5901–5912.

Thompson, D. W., S. Solomon, P. J. Kushner, M. H. England, K. M. Grise, and D. J. Karoly (2011), Signatures of the antarctic ozone hole in southern hemisphere surface climate change, *Nature geoscience*, *4*(11), 741–749.

Tian, B., E. J. Fetzer, B. H. Kahn, J. Teixeira, E. Manning, and T. Hearty (2013), Evaluating cmip5 models using airs tropospheric air temperature and specific humidity climatology, *Journal of Geophysical Research: Atmospheres*, *118*(1), 114–134.

Ting, M., R. Seager, C. Li, H. Liu, and N. Henderson (2018), Mechanism of future spring drying in the southwestern united states in cmip5 models, *Journal of Climate*, *31*(11), 4265–4279.

Trenberth, K. E., A. Dai, R. M. Rasmussen, and D. B. Parsons (2003), The changing character of precipitation, *Bulletin of the American Meteorological Society*, *84*(9), 1205–1218.

Viale, M., R. Valenzuela, R. D. Garreaud, and F. M. Ralph (2018), Impacts of atmospheric rivers on precipitation in southern south america, *Journal of Hydrometeorology*, *19*(10), 1671–1687.

Waliser, D., and B. Guan (2017), Extreme winds and precipitation during landfall of atmospheric rivers, *Nature Geoscience*, *10*(3), 179–183.

Wallace, J. M., C. Smith, and C. S. Bretherton (1992), Singular value decomposition of wintertime sea surface temperature and 500-mb height anomalies, *Journal of climate*, *5*(6), 561–576.

Wang, Z., J. Walsh, S. Szymborski, and M. Peng (2020), Rapid arctic sea ice loss on the synoptic time scale and related atmospheric circulation anomalies, *Journal of Climate*, *33*(5), 1597–1617.

Warner, M. D., C. F. Mass, and E. P. Salathé (2015), Changes in winter atmospheric rivers along the north american west coast in cmip5 climate models, *Journal of Hydrometeorology*, *16*(1), 118–128.

Wick, G. A., P. J. Neiman, and F. M. Ralph (2012), Description and validation of an automated objective technique for identification and characterization of the integrated water vapor signature of atmospheric rivers, *IEEE Transactions on Geoscience and Remote Sensing*, *51*(4), 2166–2176.

Wille, J. D., V. Favier, A. Dufour, I. V. Gorodetskaya, J. Turner, C. Agosta, and F. Codron (2019), West antarctic surface melt triggered by atmospheric rivers, *Nature Geoscience*, *12*(11), 911–916.

Wille, J. D., V. Favier, N. C. Jourdain, C. Kittel, J. V. Turton, C. Agosta, I. V. Gorodetskaya, G. Picard, F. Codron, C. L.-D. Santos, et al. (2022), Intense atmospheric rivers can weaken ice shelf stability at the antarctic peninsula, *Communications Earth & Environment*, *3*(1), 1–14.

Woods, C., and R. Caballero (2016), The role of moist intrusions in winter arctic warming and sea ice decline, *Journal of Climate*, *29*(12), 4473–4485.

Xiong, Y., and X. Ren (2021), Influences of atmospheric rivers on north pacific winter precipitation: Climatology and dependence on enso condition, *Journal of Climate*, *34*(1), 277–292.

Yang, D., J. M. Arblaster, G. A. Meehl, M. H. England, E.-P. Lim, S. Bates, and N. Rosenbloom (2020), Role of tropical variability in driving decadal shifts in the southern hemisphere summertime eddy-driven jet, *Journal of Climate*, *33*(13), 5445–5463.

Yang, W., and G. Magnusdottir (2017), Springtime extreme moisture transport into the arctic and its impact on sea ice concentration, *Journal of Geophysical Research: Atmospheres*, *122*(10), 5316–5329.

Yang, Y., T. Zhao, G. Ni, and T. Sun (2018), Atmospheric rivers over the bay of bengal lead to northern indian extreme rainfall, *International Journal of Climatology*, *38*(2), 1010–1021.

Zavadoff, B. L., and B. P. Kirtman (2020), Dynamic and thermodynamic modulators of european atmospheric rivers, *Journal of Climate*, *33*(10), 4167–4185.

Zhang, P., G. Chen, W. Ma, Y. Ming, and Z. Wu (2021), Robust atmospheric river response to global warming in idealized and comprehensive climate models, *Journal of Climate*, *34*(18), 7717–7734.

Zhang, T., M. P. Hoerling, K. Wolter, J. Eischeid, L. Cheng, A. Hoell, J. Perlwitz, X.-W. Quan, and J. Barsugli (2018), Predictability and prediction of southern california rains during strong el niño events: A focus on the failed 2016 winter rains, *Journal of Climate*, *31*(2), 555–574.

Zhang, W., Z. Wang, M. F. Stuecker, A. G. Turner, F.-F. Jin, and X. Geng (2019a), Impact of enso longitudinal position on teleconnections to the nao, *Climate Dynamics*, *52*(1), 257–274.

Zhang, Y., J. M. Wallace, and D. S. Battisti (1997), Enso-like interdecadal variability: 1900–93, *Journal of climate*, *10*(5), 1004–1020.

Zhang, Z., F. M. Ralph, and M. Zheng (2019b), The relationship between extratropical cyclone strength and atmospheric river intensity and position, *Geophysical Research Letters*, *46*(3), 1814–1823.

Zhou, Y., H. Kim, and D. E. Waliser (2021a), Atmospheric river lifecycle responses to the madden-julian oscillation, *Geophysical Research Letters*, *48*(3), e2020GL090,983.

Zhou, Y., T. A. O'Brien, P. A. Ullrich, W. D. Collins, C. M. Patricola, and A. M. Rhoades (2021b), Uncertainties in atmospheric river lifecycles by detection algorithms: climatology and variability, *Journal of Geophysical Research: Atmospheres*, *126*(8), e2020JD033,711.

Zhu, Y., and R. E. Newell (1998), A proposed algorithm for moisture fluxes from atmospheric rivers, *Monthly weather review*, *126*(3), 725–735.